BLAST RETROFIT OF UNREINFORCED MASONRY WALLS USING ECC SHOTCRETE

By

Jordan Gandia

Thesis submitted to the
Faculty of Graduate Studies and Research
in partial fulfillment of the requirements for the degree of
Master of Applied Sciences
in Civil Engineering

uOttawa

Department of Civil Engineering
Faculty of Engineering
University of Ottawa

ABSTRACT

Blast loads on buildings can originate from accidental explosions or from targeted attacks. Design against blast loads has become an increasingly important topic due to the current political climate. Unfortunately, many older buildings are constructed with unreinforced masonry (URM) walls which are particularly susceptible to out of plane failures caused by blast loads. One solution to increase the safety of these buildings is to retrofit them with advanced materials that can increase their out-of-plane stiffness and resistance. This thesis investigates the potential of using a high-performance shotcrete as a retrofit system for URM walls against blast effects. The shotcrete used in this study is made from Engineered Cementitious Composite (ECC), a special type of fiber-reinforced cementitious material, with high ductility and high energy-absorption capacity. The ECC shotcrete replaces aggregates with synthetic microfibers to increase tensile strength and ductility. A welded wire mesh was embedded in the shotcrete to provide ductile behavior.

The testing program includes a total of six large-scale unreinforced masonry wall specimens. Two walls were constructed using concrete masonry unit (CMU) blocks to be retrofitted. The first specimen was built as an infill wall, experiencing no axial load, while the second specimen was built as a load bearing wall, with 10% axial load. Four more walls were built out of stone blocks. Two of the stone walls were controls: one infill and one load bearing (4% axial load). The other two stone walls were retrofit with the shotcrete system: one infill and one load bearing (4% axial load).

The blast loads were simulated using the University of Ottawa's Shock Tube. The walls were restrained at the top and bottom with a shear restraint to induce one way bending. Pressure, displacement and strain data were acquired with the use of pressure gauges, LVDT's, strain gauges and cameras.

The specimens were subjected to gradually increasing blast pressures until failure. The performance of the specimens was observed by analyzing the displacement, crack widths, fragmentation and failure mode. The results indicate the benefits of using ECC shotcrete as a retrofit system. The displacements of the retrofit walls were very small compared to the control walls, and fragments were limited. The specimens with axial load were found to have increased resistance. While the failure mode was brittle for the retrofit walls, this can be avoided with the use of a mesh with a larger area of steel.

A SDOF analysis was performed to predict the blast response of the test walls. The analysis was done by generating resistance functions for the walls through analytical models. The analysis was found to agree reasonably well with the experimental data.

ACKNOWLEDGEMENTS

I would like to thank those who through their efforts and guidance made this thesis possible.

In particular, I would like to thank my supervisors Hassan Aoude and Murat Saatcioglu for offering their experience and time to focus and direct this study. I also would like to thank the lab Technicians, Gamal Elnabelsya and Muslim Majeed, who helped coordinate and direct the lab work. Without their help, this project would not have been possible.

For their help during my testing in the lab and their expertise with the shocktube system, I would like to thank my fellow colleagues Hyunchul Jung, Laura Ciornei, Alameer Alameer, and Yang Li.

Furthermore, I wish to show my appreciation to Kings Shotcrete Solutions who provided the shotcrete for the project, Nicolas Ginouse and Cody Fournier who oversaw the shotcrete application, and Béton Projeté MAH for expertly applying the shotcrete.

NOTATIONS

Symbol	Definition
A	Cross-sectional Area of wall
A_e	Effective area
A_{sh}	Area of the shotcrete layer
A_{st}	Area of the steel mesh
C	Compression force in the masonry
C'	Compression force due to Arching Action
E	Elastic modulus
$F(t)$	Forcing function
F_{cr}	Force that causes cracking
F_r	Maximum resistance for retrofit walls
F_u	Maximum resistance for URM walls
H	Height of the wall
I	Moment of inertia
I_g	Gross moment of inertia
I_R	Reflected Impulse
K_{LM}	Load Mass Factor
K_e	Elastic stiffness
K_{ep}	Elasto-plastic stiffness
K_p	Plastic stiffness
L_d	Driver Length
M_{cr}	Cracking moment
M_p	Plastic moment
P	Applied axial load
P_d	Driver Pressure
P_o	Axial load capacity for wall
P_r	Reflected Pressure
$R(u(t))$	Resistance function
R_e	Elastic resistance
R_{ep}	Elasto-plastic resistance
T_{sh}	Tension force in shotcrete layer
T_{st}	Tension force in the steel mesh
W_{cr}	Distributed load that causes cracking
W_u	Ultimate distributed load
Z	Scaled distance
a	Depth of the compression force in the masonry
a'	Depth of the compression force due to Arching Action
c	Location of neutral axis with respect to extreme tension fibre
d	Depth to the steel mesh
d_{max}	Maximum displacement
d_{res}	Residual displacement
f_c	Stress due to arching action
f_j'	Compressive strength of mortar cubes

f'_m	Compressive strength of masonry prisms
f_{mr}	Modulus of rupture for mortar
f_{sh}	Tension stress in the shotcrete layer
f_{st}	Stress in the steel mesh
f_u	Ultimate stress
f_y	Yielding stress
h	Thickness of the wall
l	Length of the wall
m	Mass of the wall
t	Thickness of the wall
t_{sh}	Thickness of the shotcrete layer
t_d	Duration of the positive phase of the blast
t_{max}	Time at which wall achieved maximum displacement
$u(t)$	Displacement of the wall
$\ddot{u}(t)$	Acceleration of the wall
y	Depth to the centroid of the compression force in the masonry
ε	Strain
ε_c	Compressive strain
ε_t	Tensile strain
ε_u	Ultimate strain
ε_y	Yielding strain
ε_1	Strain in mortar at start of crushing region
ε_2	Strain in mortar at end of crushing region
λ	Angle of rotation of URM wall
μ_{max}	Ratio of maximum deformation and deformation at yield
γ	Ratio between thickness of wall, t, to length of moment arm (Arching Action)
δ	Axial shortening of wall
θ	Support rotation
Δ	Midpoint displacement of wall
Δ_{cr}	Displacement at cracking
$\Delta_{\varepsilon 1}$	Displacement at start of crushing region
$\Delta_{\varepsilon 2}$	Displacement at end of crushing region

ACRONYMS

Acronym	Definition
ACI	American Concrete Institute
ASTM	American Society for Testing and Materials
CFRP	Carbon Fibre Reinforced Polymer
CMU	Concrete Masonry Unit
CSA	Canadian Standards Association
DAC	Data Acquisition system
DIF	Dynamic Increase Factor
ECC	Engineered Cementitious Composite
EDCC	Eco-Friendly Ductile Cementitious Composite
FEM	Finite Element Modelling
FRP	Fibre Reinforced Polymer
FRS	Fibre Reinforced Shotcrete
GFRP	Glass Fibre Reinforced Polymer
HPFRCC	High-Performance Fibre Reinforced Cementitious Composite
HPP	High Performance Polypropylene
HSS	Hollow Structural Steel
MDOF	Multi Degree of Freedom
NSM	Near Surface Mounted
POSS	Polyhedral Oligomeric Silsesquioxane
PVA	Polyvinyl alcohol
RC	Reinforced Concrete
SDOF	Single Degree of Freedom
SIF	Strength Increase Factor
TNT	Trinitrotoluene
TRM	Textile Reinforced Mortar
UDL	Uniformly Distributed Load
UHPFRC	Ultra-High Performance Fibre Reinforced Concrete
URM	Unreinforced Masonry
XGnP	Exfoliated Graphene Nano Platelets

Table of Contents

Lists of Figures

Lists of Tables

CHAPTER 1. INTRODUCTION

1.1. GENERAL

There has been a growing need in the current political climate to strengthen buildings, such as government facilities or embassies, to resist blast loads. Targeted and malicious explosions, such as the Oklahoma bombing in 1995, are becoming more common as national symbols and ideologies are increasingly coming under attack. There have been several bombing attacks since 1965 in Canada, some of which are listed below (Braimah, 2017):

- Yugoslav Consulate Bombing, Toronto, 1965
- Yugoslav Embassy Bombing, Ottawa and Toronto, 1969
- Montreal Stock Exchange Bombing, 1969
- Cuban Consulate Bombing, Montreal, 1980
- Cheekye-Dunsmuir Bombings, 1982
- Litton Industries Bombing, Toronto, 1982
- Montreal Central Station Bombing, 1984
- Ben Wider Community Centre Bombing, Montreal, 2007
- EnCana Sour Gas Pipeline Bombing, Dawson Creek, 2008s

Blast loads can also originate from accidental explosions. The damage caused by accidental explosions varies greatly with the circumstances. In 1917 in Halifax, two ships collided together in an explosion with around 2500 metric tonnes of explosives (Braimah, 2017). The explosion caused severe damage to the surrounding buildings. In 1994 in Alaska, a worker at the Halliburton Perforator Gun Assembly Factory accidently hit the detonation cord of a charge which caused severe damage to the facility, including killing 1 employee and injuring another 5 (Braimah, 2017). In 1998 in Kean Canyon, Nevada, two explosions with an estimated mass of 22000 kg destroyed the buildings in the surrounding area, killing 4 and injuring 6 (Braimah, 2017). In 2001, Toulouse, France, a fertilizer factory exploded which killed 31 and injured 2400 more people (Braimah, 2017). A recent explosion occurred in 2013 in Lac Megantic, Quebec. Train cars containing crude oil derailed and exploded, leaving 47 dead and destroying nearby buildings (The Canadian Press, 2016).

Masonry buildings are exceptionally vulnerable to blast loads. According to Bruneau (1994), a "large proportion of North America's older building inventory is of unreinforced masonry (URM), constructed in the absence of mandatory earthquake design requirements, and unquestionably recognized as the type of construction most vulnerable to earthquakes". URM is often found as infill and load bearing walls in these older buildings. The poor out-of-plane resistance of URM walls also makes them very vulnerable to failure under blast loads. Dangerously, blast loads can demolish URM walls, often creating projectiles that can harm building occupants.

Polyurea and fibre reinforced polymer (FRP) retrofit systems are two retrofit strategies that have been studied in the literature and used in the industry to strengthen URM walls to resist out-of-plane loads. Polyurea systems are comprised of spraying an elastomeric coating on the surface of the masonry wall, potentially in tandem with vertical steel rebar. Fundamentally, FRP retrofit systems are made by applying an FRP fabric with adhesive to the surface of the masonry wall.

This research investigates the potential of using high-performance shotcrete to retrofit URM walls against blast effects. Engineered cementitious composite (ECC) is a special kind of fiber-

reinforced concrete material, which can be applied as a shotcrete to retrofit structures. ECC consists of a dense cementitious matrix containing a high a dose of synthetic fibres and lacks any coarse aggregate. While there has been some research related to the material properties of ECC, as well as using ECC for seismic strengthening, there has been very little research done on the effectiveness of ECC shotcrete retrofit systems used to strengthen URM walls against blast loads.

The following sections present the objectives and scope of this research, as well as the breakdown of the thesis.

1.2. OBJECTIVES AND SCOPE

The objective of this thesis is to experimentally investigate the effectiveness of fiber reinforced shotcrete (FRS) to enhance the blast performance of URM walls. The fiber-reinforced shotcrete used in this study can be categorized as an Engineered Cementitious Composite (ECC). The use of ECC retrofit systems can then be recommended as a viable blast mitigation method. Analytical models will be developed to corroborate the experimental tests.

The scope of this research includes:

1. A literature review providing background information on masonry wall failure modes for both URM walls and retrofit walls. Different retrofit techniques investigated in the literature are presented, including FRP, Polyurea and Shotcrete retrofit systems. Previous research done on seismic and blast retrofit of masonry walls is also presented, and analytical models which can be used to predict their behaviour are reviewed.
2. An experimental program designed to evaluate the effectiveness of ECC shotcrete retrofit systems to improve the blast performance of unreinforced masonry (URM) walls. The testing program includes 6 specimens (2 control walls and 4 retrofit walls) and includes infill and load-bearing walls made of concrete masonry units (CMU) and stone blocks. The parameters investigated include: the effect of the retrofit, the effect of axial load and the effect of masonry type on blast performance.
3. Analytical modelling of the walls used to predict the strength and blast response of the shotcrete retrofit systems. A comparison of the analytical and experimental results.
4. Recommendations for the use of shotcrete retrofit systems for blast loading applications.

1.3 THESIS BREAKDOWN

Chapter 1 - Introduction:

- Provides a general overview of the paper. Outlines the objective and scope of the testing program.

Chapter 2 - Literature review:

- Provides an overview of URM walls and various blast retrofit systems. Reviews failure modes of unreinforced and retrofit masonry walls. Discusses different models used to predict masonry wall behaviour. Summarizes previous research on FRP, polyurea and shotcrete retrofit systems.

Chapter 3 - Experimental program:

- Presents an overview of the experimental program and details of the test specimens. Details the construction of the walls and the application of the shotcrete. Outlines the material tests conducted and the properties of the materials used. Details the test sequence, data acquisition system and the shock-tube setup.

Chapter 4 – Experimental Results:

- Presents the results for each wall. The pressure, impulse and displacement histories are shown in figures, as well as strain data taken for the last two walls tested. Photos of each test are presented in this section.

Chapter 5 – Discussion:

- Comparisons are drawn from the different walls tested in this study. The effects of the different parameters on blast capacity, displacements and failure mode are discussed: Retrofit vs control, CMU vs Stone, infill vs load bearing. The shotcrete retrofit systems are also compared with the polyurea retrofit systems tested by Ciornei et al. (2012).

Chapter 6 – Analysis

- The resistance functions of the walls are determined using the experimental response data. Sectional analysis is also performed to determine the out-of-plane capacity of the walls. The resistance functions are then used to predict the blast response of the walls using single-degree-of-freedom analysis. The analytical results are compared to the measured results.

Chapter 7 – Conclusion

- The conclusions drawn from the experimental tests are summarized, as well as the comparisons of the analytical and experimental results. A conclusion is reached as to the effectiveness of fiber-reinforced shotcrete systems for the blast retrofit of URM walls.

CHAPTER 2. LITERATURE REVIEW

2.1. CHAPTER OVERVIEW

This chapter provides a literature review related to this thesis. Section 2.2 provides background on masonry as a construction material. Different failure modes for unreinforced masonry (URM) walls and current blast design requirements for masonry construction are also reviewed. Section 2.3 provides a review of the different retrofit systems discussed in this research including: shotcrete and engineered fiber-reinforced shotcrete and spray-on polymer systems. To put the research into context, previous blast studies on the use of FRP and spray-on polyuria retrofits are reviewed in Section 2.4. Section 2.5 reviews previous research on the use of shotcrete and fiber-reinforced concrete systems for the seismic and blast retrofit of masonry walls. Finally, Section 2.6 discusses various modelling approaches that can be used in the analysis of URM and retrofitted walls.

2.2. INTRODUCTION TO UNREINFORCED MASONRY WALLS

2.2.1. Masonry as a Construction Material

Masonry is commonly used to build walls in the construction industry, with materials including concrete, clay or stone. Concrete blocks are known as Concrete Masonry Units (CMU), and are characterized by being hollow to allow reinforcing rebar to pass through. According to Drysdale and Hamid (2005), the standard CMU block refers to the most commonly used size, which is 200x200x400mm. The architectural CMU blocks used in this research have dimensions of 100x200x400mm. CMU blocks also come in different shapes (see **Figure 2-1**). Plain end blocks and splitter blocks were used to construct the walls in this study.

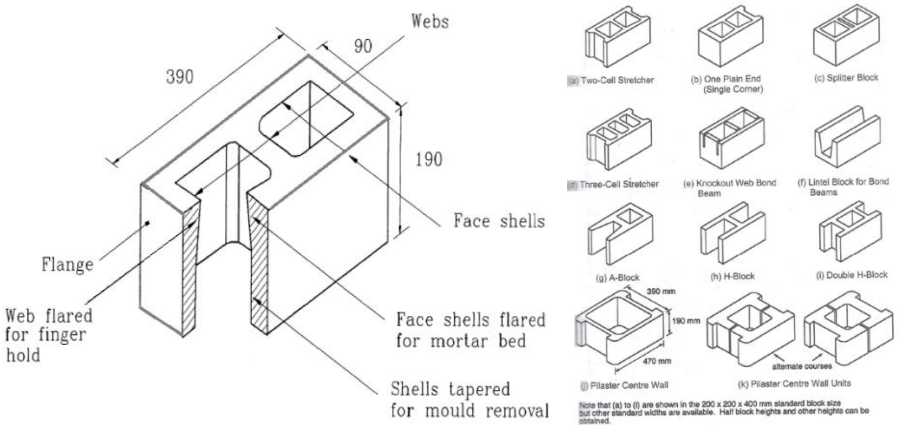

A) B)

Figure 2-1. A) CMU blocks used in this research (Glanville, 1996). B) Different types of CMU blocks (Drysdale et al., 2005)

Stone blocks are available "in a virtually limitless range of sizes and shapes, varying from brick-size units to storey-height panel" (Drysdale and Hamid, 2005). The stones used in this research were sedimentary in origin and came in three different sizes: small (90x60x600mm), medium (90x135x600mm), and large (90x200x600mm). While stone blocks are still being used in the

industry, they are commonly found in older or historical buildings. **Figure 2-2** shows an example of the stone and CMU blocks used in this research.

A) B)

Figure 2-2. A) Stone Blocks and B) CMU blocks

2.2.2. Unreinforced Masonry walls

Masonry walls can either be categorized as infill or load bearing walls. Infill walls are not designed to carry building loads and are just used to fill the wall space between concrete or steel frames. Masonry walls usually have gaps between the frame and the wall to account for the deformability of the structure, which greatly decreases the out-of-plane resistance of the wall (Ciornei, 2012). Filling these gaps to activate arching action is one possible retrofit to increase the out-of-plane resistance of these walls. Conversely, load bearing masonry walls are designed to carry the weight of the structure, and as a result have more pronounced arching action. Arching action occurs when a wall bends in an out-of-plane direction, which creates a stress between the wall and the frame. The induced stress creates a resisting moment to the out-of-plane force, as shown in **Figure 2-3**.

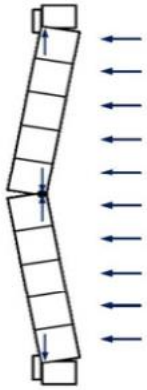

Figure 2-3. Arching Action. (Ciornei, 2012)

While modern codes such as the CSA S304.1-14 standard require the use of reinforcement in the construction of masonry walls, older buildings were often built without such reinforcement (Ciornei, 2012). Unreinforced Masonry (URM) walls are very weak to out-of-plane loading and can completely fail at relatively low loads caused by earthquakes (see **Figure 2-4** which shows examples of failures of URM walls in past earthquakes). The weak out-of-plane resistance of URM walls also makes them vulnerable under blast loads, where failure can occur under very low blast pressures (Ciornei, 2012). Failure of masonry walls under blast loads can also lead to

fragmentation and the ejection of blocks at high speeds, which can injure building occupants. There is therefore a need to reinforce and retrofit such walls to strengthen their resistance.

Figure 2-4. Examples of Out-of-plane failure of URM walls caused by earthquakes (Bruneau, 1994)

2.2.3. Failure Modes of Unreinforced Masonry Walls

Masonry walls can experience two different types of directional loading: in-plane and out-of-plane. These loading directions determine how the wall will behave and results in different failure modes. An understanding of these failure modes is important to evaluate wall resistance and possible retrofit options. The objective of this thesis is to study the effect of retrofitted walls to blast in the out-of-plane direction, therefore more emphasis will be placed on out-of-plane failure modes.

2.2.3.1. In-plane Failure modes

Dynamic in plane loading can be experienced by masonry walls during earthquakes. As shown in **Figure 2-5**, there are four different types of failure modes for masonry walls loaded in the lateral in-plane direction: 1) shear failure, 2) sliding failure, 3) rocking and 4) toe crushing failure. The type of failure mode depends on various factors, including: "load combinations, wall geometry, properties of materials, and details of reinforcement" (Sabri, 2018).

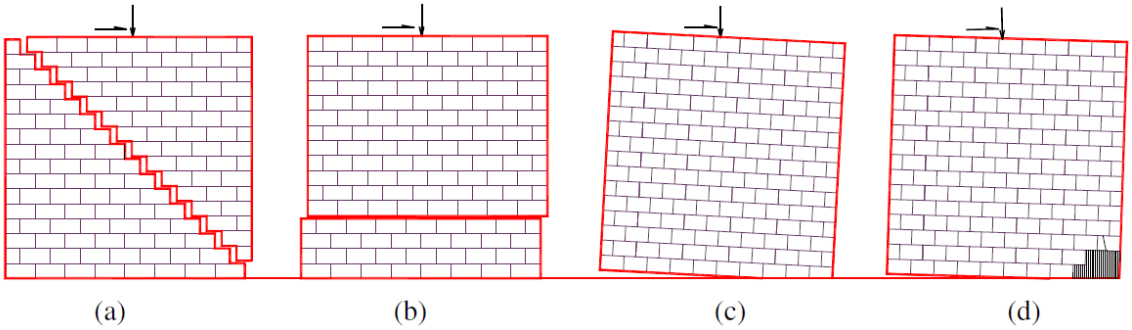

Figure 2-5. In-plane Failure modes. a) Shear failure. b) Sliding Failure. c) Rocking Failure. d) Toe crushing. (ElGawady, 2006)

2.2.3.2. Out-of-plane Failure modes

Out-of-plane loading can be experienced by masonry walls during earthquakes and blasts. For unretrofitted masonry walls, out-of-plane failure modes include cantilever and beam bending failure. Retrofitted masonry walls can exhibit failure modes which include beam bending failure, shear failure, and debonding of the retrofit.

Cantilever

Cantilever failure occurs when the wall rotates around its base, and the wall becomes unstable when it deflects beyond the point of failure (Sharif et al., 2007). As shown in **Figure 2-6**, the wall fails when the center of mass deflects over the base of the wall. This failure mode will occur due to lack of shear restraints, or if the shear restraints along the wall do not have adequate resistance. According to Bruneau (1994), many older URM buildings in North America have no floor or roof anchors connecting to the masonry walls. Furthermore, designers of older buildings that did include shear restraints did not typically consider earthquake loads when designing for anchors. Bruneau (1994) indicates that the potential of failure of the anchors in older URM buildings is high; the metal may shear, or the anchor may pull out of the diaphragm or the masonry wall. For the walls tested in this thesis, the walls will be designed and modelled to have adequate shear resistance to prevent this mode of failure. In the experimental tests conducted by Wang et al. (2016), the setup allowed for the wall to behave as a partial cantilever. The walls were supported with vertical restraints on both sides, with no horizontal shear restraint along the top of the wall (Wang et al., 2016). The failure modes of the unreinforced walls show that the top of the walls failed in a cantilever manner (Wang et al., 2016).

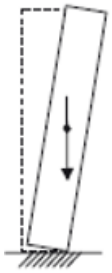

Figure 2-6. Cantilever Failure mode (Sharif et al., 2007)

Beam Bending Failure

Beam bending failure will occur when there is adequate shear restraint along the top and bottom diaphragms. A schematic representation of the beam bending failure mode is shown in **Figure 2-7**. The wall will act as a simply supported beam since the inertial forces generated by the wall are distributed to the top and bottom supports (Meisl et al., 2007). As the wall deflects, it generates moment resistance along its height, with the largest moment at mid-height. The moment creates a tensile stress along the back end of the wall, and results in a crack being created in the mortar. Meisl et al. (2007) states that the crack is usually found above mid-height. According to Sharif et al. (2007), "this crack will cause the wall to behave as two semi-rigid bodies, which rock in the out-of-plane direction". Failure will likely occur when the wall continues to deflect and becomes unstable at a deflection equal to the width of the wall (Sharif et al., 2007). The control walls tested by Baylot et al. (2005) acted in a beam bending manner. Three walls tested in the paper experienced a primary crack developing in the mid-height mortar joint (Baylot et al., 2005).

Ciornei (2012) tested two walls, one infill and one load bearing, under shock-tube induced blast loading. The infill wall failed in a beam bending manner with a hinge developing at mid-height (Ciornei, 2012). The load bearing wall acted similarly; the wall failed beginning with "the formation of a hinge in the middle, [followed by] the opening of the middle mortar joint, [and] by the opening of other joints" (Ciornei, 2012). Myers (2004) tested two control walls under live blast loads with no retrofit and noted the same failure mechanism. Myers (2004) noted that they failed "in a tensile failure mode in zones of high flexure".

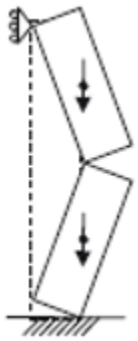

Figure 2-7. Beam Bending Failure (Sharif et al., 2007)

2.2.3.3. Masonry Wall Retrofit Failure Mechanisms

Masonry walls retrofitted on the tension side have increased resistance to out-of-plane loading. Depending on the technique used, retrofitted walls may have higher stiffness than as-built URM walls, as well as higher resistance to flexural beam bending. However, along with the increased out-of-plane resistance comes different failure mechanisms. Retrofit masonry walls may commonly fail through beam bending, shear failure and debonding of the retrofit.

Retrofit masonry walls which are properly supported to enable one-way bending may experience beam bending failure, like as-built URM walls (**Figure 2-8**). Some of the polymer retrofit walls that Irshidat et al. (2011) tested failed in tension due to beam bending failure. The polymer applied on the tension face increased the out-of-plane resistance of the wall, and the wall experienced beam bending failure (Irshidat et al., 2011). Additionally, retrofit walls may experience compression failure due to beam bending. Retrofit techniques such as FRP and polyurea significantly increase the tensile resistance of the wall, which allows the compression face of the wall to resist significantly higher loads. As a result, the faces of the masonry blocks may crumble or spall off due to the increase compressive forces. This type of failure is generally only observed in reinforced walls (Dinan et al., 2003). In the fourth wall tested by Ciornei (2012), the wall was reinforced with steel rebar and polyurea on the tension side and it was noted that the blast pressure "caused splitting of the mid-height concrete masonry unit face shells on the blast face" (Ciornei, 2012). Davidson et al. (2005) tested masonry walls retrofit with polyurea, which also experienced front (compression) face fracture. Davidson et al. (2005) notes that "the fracture tends to be concentrated closest to the supporting edges" as opposed to mid height of the wall in Ciornei's (2012) tests. In one of the later tests conducted by Irshidat et al. (2011), the spalling also occurred near the supports. Spalling of the face blocks can also be seen in the tests conducted by Johnson et al. (2004).

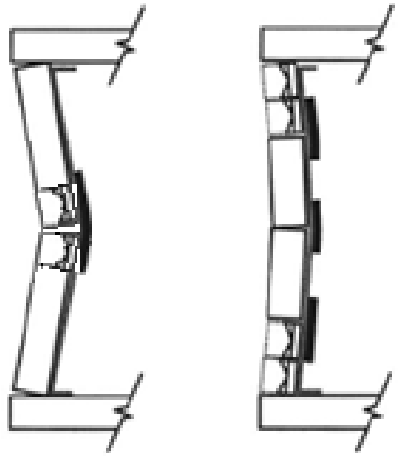

Figure 2-8. Beam Bending mode with tensile reinforcement. (Davidson et al., 2005)

If properly secured to the diaphragms, the retrofit masonry walls may shear off near the supports (**Figure 2-9**). In masonry, cracking may form between the mortar and blocks, which would cause the blocks to slip in the out-of-plane direction. Shear cracks may also appear diagonally, shown in tests conducted by Oesterle et al. (2009). Oesterle et al. (2009) tested FRP retrofit masonry walls under a blast simulation, and some walls experienced diagonal shear cracks near the top and bottom supports. Similarly, the FRP retrofit walls tested by Chen et al. (2014) experienced shear ruptures in the masonry. It was noted that "much of the area retrofitted by the CFRP strips has damaged, a large amount of CFRP strips had been sheared, ruptured or delaminated" (Chen et al., 2014). The retrofit system can also experience shear failure; the retrofit material itself may fail in shear near the support (Urgessa et al., 2010), or the shear restraints holding the retrofit may fail (Baylot et al., 2005). For example, researchers have reported shear restraints for the FRP retrofit walls cut like a "knife edge" at the FRP near the support, causing rupturing of the retrofit (Urgessa, 2010). Shear failure was also experienced by Baylot et al. (2005) when using steel plates as a retrofit. In this case, the "bolts attaching clamping plates to the structure failed, resulting in some debris entering the structure" (Baylot et al., 2005). These tests demonstrate the importance of proper shear reinforcement to prevent brittle failure.

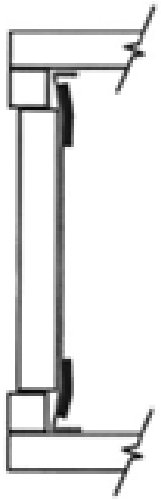

Figure 2-9. Shear Failure mode (Davidson et al., 2005)

Failure of retrofit masonry walls may also occur from delamination of the reinforcing materials. Debonding occurs when the bond strength between the wall and the reinforcement is exceeded as the wall deflects in the out-of-plane direction. Once the reinforcing material debonds, the wall no longer acts compositely with the retrofit. The reinforcing material can also debond from the frame supporting the wall, effectively destroying the shear restraint which prevents the wall from entering the structure. In the tests conducted by Chen et al. (2014), it was noted that some of the FRP delaminated from the walls, which facilitated the failure of the reinforced specimens. Chen et al. (2014) notes that delamination and shear failure were more common with FRP reinforcement than with steel bar reinforcement. Alsayed et al. (2016) performed tests on GFRP strengthened masonry walls and noted that smaller blasts which only caused minor damage to the control walls caused partial delamination of the reinforced walls. For larger blasts, the FRP strengthened wall failed due to debonding of the FRP from the reinforced concrete frame and wall (Alsayed et al., 2016). Baylot et al. (2005) also tested FRP reinforced walls and noted that in some tests the "FRP separated from the top of the reaction structure frame for the entire length of the wall and separated from the bottom of the frame over part of the length". When designing blast retrofit systems, it is important to ensure that the system will not fail at the supports. Ensuring proper anchorage of the reinforcement will prevent premature failure of the wall and retrofit system.

2.2.4. Existing Blast Design Requirements of Masonry Walls

In Canada, the design and assessment of buildings subjected to blast loads is governed by CSA S850-12. For reinforced masonry walls, the standard details the design of the reinforcement in the masonry walls, as well as regulates the strength of the materials used. The code ensures that the shear capacity of the designed wall exceeds the calculated shear demand. Since all new construction for masonry must be designed with reinforcement, there are no design provisions for the blast design of URM walls (save that they be reinforced). However, it is noted that if it can be determined that an existing URM wall can develop arching action, then the walls shall be limited to Level of Protection 'Low'. A low LOP indicates that "progressive collapse is mitigated, but repair might be costly. Evacuation and temporary return of surviving occupants are likely. Building contents [remain] intact but [are] not functional" (CSA S850-12, Clause 4.4.2). This clause recognizes the benefit of utilizing arching action to increase the out-of-plane resistance of the wall.

Table 2-1. DIF for Various Materials and Stress Types (Braimah, 2017)

Stress type	DIF			
	Reinforcing steel		Concrete	Masonry
	Fdy/Fy	Fdu/Fu	f'dc/f'c	f'dm/f'm
Flexure	1.17	1.05	1.19	1.19
Compression	1.10	1.00	1.12	1.12
Diagonal tension	1.00	1.00	1.00	1.00
Direct shear	1.10	1.00	1.10	1.00
Bond	1.17	1.05	1.00	1.00

When designing or assessing the performance of masonry walls, the code outlines the acceptable response limits in Section 4 (CSA S850-12). Response limits are a method of determining the level of damage sustained by the structural member and are intended for single degree of freedom model analysis. Depending on the level of protection required, Table 4.4 in the code gives the design

response limits in terms of the ratio of maximum deformation and deformation at yield (μ_{max}) or support rotation (θ_{max}). Alternatively, as is the case for URM walls, the table can give the designer the level of protection that a member provides if the response limits are known from testing or analysis.

Table 2-2. SIF for Various Materials (Braimah, 2017)

Material	SIF
Structural steel ($F_y \leq 345$ kPa (50 ksi))	1.10
Reinforcing steel ($f_y \leq 414$ kPa (60 ksi))	1.10
Cold-formed steel	1.21
Concrete*	1.00

*some literature sources specify a SIF of 1.1 for concrete (UFC 3-340-01)

The code also details the dynamic increase factor (DIF) and strength increase factor (SIF) for masonry materials, which are to be used for analysis and design. The DIF factors shown in **Table 2-1** consider the apparent increase in strength that a material shows under higher strain rates, and the SIF factors shown in **Table 2-2** consider that the mean strength found in the field is larger than the specified design strength.

2.3. RETROFIT SYSTEMS

2.3.1. FRP and Polyurea Retrofit Systems

FRP has been used for several decades as a reinforcement material commonly replacing steel plate bonding systems (Teng et al., 2003). FRP has been used because it is lightweight and does not take up as much space as other jacketing techniques. Due to its tensile strength properties, FRP is a good solution to prevent out-of-plane collapse of walls. FRP is composed of carbon or glass fibers in the form of fabric, strips or rods. The material is anchored to the frame supporting the wall and is bonded to the wall itself with an epoxy adhesive. FRP is typically unidirectional but can be applied in different directions and in multiple layers on the wall for additional strength.

Polyurea is another retrofit that can be applied to improve the blast resistance of URM walls. Polyurea is an elastomeric coating that has "exceptional physical properties such as high hardness, flexibility, tear and tensile strength, and chemical and water resistance" (Broekaert, 2002). The polyurea can either be applied via spraying or can be trowelled on by hand (Johnson et al., 2004). The polyurea itself can further be reinforced with nanoparticles, which impart different qualities to the polyurea (Irshidat et al., 2011).

2.3.2. Shotcrete Retrofit Systems

2.3.2.1. Conventional and Fiber-Reinforced Shotcrete

Shotcrete has been used for tunnel mining applications for many years (Stacey and Ortlepp, 2001). The ACI *Concrete Terminology manual* defines shotcrete as: "concrete placed by a high velocity pneumatic projection from a nozzle" (ACI CT-18, 2018). As understood from this technical definition, shotcrete is pumped out through a hose onto the application surface, where it solidifies to form an overlay. Compared to normal concrete which is poured into formwork, shotcrete can

be easier to use for many applications. Besides tunnel linings, shotcrete overlays have been used to retrofit URM walls for seismic loads (see Section 2.5.1).

Shotcrete can either be applied wet or dry, as shown in **Figure 2-10**. Hofler and Schlumpf (2004) explain that wet mix shotcrete is mixed with water, air and setting accelerators before being pumped through a hose. When compared to using dry mix, wet mix shotcrete decreases the amount of dust produced, has a higher output, has less rebound of fibers and is more durable due to the controlled amount of water added (Hofler and Schlumpf, 2004). Conversely, dry mix shotcrete is pumped through a hose, with water and setting accelerators being added at the nozzle (Hofler and Schlumpf, 2004). The worker who is handling the nozzle has control over how much water is added, which can change the mechanical properties and durability of the concrete (Jolin et al., 2015). Hofler and Schlumpf (2004) state the benefits of dry mix shotcrete as being its flexibility, since it can be stored indefinitely, and its early high strength.

Shotcrete can be reinforced with fibers to improve cracking resistance and partially or fully replace steel wire mesh. Common fiber types used in shotcrete applications include steel, polypropylene or polyethylene fibers. According to ACI 506.1 *Guide to Fiber-Reinforced Shotcrete*, the inclusion of fibers is the one of the most effective methods to increase the impact resistance of shotcrete. Once the shotcrete matrix begins cracking, the fibers begin to act by bridging and arresting cracks to prevent sudden failure, allowing the shotcrete to continue to deform and absorb energy. The ability to absorb more energy and provide tensile resistance is an important characteristic which makes fiber-reinforced shotcrete (FRS) well-suited for the blast retrofit of structures. Recent advances in material science have led to the development of more advanced fiber-reinforced shotcrete systems, including ECC systems, as described in the next section.

A) B)

Figure 2-10. A) Dry spray and B) wet spray shotcrete (Hofler and Schlumpf, 2004)

2.3.2.2. Engineered Cementitious Composite

Engineered cementitious composite (ECC) is a special type of fiber reinforced cementitious material, that can be applied like shotcrete (Lin et al., 2016). Unlike conventional fiber-reinforced concrete, ECC does not contain coarse aggregate and its matrix is carefully tailored to ensure high tensile resistance and strain capacity. ECC typically contains a lower amount of cement and higher volumes of fly ash or other supplementary cementing materials (Soleimani-Dashtaki et al., 2017). Moreover, ECC is typically reinforced with a large volume of micro-synthetic PVA fibers which provides ECC with sustained tensile capacity after cracking. According to Sahmaran et al. (2009), ECC is a type of High-Performance Fibre Reinforced Cementitious Composite (HPFRCC) that

strain hardens after it cracks, and "demonstrates a strain capacity 300 to 500 times greater than normal concrete". Furthermore, Sahmaran et al. (2009) states that even at large deformations, the crack widths remain small. **Figure 2-11** shows the typical compression and tension response of ECC and **Figure 2-12** shows multiple cracking that characterizes ECC composites. These properties of ECC make it an ideal solution for the blast retrofit of URM walls.

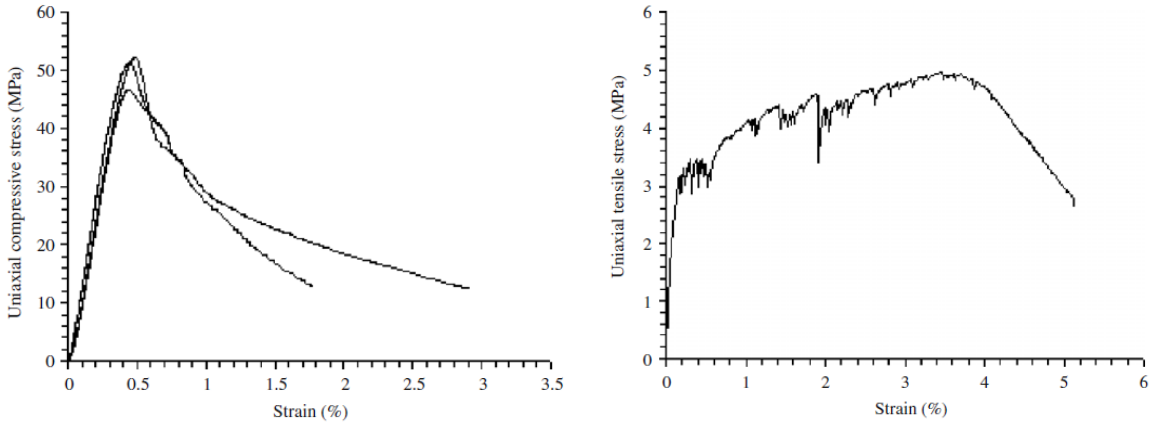

Figure 2-11. A) Typical Compression Response of ECC. B) Typical Tension Responce of ECC (Maalej et al., 2010)

The ECC used in this thesis is produced by King Shotcrete Solutions. The *FS-T3* shotcrete (also termed engineered fiber-reinforced shotcrete) was originally developed for underground mining applications. The shotcrete has over "1000 Joules in flexural toughness measured only after 24 hours" (Ginouse et al., 2015). Furthermore, its "enhanced tensile strength and post peak behavior under tensile/flexural loading [increases] its resistance against spalling caused by seismic events" (Ginouse et al., 2015). The improved material properties of this shotcrete would be advantageous for use as a URM wall retrofit.

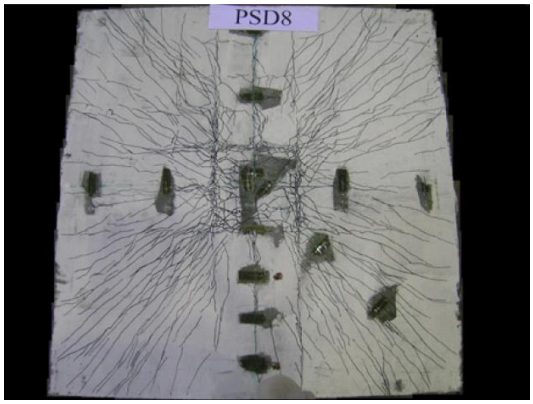

Figure 2-12. Typical Cracking pattern in ECC retrofit of Masonry panel (Maalej et al., 2010)

2.3.2.3. Mesh and Textile Reinforcement

FRS by itself can absorb energy even after cracking occurs, however, once the cracks become too wide, the fibers are no longer effective at absorbing energy. To provide ductile behaviour beyond this point, mesh can be embedded into the shotcrete to act as tensile reinforcement. Different kinds

of meshes can be used, as seen by the research performed by Stacey and Ortlepp (2001), Ismail and Ingham (2016), Cengiz and Turanli (2004), and Maalej et al. (2010). The meshes may be composed of different patterns, including diamond patterns or welded wire mesh. Textile Reinforced Mortar is another more recent retrofit technique that relies solely on the textile to provide tension reinforcement. **Figure 2-13** presents the different types of mesh used in practice.

A) B) C)

Figure 2-13. A) Textile reinforced mortar system (Papanicolaou et al., 2008). B) Welded Wire Mesh. C) Diamond Mesh (Impi Wire)

2.4. PREVIOUS RESEARCH ON FRP AND POLYUREA BLAST RETROFIT FOR MASONRY WALLS

The use of FRP and polyurea to reinforce URM walls has been studied much more extensively than the use of shotcrete overlays for blast loads. Section 2.4.1 covers some of the research performed on FRP as a blast retrofit, while section 2.4.2 presents research on the use of polyurea as a retrofit. **Table 2-3** and **Table 2-4** summarizes the findings for FRP and polyurea, respectively.

2.4.1. Blast Retrofit Using FRP

S. H. Alsayed, H.M. Elsanadedy, Z. M. Al-Zaheri, Y. A. Al-Salloum, H. Abbas (2016)

Alsayed et al. (2016) tested 6 masonry walls under three different live explosives. The walls were built within a reinforced concrete frame and were retrofit with two layers of unidirectional GFRP which were applied orthogonal to each other. The setup and results of one test is shown in **Figure 2-14**. During the first blast loading, there was no damage sustained by the control or retrofit wall. During the second increased blast load, both walls sustained minor damage, with the damage of the retrofit wall in the form of FRP debonding. For the final blast, both walls failed completely, however the FRP contained fragments from the retrofit wall. The authors note that FRP retrofitted walls can fail in either tension, compression or shear. The tension or compression failure occur in the center of the wall where there is bending, while shear occurs near the supports. The bending motion of the wall creates arching action, which substantially increases the resistance of the wall. A finite element model (FEM) analysis was conducted on the masonry walls under blast, with the analytical results correlating well with the experimental results. The authors conclude that glass

fibre reinforced polymer (GFRP) shows good potential as a retrofit material with the added benefit of containing fragments, but the FRP needs to have proper end anchorage to achieve full capacity.

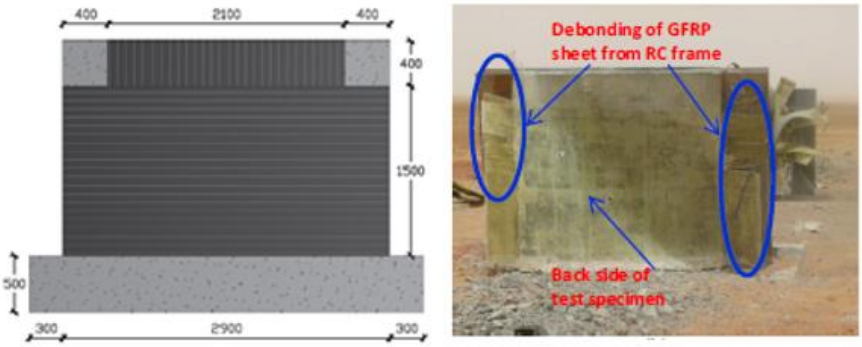

Figure 2-14. Retrofit setup and results. (Alsayed et al., 2016)

L. Chen, Q. Fang, J. Fan, Y. Zhang, H. Hao, J. Liu, (2014)

Chen et al. (2014) tested 4 masonry walls under increasing and repeated live blast loads. The walls were built with a Flemish bond and were reinforced with carbon fibre reinforced polymer (CFRP) strips, steel wire mesh, and steel bar. The CFRP strips and steel bar were applied vertically and horizontally and were anchored to the reinforced concrete (RC) frame surrounding the wall. The setup and results of a CFRP wall are shown in **Figure 2-15**. The retrofit walls performed significantly better than the control walls, which showed signs of spalling at the fourth detonation. At the sixth detonation, the control wall was destroyed, while the wall with CFRP strips showed signs of shear rupture and delamination. According to post-test observations, the steel mesh performed the best, with little damage. Next in performance was the CFRP, which showed delamination. The steel bars performed slightly worse than the CFRP, due to more fragmentation and less energy dissipation. The authors conducted a Finite Element analysis and found that the results reflected those of the live tests. It was concluded that the retrofit techniques notably increased the blast resistance of URM walls.

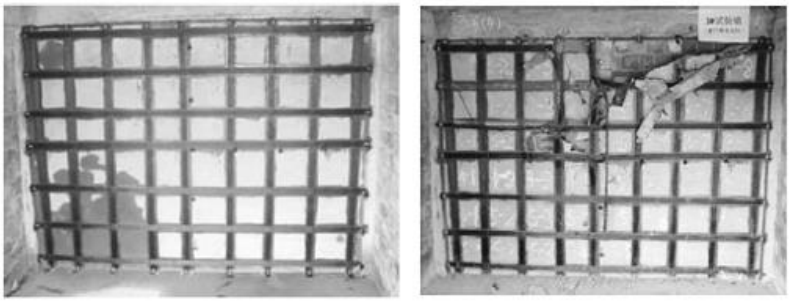

Figure 2-15. Retrofit setup and results for FRP reinforcement. (Chen et al., 2014)

G. S. Urgessa, A. K. Maji, (2010)

Urgessa and Maji (2010) tested 8 masonry walls reinforced with two or four layers of FRP with a live explosive. The FRP was unidirectional carbon fiber applied as three side by side vertical sheets along the height of the wall, as shown in **Figure 2-16**. The wall and FRP fabric were restrained at the supports with steel angles. Two different matrix polymers were used to adhere the FRP to the wall: a geopolymer containing of liquid potassium silicate and amorphous silica powder, and an

organic matrix containing thixotropic epoxy resin and a 2:1 hardener. The walls were subjected to a blast from 0.64kg of TNT equivalent at a distance of 1.83m. The walls with 4 layers of FRP were stiffer than the walls with 2 layers, and as a result they did not deflect as much. The 2 layered walls formed large horizontal cracks at the mortar joints, and the carbon fiber ruptured at mid-height. The stiffer 4 layered walls contained fragmentation better, but the carbon fibers sheared at the base where the knife angle held the wall. There were no significant differences between the two matrices used. The measured blast loads were shown to agree with the predicted blast wave values, and displacement measurements showed moderate agreement to SDOF values. The authors conclude with a proposed design procedure to retrofit walls with FRP. Step 1 is to assess the threat and required level of protection. Step 2 is to determine the blast wave parameters. Step 3 is to analyze the system with a non-linear SDOF model. The final step is to detail proper FRP application methods.

Figure 2-16. Retrofit setup (Urgessa and Maji, 2010)

M. G. Oesterle, G. A. Hegemier, K.B. Morril (2009)

Oesterle et al. (2009) tested 3 different walls under increasing lateral out-of-plane loads that simulated blast pressures. Two of the walls were reinforced with four layers of unidirectional CFRP on the tension side. The third wall was additionally reinforced with 2 layers of CFRP on the compression side. Each wall was supported to allow for one-way bending. The loading device applied a uniformly distributed impact load specifically designed to simulate blast loads (**Figure 2-17**). None of the walls failed in a catastrophic manner. The failure mode for each wall was spalling at the base and diagonal shear cracks at the top of the wall. The authors state that if the shear cracks were prevented, then the wall would have been able to sustain higher impact loads. The CFRP was noted to debond where the shear failure occurred on the wall. The authors conclude that CFRP greatly increases the flexural strength of URM walls. A finite element analysis was conducted with results agreeing well with the experimental tests.

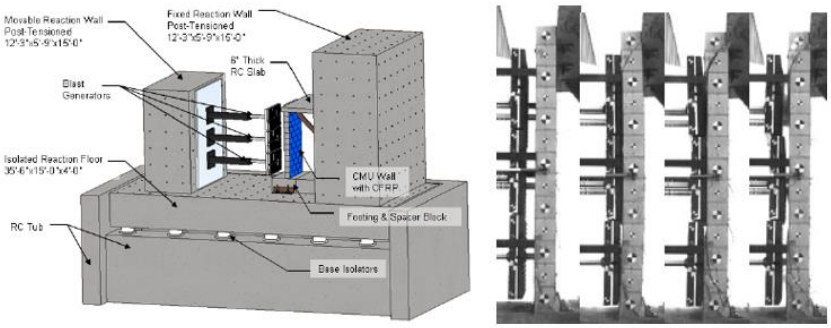

Figure 2-17. Test setup and results of Wall 3 (Oesterle et al., 2009)

K. H. Tan, M. K. H. Patoary (2009)

Tan and Patoary (2009) tested the blast behavior of six square concrete masonry units composed of three walls each as seen in the figure below. The brick masonry walls were retrofit with GFRP, CFRP and woven roving bidirectional fiberglass. The retrofit materials were applied in layers of two or four, in different combinations on both sides of each wall. Another parameter was the thickness of the walls, which was either one brick or half a brick thick. The setup is as shown in **Figure 2-18**. None of the walls sustained any damage or failed due to the lower than expected blast pressure. During the first test, the box structures were fixed to the ground, so some of the walls sustained minor deflections. During the second test, the structures were not fixed and were displaced by a few centimeters each. The thicker walls and walls with more layers of FRP sustained lower displacements than the thinner walls. It was found that all types of reinforcement were equally effective. Although some walls were designed to fail according to SDOF analysis and strain rate effect considerations, the recorded blast was much lower than anticipated.

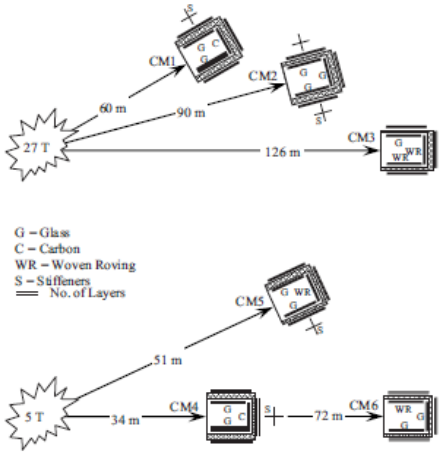

Figure 2-18. Test setup. (Tan et al., 2009)

J. T. Baylot, B. Bullock, T. R. Slawson, S. C. Woodson, (2005)

Baylot et al. (2005) tested three different series of walls to live blast loads, with the first series focusing on FRP retrofit. The GFRP unidirectional fabric was bonded to the back of the masonry wall with epoxy coating. The FRP overlapped the top and bottom supports, and in one of the trials a steel clamping plate was used to restrain the FRP in place. During the trials, FRP reinforcement prevented debris from entering the structure, and was thus considered a successful retrofit material.

However, the FRP fabrics debonded from top support and partially from the bottom. The second FRP reinforced wall remained intact, but FRP debonded from the top support and the wall fell in. To prevent the FRP debonding, the same test was conducted but with steel plates clamping the FRP at the supports. Even with the additional precautions, the FRP still slipped out with a little debris entering the structure. While the FRP retrofit prevented fragmentation, the study concludes the support conditions need to be improved to successfully use this retrofit material.

J. J. Myers, A. Belarbi, K. A. El-Domiaty, (2004)

Myers et al. tested 8 URM walls retrofitted with different configurations of GFRP laminates and rods. The walls were tested under live explosives. Retrofit A consisted of horizontal GFRP rods along the mortar joints, Retrofit B consisted of three vertical GFRP laminate strips, and Retrofit C combined the GFRP vertical laminates and horizontal rods. The different systems of retrofit are shown in **Figure 2-19**. Series 2, which included arching action, had walls double the thickness than in Series 1 which did not include arching action. The unreinforced control walls failed in a beam bending failure mode, with horizontal cracks appearing at the mortar joints. Due to the absence of arching action in Series 1, the walls retrofit with GFRP were more likely to fail in shear since there were no wall to frame connections. As such, Retrofit C of series 1 had a lower blast capacity than the control since it failed prematurely in shear (**Figure 2-20**). However, Retrofit B was an improvement to the control. In series 2, the retrofit walls performed better than the control, and their respective counterparts in series 1. With an increased amount of retrofit material, Retrofit C of series 2 did not have any tearing or rupturing of the FRP fabric or bars. Regardless of the presence or absence of arching action, FRP was found to improve the performance of the masonry walls. The FRP laminates performed better than the near surface mounted (NSM) rods for containing debris. The authors conducted a SDOF analysis to corroborate the experimental tests and found the measured values agree with the calculated values and failure modes. The authors conclude that by comparing the calculated support rotations and ductility ratios it is possible to predict the level of damage for a given load.

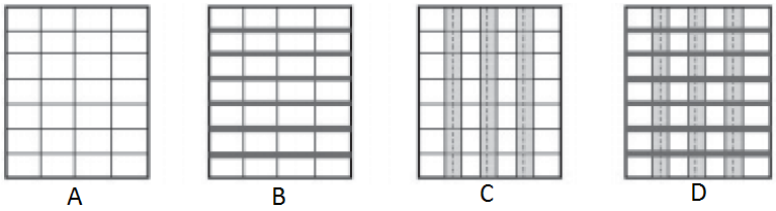

Figure 2-19. Retrofit systems (Myers et al., 2004)

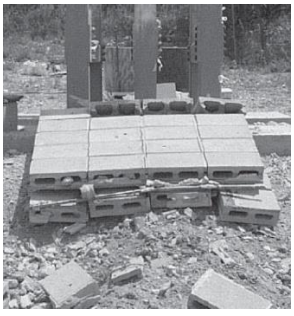

Figure 2-20. Results of wall C1 (Myers et al., 2004)

Table 2-3. Summary of FRP Retrofit Studies

Author(s)	Masonry Type	Wall Type	Wall dimensions (hxwxl)	Dynamic loading	Dynamic Load properties	FRP type/# layers/direction	Applied Surface	Retrofit Details
Alsayed et al. (2016)	CMU	Infill	1.5mx2.1mx200mm	Live Explosion	Charge 1: 1.134kg, 4.8m Charge 2: 49.9kg, 4.8m Charge 3: 14.2kg, 2m	GFRP/2/vertical and horizontal for each wall	Tension Face	Six masonry walls retrofit with 2 layers of GFRP with fibers orthogonal to each other
Chen et al. (2014)	P type porous brick	Infill	1.5mx2mx200mm	Live Explosion	Charge 1: 3.9kg, Charge 2: 34.2kg, Charge 3: 21.1kg, 30kg Distance:5.85m	CFRP/1/horizontal and vertical	Tension Face	Four masonry walls were reinforced with either CFRP strips, steel wire mesh or steel bar
Urgessa and Maji (2010)	CMU	Infill	3mx1mx203mm	Live Explosion	Charge: 0.64kg TNT, 1.83m	CFRP/2 or 4/ vertical	Tension Face	8 masonry walls retrofit with 2 or 4 layers of FRP strips and 2 different adhesive matrix types.
Oesterle et al. (2009)	CMU	Infill	2.6mx1.2mx203mm	Impact Blast Generators	Velocity, Impulse Test 1: 8.1m/s, 293 psi-ms Test 2: 6.9m/s, 243psi-ms Test 3: 7.9m/s, 287psi-ms	CFRP/4/vertical	Tension Face	Three CMU walls were retrofit with 4 layers of CFRP on the tension side. The third wall was also retrofit with 2 layers on the compression side.
Tan and Patoary (2009)	Clay Bricks	Infill	Not Given	Live Explosion	Charge 1: 27 tons Distance:60m,90m,126m Charge 2: 5 tons Distance:34m, 51m, 72m	GFRP, CFRP, Bidirectional fiberglass/2 or 4/Perpendicular to continuous mortar joint	Tension and Compression Face	Six square masonry units with 3 walls each were tested with different retrofit materials and layers, on both tensile and compressive faces
Baylot et al. (2005)	CMU	Infill	Not Given	Live Explosion	Not given. Distance variable to achieve desired pressure and impulse	GFRP/1/vertical	Tension Face	Three masonry walls were retrofit with unidirectional GFRP with varying thickness. One wall tested with FRP and steel plates
Myers et al. (2004)	CMU	Infill	2.24mx1.22mx102mm	Live Explosion	Charge: 2.3kg TNT Series 1 Distance: 1.83 to 3.66m Series 2 Distance: 0.91 to 3.66m	GFRP/1/vertical and horizontal	Tension face	Myers et al. tested 8 masonry walls with different thickness, arching action and GFRP fabric and rods retrofit applications

2.4.2. Blast Retrofit Using Polyurea

J. Wang, H. Ren, X. Wu, C. Cai, (2016)

Wang et al. tested six clay brick masonry walls reinforced with spray on polyurea under live explosives. The walls were built with a Flemish bond and were supported at the sides with the top of the wall unsupported. The polyurea was either applied to the front face, or to both faces. The polyurea retrofit improved the blast performance of the walls. The wall with polyurea applied to the front face only failed in tension (see **Figure 2-21**). The walls with polyurea applied to both sides decreased the deflection of the wall and prevented the tension crack from growing. When the blast charge was increased, the wall with both sides retrofitted failed through rotation along the bottom support, since the top was unsupported. However, even though the wall completely failed, the polyurea adequately contained fragmentation. When comparing the walls built with normal clay brick and aerated clay brick, the normal bricks performed much better.

Figure 2-21. Test setup and result of wall retrofit with one side of polyurea (Wang et al., 2016)

L. Ciornei (2012)

Ciornei tested 4 URM walls retrofit with spray on polyurea using a shock tube. The blast loading was increased and repeated until failure for each wall. The four walls were split in two groups: load bearing and non-load bearing. Each group had a retrofit wall and a control. The retrofit wall in the load bearing group was also reinforced with 6.3mm rebar applied vertically and attached to the steel frame (see **Figure 2-22**). The walls were built with CMU blocks in running bond and were supported at the top and bottom to allow one way bending. The polyurea retrofit was found to be successful in preventing fragmentation and increasing the strength of the walls. The retrofit caused the walls to fail in a ductile manner instead of failing due to a brittle hinge at the mid mortar joint. The load bearing walls performed better than the non-load bearing walls due to the activation of a stronger arching mechanism. The arching mechanism was found to increase the strength of the unreinforced wall significantly. It is noted that arching action can be activated by reducing the gap between the top support and the wall for non-load bearing walls. Ciornei (2012) concludes that polyurea is excellent at absorbing the energy of blast loads for URM walls.

Figure 2-22. Wall reinforced with polyurea and steel rebar. (Ciornei, 2012)

M. Irshidat, A. Al-Ostaz, A. H.-D. Cheng, C. Mullen, (2011)

Irshidat et al. (2011) tested with a shock tube three walls retrofitted with polyurea and two different nanoparticles, polyhedral oligomeric silsesquioxane (POSS) and exfoliated graphene nano platelets (XGnP). The walls were built with quarter scale CMU bricks. The control wall was retrofitted only with polyurea and failed in tension at a pressure of 208kPa with horizontal cracks at every mortar line. The wall retrofitted with polyurea and XGnP also suffered horizontal cracking at every mortar joint, and completely failed at pressure of 224kPa. For the first two walls, the polyurea layer failed in tension, but helped to prevent complete fragmentation of the wall. The third wall that was retrofitted with polyurea and POSS resisted a blast pressure of 218kPa. The top left corner sustained shear damage, but the wall remained standing (**Figure 2-23**). The authors conclude that polyurea retrofit systems increase the flexural resistance of the wall, with the POSS system performing the best.

Figure 2-23. Wall 3 retrofit with polyurea and POSS. (Irshidat et al., 2011)

J. T. Baylot, B. Bullock, T. R. Slawson, S. C. Woodson, (2005)

Baylot et al. (2005) also tested masonry walls retrofit with a layer of spray-on polyurea to live explosives. One of the walls with polyurea had additional steel clamps to hold the polyurea layer at the supports. As with the FRP retrofit (discussed above), the polyurea prevented debris from entering inside the structure, and was thus considered successful. The polyurea experienced debonding like the FRP. In the first test, only partial debonding was observed. During the second test, the entire top layer was debonded, with a little amount of debris entering the structure. Steel

clamps were put in place to resist support debonding and this detail was largely successful in keeping the failed wall from entering the structure. The only hazard was that the bottom steel plate failed and hit the back wall.

J. S. Davidson; J. W. Fisher; M. I. Hammons; J. R. Porter; and R. J. Dinan, (2005)

Davidson et al. (2005) studied the failure mechanisms of 12 CMU walls retrofit with polyurea under live blast loads. A common form of failure in CMU walls is front face fracture, which Davidson suggests can occur due to two possible reasons: (1) first, it can be caused by the impact of the blast wave itself; (2) the second suggestion is that the front of the masonry blocks are crushed in compression as the wall behaves in flexure, due to arching action. To explore arching action, two walls were built without mortar. One wall had polyurea sprayed on directly, while the other wall had polyurea sprayed on a membrane to prevent bonding to the bricks. The first wall did not collapse during the testing. It was seen that the top membrane was displaced vertically during testing, indicating that arching action contributed to the resistance of the wall. When analysing blast loads on masonry walls in a Finite Element Software, the presence of arching action was seen to be significant. The second wall failed since the polyurea membrane only acted as a catcher system, so the stress was concentrated at the supports which caused shear failure. Due to the fracture of mortar joints at early stages of flexure near the supports, those areas must have adequate shear resistance to prevent shear failure. Four additional walls were tested with door and window openings (**Figure 2-24**). It was found that polyurea had the same effectiveness in these walls when compared to walls without openings. For walls with openings, mortar joint fractures were more prevalent, and polyurea tended to tear starting at the corners of the openings. The authors noted that wall resistance is highly dependent on the integrity of the wall. The presence of large mortar joint cracks and front face compression cracks can greatly inhibit the flexural response of the walls. When applying polyurea, a balance of stiffness and elongation capacity is needed, with deformability being the more important of the two. The authors conclude that polyurea as a retrofit material is a highly effective solution and not overly cumbersome to apply.

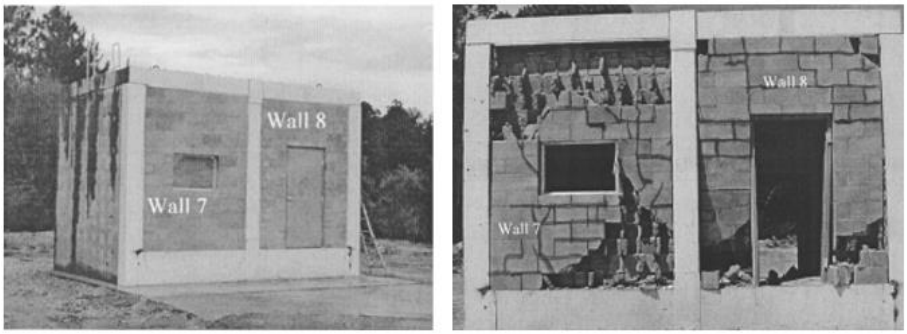

Figure 2-24. Walls tested with door and window openings. (Davidson et al., 2005)

J. S. Davidson, J. R. Porter, R. J. Dinan, M. I. Hammons, J. D. Connell (2004)

Davidson et al. conducted 3 live explosive tests on a total of 8 CMU walls. The walls were set up to ensure one way bending. Another parameter tested was the application of a layer on the compression face of the wall. For the first test, two walls were built alongside each other in a reaction structure; one of the walls was retrofit with polyurea and the other was the control. For the first test charge and distance, the control wall collapsed while the repaired wall remained intact but sustained local compressive fracturing of the CMU blocks (**Figure 2-25**). For the second test,

the charge weight was doubled, and the distance reduced by 14%. Both walls failed during this test, with the control being destroyed and the repaired wall failing in shear at the supports. For the third test, two additional walls were built in cubicles for a total of four walls. The charge remained the same as in test 2, but the distance was 30% larger than in test 1. All retrofitted walls sustained significant damage but remained intact. The walls repaired with polyurea were in much better condition than the control. The wall with polyurea on both compression and tension sides did not have a significant increase in capacity. The authors conclude that the application of polyurea greatly increased the flexural resistance of the wall.

Figure 2-25. Comparison of control and retrofit wall for Test 1. (Davidson et al., 2004)

C.F. Johnson, T.R. Slawson, T.K. Cummins, J.L. Davis (2004)

Johnson et al. (2004) tested seven quarter scale walls in a hydrostatic chamber and under blast loads along with four full scale walls tested under live explosives. The hydrostatic chamber can record the flexural resistance of the wall until failure. **Figure 2-26** shows wall set 1 which contains two of the four full scale walls. The first two quarter scale walls tested the difference between spray on polyurea and trowelled polyurea. The next three-quarter scale walls tested the addition of open weave Aramid fabric applied with different thickness and orientation along with spray on polyurea. The fabric has fibers running perpendicular to each other and were applied either at a 0/90 or +/-45 orientation. The last two quarter scale walls were retrofit with a thermoplastic film attached with spray on adhesive and polyurethane film attached with epoxy.

All forms of retrofit greatly increased the capacity of the walls over the control. The walls with only polyurea deflected more than 2 times over those retrofit with polyurea and fabric. The wall retrofit with a thicker fabric deflected as much as the walls with thinner fabrics but failed at a much greater load. The walls retrofit with thermoplastic and polyurethane film behaved similarly, with a deflection slightly larger than the walls with only polyurea, but while resisting a higher load. The diaphragm used to apply loading ruptured before failure of the wall reinforced with polyurethane film. The two different orientations of fabric did not drastically change the response of the walls. The +/-45 orientation achieved a higher initial load and displacement, but the 0/90 orientation achieved a higher failure load and displacement. The results of the quarter scale walls under blast loading resembled the results from the hydrostatic chamber, with all reinforced walls performing better than the control. The walls with fabric reinforcement further increased the flexural capacities

of the walls. The +/-45 orientation proved to be a better reinforcement than the 0/90 orientation since it was less stiff, where the 0/90 wall failed at the support under the same dynamic loading. The spray on polyurea performed better than the wall with troweled on reinforcement.

The first full scale wall had spray on polyurea with +/-45 orientated fabric, the second only had trowelled on polyurea, and the last was retrofit with trowelled on polyurea and thermoplastic film. While the faces of the walls were destroyed, there was no debris on the tension side of the wall (**Figure 2-27**). The full-scale tests demonstrated that the quarter scale tests achieved valid results. The authors conclude that spray on or trowelled polyurea is an effective solution for blast loading.

Figure 2-26. Setup of Wall 1 explosive test. (Johnson et al., 2004)

Figure 2-27. Results of wall retrofit with spray on polyurea. (Johnson et al., 2004)

R. Dinan, J. Fisher, M.I. Hammons, J.R. Porter (2003)

Dinan et al. (2003) tested 12 full scale CMU walls reinforced with polymer to live explosive for collecting data to study the failure mechanisms and to create analytical models. The walls were built and supported to allow one way bending. The authors noted that adding a 3mm thick polymer layer increases the flexural capacity of the wall more than twice that of an unreinforced wall. The authors note a common failure mode relates to the formation of tensile cracks in the mortar joints on the tension face of the wall, where the load is being redistributed to the polymer coating (**Figure 2-28**). As the polymer extends, cracks will begin to form in the masonry elements themselves. Common damage sustained by blocks include spalling or crushing on the front face, which can cause failure of the wall. This form of failure is more common with retrofitted walls. The authors note that arching action can increase the flexural resistance of the wall if the boundary conditions

allow for it, and as long as the wall does not fail in shear or due to crushing on the front face. Even though CMU walls can suffer varying failure mechanisms, the authors conclude that the elasticity of a polymer coating allows it to strengthen the wall regardless of the failure mode.

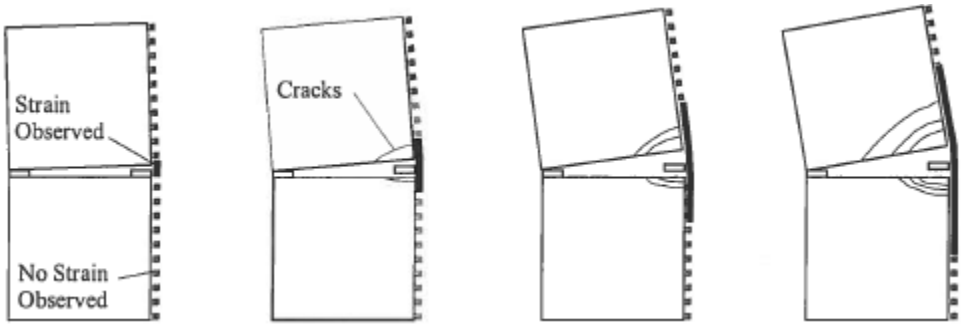

Figure 2-28. Strain in the polymer coating at a mortar joint (Dinan et al., 2003)

Table 2-4. Summary of Polyurea Retrofit Studies

Author(s)	Masonry Type	Wall Type	Wall dimensions (hxwxl)	Dynamic loading	Dynamic Load properties	Applied Surface	Thickness	Retrofit Details
Wang et al. (2016)	Clay Brick	Infill	2.8mx3.6mx240mm 2.2mx2.4mx240mm	Live Explosion	Charge 1: 2kg, 1m Charge 2: 5kg, 1m Charge 3: 8kg, 1m Charge 4: 20kg, 1m Charge 5: 5kg, 10m Charge 6:5kg, 3m	Compression face, both	3mm	Six masonry walls were tested with spray on polyurea applied to the front face for one wall, and to both faces for the next three walls
Ciornei (2012)	CMU	Infill/Load bearing	2mx2mx100mm	Shock Tube Blast	Reflected Pressure: Wall 1: 31kPa Wall 2: 78kPa Wall 3: 51kPa Wall 4: 97kPa	Tension face	3mm	Two controls and two walls retrofit with spray on polyurea were tested. The four walls were split into two groups: infill and load bearing. The retrofit load bearing wall was additionally reinforced with vertically applied steel rebar.
Irshidat et al. (2011)	CMU	Infill	0.86mx1.38mx57mm	Shock Tube Blast	Reflected Pressure: Wall 1:208kPa Wall 2:224kPa Wall 3:218kPa	Tension face	Wall 1:1.5mm Wall 2:1.5mm Wall 3:1.8mm	Quarter scale concrete masonry infill walls retrofit with Polyurea reinforced with nanoparticles
Baylot et al. (2005)	CMU	Infill	Not Given	Live Explosion	Not given. Distance variable to achieve desired pressure and impulse	Tension face	3.2mm	Baylot et al. also tested masonry walls retrofit with spray on polyurea. One wall had clamping plates attaching the polyurea layer to the supports
Davidson et al. (2005)	CMU	Infill	3.7mx2.3m 2.4mx2.4m 3mx2.3m 3.7mx4.9m	Live Explosion	Not Given	Tension face	3mm, 6mm	Summary of several tests involving polyurea and arching action, some walls included doors and windows
Davidson et al. (2004)	CMU	Infill	2.24mx3.66m	Live Explosion	Not Given	Tension face, both faces	3.2 to 9.5mm	Live explosive tests on CMU walls retrofit with polyurea of varying thicknesses
Johnson et al. (2004)	CMU	Infill	Quarter scale: 0.78mx1.62mx50mm, Full scale: 2.81mx4.42mx203mm 3.30mx5.69mx203mm	Live Explosion	Not Given	Tension face	Not Given	Static and live explosive tests on quarter scale and full scale masonry infill walls reinforced with polyuria, Aramid fabric, thermoplastic film and polyurethane film
Dinan et al. (2003)	CMU	Infill	3.7mx2.3m 2.4mx2.4m 3mx2.3m 3.7mx4.9m	Live Explosion	Not Given	Tension face	3mm, 6mm	12 CMU walls were retrofit with polymer coating for the purpose of gathering data to study the failure modes and create analytical models.

2.5. PREVIOUS RESEARCH ON SEISMIC, BLAST AND IMPACT RETROFIT OF URM WALLS USING CEMENTITIOUS RETROFIT SYSTEMS

There is limited research on the use of fiber-reinforced shotcrete (FRS) systems for blast retrofitting URM walls when compared to FRP or polyurea. Due to the limited blast research, Section 2.5.1 presents research related to out-of-plane seismic behaviour of URM walls reinforced with cement-based materials. In this section, only three papers use shotcrete as a material. Two of these papers use FRS as a retrofit for masonry walls. The other paper, presented by Cengiz and Turanli (2004), focuses on the performance of shotcrete panels to understand their behaviour for tunnel linings. While the objective of this research is for a different application, the results show the benefits of using FRS in out-of-plane load applications. The other four papers use TRM retrofit systems for seismic reinforcement. These papers were included to show the effectiveness of the textile fabrics, which have a similar role as the steel meshes that will be tested in this paper. **Table 2-5** summarizes the details of each paper.

Section 2.5.2 outlines previous research that used FRS to retrofit walls subjected to impact and blast loads. Maalej et al. (2010) performed impact tests on ECC retrofit masonry walls. Maji et al. (2008) tested URM retrofit with GFRP and shotcrete to blast loads, however the focus of the paper was on the performance of GFRP as a retrofit. There are two papers which present research on FRS panels subjected to impact loads. These papers focus on the shotcrete properties under impact for tunnel lining applications, however, the successful results speak to the benefits of masonry walls reinforced with FRS. Zhang et al. (2007) compared RC and FRC blast panels to ECC blast panels under impact loads. The final paper in Section 2.5.2 presents the research of FRS panels subjected to high velocity impact tests.

2.5.1. Seismic Retrofit

S. Soleimani-Dashtaki, C. Ventura, N. Banthia, (2017)

Soleimani-Dashtaki et al. (2017) tested six full scale URM walls retrofit with sprayed Eco-Friendly Ductile Cementitious Composite (EDCC) to out-of-plane loads caused by variable earthquake load intensities. Half the walls were tested with a double-sided retrofit, while the other half was tested with only a single side of EDCC. The specimens were 2m wide by 3m high, and the retrofit was 20mm in thickness. The results indicate that a single layer of retrofit changes the behaviour of the wall from a rocking mechanism to beam bending. The added level of energy dissipation increased the performance of the wall before failure. While a single sided retrofit was found to be satisfactory for earthquakes in the BC area, a double-sided retrofit was recommended for walls where drift should be limited. **Figure 2-29** shows the test setup and results of one of the walls.

Figure 2-29. Test setup and Results (Soleimani-Dashtaki et al., 2017)

Y. Lin, D. Lawley, L. Wotherspoon, J. M. Ingham, (2016)

Lin et al. (2016) tested 6 walls retrofitted with fiber reinforced ECC shotcrete and near surface mounted rebar under cyclic and monotonic out-of-plane loading. The walls were built with clay bricks laid in common bond configuration (**Figure 2-30**). The authors also tested the effect of thickness of the ECC overlay. While ECC applied to either side of the wall increased its capacity, layers of ECC on the tension side showed a greater improvement than layers applied to the compression side. The addition of near surface mounted rebar further increased the load capacity of the wall but changed the mode of failure to debonding of the rebar. The walls with thicker ECC layers were shown to have increased capacity than the thinner specimens. It was concluded that ECC shotcrete is a feasible option for retrofitting URM walls for out-of-plane seismic loads.

Figure 2-30. Test setup and results. (Lin et al., 2016)

N. Ismail, J. M. Ingham, (2016)

Ismail and Ingham (2016) tested 8 walls retrofitted with TRM systems that were loaded with in-plane and out-of-plane reverse cyclic forces. The clay bricks were chosen to represent common URM walls used in New Zealand and were laid in a common bond pattern. The two textiles used were chosen based on a preceding study and are commercially available for TRM systems. The first three tests focused on in-plane loading, where two brick piers were connected on top by a brick spandrel. The retrofitted walls had a higher energy absorption capacity than the control walls. For the first repaired wall, the failure mode (weak beam failure) was the same as the control.

However, for the second repaired wall, the failure mode was a step joint sliding shear failure in one of the piers. The authors note the importance of increasing the resistance of the pier with respect to the spandrel to prevent brittle shear failure at the pier. The results of these walls are shown in **Figure 2-31**. The next three walls underwent out-of-plane loading in two stages. The first stage loaded the walls in a bi-directional cyclic test, and the second stage loaded the same walls in a single direction until failure (**Figure 2-32**). The last wall in this series was reinforced with additional steel mesh. It was noted that the TRM systems significantly increased the flexural strength of the wall when acting in tension rather than compression. The walls exhibited a bi-linear behaviour until the tensile resistance of the textile was exceeded and the walls collapsed. The wall with a steel mesh added alongside the textile fabric performed relatively better than the wall without the steel mesh. The authors conclude that the two TRM systems can retrofit piers adequately for moderate to large magnitude earthquakes to prevent catastrophic failure.

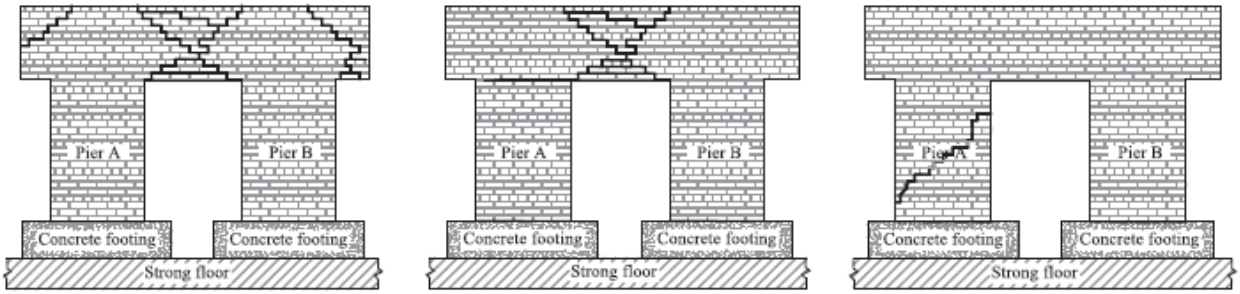

Figure 2-31. In-Plane testing results. (Ismail and Ingham, 2016)

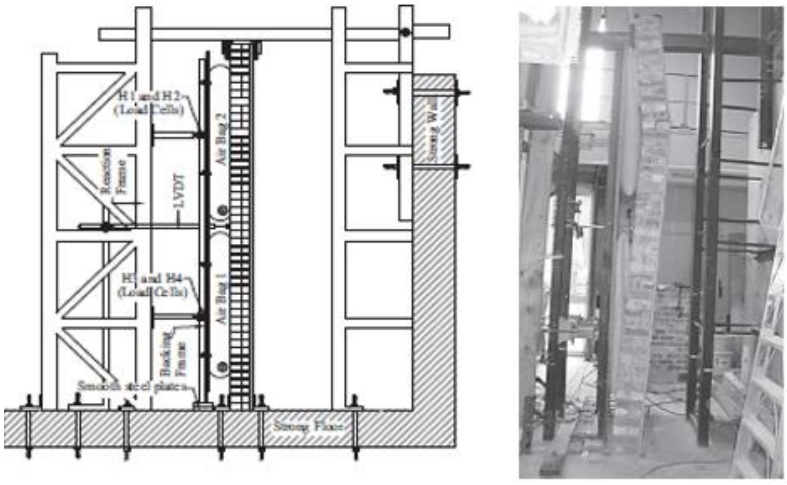

Figure 2-32. One way loading test setup and results of wall with steel mesh. (Ismail and Ingham, 2016)

C. G. Papanicolaou, T. C. Triantafillou, M. Papathanasiou, K. Karlos, (2008)

Papanicolaou et al. (2008) conducted 12 tests on walls retrofitted with TRM systems (either resin based, or mortar based) and near-surface mounted (NSM) CFRP strips. The quasi-static increasing cyclic load was applied at the center of the walls by using a hydraulic piston (**Figure 2-33**). The tests were split into two groups based on failure patterns; Series A with the failure plane parallel to the bed joints and Series B with the failure plane perpendicular to the bed joints. Other parameters studied include the number of layers of textiles and the performance of TRM or FRP jackets in addition to NSM strips. When compared to the control walls, all three retrofit methods

significantly increased the flexural strength of the walls. The strength of the walls was proportional to the number of textile fabrics added, however, as more textiles were added, the deformability of the walls decreased. When comparing the mortar based and resin based retrofit, the mortar based system was found to have a higher strength and deformation capacity. The NSM retrofit had lower strength than either TRM method, but with a higher deformation capacity. The authors conclude that TRM retrofitting is a promising solution for walls subjected to out-of-plane seismic loads.

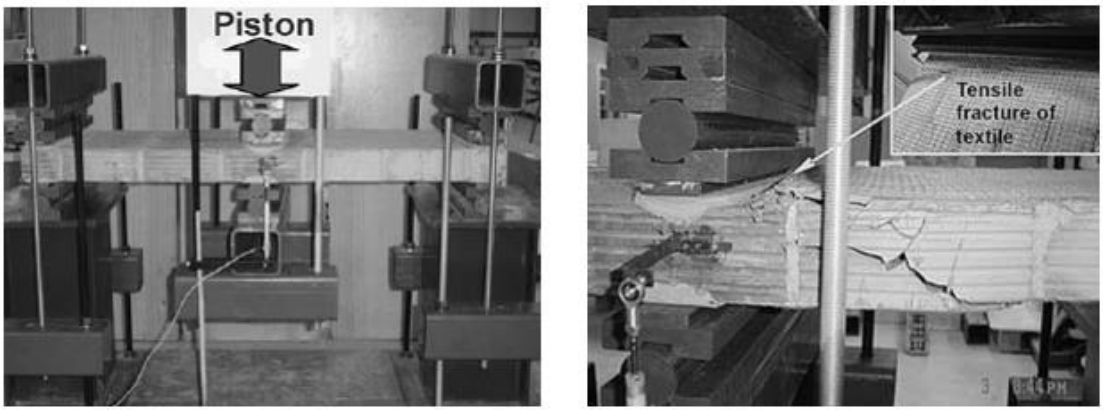

Figure 2-33. Test setup and tensile failure of the textile. (Papanicolaou et al., 2008)

O. Cengiz, L. Turanli (2004)

Cengiz and Turanli tested 18 dry-mix shotcrete panels under quasi-static loading to determine the behaviour of FRS and steel mesh reinforced shotcrete used in tunnel linings. The panels were reinforced with steel mesh, steel fibers, high performance polypropylene fibers (HPP) and a mixture of the two fibers. The test setup is shown in **Figure 2-34**. For each type of fiber, two different fiber amounts were used. When comparing the average load deflection curves for each panel, all panels had similar initial peak loads. However, the steel mesh panels had a second peak load greater than the first which greatly increased energy absorption when compared to the fiber reinforced panels. For the panels with steel fibers, the increase in energy absorption and peak load was found to be proportional to the increase in the amount of steel fibers. Conversely, increasing the polypropylene fiber content decreased the peak load but did not affect the energy absorption. The panel that had a mix of steel and polypropylene fibers had the second highest energy absorption of all panels (second to the steel mesh). The results of this panel can be seen in **Figure 2-34**. It should be noted that the polypropylene fibers had a higher fiber content per volume when compared to the steel fiber panels. The usage of the HPP fibers was noted to be advantageous due to the reduced amount of rebound when compared to the steel fibers. The authors conclude that the shotcrete panels adequately reached a toughness class required for tunnel repair jobs.

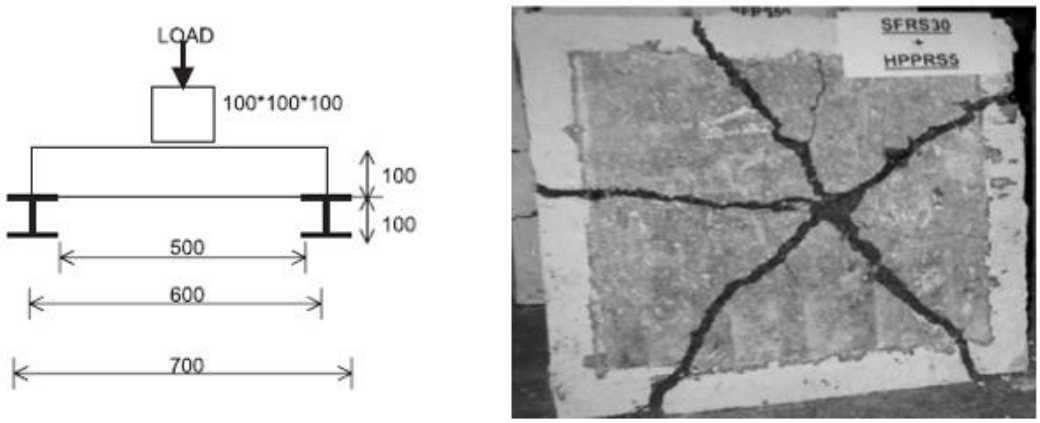

Figure 2-34. Test setup and results of the panel with a mixture of fibers (Cengiz et al., 2004)

H. Kolsch (1998)

Kolsch (1998) tested eight concrete beams and one masonry wall coated with a carbon fiber cement matrix overlay (TRM). The beams were tested under quasi-static three-point loading. Two beams each were reinforced with either glass filament fabric and epoxy resin matrix, glass filament fabric and cementitious matrix, or a carbon filament fabric and cementitious matrix. Compared to the two control beams, all forms of retrofit greatly increased the energy absorption of the beam specimens. The glass and cement combination performed the best, with the carbon/cement retrofit having a similar load capacity, but less deflection. The glass/epoxy combination had a lower load capacity but had about the same amount of deformation as the glass/cement combination. The masonry wall specimen was built with sand-lime bricks that were laid in a cross-bond pattern (**Figure 2-35**). The wall was uniformly loaded with a quasi-static cyclic load. The retrofitted wall had a significantly increased load and deflection capacity when compared to an unreinforced wall. Additionally, the overlay allowed the wall to hold cyclic loads without catastrophic failure.

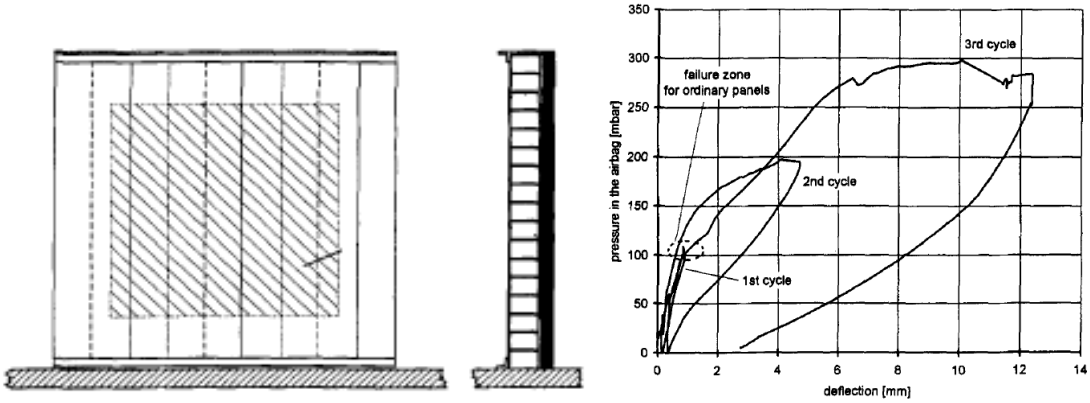

Figure 2-35. Test Setup and Results. (Kolsch, 1998)

Table 2-5. Summary of Seismic Retrofit of URM walls with Cementitious Overlay

Author(s)	Masonry Type	Wall Type	Wall Dimensions	Loading	Load Properties	Applied Surface	Overlay Type	Fiber Type	Overlay Thickness	Retrofit Details
Soleimani-Dashtaki et al. (2017)	Concrete Masonry Unit	Infill	3mx2m	Shake Table	Earthquakes of varying intensities	Single and double face	EDCC	Synthetic	20mm	Single and double side of sprayed EDCC retrofit.
Lin et al. (2016)	Clay Brick	Infill	4.1mx1.15mx230 mm	UDL	Quasi static, Monotonic, cyclic	Single face	ECC	Synthetic (0.26 kg/m^3)	25mm, 30mm	Single side of ECC shotcrete overlay. One wall also reinforced with near surface mounted rebar.
Ismail and Ingham (2016)	Clay Brick	Infill	3.67mx1.2mx220 mm (out-of-plane)	UDL	Quasi static, Reversed Cyclic, One Direction Cyclic	Single face	TRM	n/a	~20mm	Single side of mortar overlay reinforced with polymer textile fabric
Papanicolaou et al. (2007)	Perforated Clay Brick	Infill	1.3mx0.4m	3 point loading	Quasi-static increasing cyclic loading	Single face	TRM	n/a	Variable	Compared TRM (mortar and resin based), FRP and NSM retrofit methods
Cengiz and Turanli (2004)	n/a	Shotcrete panels	0.6mx0.6mx100 mm	Point Load	Quasi-static increasing load at center of panel	n/a	TRM and FRS	Steel Fiber (35 and 50 kg/m^3), Polypropylene Fiber (7 and 10 kg/m^3)	n/a	Panel tests compared steel mesh TRM, steel fiber and polypropylene fiber shotcrete
Kolsch (1998)	Sand-Lime Bricks	Infill	3mx3mx240mm and 2mx2mx240mm	UDL	Quasi static, One Direction increasing Cyclic loading	Single Face	TRM	n/a	4.5mm	Single face of carbon fiber cement matrix overlay.

2.5.2. Impact/Blast Retrofit

M. Maalej, V.W.J. Lin, M.P. Nguyen and S.T. Quek, (2010)

To prevent out-of-plane failure of unreinforced masonry walls, Maalej et al. (2010) tested 18 masonry wall panels retrofitted with engineered cementitious composite (ECC) overlay. The panels were tested under patch loads, UDL, and impact loads. Each panel was 1000x1000x100mm and rested horizontally with simple supports on all sides. The solid clay bricks used were 215x100x70mm in dimension and were laid in a running bond layout with 10mm of mortar. The ECC mix contained 0.5% steel fibers and 1.5% high performance polyethylene fibers with 200 μm diameters. The 18 panels were split into three series. Each series tested a) two control panels, b) one 34mm thick ECC layer single sided, c) one 34mm thick ECC layer double sided, d) one 34mm thick ECC layer single sided with 8 mm diameter steel mesh, and e) one 34mm thick ECC layer double sided with 8mm diameter steel mesh. The first series focused on quasi-static patch load of 100mmx100mm applied in the centre of the panel. In addition to the above panels, the first series also tested a single face ECC layer with a thickness of 20mm. The second series tested quasi static uniformly distributed loads applied via air bags over an area of 780x780mm at the center of the panels (see **Figure 2-36**). The third series tested impact loading by releasing a drop weight of 51 kg from a 4m height to the center of the panel. Only one control was tested for the third series.

Figure 2-36. UDL testing setup (Maalej et al. 2010)

For series 1, it was found that the ECC retrofit greatly increased energy absorption, maximum load and deflection capacities of the unreinforced masonry wall. The wall reinforced with two sides of ECC decreased the energy absorption when compared to a single side of ECC due to the creation of a compression buckling debonding failure. When the thickness of the ECC layer (single sided) was decreased to 20mm, the energy absorption also decreased, however the lower stiffness of the wall allowed for more deflection. In all cases, adding a steel mesh decreased the deflection capacity of the wall, at the expense of a much lower energy absorption.

For series 2, all wall capacities were much greater than in series 1 due to the larger surface area of the load which delayed the failure mechanisms. The wall reinforced with two sides of ECC increased the energy absorption significantly when compared to only one side of ECC overlay. As with series 1, the inclusion of steel meshes increased the stiffness of the wall, but ultimately lowered the energy absorption.

In the series 3 impact tests, it was shown that the ECC retrofit greatly enhanced the performance and resilience of the wall by allowing it to withstand multiple impacts and prevent projectiles and catastrophic failure. Walls with two sides of reinforcement decreased the crater diameter and indent depth compared to specimens with one side of reinforcement. The addition of steel meshes further decreased the damage compared to trials with no mesh (**Figure 2-37**).

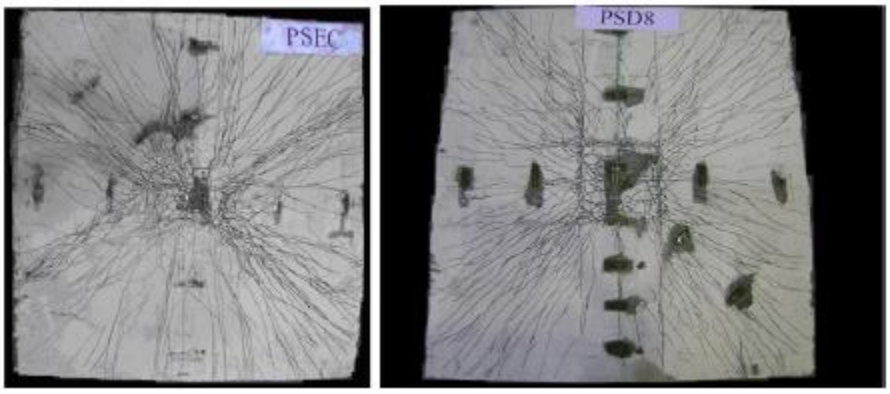

Figure 2-37. Impact results for panels without steel mesh (left), and with steel mesh (right) (Maalej et al., 2010)

T.R. Stacey and W.D. Ortlepp, (2001)

Stacey and Ortlepp (2001) tested different types of shotcrete and meshes under impact loading used for underground mining wall applications. The wire meshes tested included: welded wire mesh, diamond (chain link) wire mesh, 'special meshes' (available commercially), and the above meshes with yielding wire rope lacing. The welded wire meshes had apertures and diameters of 100x3.5mm and 100x4mm. The diamond meshes had apertures and diameters of 75x3.2mm, 100x3.2 and 100x4mm. The wire rope lacing had diameters of 8mm, 10mm and 12mm. The shotcrete specimens tested included: normal shotcrete, shotcrete reinforced with welded wire mesh, shotcrete reinforced with monofilament polypropylene fibers and wire rope lacing, and shotcrete reinforced with monofilament polypropylene fibers and hooked-end steel fibers. The shotcrete had a compressive strength of 25MPa with a nominal thickness of 75mm. The specimen that had shotcrete reinforced with welded wire mesh used a mesh with an aperture and diameter of 100x4mm. The length of steel and polypropylene fibers used in the shotcrete was 30mm and 40mm, respectively. Each specimen was 1.6x1.6m in area and were placed on support beams with 4 rock-bolts at 1m apart. Wire ropes were attached to the membrane support to apply a tensile force to account for the continuous nature of the boundary conditions. A pyramid of concrete blocks was laid onto the membrane (250x250x100mm in dimension), with a 40mm thick steel impact plate on top to distribute the load of the impact evenly. The drop weights used had masses of 1050kg and 2700kg and were dropped from a height of 3.3m. The estimated impact velocity and maximum energy input was 8.1m/s and 70kJ/m^2, respectively. **Figure 2-38** details the test setup.

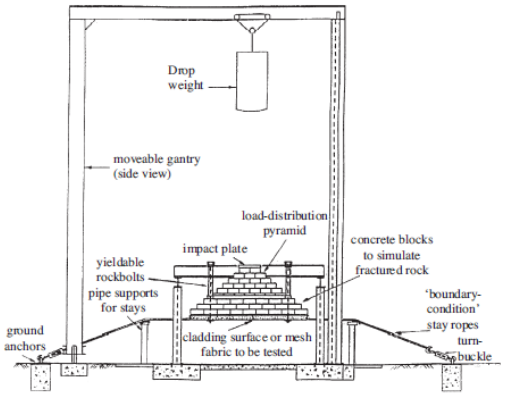

Figure 2-38. Test setup (Stacey and Ortlepp, 2001)

When comparing deflection and energy absorption, the unreinforced shotcrete panel performed the worst, with welded wire mesh not fairing much better. The diamond mesh had improved performance to welded wire mesh in both categories. The addition of rope lacing to the meshes reversed the results, with the welded wire mesh performing better than the diamond mesh. The diamond mesh tended to unravel once a strand broke, where the welded wire mesh still held with several failed strands. The Special mesh with rope lacing had a similar performance to welded wire mesh with rope lacing. However, the best results that were recorded came from the specimen with special meshes and yielding wire rope lacing. Fiber-reinforced shotcrete performed similarly to diamond meshes, but with less deflection due to a higher stiffness. The steel fiber-reinforced shotcrete performed slightly better than shotcrete with polypropylene fibers in terms of energy absorption. When rope lacing was added, catastrophic failure was prevented, and the energy capacity of the specimen was greatly improved. The authors also note that both a thickness of less than 75mm of shotcrete and rockbolt spacing of greater than 1.2m would not prove satisfactory.

The authors split the results into three categories in terms of performance (**Figure 2-39**). The first category contains the wire meshes. The performance of wire meshes varies greatly, with the special meshes having an absorption capacity of over four times compared to the welded wire mesh. The second category includes the wire meshes with rope lacing. The rope lacing decreased the deflection capacity but increased the energy absorption of the specimens. The third category includes the shotcrete-based systems. These systems have a higher initial stiffness and as a result lower deflection capacity but have about the same energy absorption as the other categories.

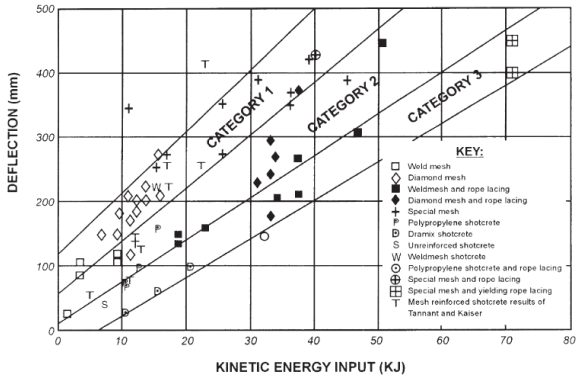

Figure 2-39. Kinetic energy absorption relative to deflection (Stacey and Ortlepp, 2001)

P. Gupta, N. Banthia, and C. Yan (2000)

Gupta et al. applied quasi-static and impact loads to FRS panels and beams to develop strong wet mix shotcrete materials for tunnel lining applications. Ten different shotcrete fibers were tested, including four deformed steel fibers, two straight polypropylene fibers, one crimped polypropylene fiber, two straight carbon micro-fibers, and one deformed polyvinyl alcohol fiber. All the fibers are available commercially and were used in dosages recommended by the supplier.

The test was split into static and dynamic tests, and further into beam and panel tests. The static beam tests were performed according to ASTM C 1018-96 standard, with dimensions of 100mmx100mmx350mm. The static plate tests were conducted by applying a load at the center of the plate under simply supported conditions (**Figure 2-40**). The plates had dimensions of 350mmx350mmx100mm. The impact tests on the beams were carried out as three-point tests using a drop weight of 60.3kg dropped from a height of 0.45m. The potential energy of the impact was 266J with and expected velocity of 2.97m/s. The impact tests on the plates were identical to the static tests, save for the drop weight of 578kg dropped from a 0.45m height. The potential energy of the impact was 2551J with an expected velocity of 2.97m/s.

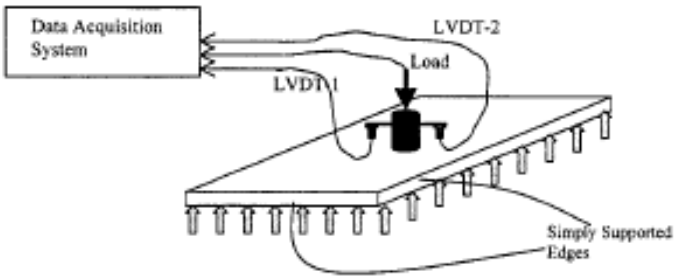

Figure 2-40. Test setup for plates (Gupta et al., 2000)

For the beam tests, the best performance came from the steel fibers for static loading. For impact loading, all the fibers performed similarly. All specimens under impact achieved greater peak loads and flexural strengths than under static loads. The shape and length of the fiber affected the performance of the beam significantly. Fibers that were deformed or crimped had a higher load capacity than those that were straight. Furthermore, the microfibers had the lowest performance since they did not span the macro-cracks and therefore did not increase the flexural resistance of the beam significantly.

For the plate tests, the steel fibers again performed better than carbon or polymer fibers, with specimens under impact outperforming those subjected to quasi-static loads. The steel fiber plates kept their integrity after the impact loading unlike the plates with polypropylene fibers (**Figure 2-41**). The plates with fibers also had a noticeable increase in peak load when compared to the control, unlike with the beam tests. Plates with less efficient fibers showed a greater increase in capacity from static to impact loading than plates with more efficient fibers. With respect to load capacity, the effect of fiber reinforcement is more pronounced under static loads than under dynamic loads.

The authors note that the plate tests are more representative of shotcrete strength due to in-situ application of shotcrete. They conclude that the usage of fibers in shotcrete greatly improves energy absorption and toughness under dynamic loads but is dependent on the shape and type of fiber used.

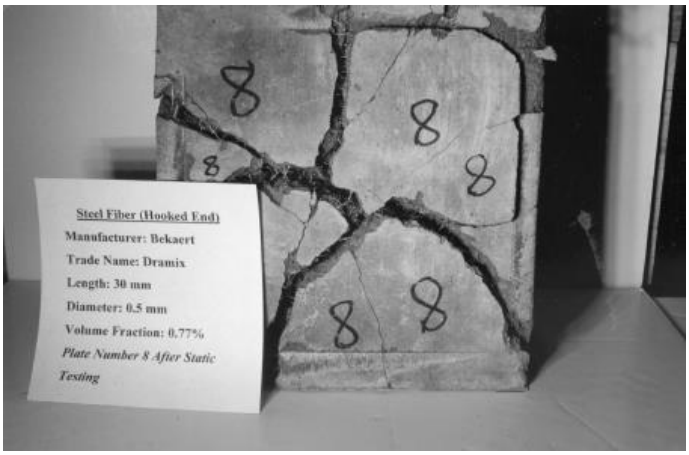

Figure 2-41. Results of plate test with hooked steel fibers (Gupta et al., 2000)

A. K. Maji, J. P. Brown, G. S. Urgessa, (2008)

Maji et al. (2008) set up a rectangular room (6.1mx3.7m, 4m high in dimension) with masonry walls on each side and set a charge 0.76m above the center of the room. **Figure 2-42** shows the setup of the experiment. The walls were constructed using hollow masonry units set in running bond. The walls were restrained by a reinforced concrete frame. All the walls were retrofit with GFRP on the tension face, but the north and south walls (the two larger walls) were also reinforced with two inches of shotcrete on the compression face. Two GFRP laminates were used, a unidirectional fabric that was applied vertically, and a ply that ran 0/90 in direction. Iron angle connections were attached to the bottom of the walls to simulate simple support conditions.

Figure 2-42. Test setup (Maji et al., 2008)

The west wall which was only reinforced with GFRP, remained standing after the test. However, the masonry bricks failed in compression, which meant the front face completely crumbled. The back face remained attached to the GFRP laminates. The east wall was similarly reinforced but had the addition of a door. While the back face remained attached to the reinforcement, the wall was destroyed. The stress concentrations near the door caused the GFRP to fail in shear in several places, with tears running both vertically near the center of the wall and horizontally near the top support.

The north and south walls, which were retrofit with shotcrete, remained intact and standing after the test (**Figure 2-43**). The GFRP remained bonded to the wall and to the supports, and the shotcrete received minor damage in the form of spalling.

The authors conducted an analytical examination of the walls supported with shotcrete and GFRP and GFRP only. It was found that the models agreed with the experimental results adequately. The additional mass and resistance to bending that the shotcrete provides allowed the north and south walls to withstand the blast. The authors conclude that GFRP retrofit is an effective solution for URM walls subjected to blast.

Figure 2-43. Results of the test. The north and south walls remained intact. (Maji et al., 2008)

J. Zhang, M. Maalej, S. T. Quek, 2007

Zhang et al. (2007) tested ten ECC blast shelter panels under impact loads imparted by a 45kg hammer dropped from a height of 4m (**Figure 2-44**). The impact was repeated until perforation of the panel. The panels were each 2m x 1m in area, and each had 8mm rebar reinforcement spaced at 150mm to centre. The ten panels were split into five groups, each group containing two identical panels. The first two groups tested simple RC panels and FRC panels. The concrete used had a strength of 40MPa, and the FRC had a mix containing 1% of steel fibres. The next three groups were all composed of ECC panels with thicknesses of 100mm, 75mm and 50mm, respectively. The panel with 50mm thickness had 6mm rebar instead of 8mm rebar. The ECC was composed of 0.5% steel fibres and 1.5% polyethylene fibres by volume.

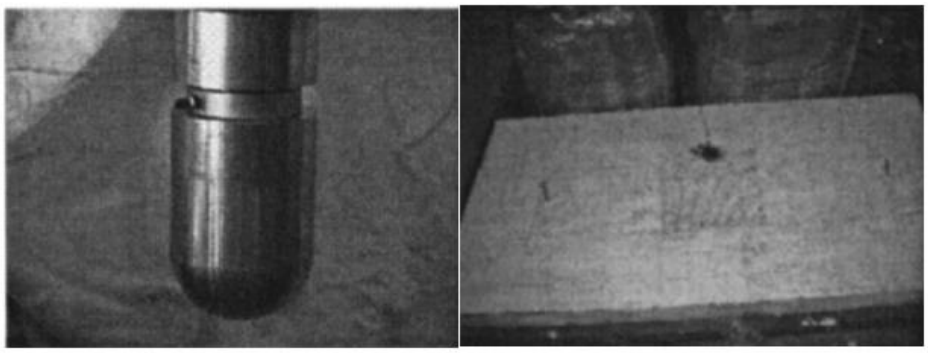

Figure 2-44. Hammer and panels

The RC panels perforated after about 3 impacts (**Figure 2-45**), with severe scabbing occurring after the second impact. The FRC panels fared better than the RC panels, perforating after seven impacts. However, scabbing occurred after only three impacts. The RC and FRC panels failed in a brittle manner due to shear. The ECC panels were found to perform much better than the RC and FRC panels. The 100mm thick ECC panel only sustained very minor micro-cracking, and the test was discontinued after ten impacts due to the panel's resistance to damage. Similarly, the 75mm thick ECC panel only sustained minor cracks with no scabbing after ten impacts, and only perforated at 17 impacts. The 50mm thick ECC panel did sustain damage after the fifth impact but failed after 12 impacts. The authors note the ability of the ECC panels to absorb energy by deforming more than the normal concrete panels. The ECC panels could also resist more impacts after scabbing. After perforation, the ECC panels were also found to be more structurally sound, since the hole's diameter in the ECC panels were less than 3 times smaller than the holes found in the normal concrete panels. Furthermore, the ECC panels prevented the formation of a critical macro-crack by distributing the energy through many smaller cracks.

The authors present a SDOF concept to describe the experimental results and conclude by stating the benefits of using ECC for "protective structures".

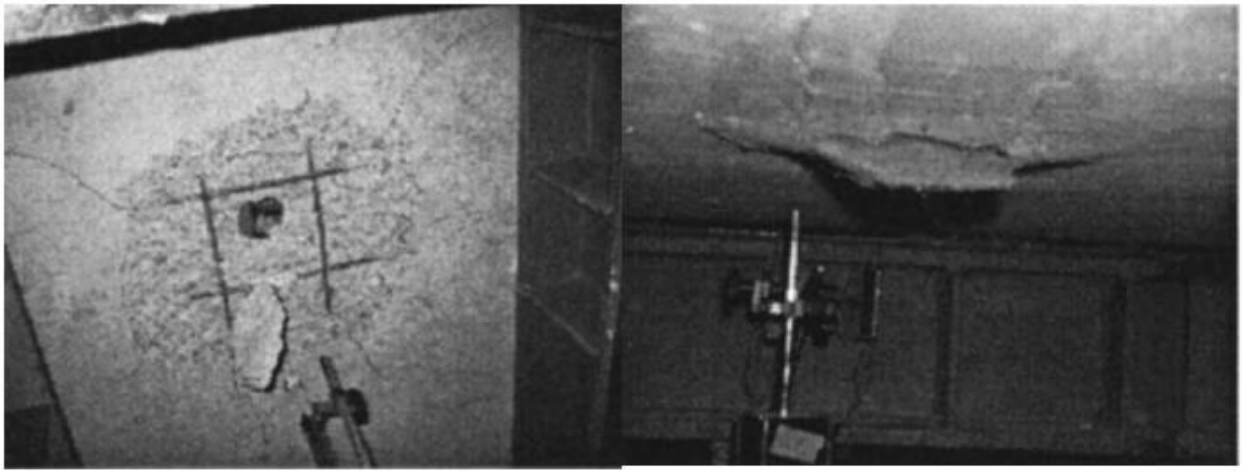

Figure 2-45. RC panel after three impacts, and ECC 50mm panel after ten impacts

M. Maalej, J. Zhang, S.T. Quek & S.C. Lee, 2004

Maalej et al. (2004) conducted static and dynamic tests to study the effect of high velocity projectiles on hybrid fiber ECC. By following the critical volume fraction concept for hybrid fiber ECC, the authors chose the mix to contain 0.5% steel and 1.5% polyethylene by volume.

For the uniaxial tensile tests, specimens measured 300mmx75mmx15mm and were loaded at a rate of 0.2mm/min. The stress strain relationship shows that after the first crack appears, the stiffness is reduced, and there is a sudden decrease and subsequent increase in stress as cracks are formed and stress transfers to fibers. On average, the specimens failed at a strain of 5%, with an ultimate capacity of 5MPa at 4% strain. An increase in strain rate caused an increase in strength and stiffness. The Dynamic Increase Factor (DIF) was found to be higher than that of normal concrete of the same strength. The authors also noted the average strain capacity slightly decreased as strain rate increases. Furthermore, the authors noted that ECC created multiple micro cracks under high strain rates, and not one large failing crack as is common with normal concrete.

Uniaxial compressive tests were also conducted on 50mm cube specimens (70MPa) and 100mmx200mm cylinder specimens (55MPa). Young's modulus was found to be 18GPa.

Ballistic tests were performed with 15-gram projectiles with an impact velocity of 800m/s to evaluate damage done to panels 300mmx170mm of varying thickness (55,75,100,120,150mm). The recorded data included depth penetration, crater size, cracking, spalling, scabbing, and fragmentation. There was no correlation of impact velocity to crater size. The thicker ECC specimens had a reduced penetration depth compared to the thinner ones, but not much improvement over normal concrete. There was no fragmentation or scabbing on the opposite face in the ECC panels, and very little spalling on the impact face. There was significant improvement to crack distribution in the ECC panels with respect to normal concrete panels. Upon impact, the ECC panels produced thin micro-cracks as opposed to larger cracks leading to failure (**Figure 2-46**). Furthermore, the integrity of ECC panels remained intact after impact.

Figure 2-46. Ballistic Tests (Maalej et al., 2004)

2.6. MODELLING METHODS OF MASONRY WALLS

There are several models used by researchers to predict the behavior of masonry walls under dynamic loading. The methods include the Rigid Stiffness model, the Rocking Block model, and Finite Element Modelling.

2.6.1. Rigid Stiffness Model

The Rigid Stiffness model assumes that the wall acts in rigid bodies, which rotate about their base. The rigid bodies are separated by fully cracked cross-sections (Doherty et al., 2002). Different models can be built from these assumptions, ranging from SDOF systems to MDOF systems.

2.6.1.1. SDOF Systems

For SDOF systems, the governing degree of freedom is taken at the mid-height of the wall (Abou-Zeid, 2011). Doherty et al. (2002) explains that the system can be generalized into a lumped mass SDOF model (**Figure 2-47**). Furthermore, "the mass of the system models the overall inertia force developed in the wall, whilst the spring models the ability of the wall to return to its vertical position during rocking by virtue of its self-weight" (Doherty et al., 2002).

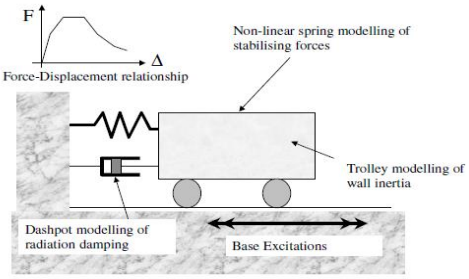

Figure 2-47. Lumped Mass SDOF model (Doherty et al., 2002)

This method of analysis was also performed by Ciornei (2012) and was found to conform well with the experimental wall displacement results (see **Figure 2-48**). The governing equation of motion for this system is shown by Equation 2.1, where m is the mass of the wall, $\ddot{u}(t)$ is the acceleration experienced by the wall, R is the resistance of the wall, u(t) is the displacement experienced by the wall and F(t) is the forcing function. K_{LM} is the load mass factor, which is dependant on the shape function of the system being analyzed. Load mass factors have been tabulated for common one-way systems. Once the resistance function is determined through numerical or experimental means, Equation 2.1 can be solved with numerical integration, such as the average acceleration method.

$$K_{LM}m\ddot{u}(t) + R(u(t)) = F(t) \qquad [\mathbf{2.1}]$$

The Resistance function is built to predict the change in resistance of the wall as it deflects. Ciornei (2012) states that the "resistance function is dependent on the dynamic strength of materials under high strain-rate loading". The Resistance function also describes the transition from elastic to plastic responses of the member (Ciornei, 2012).

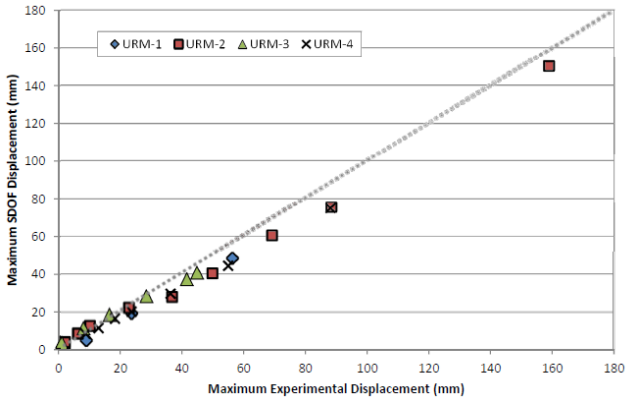

Figure 2-48. Maximum measured response vs Maximum SDOF response (Ciornei, 2012)

Factors that affect the resistance of a URM wall include axial load, flexural resistance and arching action. Different retrofit methods will also affect the resistance function, as the may increase the stiffness and strength of the wall or solely contribute to membrane action. **Figure 2-49** compares the resistance of an infill URM wall to the resistance of an infill polyurea retrofit URM wall as formulated by Ciornei (2012). For the non-retrofit wall, the resistance function depends on the flexural response of the wall, and the activation of arching. Arching action was delayed since there was a small gap between the wall and the top support. For the retrofit wall, the resistance is dependant on the flexural response, the activation of both stages of arching action, and the presence of the polyurea retrofit. There are two stages to arching action for this wall, since it was assumed that the initial arching action would crack the mortar in the wall (Ciornei, 2012). The second stage

of arching action would occur as the top edge of the wall pressed against the top support (Ciornei, 2012). The resistance increases until over a deflection of 350mm and a force of 100kN due to the membrane action of the polyurea.

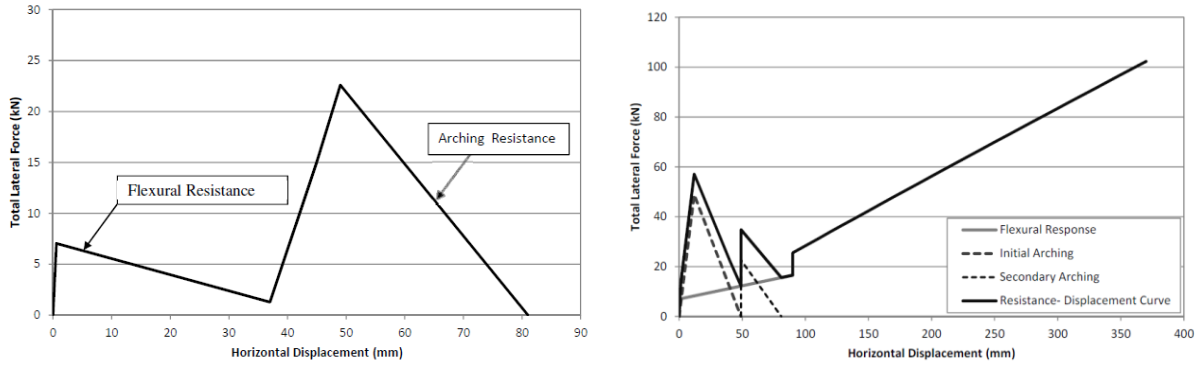

A) B)

Figure 2-49. A) Sample Restoring force-displacement relationship for sample URM wall. B) Sample Restoring force-displacement relationship for retrofit URM wall (Ciornei, 2012)

Elsayed et al. (2015) also conducted SDOF modelling on reinforced masonry walls using the same methodology. The load-mass factor is determined from the shape function, and simplified DIF and SIF factors can be taken from the CSA S850-12 standard. Instead of building the resistance functions from theory, Elsayed et al. (2015) used the trilinear restoring force-displacement relationship suggested by UFC 3-340-02 with Equations 2.2a through 2.3b. The equations shown are for a one-way out-of-plane bending element with fixed-fixed conditions (Elsayed, 2015). EI is the stiffness of the wall and H is the height of the wall. M_p is the plastic moment of the wall and is determined by sectional analysis (see Section 2.6.4). The resistance function can be seen in **Figure 2-50**.

$$\mathrm{K_e} = \frac{384\mathrm{EI}}{\mathrm{H^3}} (Elastic\ Stiffness) \qquad [\mathbf{2.2a}]$$

$$\mathrm{K_{ep}} = \frac{384\mathrm{EI}}{5\mathrm{H^3}} (Elasto-Plastic\ Resistance) \qquad [\mathbf{2.2b}]$$

$$K_p = 0\ (Plastic\ Stiffness) \qquad [\mathbf{2.2c}]$$

$$R_e = \frac{12M_p}{L}\ (Elastic\ Resistance) \qquad [\mathbf{2.3a}]$$

$$R_{ep} = \frac{16M_p}{L}\ (Elasto-Plastic\ Resistance) \qquad [\mathbf{2.3b}]$$

Elsayed et al. (2015) then used Equation 2.1 to solve the behaviour of the wall. From the mid-height displacement, the support rotation was found, and the resulting response limit from CSA S850-12 (see Section 2.2.4).

Elsayed et al. (2015) ensured their SDOF model was accurate by performing several experimental tests to compare the results; and they concluded that their calculated results agreed with the measured values. Using their proven SDOF model, Elsayed et al. (2015) performed a parametric

study, determining the effects of charge, standoff distance, reinforcement properties and configuration, wall height and block size on blast performance.

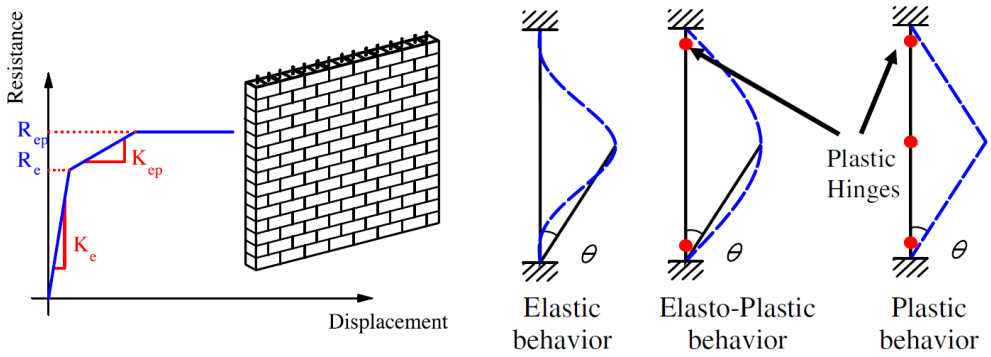

Figure 2-50. Resistance Function from wall behaviour (Elsayed et al., 2015)

2.6.1.2.MDOF Systems

Simsir et al. (2004) developed a MDOF system to account for the "flexibility of the diaphragm, the stiffness of the wall, and the possibility for horizontal cracks developing under combined flexural moments and axial forces". The MDOF system assumes that the concrete blocks are linear elastic beam elements, and the mass of each course is lumped at the mortar joints (Simsir et al., 2004). The mortar joints are modelled as non-linear beam fiber elements (Simsir et al., 2004). This model was developed for the DRAIN-2DX program, which is shown in **Figure 2-51**.

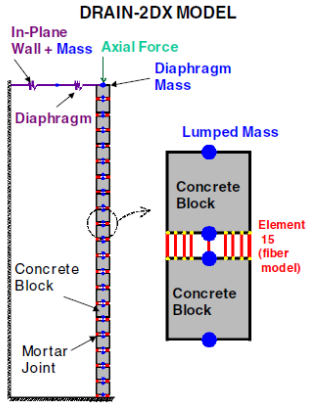

Figure 2-51. MDOF system (Simsir et al., 2004)

To simplify the MDOF model, Simsir et al. (2004) also developed a 2DOF model, shown in **Figure 2-52.** The model is composed of two rigid bodies "interconnected by hinges; relative rotations of the bars are resisted by rotational springs k1 and k2 located at the hinges" (Simsir et al., 2004). For this method, moment-rotation relationships are derived in the place of restoring force-displacement graphs.

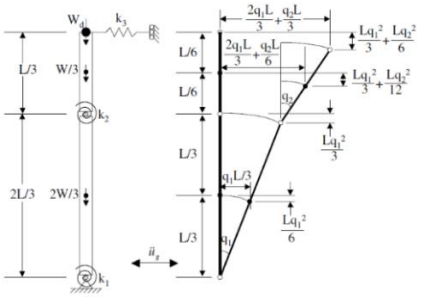

Figure 2-52. 2DOF developed by Simsir et al. (2004)

2.6.2. Rocking Block Model

The Rocking Block model was developed by Makris and Konstantinidis (2003). This model attempts to describe the rocking motion of a rigid body using gravity as the restoring force instead of from the elasticity of the structure (Makris and Konstantinidi, 2003). The differences between a Rigid SDOF model and the Rocking Block model are shown in **Figure 2-53**. Makris and Konstantinidis (2003) explains that "SDOF oscillator has a positive and finite stiffness, k, and energy is dissipated as the force–displacement curve forms closed loops". On the other hand, the Rocking Block model "has infinite stiffness until the magnitude of the applied moment reaches mgRsinα, and once the block is rocking, its stiffness assumes a negative value and decreases monotonically, reaching zero when θ=α=block slenderness" (Makris and Konstantinidis, 2003). Additionally, the masonry wall has a specific frequency in the rigid stiffness model but does not have a distinct frequency in the rocking block model (Sharif et al., 2007).

According to Sharif et al. (2007), the rigid body rocking model more accurately predicts response of cracked URM walls as opposed to the stiffness models. The rocking model is not based on the mass of the block, but rather on the dimensions of the block (Sharif et al., 2007). The commercial software *Working Model* can be used to predict behavior of the URM walls subjected to earthquakes and uses Newtonian physics and numerical methods (Sharif et al., 2007).

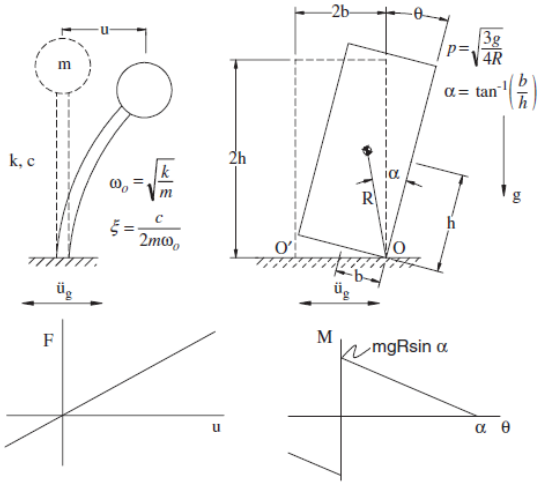

Figure 2-53. Rigid SDOF Model compared to Rocking Block Model (Makris and Konstantinidis, 2003)

2.6.3. Finite Element Modelling (FEM)

Finite Element models can also be used to predict the response of masonry walls to out-of-plane loads. Irshidat et al. (2011) developed a finite element model in AUTODYN to predict the response of URM walls retrofit with a polymer subjected to blast. Each experimental wall was split into 8670 small Lagrangian cells (Irshidat et al., 2011). Each cell was identified with the material model chosen to simulate the behavior of masonry, mortar, and the polymer, respectively. It was concluded that the FE model reasonably fit the experimental data, by "generally matching failure shape, location of break lines, and midpoint deflection at failure" (Irshidat et al., 2011). Sample FEM results are shown in **Figure 2-54** below.

Lampropoulos et al. (2018) used the ATENA finite element software to model a retrofit of masonry walls retrofit with an overlay of ultra high-performance fiber reinforced concrete (UHPFRC). The in-plane loading was applied in a quasi-static manner at the top of the wall. The study concluded that the overlay of UHPFRC increased the structural performance of the wall, especially when the slip between the overlay and wall was limited. The study recommends adding UHPFRC into the joints to further the bond between the wall and overlay.

Davidson et al. (2005) and Alsayed et al. (2016) also found success with their FE models. Davidson et al. (2005) notes that one of the difficulties was to properly simulate the interaction between the walls and supports to incorporate the arching mechanism. Other difficulties include properly modelling gravity and preload effects, modelling the interface between the wall and retrofit, and choosing material models under high strain rates (Davidson et al., 2005).

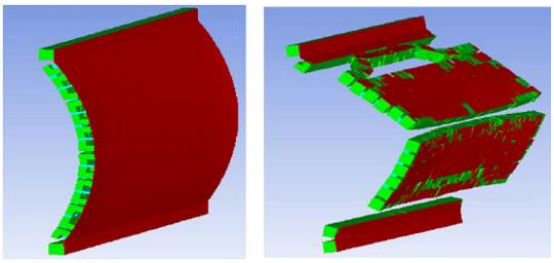

Figure 2-54. FEM of the retrofit wall and the a) beginning and b) end of failure (Irshidat et al., 2011)

2.6.4. Sectional Analysis of Walls Retrofitted with Fiber-reinforced Concrete Overlays

Lin et al. (2016) modelled a retrofitted masonry wall by "using concrete flexural design methodology, ignoring the tensile strength of the masonry but including the wall self-weight acting through the wall centreline". **Figure 2-55** shows the sectional analysis for determining the moment capacity of one of the walls tested. The tension (T) in the steel can be found by assuming the steel yields. The compression force (C) can be found using Equation 2.4, ultimately assuming stress blocks such as in RC beam analysis. N represents the axial load of the wall.

$$\boldsymbol{C = T + N} \qquad [\mathbf{2.4}]$$

$$\boldsymbol{M_p = T * d_1 + C * d_2} \qquad [\mathbf{2.5}]$$

The moment capacity can then be found by taking the moment around the neutral axis using the following Equation 2.5, where d_1 and d_2 are the distance from the centroid of the load to the

neutral axis for Tension and Compression, respectively. Then the load that will cause the moment M_p can be determined with static analysis of the boundary and loading conditions.

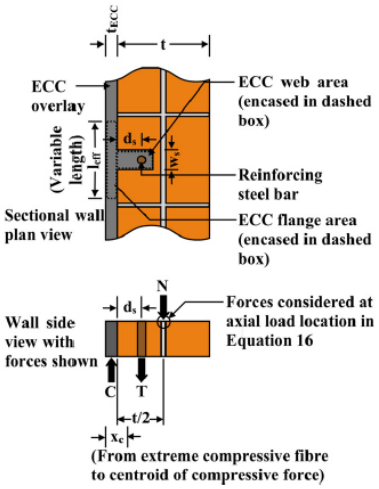

Figure 2-55. Sectional Analysis (Lin et al., 2016)

2.7. SUMMARY OF LITERATURE REVIEW

This chapter presented an overview of URM walls, their vulnerability to out-of-plane failures and common methods for blast retrofit. Previous research on the use of FRP and polyurea blast retrofits was summarized, as well as out-of-plane seismic retrofit using shotcrete and other cementitious systems. This chapter also presented different methods of modeling masonry walls. The key findings from the literature review are summarized below:

- URM walls are very weak in the out-of-plane direction, exhibiting many different failure modes. Failure mechanisms of URM and retrofit URM walls subjected to blast include shearing at the supports, bending compression, bending tension, and delamination of the retrofit. The supports must be properly reinforced to prevent shearing of the reinforcement and wall. Bending compression failure occurs when the front face of the wall breaks apart due to the bending caused by the blast. Bending tension failure occurs if the reinforcement on the back side fails in tension. Delamination of the reinforcement occurs when the retrofit system debonds from the wall. This mode of failure is prevalent in FRP systems. Shear and delamination failure modes should be avoided when designing retrofit systems.
- Arching action is found to be significant in increasing the out-of-plane resistance of URM walls. Arching occurs when a masonry wall undergoes bending within a fixed frame. The bending causes stress to build up against the frame surrounding the wall which creates a resisting moment to the out-of-plane load.
- Retrofit systems for URM walls are required to resist extreme loads caused by earthquakes and blast. Retrofit systems include FRP, polyurea and shotcrete/cementitious systems, and all have been shown to be effective strengthening methods that increase energy absorption. Fragmentation of the walls is also reduced when these systems are in place.
- ECC is special type of fiber reinforced cementitious material that typically contains a lower amount of cement and higher volumes of fly ash or other supplementary cementing

materials, as well as fibers. ECC has a much higher flexural capacity than normal FRS, which makes it an ideal blast retrofit solution. Fibers and meshes can be embedded in ECC to greatly enhance its flexural capacity. Different meshes include textile reinforcement, welded wire mesh or diamond meshes. Different types of fibers include steel or synthetic fibers; with varying shapes and sizes. Steel fibers perform better than other kinds of fibers, including polypropylene or other synthetic fibers. Additionally, deformed fibers perform better than straight fibers.

- When using ECC as a retrofit, the strength of the wall is proportional to the thickness of the ECC layer; that is, as the thickness increases so does the strength, but with diminishing returns. Increasing the thickness of the overlay or adding steel mesh increases the stiffness of retrofit.
- Retrofit systems are more effective when applied to the tension side of URM walls. When ECC systems are applied on both sides of the wall, the deflection of the wall decreases and the strength increases. Energy absorption may also decrease when ECC is applied to both sides of a URM wall since the failure mechanism can change to buckling of the compression side ECC which leads to debonding of the retrofit.
- Various modelling techniques have been used by researchers to predict masonry wall behaviour. Using the Rigid Stiffness model, SDOF analysis has been shown to accurately provide the response of masonry walls subjected to blast. Different methods of determining the resistance function of masonry walls where presented.

CHAPTER 3. EXPERIMENTAL PROGRAM

3.1. CHAPTER OVERVIEW

This chapter details the experimental program of this thesis. The details of the test specimens are outlined below, followed by an overview of their construction and shotcrete application. The material properties are summarized. The testing setup using the shock tube is explained, and the testing plan is outlined.

3.2. DETAILS OF TEST SPECIMENS

This section details the walls, retrofit and boundary conditions.

3.2.1. Specimen Overview

A total of six walls were tested for this thesis. Two concrete masonry (CMU) walls and four stone walls were built. The dimensions of each wall were 2m high by 2m wide. **Figure 3-1** shows the geometric properties of the two wall types.

The CMU walls were built with architectural concrete blocks that were 100 mm (4") thick (**Figure 3-2** shows the dimensions and properties of the standard 100 x 200 x 400 concrete masonry unit blocks used in this study). The blocks were built in running bond (as pictured in **Figure 3-1** A). The thickness was the same for the stone walls. The height of the stone blocks varied from 63.5mm (2.5"), 127mm (5") and 203.2mm (8"). Type S mortar was used for each wall. High early strength grout was placed at the top of each wall to fill in the gap between the wall and the top HSS support to promote arching action. **Figure 3-3** shows some of the CMU and stone walls that were constructed.

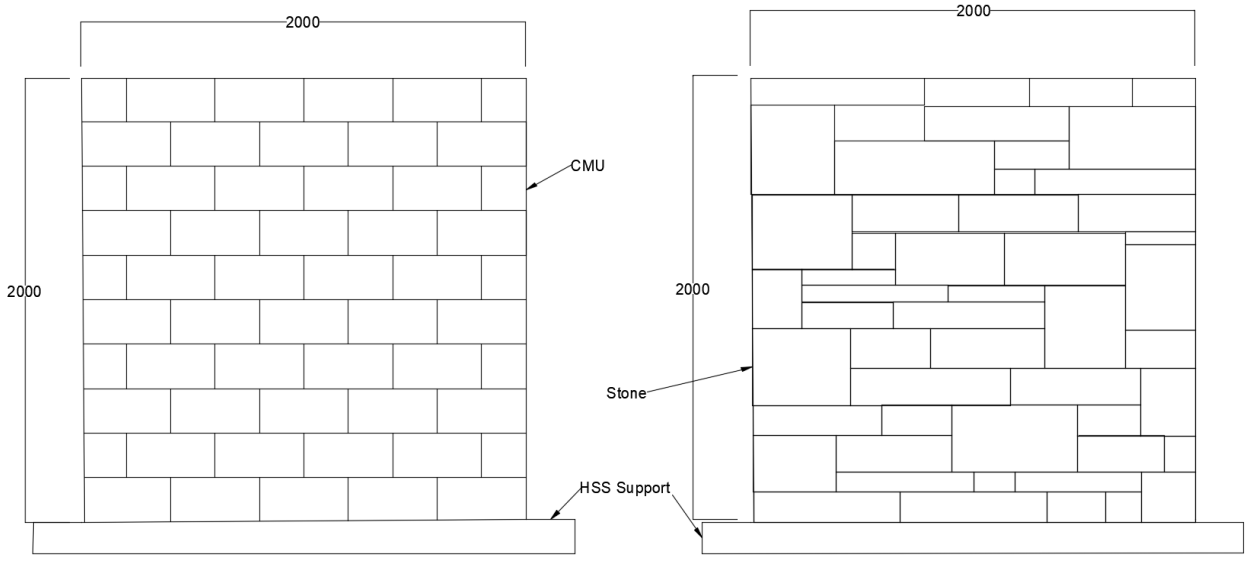

Figure 3-1. A) CMU wall. B) Stone wall

(a) Typical CMU units

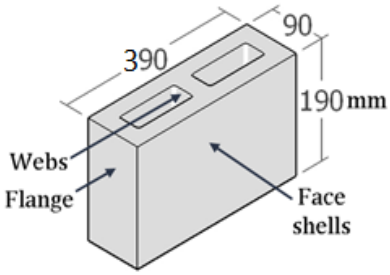

(b) Standard 100x 200 x 400 CMU units (edited from cmu.com.my/product-cmu.php

Modular Size (mm)	100
Actual Overall Width (mm)	90
Minimum Faceshell Thickness (mm)	20
Minimum Web Thickness (mm)	20
Equivalent Thickness (mm)	66
Percentage Solid	74
Approximate Mass of Wall in Place (kg/m^2)	140

(c) Standard CMU properties (Ciornei, 2012)

(d) Typical Stone units

Figure 3-2. Typical CMU and Stone blocks

A) B)

Figure 3-3. A) CMU block and B) Stone walls

3.2.2. Description of Specimens

A summary of the walls tested in this research program is displayed in **Table 3-1** below. The name designated to each wall follows the same pattern: AAA-A-A. The first three letters describe if the wall is a Retrofit Masonry Wall (RMW), or an Unreinforced Masonry Wall (URM). The next letter describes whether the wall is composed of CMU masonry blocks (C) or stone blocks (S). The last letter shows if the wall is non-load bearing (N) or load bearing (L).

Table 3-1. Summary of Retrofits

Series	Wall ID	Type of Masonry	Axial Load *KN (%Po)*	Steel Mesh *Gage (dia. in mm)*	Description & Retrofit details
CMU Series	**URM-1***	CMU	--	--	CMU Infill Control
	URM-3*		122 (10%)	--	CMU Load Bearing Control
	RMW-C-N		--	152 × 152 M W13.3 × M W13.3 Gage 6 (4.11mm)	Retrofit - CMU Infill *Overlay of ECC shotcrete (51mm)*
	RMW-C-L		146 (10%)	152 × 152 M W13.3 × M W13.3 Gage 6 (4.11mm)	Retrofit - CMU Load Bearing *Overlay of ECC shotcrete (51mm)*
STONE Series	**URM-S-N**	STONE	--	--	Stone Infill Control
	URM-S-L		171 (4%)	--	Stone Load Bearing Control
	RMW-S-N		--	152 × 152 M W34.9 × M W34.9 Gage 2 (6.54mm)	Retrofit - Stone Infill *Overlay of ECC shotcrete (51mm)*
	RMW-S-L		171 (4%)	152 × 152 M W34.9 × M W34.9 Gage 2 (6.54mm)	Retrofit - Stone Load Bearing *Overlay of ECC shotcrete (51mm)*

*Tested by Ciornei (2012)

Table 3-1 indicates the level of axial compression load applied on each wall. It is noted that the concentric capacity P_o was computed based on the CSA S304.1-04 standard:

$$P_o = f'_m A_e \quad [3.1]$$

where f'_m = average masonry prism strength and A_e = effective cross-sectional area of wall. For the CMU walls, f'_m was taken as10MPa, and A_e as 80% of the total area of the wall (90x2000mm). For the stone walls, f'_m was taken as 24MPa, and A_e as 100% of the total area of the wall. For the CMU load bearing series, an axial load of 10% was used to compare with the load that Ciornei (2012) applied to the control walls. For the stone load bearing series, an axial load of 4% was taken to compare with the walls tested by Saatcioglu et al. (2018).

URM-1 and URM-3 are CMU control walls tested by Ciornei (2012). URM-1 is a non-load bearing wall, while URM-3 is a load bearing wall with 10% of axial load applied, which is about 122kN (**Figure 3-4**). To promote arching action, the gap between the URM infill and the enclosing frame was reduced to 6 mm using structural steel filler. The load-bearing wall was constructed with no top edge gap. The boundary conditions are illustrated in the figure below and consisted of top and bottom HSS assemblies which acted as simple supports.

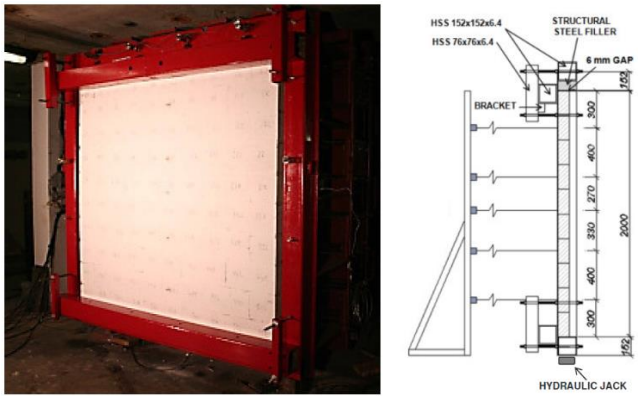

Figure 3-4. Picture and Diagram of URM-1 and URM-3 (Ciornei, 2012)

RMW-C-N was a CMU non-load bearing wall, retrofit with a 51mm overlay of ECC shotcrete. The shotcrete was from the same batch as RMW-C-L. The welded wire mesh (152x152 M W13.3xM W13.3) was placed 13mm away from the face of the wall before the shotcrete was applied. The welded wire mesh was welded to the top and bottom HSS supports to ensure the steel acted as tension reinforcement. All welded wire mesh used in this research was 152mmx152mm (6"x6"). To promote arching action, the gap between the wall and top HSS beam was filled with grout. The top and bottom restraints consisted of steel plates attached to the HSS supports as shown in **Figure 3-5**.

RMW-C-L was a CMU load-bearing wall, retrofit in the same manner as RMW-C-N (**Figure 3-5**). The welded wire mesh (152x152 M W13.3xM W13.3) was placed 13mm away from the wall, and a shotcrete layer of 51mm was applied over it. The shotcrete was from the same batch as RMW-C-N. The welded wire mesh was welded to the top and bottom HSS supports and the wall had the same boundary conditions. The load applied to the wall was 146kN, which corresponds to 10% of the axial resistance of the wall. 10% was chosen to compare with the control wall tested by Ciornei (2012). The boundary conditions were identical to RMW-C-N.

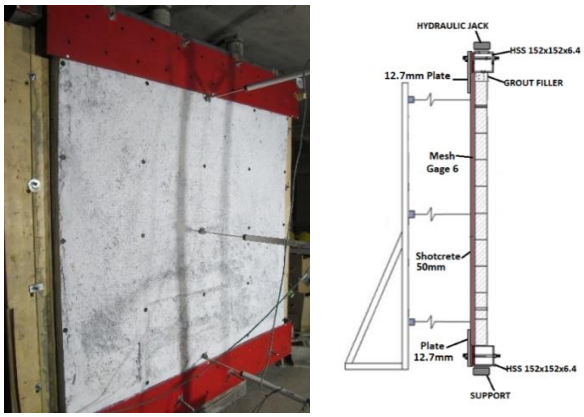

Figure 3-5. RMW-C-L and RMW-C-N

URM-S-N was a stone infill wall. No retrofit was applied on this control wall, however the gap between the wall and supporting frame was filled with grout to promote arching action.

URM-S-L was a stone load-bearing wall (**Figure 3-6**). As with URM-S-N, this was a control wall, so no retrofit was applied but the top gap was filled with grout to promote arching action. The load

applied was 171kN, which was about 4% of the total axial resistance of the wall. A value of 4% was chosen to compare the stone walls tested by Saatcioglu et al. (2018).

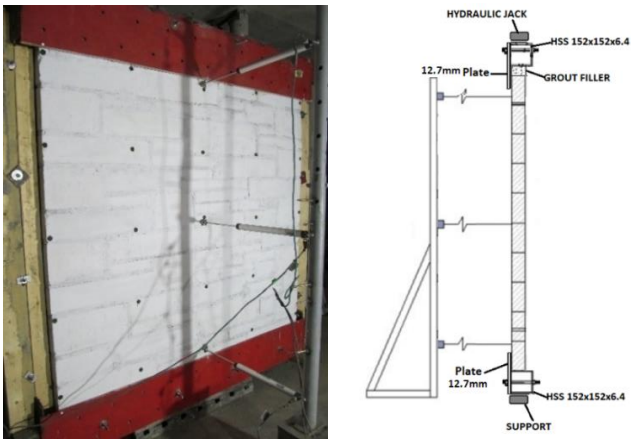

Figure 3-6. URM-S-L and URM-S-N

RMW-S-N was a stone infill wall, retrofit with ECC shotcrete and welded wire mesh. The thickness of the welded wire mesh was increased to gage 2 (152x152 M W34.9xM W34.9) to provide a more ductile response. The wire mesh (152mmx152mm) was placed 13mm away from the face of the wall and welded to the top and bottom HSS supports. The shotcrete was sprayed over the mesh with a thickness of 51mm. The top gap was filled with grout to promote arching action.

RMW-S-L was a stone load-bearing wall, retrofit in the same manner as RMW-S-N (**Figure 3-7**). Welded wire mesh (152x152 M W34.9xM W34.9) was placed 13mm away from the wall and was welded to the top and bottom HSS supports. Shotcrete was applied over the mesh with a thickness of 51mm from the wall. The applied load was 171kN, the same as the control wall tested. The top gap was filled with grout to promote arching action.

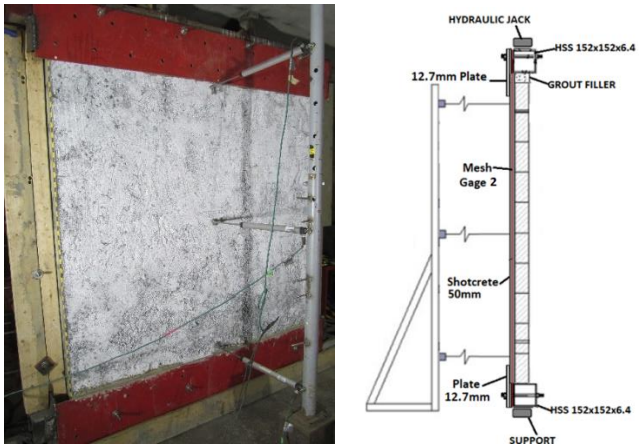

Figure 3-7. RMW-S-L and RMW-S-N

3.3. WALL CONSTRUCTION AND SHOTCRETE APPLICATION

This section details the construction of the walls and the application of the retrofit.

3.3.1. General

The walls were built on HSS beams by a professional brick layer, with dimensions of 2mx2m (**Figure 3-8**). The walls were built 13mm (1/2 in) away from the face of the HSS beams, since the mesh would be placed flush with the HSS. This allows a space of 13mm between the mesh and the wall, which can be seen in **Figure 3-8**.

A) B)

Figure 3-8. A) Mason laying out the CMU walls. B) 13mm of space between mesh and wall

The mortar used was type S and had a typical thickness of 10 mm. Water was mixed in a bucket using an electric mixer, until the desired consistency was achieved.

Once construction was finished, the walls and prisms were moist cured for one day. All walls, prisms and mortar blocks were kept in the same room for the duration of the research.

3.3.2. Retrofit Application

The wall was placed in the shocktube frame, and a layer of high strength non-shrink grout was placed on top of the wall. The purpose of the grout was to even out the top of the wall so loads would be applied equally over the wall, and to fill the space between the wall and the top HSS beam to promote arching action. After the grout had set, the HSS beam was installed at the top and fixed to the shocktube frame. It should be noted that for every wall after RMW-C-N, the grout was placed after the shotcrete was applied. **Figure 3-9** shows how the wall was prepared for retrofit.

The 152mmx152mm (6inx6in) steel mesh was placed flushed and tack welded to the top and bottom HSS beams. The mesh was kept at 13mm (1/2 in) from the face of the wall with small wooden spacers that were glued to the wall. A wooden formwork was installed around the face of the wall for the placement of the shotcrete.

Before the shotcrete was applied by a professional nozzleman, the wall was sprayed with water to prevent the dry CMU blocks from absorbing the moisture from the shotcrete. Next, the shotcrete was applied in a layer about 51mm thick (2 in). Due to the nature of shotcrete, the layer was not completely the same thickness, but was satisfactorily uniform for the scope of this research. Please see section 3.3.4 for more information of how the shotcrete was applied. **Figure 3-10** shows the top support of the wall before and after the shotcrete was applied.

A) B)

Figure 3-9. A) Wall is placed in the shocktube frame. Grout and top HSS are placed, as well as mesh. B) Formwork is placed in preparation for the shotcrete

Figure 3-10. Before and After shotcrete was applied.

3.3.3. Retrofit of RMW-C-L

When moving RMW-C-L, the wall experienced some damage on the compression side. A total of 4 blocks at the edges were cracked and the faces of the blocks fell out. To repair this, Styrofoam was placed where the CMU block would be hollow, and the space was filled with repair concrete. The damage and repair can be seen in **Figure 3-11**. A few vertical cracks remained along the edges after the repair was completed. It should be noted that the shotcrete sustained no damage.

Figure 3-11. Damage and Repair of RMW-C-L

3.3.4. Shotcrete Application

The shotcrete used was supplied by King Shotcrete solutions. The designation of the shotcrete was FS-T3, a type of ECC shotcrete used in tunnel mining applications. See Section 3.4 and the work done by Ginouse et al. (2015) for the properties of the shotcrete used. Béton Projeté MAH was contracted to apply the shotcrete on the walls.

The shotcrete was placed using a dry mix system. The air pressure was supplied by a Doosan P600 air compressor that can operate at 400-450 cfm with a pressure of 100-125 psi. The air pressure powered the dry cement intake machine, which pressurized the dry cement through the hose. A worker ensured that enough cement was placed into the intake, and that it was not clumped together. **Figure 3-12** shows the worker operating the cement intake machine.

Figure 3-12. Cement Intake Machine

At the same time, water was pumped through a separate hose. Both hoses lead to the nozzleman, who oversees mixing the desired amount of water and cement while spraying them onto the walls. **Figure 3-13** shows the nozzleman testing the shotcrete mix on a wooden panel, and the application

of shotcrete onto the wall. Due to the nature of shotcrete application, the material properties of the shotcrete are variable, as seen with the shotcrete material test results in Section 3.4.2.

Figure 3-13. Nozzleman tests the consistency of the shotcrete before applying it to the wall

After the shotcrete was applied, the overlay was cured with a water hose for 14 days. Burlap and plastic sheets were placed to retain the moisture.

Due to space constraints in the lab, the RMW-C-N and RMW-C-L were shotcrete together and were tested at an age ranging from 70 days to 120 days. After these walls were tested, space was made to shotcrete the next set of walls, RMW-S-N and RMW-S-L. This second set of walls was tested at ages ranging from 60 to 70 days.

3.4. MATERIAL PROPERTIES

3.4.1. Masonry and Concrete Properties

Mortar Tests: (ASTM C109) The mortar cubes (50mm) were tested using the concrete cylinder testing machine on the days of blast testing. A total of 5 cubes were tested. The mortar strengths were measured to be 16.0MPa, 16.7MPa, 16.9MPa, 16.3MPa, and 17.3MPa. The average of the tests is 16.6MPa. The following figure (**Figure 3-14**) presents the mortar tests.

Mortar Cube Setup	Sample Failure	Sample Load/Time curve
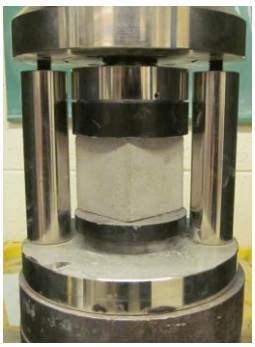	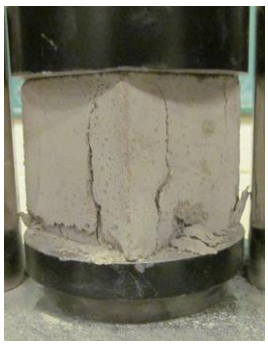	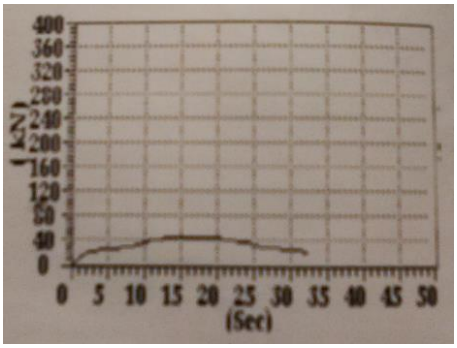

Figure 3-14. Mortar cube testing

Repair Concrete Tests: (ASTM C39) The leftover concrete used to repair RMW-C-L was tested as a cylinder on the days of testing RMW-C-L. The testing was performed by the concrete cylinder testing machine and measured a strength of 30.2MPa. The following figure (**Figure 3-15**) presents the performed test.

Repair Concrete Test	Failure Mode	Load/Time curve
		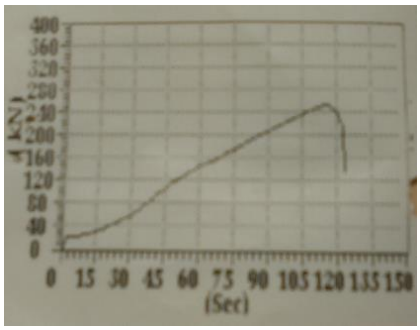

Figure 3-15. Concrete Cylinder Test

Stone Masonry Tests: The stone masonry was tested by Saatcioglu et al. (2018) (**Figure 3-16**). The stone blocks were one of three different sizes, small (300x90x60mm), medium (300x90x135mm), and large (300x90x200mm). According to Saatcioglu et al. (2018) the strength of the small blocks were: 33.3MPa; 32.4MPa; 32.0 MPa, with an average of 35.6MPa. The strengths of the medium blocks were: 27.5 MPa; 30.5 MPa; 28.0 MPa, with an average of 28.7MPa (Saatcioglu et al., 2018). The strengths of the large stones were: 23.2 MPa; 23.7 MPa; 24.5 MPa, with an average of 23.8MPa (Saatcioglu et al., 2018).

Figure 3-16. One of the stones tested by Saatcioglu et al. (2018)

Stone Prism Tests: (CSA S304.1-04 Annex D) Five single wythe stack prisms were constructed with the smallest stone blocks. Each prism is composed of four blocks, one on top of the other, with a layer of mortar in between. The dimensions of the prisms are on average 205x98x288mm. The prisms were cured in the same manner as the walls and were tested on days when the blast tests were conducted. With a h/t factor of 0.9, the strength was measured to be: 25.6MPa, 19.3MPa, 23.4MPa, 20.6MPa and 12.5MPa. The last prism will be counted as an outlier. The average strength of the stone prisms is 22.2MPa. The failure of the stone prisms was largely similar. The stones experienced vertical cracks along the height of the prism. The face of the stones fell off from one prism. Due to the strength of the type S mortar, the failure of the prisms was in the stone blocks. The strength of the stone prisms mirrored that of the stone blocks tested by Saatcioglu et al. (2018). The testing of the prisms is presented in **Figure 3-17**.

Stone Prism Test Setup	Failure Modes
	
	

Stone Prism Stress Strain Relationship (Test not strain controlled)

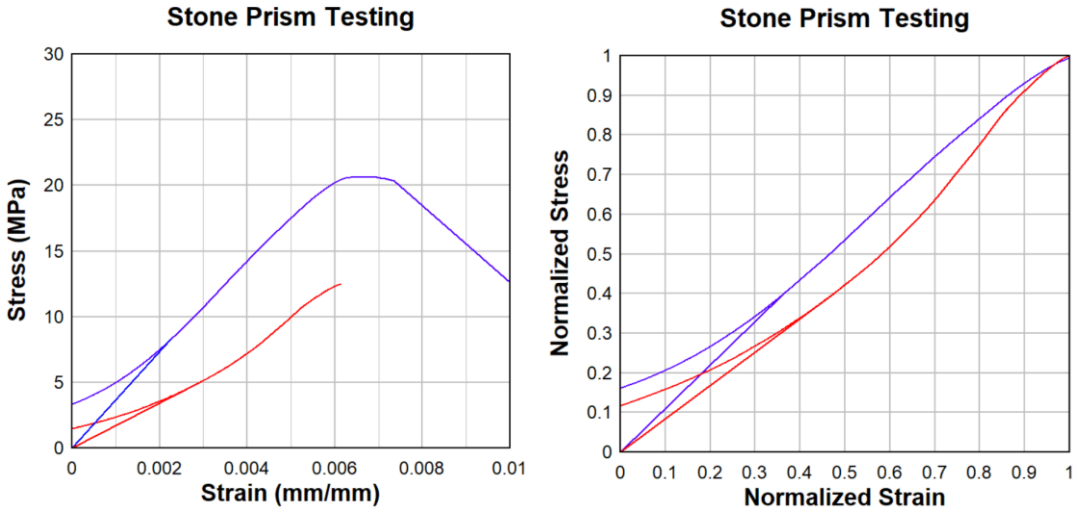

Figure 3-17. Stone Prism Testing

CMU Prism Tests: (CSA S304.1-04 Annex D) Four single wythe stack CMU prisms were constructed, with dimensions of 390x90x390mm. The dimensions of the individual CMU blocks were 390x90x190mm. Each prism was composed of two blocks, one on top of the other with a layer of mortar in between. The prisms were cured in the same manner as the walls and were tested on days when the CMU walls were tested. With a h/t factor of 0.9, the strength of the prisms was measured to be 9.9MPa, 7.8MPa, 9.3MPa and 10.9MPa. The average strength of the prisms is calculated to be 9.5MPa. The tests are presented in the following figure (**Figure 3-18**).

Stone Prism Setup	Stone Prism Sample Failure Modes
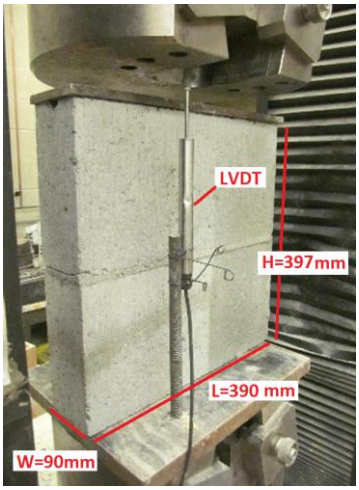	

CMU Prism Stress Strain Relationship (Test not strain controlled)

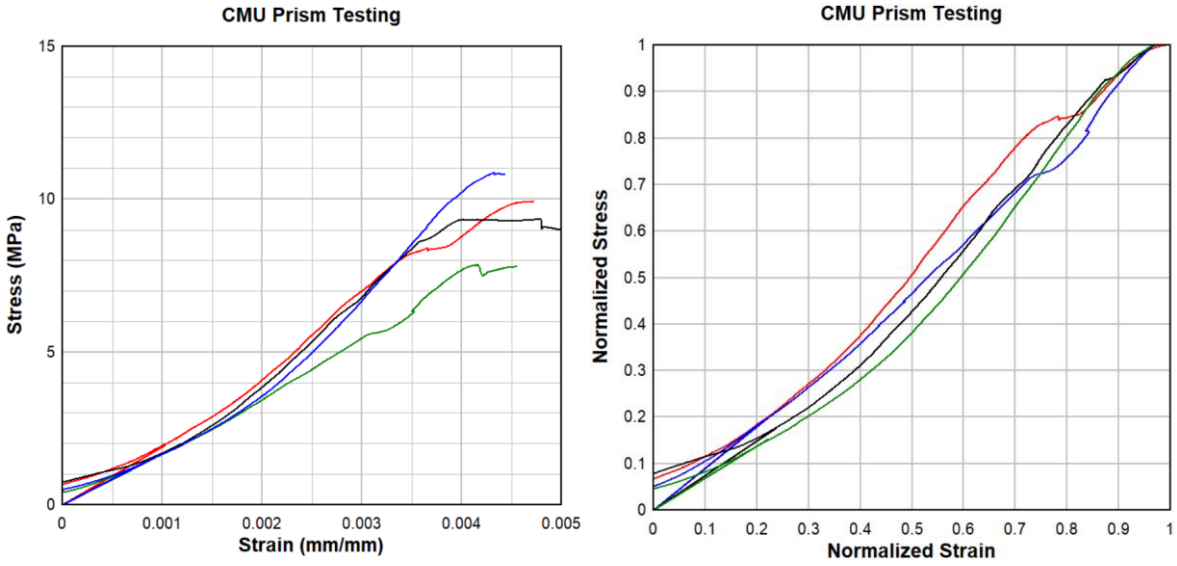

Figure 3-18. CMU Prism Testing

3.4.2. Shotcrete Properties

The ECC shotcrete used in this study was provided by King Shotcrete Solutions. According to the supplier the FS-T3 is a "high performance, fiber-reinforced, prepackaged shotcrete material for the dry-mix process. This product is a pre-blended, pre-packaged, cement-based, drymix shotcrete material containing a high dosage of synthetic fiber, set-time accelerator, silica fume, blended aggregates and other carefully selected components" (King, n.d.). The properties of the shotcrete as provided by the supplier are shown in **Table 3-2**. Properties of the shotcrete as reported by Ginouse et al. (2015) are reproduced in **Figure 3-19**. Further details can be found in Ginouse et al. (2015).

Table 3-2. FS-T3 Shotcrete Properties (King, n.d.)

COMPRESSIVE STRENGTH		
	ASTM C 116	**(MODIFIED)**
		21 °C (70 °F)
	1 Hour	5 MPa (725 psi)
	2 Hour	6 MPa (870 psi)
	4 Hour	10 MPa (1500 psi)
	6 Hour	20 MPa (2900 psi)
	24 Hour	35 MPa (5075 psi)
	ASTM C 1604	**21 °C (70 °F)**
	7 Day	45 MPa (6500 psi)
	28 Day	55 MPa (8000 psi)
FLEXURAL STRENGTH		
	ASTM C 78	**21 °C (70 °F)**
	28 Day	8.2 MPa (1180 psi)
SPLITTING TENSILE STRENGTH		
	ASTM C 78	**21 °C (70 °F)**
	28 Day	6.5 MPa (940 psi)
UNIAXIAL TENSILE STRENGTH		
		21 °C (70 °F)
	28 Day	4.0 MPa (580 psi)
FLEXURAL TOUGHNESS		
	ASTM C 1550	**21 °C (70 °F)**
	1 Day	
	Peak Load	47 kN
	Cumulative Energy	1000 J

(a) End beam test setup

Age	*Compressive Strength (MPa)*
1 hour	5.5
2 hours	6.5
4 hours	10.9
6 hours	20.3
24 hours	36.8

(b) Early age compressive strength using End-beam setup

Properties	*Age*	
	7 days	*28 days*
Compressive Strength (MPa) - ASTM C1604	48.8	57.2
Flexural Strength (MPa) – ASTM C78	8.5	8.2
Splitting Tensile Strength (MPa) – ASTM C496	6.25	6.55

(b) Later age strength properties

Figure 3-19. Properties of FS-T3 shotcrete as reported by Ginouse et al. (2015)

Preparation of Shotcrete: (ASTM C1140) One shotcrete panel was prepared for the first two walls, and one for the last two walls. Alongside the panels, shotcrete was also applied into prism molds for flexural tests. The panels and molds were cured in the same manner as the shotcrete on the walls, with sprayed water onto burlap sheets. The panels and molds were covered with plastic sheets. The sides of the panel were cut with a concrete saw, and cores were drilled from the panels (**Figure 3-20**). Care was used to ensure that the cores were perpendicular to the application of the shotcrete, like the tests performed by Ginouse et al. (2015). The tension and compression tests would therefore be in the same plane as tension and compression is experienced for the shotcrete on the walls. The diameter of the cored cylinders was taken to be the largest permissible by the shotcrete panel. The cylinders were cut to the desired length (2X the diameter) with a concrete saw and were dried before being placed into individual plastic ziplock bags.

Figure 3-20. The shotcrete panel is cored for the cylinders. The smaller core represents the size for the first set of shotcrete cores

Shotcrete Compression Tests: (ASTM C1604) The supplier strength was given as 36.8 MPa and 57.2 MPa at 24 hours and 28 days, using the end beam compression test (Ginouse et al., 2015). In the current study the compressive strength was determined by testing cylinder cores in compression as shown in **Figure 3-21**.

For the first batch, a total of nine cylinders were tested in compression at an age of around 144 days. The dimensions of these cylinders were on average 60x124mm. The average strength was measured to be 31.4MPa. For the second batch, a total of eight cylinders were tested at an age of around 36 days. The dimensions of these cylinders were on average 69x143mm. The dimensions differ between the two sets of walls due to the size of the shotcrete panel. The average strength of these cylinders was found to be 20.9MPa. The panel for the second wall had less curing time and had layers in the shotcrete that affected the overall strength of the cored cylinders (pictured in **Figure 3-21**).

For batch 1, the cylinders seemed to have failed in a mixture of Type 1, Type 2 and Type 3 failure modes. Some cracks form a V pattern, while others are completely diagonal along the height of the cylinder. One cylinder failed with many vertical cracks. For batch 2, the failure modes are mostly Type 3 since there were many vertical cracks throughout the cylinder. The higher strength of batch 1 can be seen in **Figure 3-22**, which depicts the stress strain relationships of both batches.

Shotcrete Cylinder Batch 1 Setup	Shotcrete Cylinder Batch 2 Setup
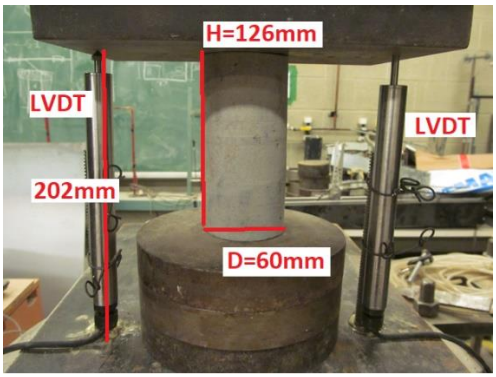	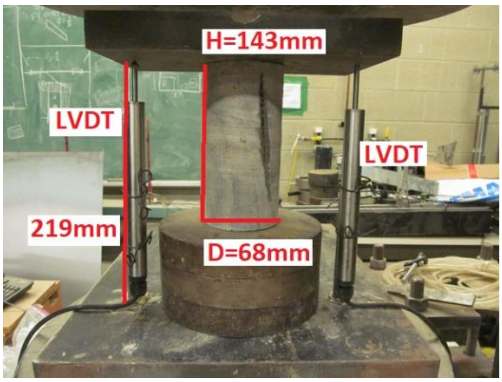
Sample Failure Modes Batch 1	Sample Failure Modes Batch 2
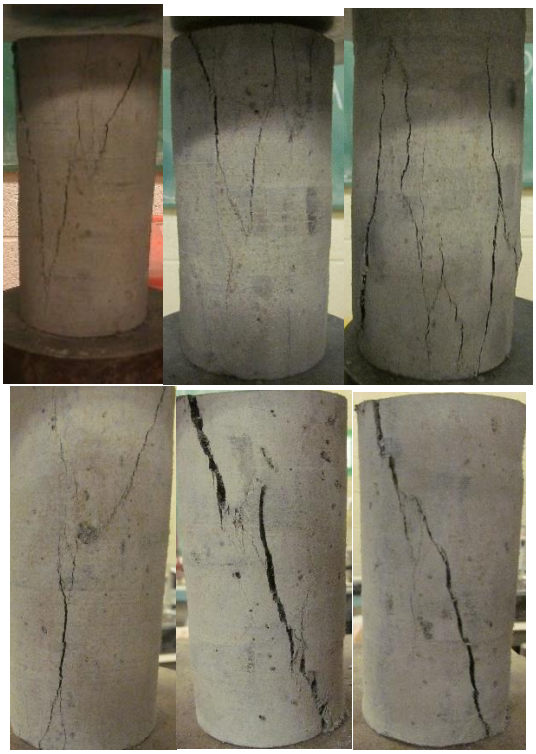	

Figure 3-21. Shotcrete Cylinder Testing

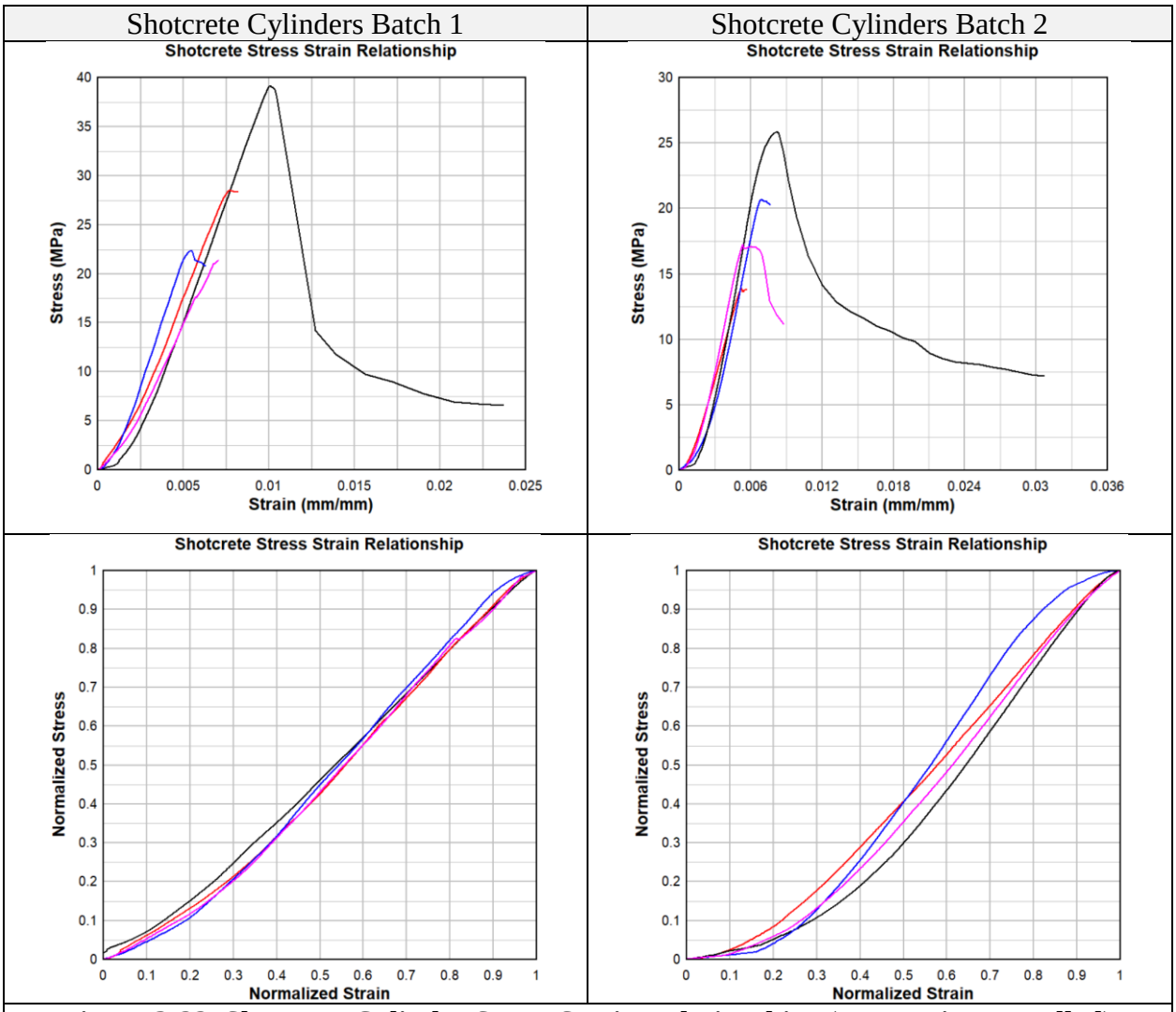

Figure 3-22. Shotcrete Cylinder Stress Strain Relationships (Not strain controlled)

Shotcrete Flexural Tests: (ASTM C1609) Four flexural prisms were prepared and tested for each batch, for a total of eight prisms. The prisms had a dimension of 100x100x400mm and were tested under four-point bending over a simply supported span of 300 mm.

The flexural strength given by the supplier is 8.2MPa at 28 days. For the first batch, the flexural load was measured to be: 35.1kN, 43.7kN, 22kN and 15.4kN. The first and last values are discounted due to the failure occurring outside the centre third of the span. The remaining two values are very different, due to the different failure mechanisms experienced by the two prisms, as seen in **Figure 3-23**. The prism that failed at 22kN had a much straighter and cleaner failure crack than the prism that failed at 43.7kN. The average flexural load for the first batch is 32.8kN, with a strength of 9.8MPa.

For the second batch, the measured flexural load was: 22.0kN, 20.9kN, 40.6kN and 32.1kN. The two last tests will be discounted due abnormal failure conditions. The average flexural load is 21.4kN, with a strength of 6.4MPa.

Figure 3-23 details the testing for the prisms and **Figure 3-24** shows the deflection curves for the two batches. **Table 3-3** shows the values derived from ASTM C1609.

Shotcrete Flexural Strength Test Setup

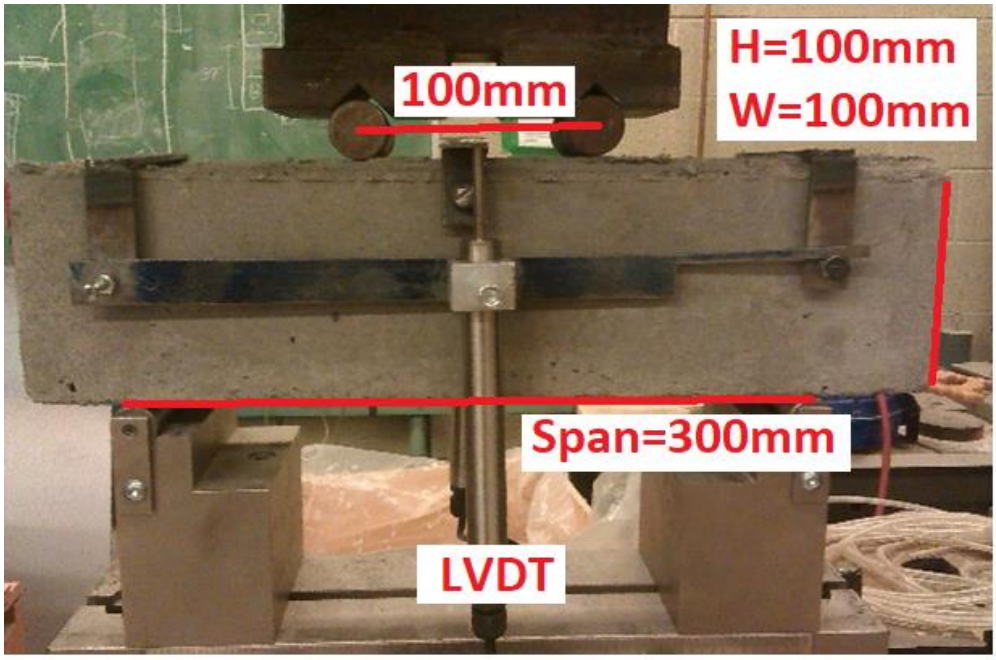

Sample Failure Modes

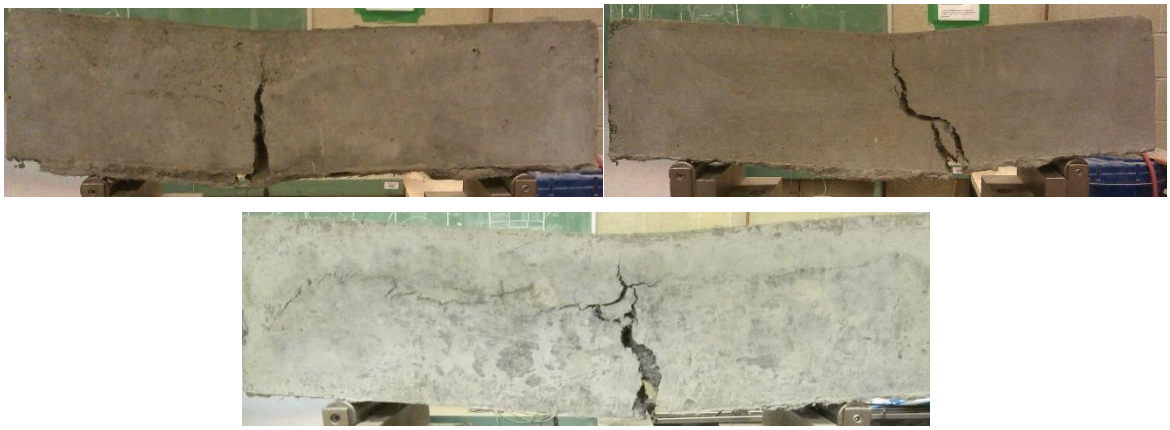

Figure 3-23. Flexural Prism Tests

Flexural Strength Batch 1	Flexural Strength Batch 2
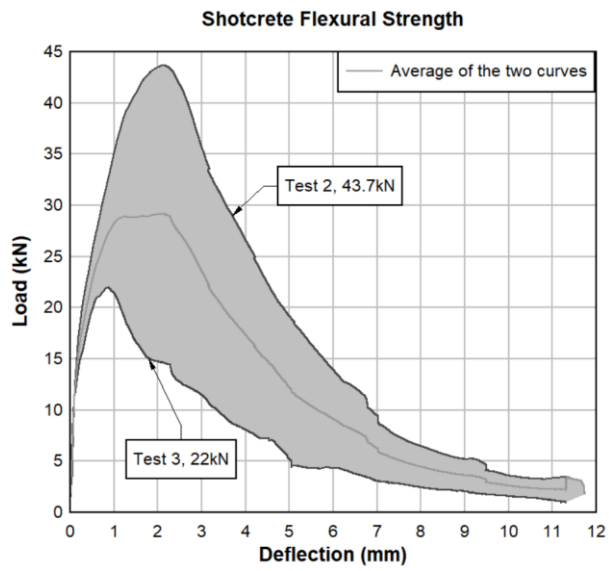	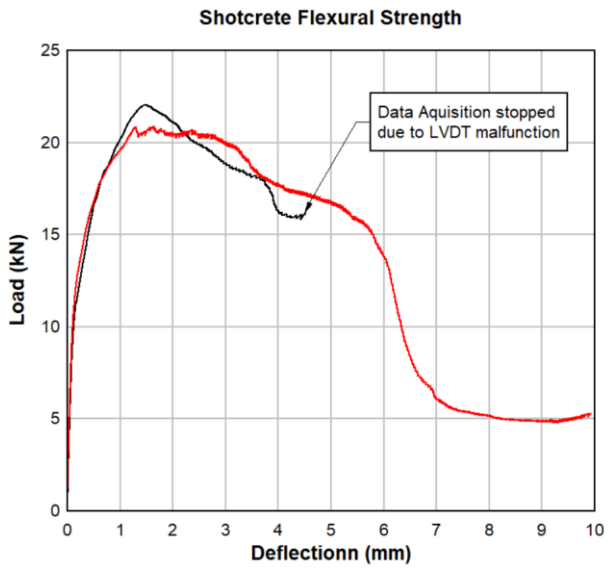

Figure 3-24. Shotcrete Load Deflection Curves

Table 3-3. ASTM C1609 Flexural Test

	P1	δ1	Pp	δp	f1	fp	P600	f150	P150	f150	T150
RMW-C	39.90	1.36	43.68	2.14	11.97	13.10	25.36	7.61	43.51	13.05	64.18
	21.12	0.67	21.98	0.86	6.34	6.59	19.72	14.74	5.92	1.77	34.91
Average	**30.51**	**1.02**	**32.83**	**1.50**	**9.15**	**9.85**	**22.54**	**11.17**	**24.71**	**7.41**	**49.55**
RMW-S	11.32	0.17	22.06	1.46	3.40	6.62	16.58	4.97	21.10	6.33	36.65
	20.90	1.64	n/a	n/a	6.27	n/a	16.80	5.04	20.51	6.15	35.92
Average	**16.11**	**0.91**	**22.06**	**1.46**	**4.83**	**6.62**	**16.69**	**5.01**	**20.81**	**6.24**	**36.29**

L = Span Length (300 mm), (L/600 = 0.5, L/150 =2)
P_1= First-Peak Load (kN)
δ_1= Net Deflection at First-Peak Load (mm)
P_p= Peak Load (kN)
δ_p= Net Deflection at Peak Load (mm)
f_1= First-Peak Strength (MPa)
f_p= Peak Strength (MPa)
P_{600}= Residual Load at net deflection of L/600 (kN)
f_{600}= Residual Strength at net deflection of L/600 (MPa)
P_{150}= Residual Load at net deflection of L/150 (kN)
F_{150}= Residual Strength at net deflection of L/150 (MPa)
T_{150}= Area under load vs. net deflection curve (0 to L/150), (kN*mm)
FT = Flexural Toughness Factor = $(T_{150}*L)/(L/150 *b*d^2)$

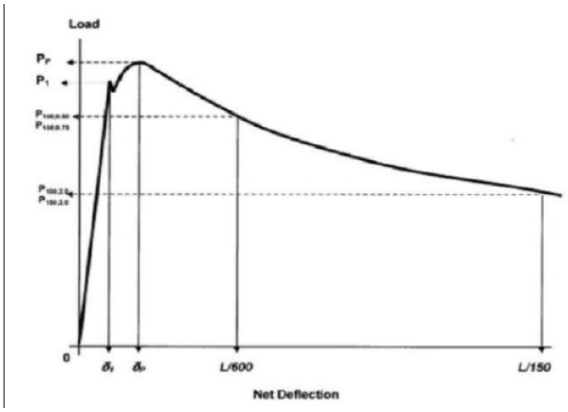

Shotcrete Direct Tension Tests: Direct tension tests were performed by Ginouse et al. (2015). The cylinders were glued to the aluminum plates and had a 5mm notch cut at mid-height to localize the tensile failure. The peak tensile strength was measured to be 4.1MPa at 28 days. After the initial peak load, the cylinders exhibited post-peak tensile resistance due to the fibers spanning the crack. **Figure 3-25** shows the test setup and resulting load vs. crack-opening curve (Ginouse et al. 2015). For this thesis, **Figure 3-25** B) was emphasised to show the different stages of fiber pullout: A) First Cracking, B) Hardening, C) Softening, D) Fiber pullout.

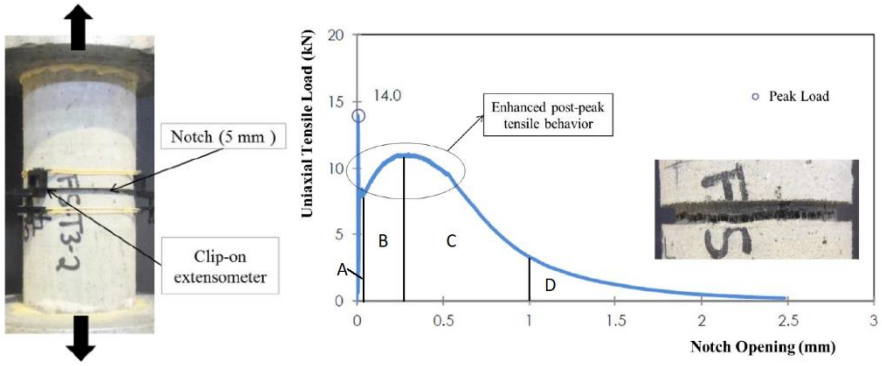

A) B)

Figure 3-25. A) Tension Test Setup. B) Load Displacement Relationship (Ginouse et al., 2015)

3.4.3. Steel Properties

Steel Tension Tests: (ASTM E8) Direct tension tests were performed on both mesh sizes (gage 2 and gage 6 mesh sizes). Lengths of the mesh were prepared by cutting off horizontal bars that were welded to the specimen. A 50 mm extensometer was placed in the center of the steel bar. Using the 0.2% offset method, the gage 2 wire mesh yielded at 590.6MPa, while the gage 6 wire mesh yielded at 921.7MPa. However, the thicker mesh failed after almost double the strain of the thinner mesh: up to 0.021 strain compared to 0.011 strain. The elastic modulus for the both meshes are similar: 263 000MPa for the larger mesh and 295 000MPa for the thinner mesh. Figure 3-26 shows the test setup and stress strain curves. **Table 3-4** details the steel specimens.

Steel Test Setup	Stress Strain Results
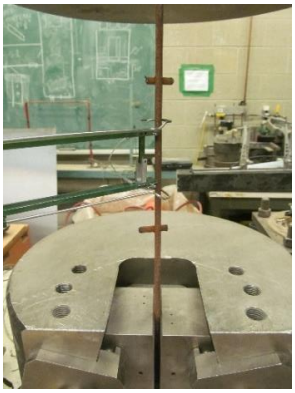	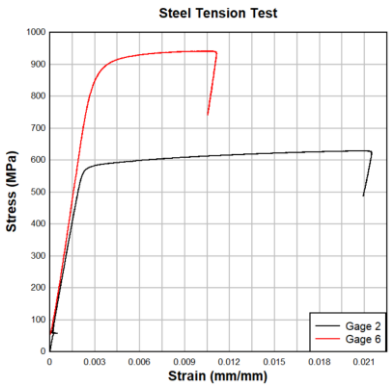

Figure 3-26. Steel Tension Tests

Table 3-4. Steel Properties

				Yield (0.2% offset)		Ultimate	
Mesh type	Mesh Dimensions (mm)	Bar Diameter (mm)	Bar Area (mm^2)	εy	fy (MPa)	εu	fu (MPa)
Gage 6	152x152	4.11	13.3	0.005	921.7	0.011	939.7
Gage 2	152x152	6.54	33.6	0.00422	590.6	0.021	627.6

3.5. SHOCKTUBE SETUP AND INSTRUMENTATION

The experimental setup consists of the University of Ottawa's shock-tube and data acquisition system. The wall is placed onto the end of the shock-tube, which is utilized to simulate blast loading with air pressure.

3.5.1. Shocktube Setup

The shock-tube consists of a driver section, a spool section, and an expansion section which ends at the rigid test frame (**Figure 3-27).** The driver is separated from the spool section by a set of thin aluminum diaphragm sheets. Likewise, the spool section is also separated from the expansion section by an identical set of aluminum sheets. The diaphragm sheets are placed to allow the pressure to build up in the driver to the desired level.

Air is then pumped into the driver section. As pressure is built up in the driver, the spool section is filled up simultaneously at a lower amount. Usually, the spool section is filled at around half the pressure as the driver. This ensures that the pressure differential between the driver and the spool is lower than the resistance of the sheet. Likewise, the pressure differential between the spool and the expansion section is also lower than the resistance of the sheet. When the desired driver pressure is achieved, the spool section is drained of pressure with the firing station. This results in a pressure differential between the driver and the spool which is larger than the resistance of the aluminum sheets, which ruptures, and the blast is released.

The blast travels through the expansion section towards the rigid frame, where the test specimens are placed. To ensure that the full blast is resisted by the wall specimen, any openings at the rigid frame are closed with wood bolted to the shock-tube. Pressure relief vents are placed near the sides of the rigid frame to allow the blast pressure to dissipate quickly. This ensures the blast behaves as in an outside setting, and not in an enclosed space.

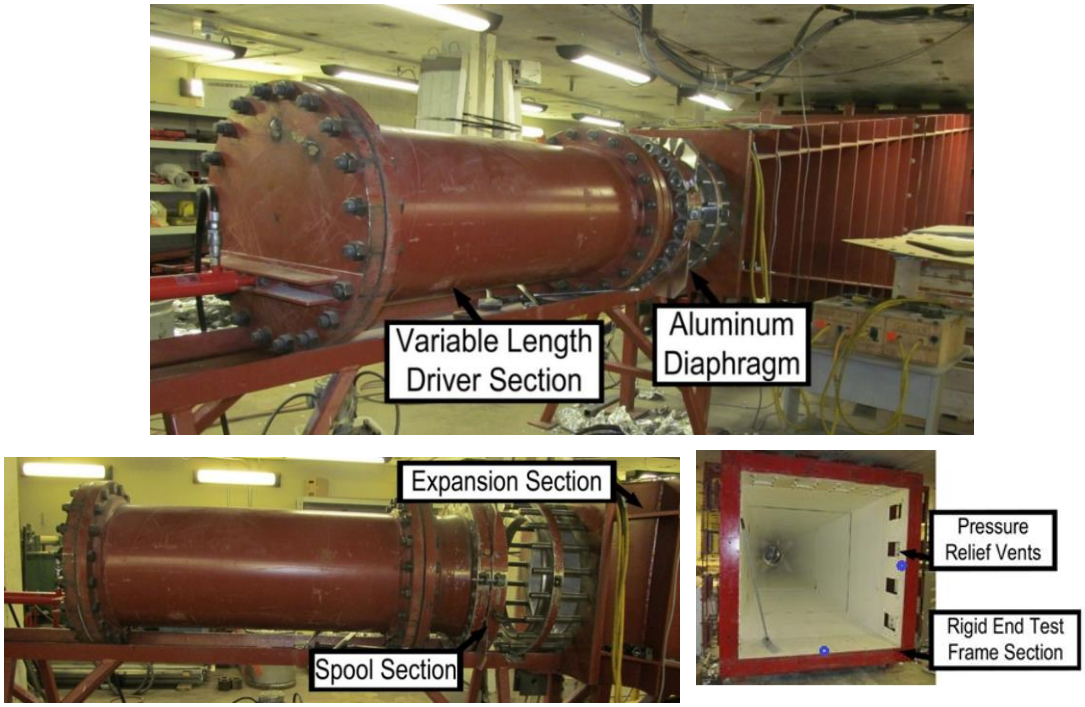

Figure 3-27. UOttawa Shocktube. The blue marks indicate the pressure sensor locations (emphasis mine). (Melançon, 2016)

3.5.2. Test Setup/Boundary Conditions

The test setup for the walls is detailed in **Figure 3-28**, and **Figure 3-29** shows a picture of the setup.

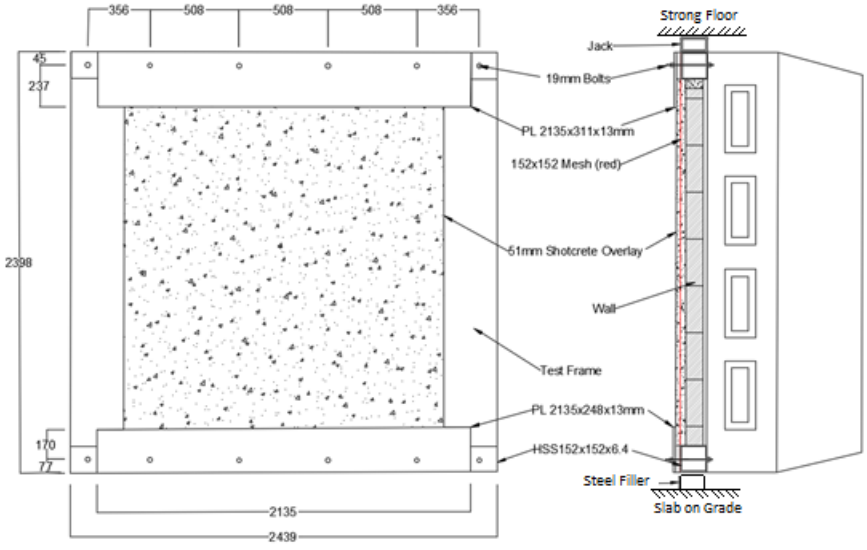

Figure 3-28. Wall Setup

The boundary conditions of each wall were set up to ensure one way bending. The top and bottom beam supports consisted of HSS152X152X6.4 sections. A total of six 19mm (¾") steel bolts on the top and bottom were used to hold the HSS supports to the shocktube frame, spaced at 356mm (14") and 508mm (20") apart. In all cases the gap between walls and the top HSS beam was filled with high-strength grout to promote arching action. Steel plates (12.7mm, ½" thick) were installed to act as shear restraints to prevent the wall from drifting horizontally when testing. The plates overlapped the wall for one half the height of a CMU block (about 100mm). For the top support, the distance from the bolts to the edge of the plate was 10-1/2". For the bottom support, the distance from the bolts to the edge of the plate was 6-3/4". A 300x250x12.7mm (12x10x½") steel stiffener was welded to the top/bottom HSS and plates to prevent excessive support rotation, as shown in **Figure 3-30**.

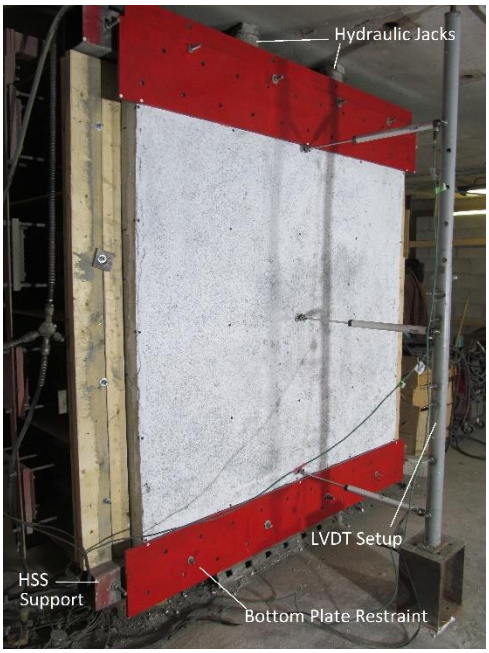

Figure 3-29. Picture of Wall Setup

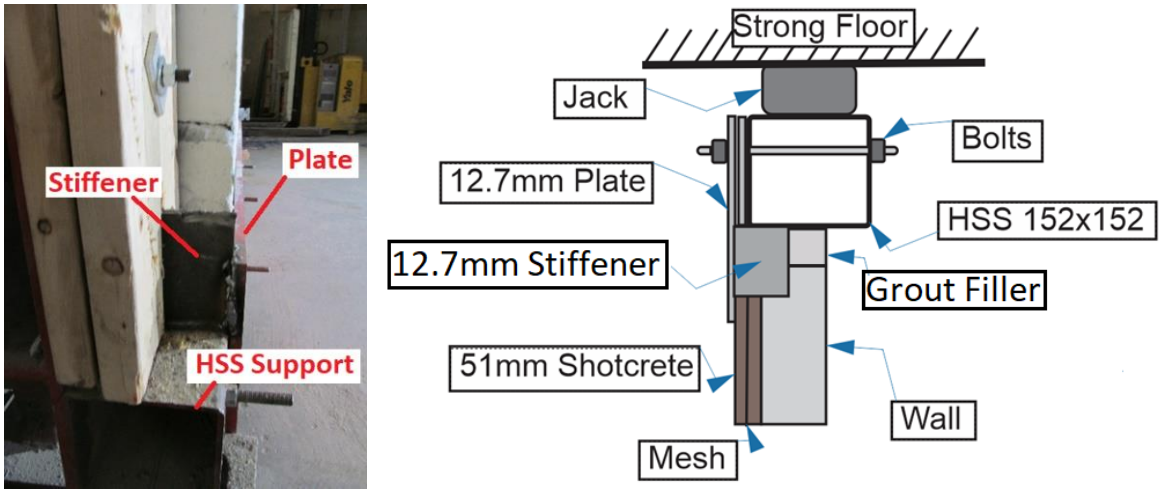

Figure 3-30. Boundary Conditions

3.5.3. Data Acquisition

The data acquisition system (DAC) continuously overwrites data at 100 000 samples per second in a 3 second loop until the pressure sensors receive a trigger from the blast (Lloyd, 2010). Two channels in the DAC system were recording pressure, five channels were recording strain, and three channels were recording displacement. To ensure no data was lost, 10% of the saved data occurs prior to the trigger. Once the trigger is received, a signal is sent out to the high-speed cameras to record the video of the test.

The pressure time history was recorded using two pressure gauges at the bottom and side of the rigid frame. The placement of the gauges is shown in **Figure 3-31**. The pressure gauges record the reflected pressure experienced by the specimen.

Displacement-Time histories of the wall and supports are recorded with the use of LVDT's and camera imaging software. Three LVDT's were used to track the displacement of the walls; one at midpoint of the walls, and the other two at the top and bottom supports, respectively. The LVDT placement is shown in **Figure 3-32**.

For Wall 5 and 6, five 6mm, 350 ohm strain gages were placed along the height of the wall in the centre. The gages were labelled from one through 5 starting from the top of the wall. Each gage was distanced 330mm from each other. **Figure 3-32** shows the strain gage setup.

Two high speed cameras were also used to track the displacements of the wall and supports (**Figure 3-33**). The cameras could be used to track in either 3D or 2D. For 3D tracking, the cameras were placed at about 45-degree offsets from the front of the shock-tube and were calibrated using a fixture. Using 3D analysis software, the two videos can be combined to track points in 3D. For 2D tracking, one camera was placed at the side of the wall, and the other was placed to view the front of the wall. Only the side camera is used to track the wall, using a visible scale on the wall to calibrate the camera.

Pressure sensors (circled)	Firing Station
	

Figure 3-31. Left: Pressure sensors circled. Right: Firing Station

LVDT Setup	LVDT Diagram
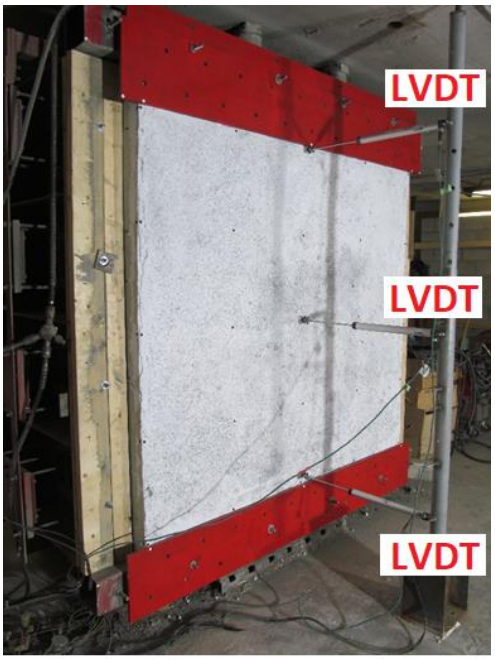	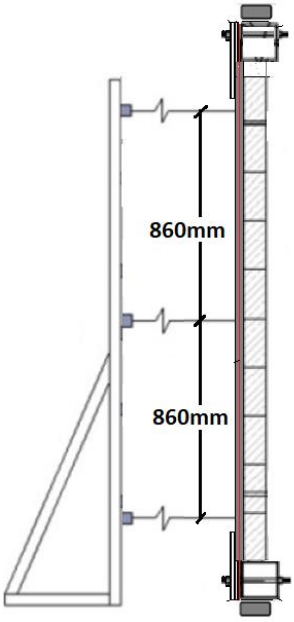
Strain Gage Setup	Strain Gage Diagram
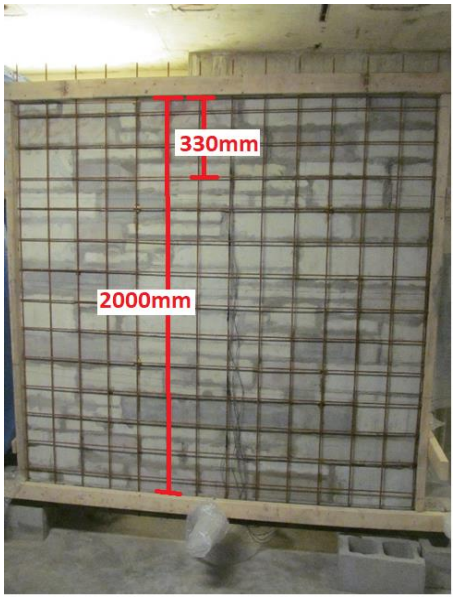	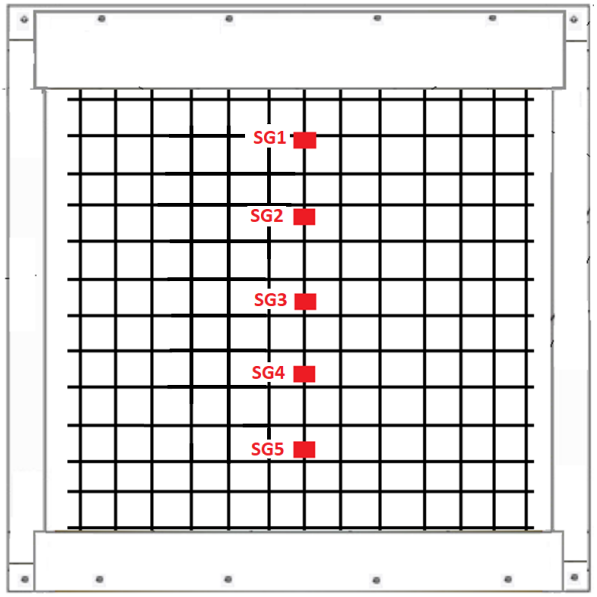

Figure 3-32. LVDT and Strain Gage Placement (spaced at 330mm)

3D Camera Calibration and Setup	2D Camera Tracking
	

Figure 3-33. Camera Setup for 2D and 3D tracking

3.5.4. Test Sequence

Each wall was tested by multiple blast loads until failure. The driver pressures will be referred to in PSI in this section as that is the unit of operation for the shocktube. The blasts were increased by multiples of 6psi, until a pressure of 60psi was achieved. From there, the blasts jumped by 20psi. **Table 3-5** details the sequence of blasts for each wall, while **Table 3-6** details the average blast properties of each blast. **Figure 3-34** shows the pressure time histories for each blast. It should be noted that all blast pressures had identical arrival times.

Table 3-5. Test Sequence: Blast ID and Driver Pressure in PSI and (KPa)

Blast ID	URM-1	URM-3	RMW-C-N	RMW-C-L	URM-S-N	URM-S-L	RMW-S-N	RMW-S-L
0	6 (40)	5 (35)						
1	11 (76)	12 (83)	12 (83)		11 (76)	12 (83)		
2	18 (126)	18 (124)	18 (124)	18 (124)	19 (131)	19 (131)	18 (124)	19 (131)
3	24 (166)	24 (165)	24 (165)			25 (172)		
4		31 (214)				31 (214)		
5		36 (248)	36 (248)	36 (248)		36 (248)	36 (248)	36 (248)
6		42 (290)				42 (290)		
7			48 (331)			48 (331)	47 (324)	48 (331)
8						54 (372)		
9			60 (413)	60 (413)			60 (413)	60 (413)
10			80 (552)	80 (552)			80 (552)	80 (552)
11							91 (627)	
12				100 (689)				101 (696)
13								112 (772)
14							120 (820)	
15								117 (807)
Total # of shots	*4 shots*	*7 shots*	*7 shots*	*5 shots*	*2 shots*	*8 shots*	*7 shots*	*8 shots*

Table 3-6. Average Blast Properties

Blast #	Driver Pressure: P_d psi (kPa)	Driver Length: L_d (mm	Avg. Reflected Pressure: P_r (kPa)	Avg. Reflected Impulse : I_r (kPa-ms)	Avg. Positive Phase Duration t_d (ms)	Scaled Distance: Z (m/kg$^{1/3}$)	Charge Weigth (kg)	Standoff Distance (m)
1	12 (83)	1828.8	13.7	190.8	14.0	12.4	19	33
2	18 (124)	1828.8	27.7	312.4	15.0	10.9	27	33
3	24 (165)	1828.8	34.9	400.2	15.7	9.3	44	33
4	30 (207)	1828.8	39.5	427.3	16.0	8.6	57	33
5	36 (248)	1828.8	46.8	508.6	16.0	7.7	78	33
6	42 (290)	1828.8	46.5	574.0	16.3	7.7	78	33
7	48 (331)	1828.8	56.4	619.6	16.7	6.9	110	33
8	54 (372)	1828.8	57.1	600.0	18.0	6.8	113	33
9	60 (413)	1828.8	67.7	806.1	17.7	6.2	151	33
10	80 (552)	1828.8	81.8	874.5	18.8	5.6	206	33
11	91 (627)	1828.8	102.9	940.0	20.0	5.0	294	33
12	100 (689)	1828.8	99.1	1165.6	19.6	5.0	278	33
13	112 (772)	1828.8	107.1	1209.5	21.0	4.9	312	33
14	120 (820)	1828.8	113.8	1177.0	20.3	4.7	341	33
15	117 (806.7)	2743.2	109.9	1734.7	29.8	4.8	1343	53

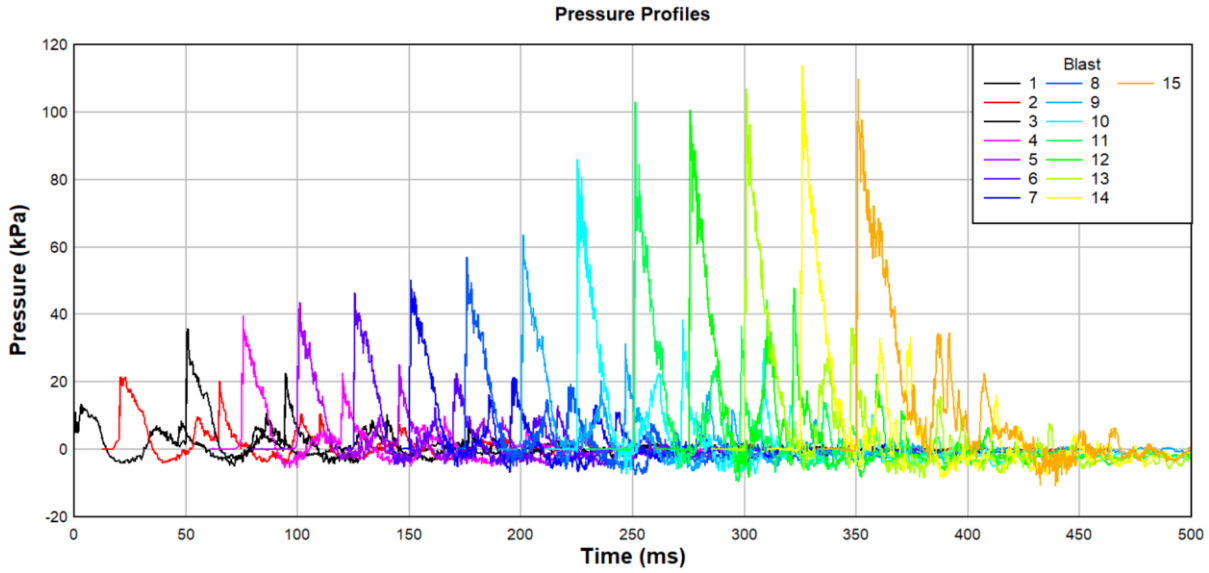

Figure 3-34. Pressure Profiles for each blast. Arrival time is shifted for each consecutive blast.

For RMW-C-N, the first three blasts were conducted using diver pressures of 12, 18 and 24psi with a constant driver length of 1830 mm (6ft). Due to resistance of the wall, the next three blasts were 36, 48 and finally 60psi. The last blast was 80psi. The decision to increase the blast increment was to limit damage to the wall from repeated blasts. For RMW-C-L, several early tests were skipped to avoid damage from repeated blasts. The first three tests were 18, 36 and 60psi. From there, the tests increased to 80, and then 100psi.

For URM-S-N, there were only two tests until failure, 11 and 19psi, also using a driver length of 1830 mm. For the next control wall (URM-S-L), the pressures were increased by 6psi until failure. It was expected that the wall would fail sooner, so no tests were skipped.

For RMW-S-N and RMW-S-L, the same pattern was used. The first three tests were 18, 36, and 48psi. These pressures were chosen for their comparability to the previous walls. The next tests, starting at 60psi, were increasing by an increment of 20psi until failure. The second last test for RMW-S-N was 91psi and not 100psi due to a technical issue with the pump. The last test was 120psi. The second last test performed on RMW-S-L was 112psi, and not 120psi due to a technical issue. The last shot was 117psi, with an increased driver length of 2743 mm (9ft) instead of 1830 mm.

Repeated loading causes increased damage to the wall as the testing continues. Early on, this damage is considered negligible as the wall behaves elastically. As the damage increases, the resistance of an undamaged wall is under estimated due to the damage present in the actual wall. The ultimate resistance of an undamaged wall is likely higher than the values measured.

CHAPTER 4. EXPERIMENTAL RESULTS

4.1. CHAPTER OVERVIEW

The chapter presents an overall summary of the experimental test results. The detailed description of the behaviour for each wall is also provided.

4.2. SUMMARY OF RESULTS

The following tables present a summary of the results for each wall (**Table 4-1**, **Table 4-2**). Each shot was given the notation ABC-D-E-#. The letters indicate the designation of the wall as described in Section 3.2.2. For example, RMW-C-N-2 is the second shot for wall RMW-C-N. In addition to the shock-tube parameters (driver length L_d and pressure P_d), the tables report the measured shockwave parameters (reflected pressure P_r and impulse I_r, positive phase duration t_d) and wall response (maximum displacement d_{max}, residual displacement d_{res} and time to maximum displacement t_d) for each test. The cumulative residual displacement $\sum d_{res}$ shows the total residual displacement experienced by the wall. **Table 4-3** also reports strain data as recorded by the strain gages on the steel wire mesh in walls RMW-S-N and RMW-S-L. The post-blast crack widths in the mortar joints and shotcrete are also reported in **Table 4-4**.

Table 4-1. Summary of Testing

	Blast #	P_d (kPa)	L_d (mm)	P_r (kPa)	I_r (kPa-ms)	t_d (ms)	d_{max} (mm)	d_{res} (mm)	$\sum d_{res}$ (mm)	t_{max} (ms)
RMW-C-N-1	1	82	1828.8	13.1	231.8	15.3	4.3	0.3	0.3	21.3
RMW-C-N-2	2	124.1	1828.8	21.6	356.6	15.2	8.8	0.6	0.9	22.6
RMW-C-N-3	3	165.5	1828.8	35.9	427.5	15.4	11.3	1.2	2.1	22.4
RMW-C-N-4	5	248.2	1828.8	45.5	567.8	16.2	16.6	1.9	4	22.1
RMW-C-N-5	7	336.5	1828.8	54.3	692.5	16.9	17.6	2.7	6.7	21.2
RMW-C-N-6	9	413	1828.8	63.6	761.8	19	28.8	9.9	16.6	27.2
RMW-C-N-7	10	551.6	1828.8	72.4	797.6	19	215.1	89.7	106.3	148
RMW-C-L-1	2	130.3	1828.8	25.9	329.7	16.7	11.5	3.9	3.9	23.1
RMW-C-L-2	5	249.6	1828.8	40	477.8	16.8	16.4	5.9	9.8	22.5
RMW-C-L-3	9	426.8	1828.8	61.5	704.1	18.9	24.9	9.9	19.7	23.8
RMW-C-L-4	10	544.7	1828.8	71.6	847.8	20.4	28.2	7.5	27.2	25.8
RMW-C-L-5	12	683.3	1828.8	97.4	1138.5	18.9	100.6	76.1	103.3	95.9
URM-S-N-1	1	75.8	1828.8	14.5	141	12.6	55.2	12.4	12.4	185.4
URM-S-N-2	2	131.7	1828.8	28.6	250.4	15	n/a	n/a	n/a	n/a
URM-S-L-1	1	79.3	1828.8	13.5	199.5	14.2	5.8	0	0	21.4
URM-S-L-2	2	130.3	1828.8	26.6	311.2	14.6	11.7	0.2	0.2	22.5
URM-S-L-3	3	173.7	1828.8	33.9	372.9	15.9	15.5	0.2	0.4	23.3
URM-S-L-4	4	213.7	1828.8	39.5	427.3	16	18.3	0.5	0.9	26.6
URM-S-L-5	5	248.2	1828.8	43.7	497.9	16	21.7	0.3	1.2	30.7
URM-S-L-6	6	288.2	1828.8	46.5	574	16.3	28.2	0.6	1.8	32.2
URM-S-L-7	7	330.2	1828.8	50.2	592.8	17.7	38.4	2.3	4.1	42.5
URM-S-L-8	8	370.2	1828.8	57.1	600	18	n/a	n/a	n/a	n/a

Table 4-2. Summary of Testing Continued

	Blast #	P_d (kPa)	L_d (mm)	P_r (kPa)	I_r (kPa-ms)	t_d (ms)	d_{max} (mm)	d_{res} (mm)	$\sum d_{res}$ (mm)	t_{max} (ms)
RMW-S-N-1	2	126.2	1828.8	29.3	305.6	14.2	8.8	1.4	1.4	26
RMW-S-N-2	5	247.5	1828.8	48.3	501.9	15.4	15.4	3.7	5.1	25
RMW-S-N-3	7	326.1	1828.8	59.3	577.9	16	18.3	3.3	8.4	24.7
RMW-S-N-4	9	415.8	1828.8	70.1	1020	15.1	21.8	2.5	10.9	26.5
RMW-S-N-5	10	551.6	1828.8	97	915.8	17.9	27.1	3.4	14.3	25.8
RMW-S-N-6	11	628.1	1828.8	102.9	940	20	33.5	9.4	23.7	30.4
RMW-S-N-7	14	826.7	1828.8	113.8	1177	20.3	146	n/a	n/a	125.8
RMW-S-L-1	2	129.6	1828.8	34.1	321.1	14.5	4.9	1.1	1.1	18.4
RMW-S-L-2	5	248.2	1828.8	56.4	497.8	15.5	8.1	2.6	3.7	19
RMW-S-L-3	7	330.9	1828.8	61.9	615.3	16.2	9.5	2.4	6.1	19.8
RMW-S-L-4	9	410.2	1828.8	75.6	738.4	17.9	11.4	3.4	9.5	21.1
RMW-S-L-5	10	555.7	1828.8	86	936.9	18	13.9	2.8	12.3	20.5
RMW-S-L-6	12	696.4	1828.8	100.7	1192.6	20.3	19.8	5.5	17.8	22.9
RMW-S-L-7	13	772.2	1828.8	107.1	1209.5	21	20.6	5.1	22.9	22.3
RMW-S-L-8	15	806.7	2743.2	109.9	1734.7	29.8	139.4	n/a	n/a	112.3

Table 4-3. Strain Gage Data in Micro Strain (με)

	Blast #	P_d (kPa)	L_d (mm)	P_r (kPa)	SG1	SG2	SG3	SG4	SG5
RMW-S-N-1	2	126.2	1828.8	29.3	460.8	n/a	n/a	n/a	n/a
RMW-S-N-2	5	247.5	1828.8	48.3	663	1020	871	n/a	n/a
RMW-S-N-3	7	326.1	1828.8	59.3	630	1552	1064	n/a	n/a
RMW-S-N-4	9	415.8	1828.8	70.1	957	2342	1834	n/a	n/a
RMW-S-N-5	10	551.6	1828.8	97	1191	4645	2721	n/a	n/a
RMW-S-N-6	11	628.1	1828.8	102.9	1094	4710	2497	n/a	n/a
RMW-S-N-7	14	826.7	1828.8	113.8	1070	3246	2594	n/a	n/a
RMW-S-L-1	2	129.6	1828.8	34.1	172	n/a	n/a	n/a	n/a
RMW-S-L-2	5	248.2	1828.8	56.4	274	428	267	n/a	106
RMW-S-L-3	7	330.9	1828.8	61.9	320	675	476	n/a	138
RMW-S-L-4	9	410.2	1828.8	75.6	383	966	646	311	178
RMW-S-L-5	10	555.7	1828.8	86	531	1478	1031	534	258
RMW-S-L-6	12	696.4	1828.8	100.7	1004	2510	1773	748	323
RMW-S-L-7	13	772.2	1828.8	107.1	1374	3943	2175	885	329
RMW-S-L-8	15	806.7	2743.2	109.9	1347	9034	3647	1055	412

Table 4-4. Summary of Crack Width Damage (mm)

	Shot 1	Shot 2	Shot 3	Shot 4	Shot 5	Shot 6	Shot 7	Shot 8
URM-1*	n/a	Blast 1	Blast 2	Blast 3				
	-	-	-	Failure				
URM-3*	n/a	Blast 1	Blast 2	Blast 3	Blast 4	Blast 5	Blast 6	
	-	-	-	-	-	-	Failure	
RMW-C-N	Blast 1	Blast 2	Blast 3	Blast 5	Blast 7	Blast 9	Blast 10	
	ND	HL	HL	HL	0.3	4	Failure	
RMW-C-L	Blast 2	Blast 5	Blast 9	Blast 10	Blast 12			
	HL	HL	HL	1.2	Failure			
URM-S-N	Blast 1	Blast 2						
	2.5	Failure						
URM-S-L	Blast 1	Blast 2	Blast 3	Blast 4	Blast 5	Blast 6	Blast 7	Blast 8
	HL	HL	0.1	0.4	0.7	spalling	spalling	Failure
RMW-S-N	Blast 2	Blast 5	Blast 7	Blast 9	Blast 10	Blast 11	Blast 14	
	ND	ND	HL	HL	0.7	3	Failure	
RMW-S-L	Blast 2	Blast 5	Blast 7	Blast 9	Blast 10	Blast 12	Blast 13	Blast 15
	ND	ND	ND	HL	HL	HL	HL	7

*Ciornei (2012)
**HL-hairline crack
***ND- no damage

4.3. RMW-C-N

RMW-C-N was the first wall tested for this thesis. It was a retrofitted infill masonry wall, built with CMU blocks. The shotcrete overlay was from the same batch as RMW-C-L and was applied in an overlay 51mm thick, and the mesh used was gage 6 in thickness. **Table 4-5** details the blasts, deflections and main events for each shot. **Figure 4-2** shows the pressure, impulse and displacement time histories of each blast, while **Figure 4-3** A) displays the wall setup. **Figure 4-4** shows the failure mode captured by the camera.

The residual damage for each shot is shown in **Figure 4-1**. The wall did not experience any damage from the first shot. The second shot created a small crack at the bottom right corner of the wall. The crack can be explained due to arching action. Due to the support displacement, the plates at the top and bottom were strengthened with a stiffener at each corner of the wall (**Figure 4-3** B). For each subsequent wall tested, these stiffeners were used. Over the next two shots, the wall sustained hairline cracks beginning and elongating at the front face edges of the wall at the mortar joints (**Figure 4-3** C). The cracks were roughly spaced at 152mm (6") apart, likely caused by the horizontal mesh. At the fifth shot (Blast 7), the wall sustained significantly more damage than previously. A main crack formed along the length of the wall above mid-height. The crack was measured to be 0.3mm in thickness at this point. Other minor cracks were lengthened as well. The sixth shot (Blast 9) produced no extra cracking but widened the main crack up to 4mm in thickness (**Figure 4-3** D). The PVA fibers in the shotcrete could be seen spanning the crack.

The wall completely failed during the seventh shot (**Figure 4-3** E). The failure occurred along the main crack from the previous tests. The wall completely sheared along that crack, and the top and bottom portions of the wall acted as cantilever members. The steel mesh spanning the crack was completely cut. Since the shotcrete held both pieces strongly, and the mesh was welded to the top and bottom supports, the wall did not fall over, but remained almost upright.

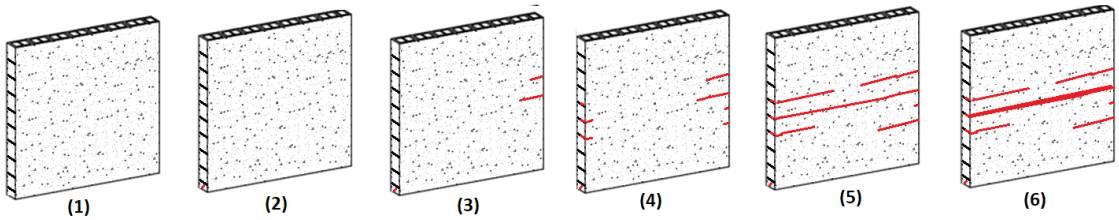

Figure 4-1. RMW-C-N Damage Progression

Table 4-5. RMW-C-N

Shot #	Blast #	P_r (kPa)	I_r (kPa-ms)	d_{max} (mm)	d_{res} (mm)	Comments
1	1	13.1	231.8	4.3	0.3	No damage
2	2	21.6	356.6	8.8	0.6	Small crack at bottom corner due to arching action
3	3	35.9	427.5	11.3	1.2	Horizontal hairline cracks at edge of wall
4	5	45.5	567.8	16.6	1.9	Elongation of hairline cracks
5	7	54.3	692.5	17.6	2.7	Main crack formed, 0.3mm wide. Hairline cracks elongated
6	9	63.6	761.8	28.8	9.9	Main crack widened to 4mm. No other damage
7	10	72.4	797.6	215.1	89.7	Wall failed along main crack

Shot 1-Blast 1

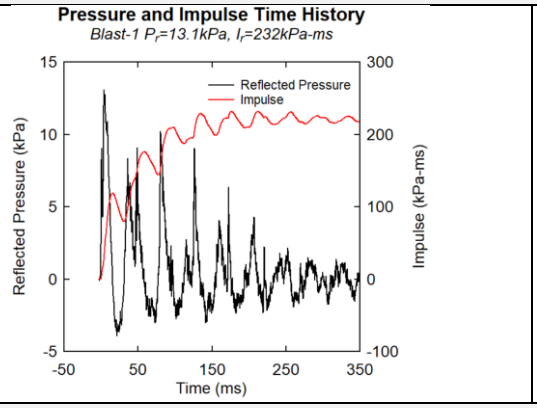

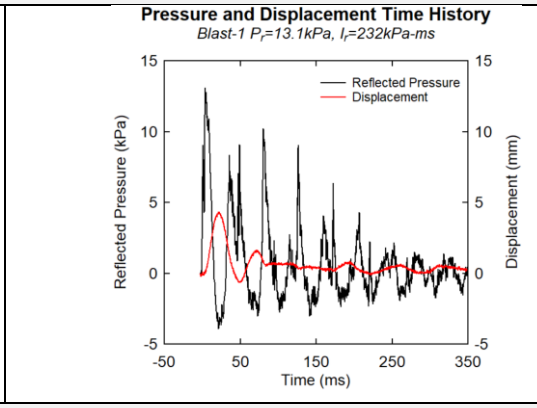

Shot 2-Blast 2

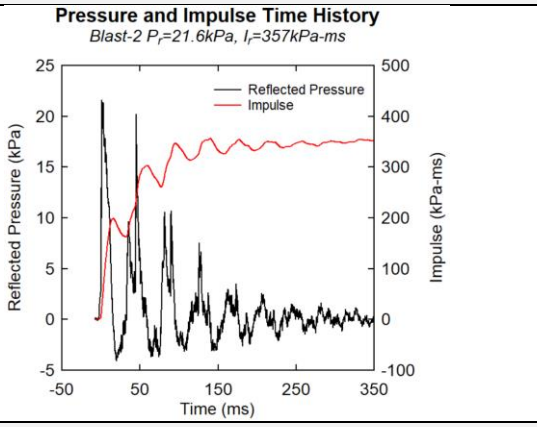

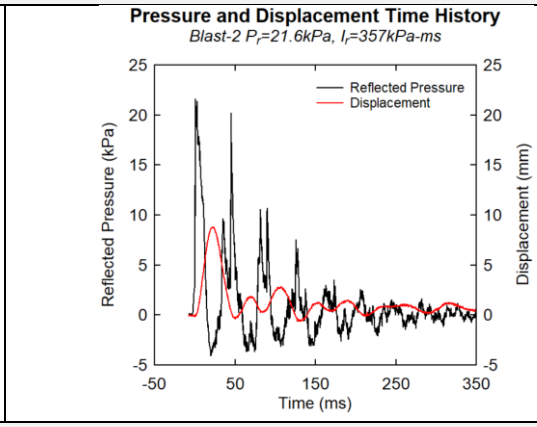

Shot 3-Blast 3

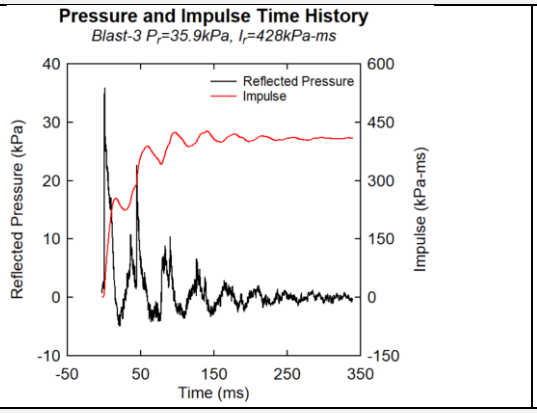

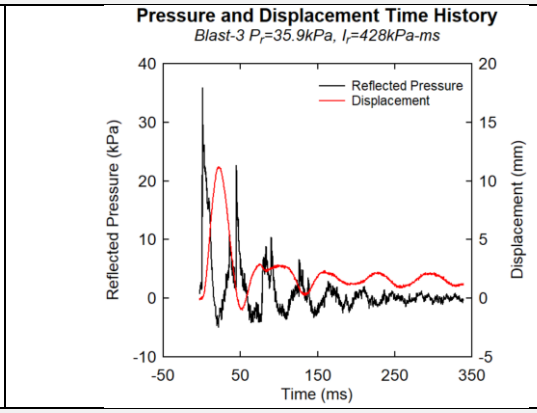

Shot 4-Blast 5

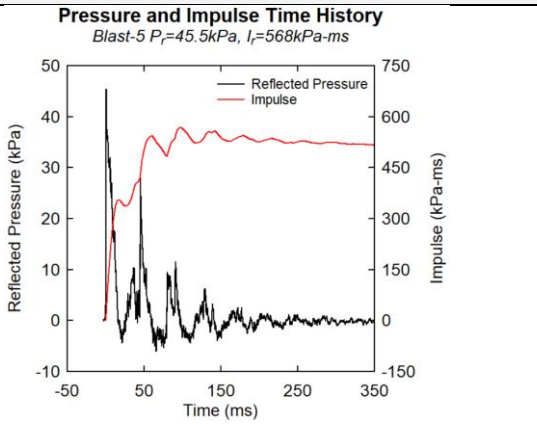

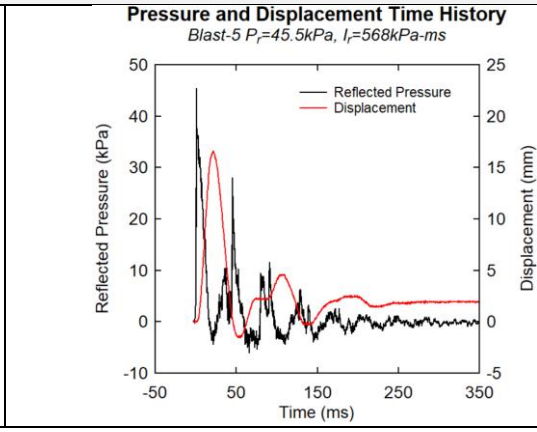

Shot 5-Blast 7

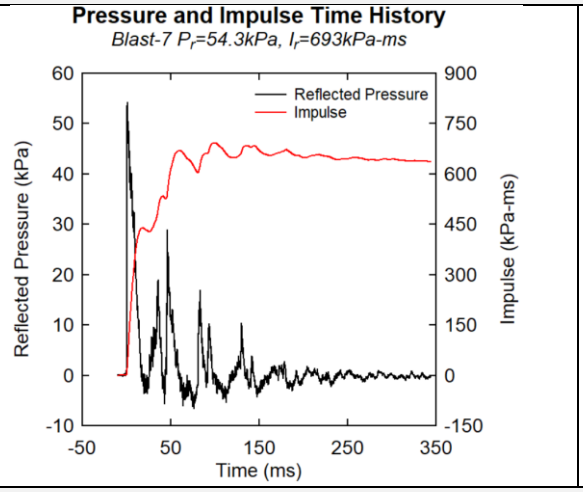

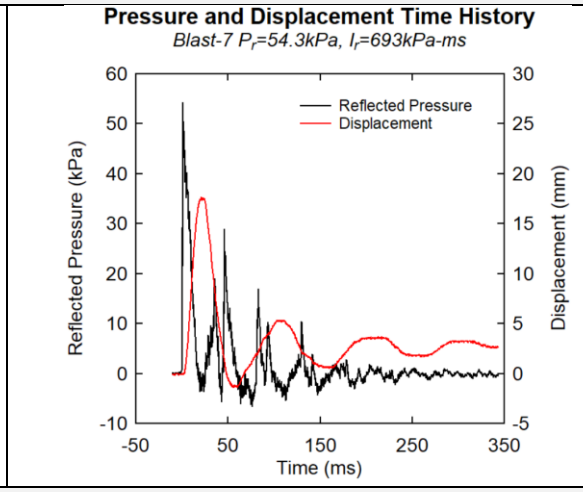

Shot 6-Blast 9

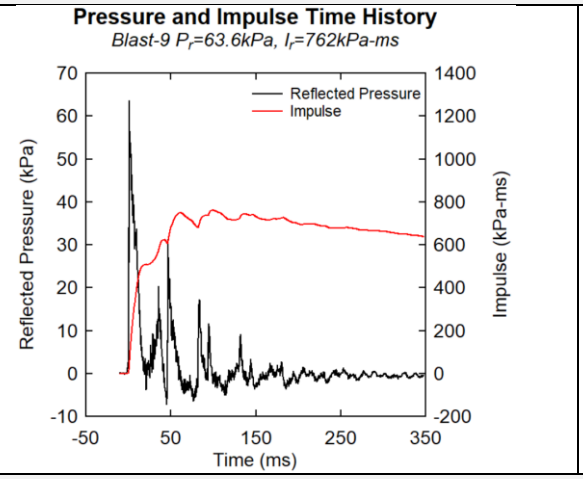

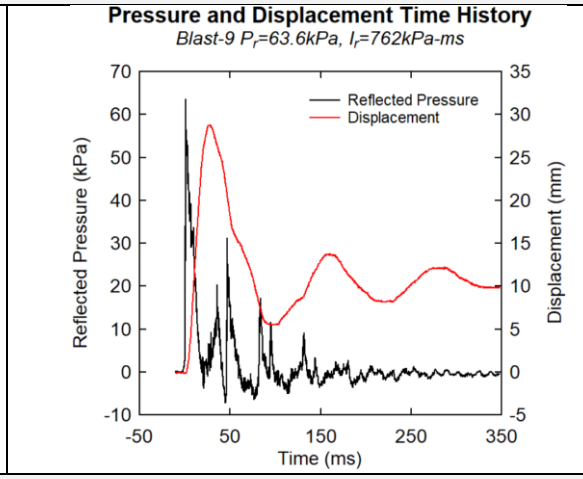

Shot 7-Blast 10

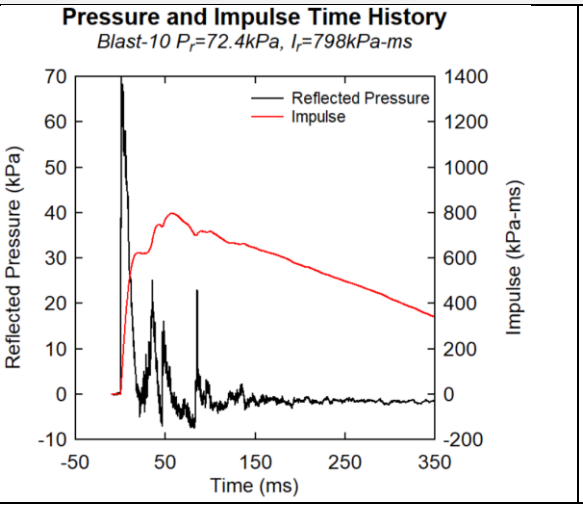

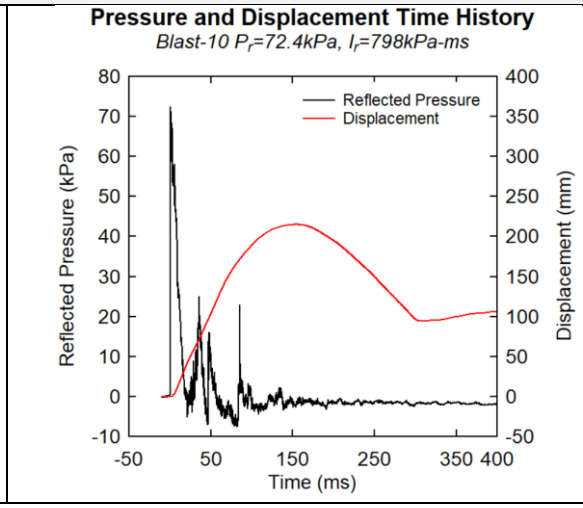

Figure 4-2. RMW-C-N Pressure, Impulse and Displacement Time Histories

A) RMW-C-N Setup

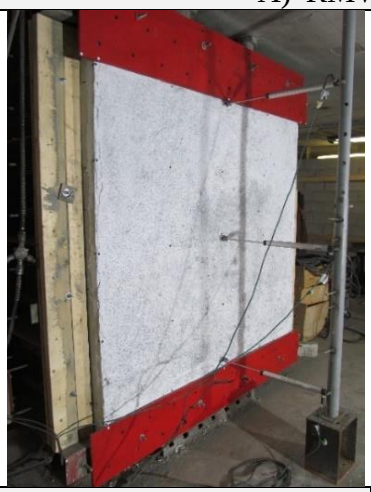

B) Stiffeners installed at Shot 2

C) Cracks at Edges at Shot 3

D) Main Crack Widening at Shot 5 (left) and Shot 6 (right)

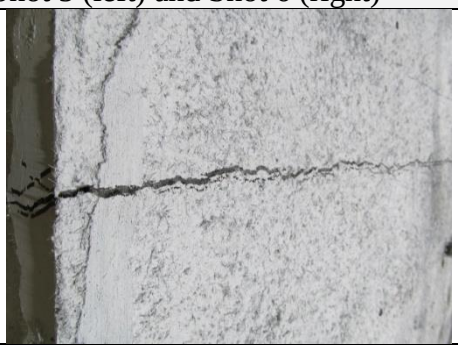

E) Failure (Shot 7)

Figure 4-3. RMW-C-N

Video stills showing Failure Mode (Shot 7)

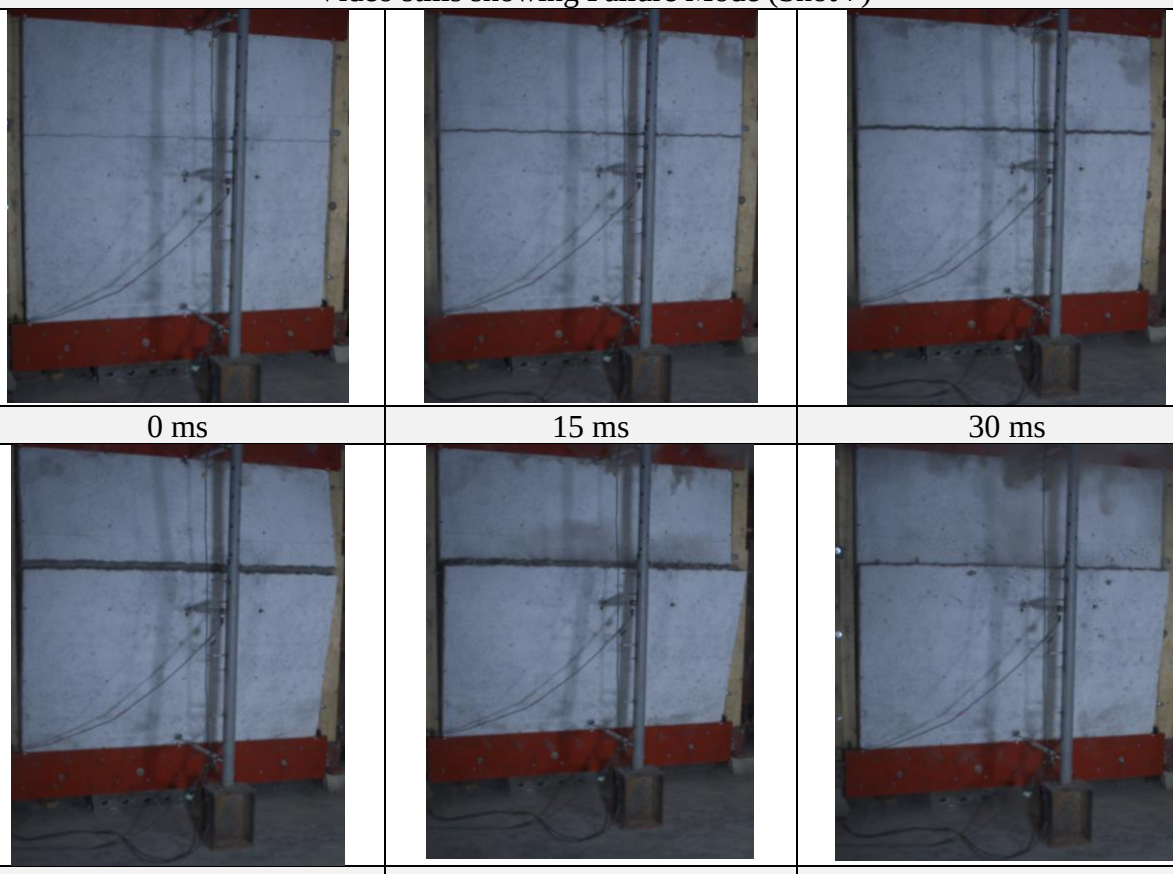

0 ms	15 ms	30 ms
60 ms	120 ms	300 ms

Figure 4-4. Video stills showing Failure Mode

4.4.RMW-C-L

RMW-C-L was the second wall tested for this thesis. It was a retrofitted load bearing masonry wall, built with CMU blocks. The shotcrete was applied in a thickness of 51mm, and was from the same batch was RMW-C-N. The mesh used was gage 6 in thickness. Due to damage sustained during installation, parts of the CMU blocks were repaired with concrete, and cracks existed in the masonry prior to testing. **Table 4-6** details the blasts, deflections and main events for each shot. **Figure 4-6** shows the pressure, impulse and displacement time histories of each blast, while **Figure 4-7** A) displays the wall setup. **Figure 4-8** shows the failure mode captured by camera.

The residual damage sustained by wall RMW-C-L is shown in **Figure 4-5**. A total of five blasts were performed until failure of the wall. The first shot (Blast 2) produced very minor cracks along the sides of the wall, near midspan. The second shot (Blast 5) produced vertical compression cracks in the CMU blocks near the top and near midspan. The cracks in the shotcrete grew slightly longer but remained on the side of the wall (**Figure 4-7** B). The third shot (Blast 9) produced hairline cracks along the front face near the edges of the wall. The two cracks on the left of the wall were spaced vertically by roughly 152mm (6”). Compression cracks at the top right CMU block appeared as well (**Figure 4-7** C). Three main cracks were formed along the face of the wall during the fourth shot (**Figure 4-7** D), with the largest one having a width of 1.2mm. Each of the three layers of cracks were roughly 152mm (6”) apart. The vertical compression cracks along the CMU blocks grew larger and penetrated through more concrete blocks. The CMU blocks at the bottom half of the wall remained intact (**Figure 4-7** D).

The wall failed at the fifth shot (Blast 12). The main crack formed along the pre-existing cracks formed in the previous test. The reason for a diagonal failure crack was because the repair concrete provided areas of higher strength material. The failure crack formed around these areas. The mesh did not completely shear as it did for RMW-C-N. The back faces of the top CMU blocks were all destroyed, and there was some debonding of the shotcrete from the repair concrete and CMU blocks (**Figure 4-7** E).

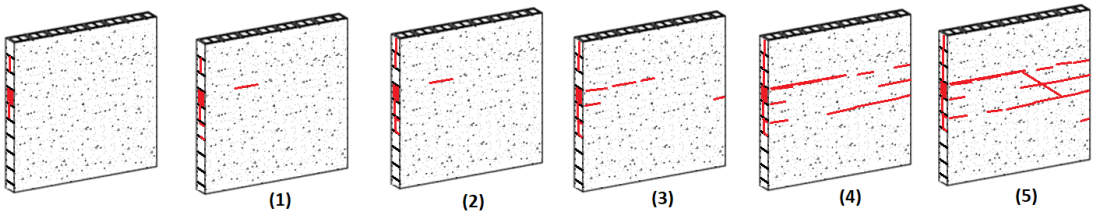

Figure 4-5. RMW-C-L Damage Progression

Table 4-6. RMW-C-L

Shot #	Blast #	P_r (kPa)	I_r (kPa-ms)	d_{max} (mm)	d_{res} (mm)	Comments
1	2	25.9	329.7	11.5	3.9	Minor horizontal hairline cracks at sides
2	5	40	477.8	16.4	5.9	Compression cracks in CMU blocks. Minor cracks at sides
3	9	61.5	704.1	24.9	9.9	Horizontal hairline cracks on front face of wall at edges. More cracking in CMU blocks
4	10	71.6	847.8	28.2	7.5	Three large cracks were formed, largest 1.2mm wide. More cracking in CMU blocks
5	12	97.4	1138.5	100.6	76.1	Failure of wall. Main crack followed cracking pattern from previous shot

Shot 1-Blast 2

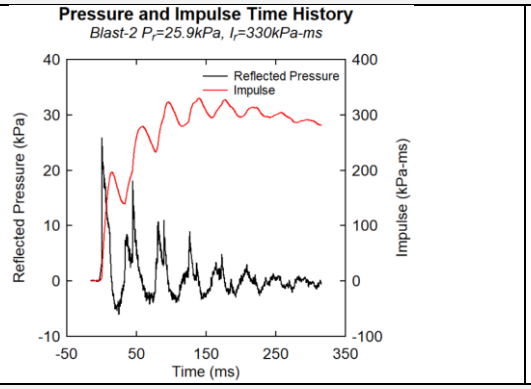

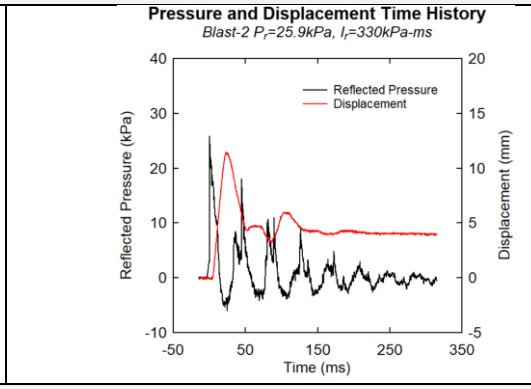

Shot 2-Blast 5

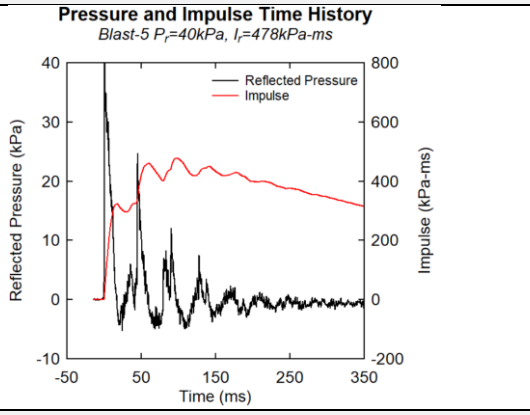

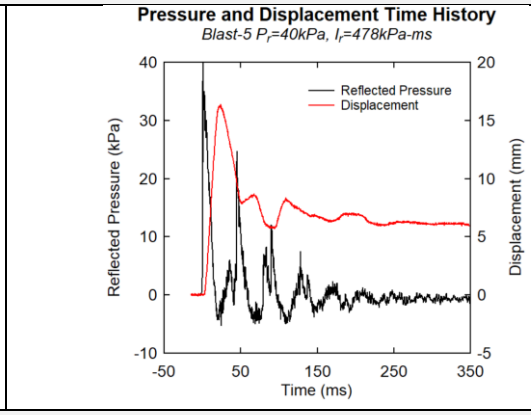

Shot 3-Blast 9

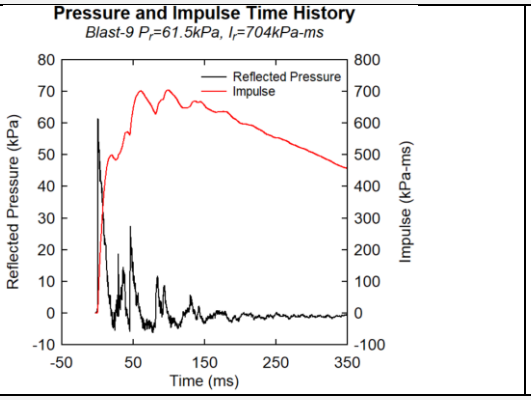

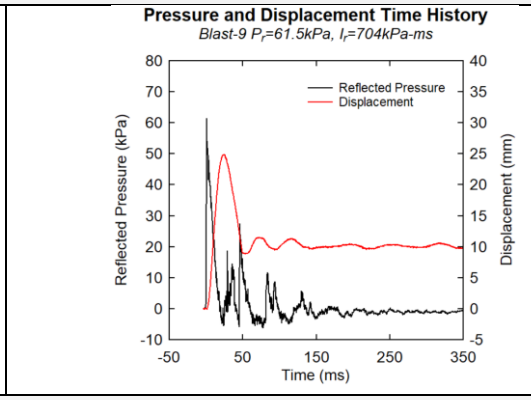

Shot 4-Blast 10

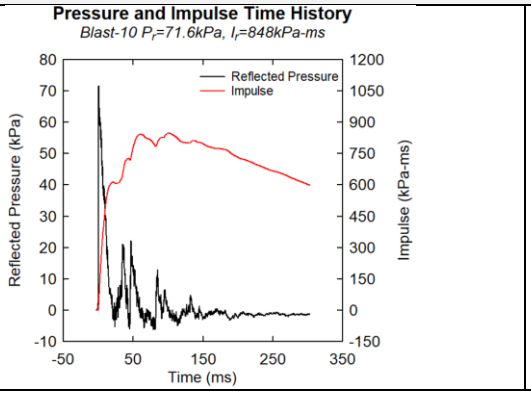

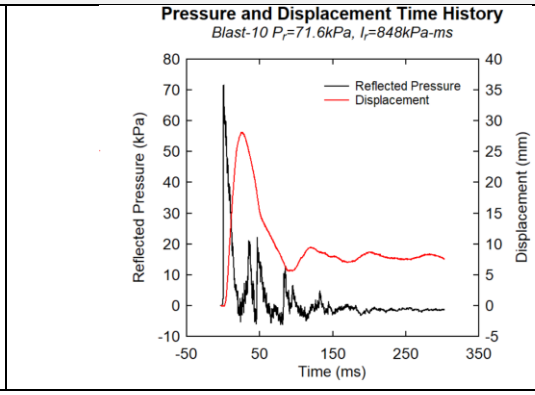

Shot 5-Blast 12

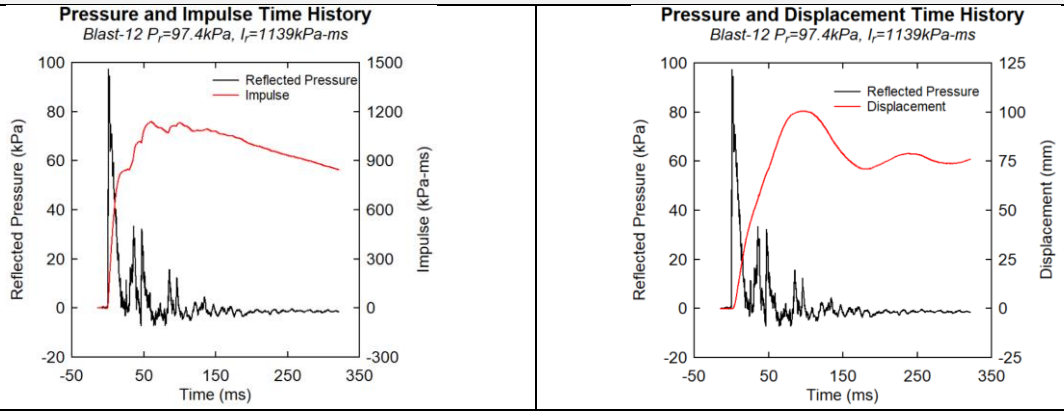

Figure 4-6. RMW-C-L Pressure, Impulse and Displacement Time Histories

A) RMW-C-L Setup

B) Shot 2

C) Shot 3

D) Shot 4

E) Failure (Shot 5)

Figure 4-7. RMW-C-L

Video stills showing Failure Mode (Shot 5)

0 ms

15 ms

30 ms

60 ms

120 ms

300 ms

Figure 4-8. Video stills showing Failure Mode

4.5. URM-S-N

URM-S-N was the third wall tested for this thesis. The wall was a stone infill wall with no retrofit. **Table 4-7** details the blasts, deflections and main events for each shot. **Figure 4-10** shows the pressure, impulse and displacement time histories of each blast, while **Figure 4-11** A) displays the wall setup. **Figure 4-12** shows the failure mode captured by camera.

The residual damage sustained by URM-S-N is shown in **Figure 4-9**. Extensive cracking was observed after the first test, with the formation of a main crack at 2.5mm wide. Two horizontal mortar joints above the midpoint of the wall had cracks almost spanning the entire length of the wall. One reason that cracking occurred at that point may be that those mortar joints were more continuous and straighter than the ones at the midpoint of the wall. Cracking can be seen at the top and bottom of the wall near the supports (**Figure 4-11** B). This is due to hinges forming at those locations.

The wall experienced three hinges at failure (Blast 2), one at each support, and one above midpoint of the wall (**Figure 4-12**). The middle hinge formed at the cracks that appeared during the first shot. The wall fragmented into many pieces, creating projectiles that landed up to 4.5m away from the wall (**Figure 4-11** C).

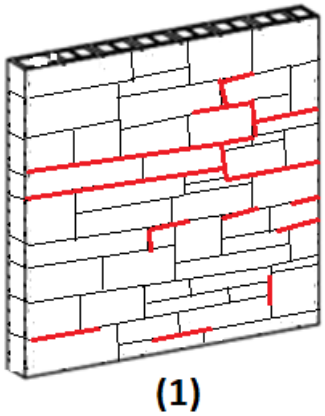

Figure 4-9. URM-S-N Damage Progression

Table 4-7. URM-S-N

Shot #	Blast #	P_r (kPa)	I_r (kPa-ms)	d_{max} (mm)	d_{res} (mm)	Comments
1	1	14.5	141	55.2	12.4	Major cracking along length of wall at mid-height and bottom hinge
2	2	28.6	250.4	n/a	n/a	Complete failure of wall

Shot 1-Blast 1

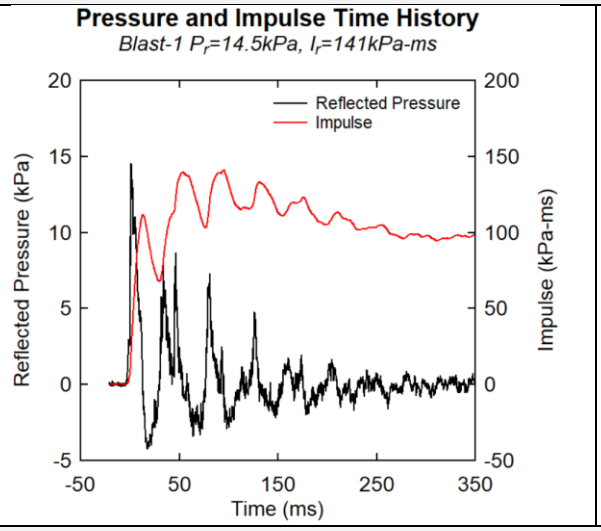

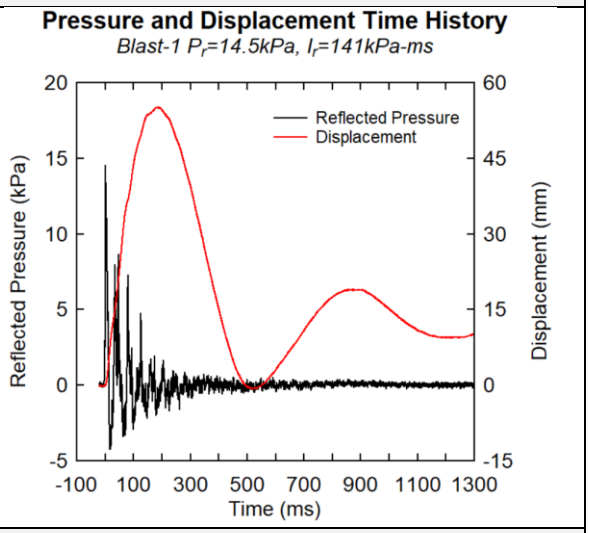

Shot 2-Blast 2

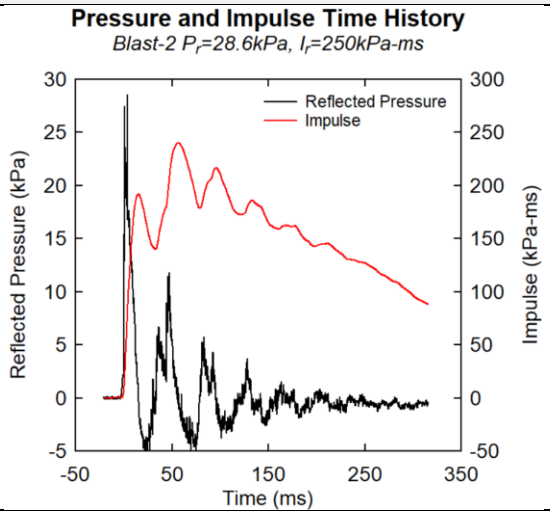

Figure 4-10. RMW-C-L Pressure, Impulse and Displacement Time Histories

A) RMW-C-L Setup

B) Shot 1

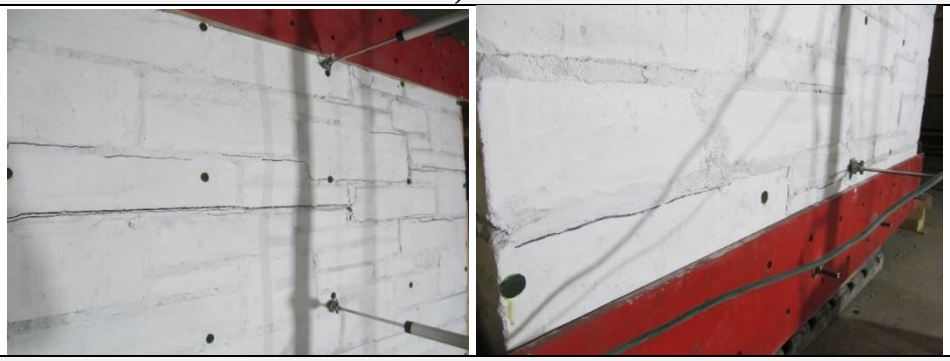

C) Debris

Figure 4-11. URM-S-N

A) Video stills showing Failure Mode (Shot 2) – Side view

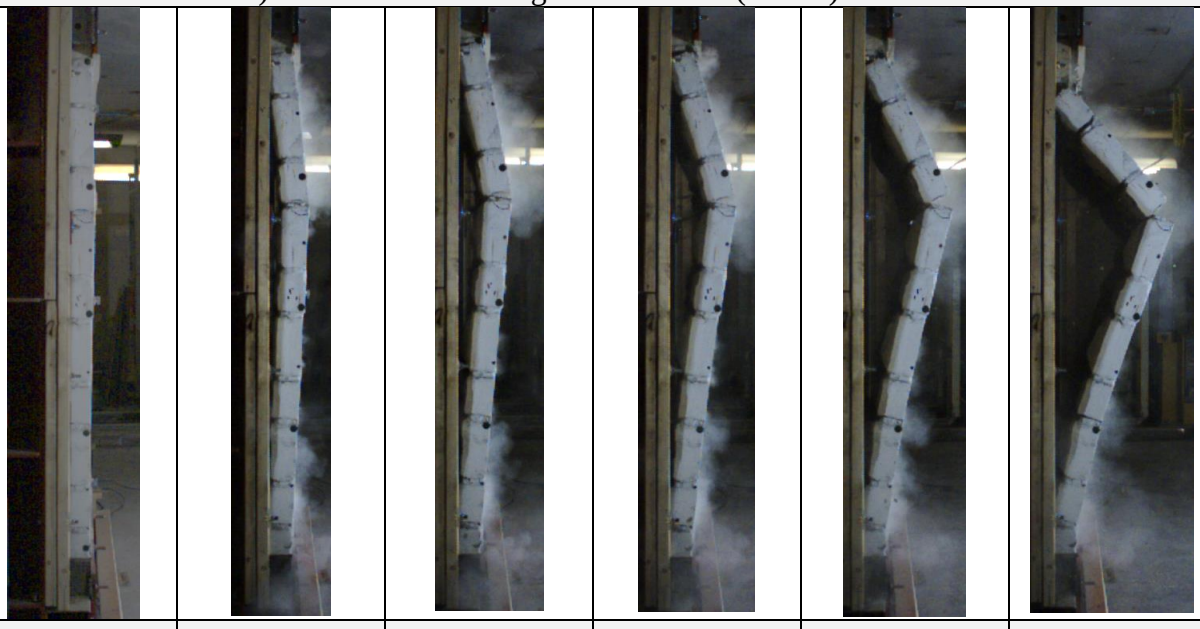

0ms	47.5ms	72.5ms	97.5ms	147.5ms	222.5ms

B) Video stills showing Failure Mode (Shot 2) – Angle view

0ms	47.5ms	72.5ms

97.5ms	147.5ms	222.5ms

Figure 4-12. Video stills showing Failure Mode

4.6. URM-S-L

URM-S-L was the fourth wall tested for this thesis. It was a stone load-bearing wall. As with URM-S-N, this was a control wall, so no retrofit was applied. The load axial applied was 171kN, which was about 4% of the total axial resistance of the wall. A value of 4% was chosen to compare the stone walls tested by Saatcioglu et al. (2018). **Table 4-8** details the blasts, deflections and main events for each shot. **Figure 4-14** shows the pressure, impulse and displacement time histories of each blast, while **Figure 4-15** A) displays the wall setup. **Figure 4-15** H) shows the displacement profile for each blast and **Figure 4-16** shows the failure mode captured by camera.

The residual damage sustained by URM-S-L is shown in **Figure 4-13**. The first shot created a very small crack along a vertical mortar joint. No major damage was observed. At the second shot (**Figure 4-15** B) small horizontal cracks appeared along the mortar joints located near mid-height of the wall. The small cracks appeared along the entire length of the wall. For the next three shots, the cracks continued to widen and elongate. In the video, the cracks appear to widen, then close due to the load applied on the wall. The cracks near mid-height of the wall formed the main crack. The main crack widened from 0.1mm at the third shot (**Figure 4-15** C), to 0.4mm at the fourth (**Figure 4-15** D), to 0.7mm at the fifth. At the fourth and sixth shots (**Figure 4-15** E), pieces of mortar fell off the wall. The seventh shot (**Figure 4-15** F) continued to widen and elongate the cracks present in the wall.

The wall failed catastrophically at the eighth shot (**Figure 4-15** G). The wall formed three hinges, one at both supports and one at mid-height of the wall. Save for the first course of blocks, no portion of the wall remained standing. Large debris fell up to 2.9m away from the wall, while the furthest projectile fell 3.4m away.

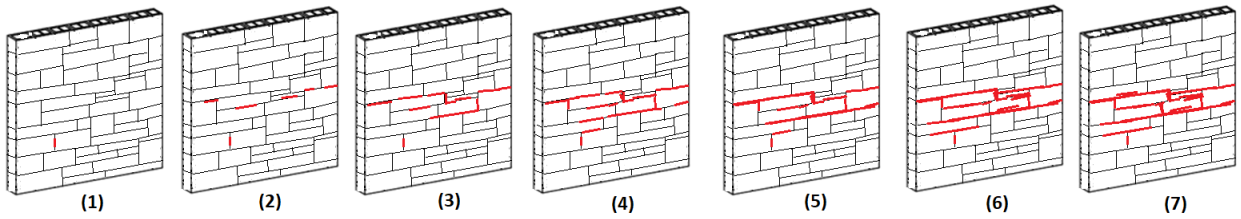

Figure 4-13. URM-S-L Damage Progression

Table 4-8. URM-S-L

Shot #	Blast #	P_r (kPa)	I_r (kPa-ms)	d_{max} (mm)	d_{res} (mm)	Comments
1	1	13.5	199.5	5.8	0	Small vertical crack at midpoint of wall
2	2	26.6	311.2	11.7	0.2	Hairline cracks along horizontal mortar joints near mid-height
3	3	33.9	372.9	15.5	0.2	Main crack widened to 0.1mm
4	4	39.5	427.3	18.3	0.5	Mortar piece fell off. Crack widened to 0.4mm
5	5	43.7	497.9	21.7	0.3	Cracks elongated and widened to 0.7mm
6	6	46.5	574	28.2	0.6	Section of mortar joint at mid-height fell out
7	7	50.2	592.8	38.4	2.3	Cracks elongated and widened
8	8	57.1	600	n/a	n/a	Complete failure of wall

Shot 1-Blast 1

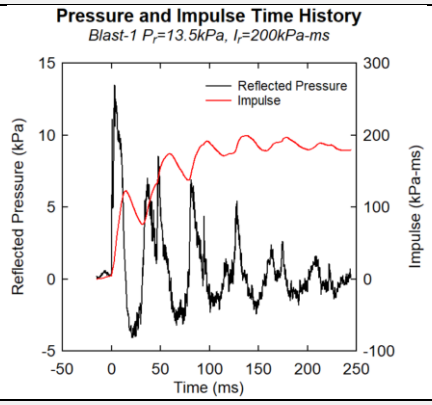

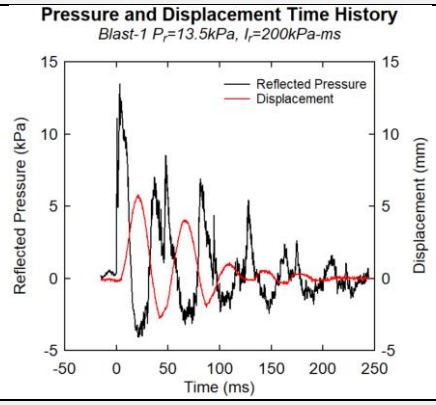

Shot 2-Blast 2

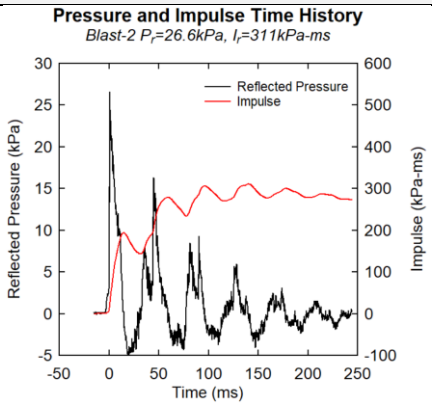

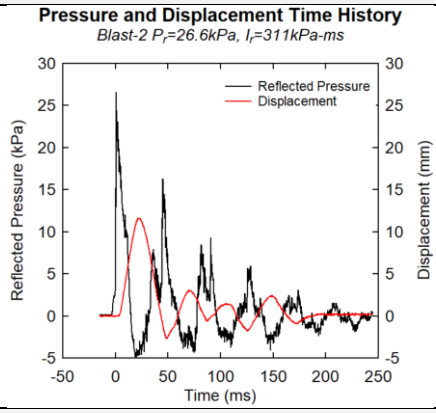

Shot 3-Blast 3

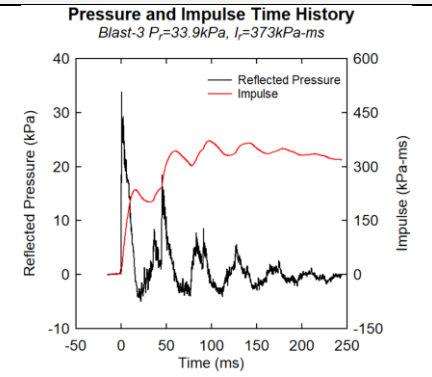

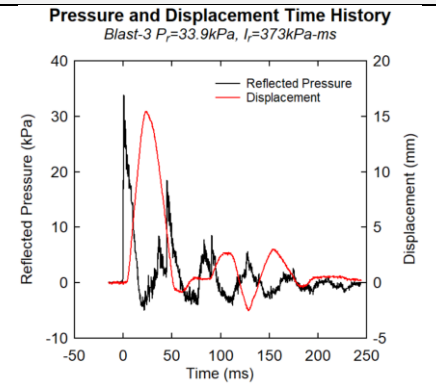

Shot 4-Blast 4

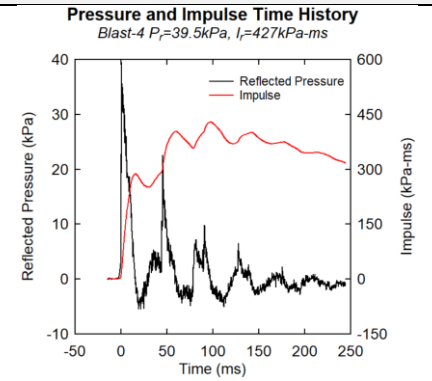

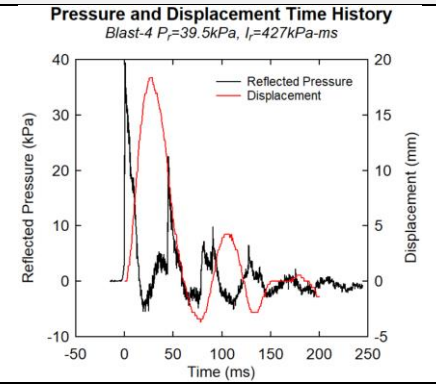

Shot 5-Blast 5

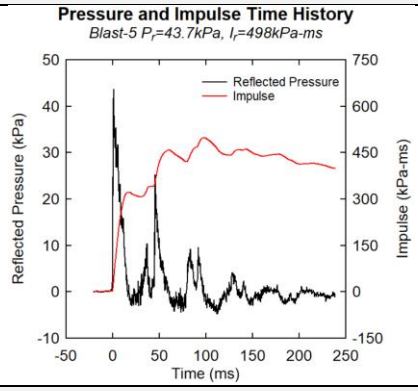

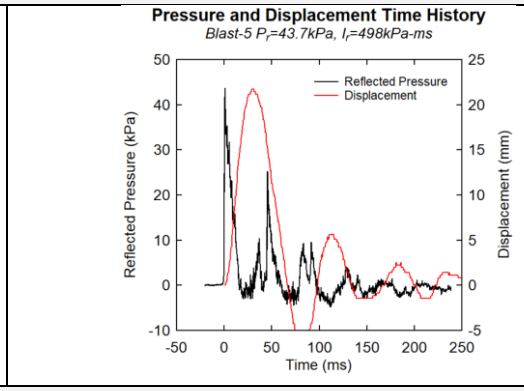

Shot 6-Blast 6

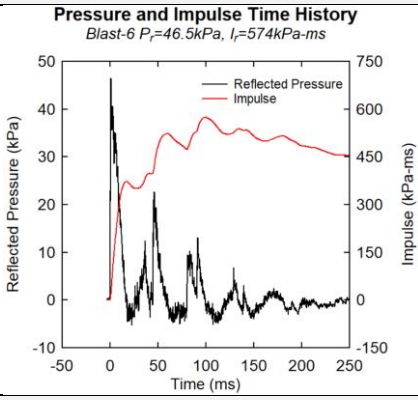

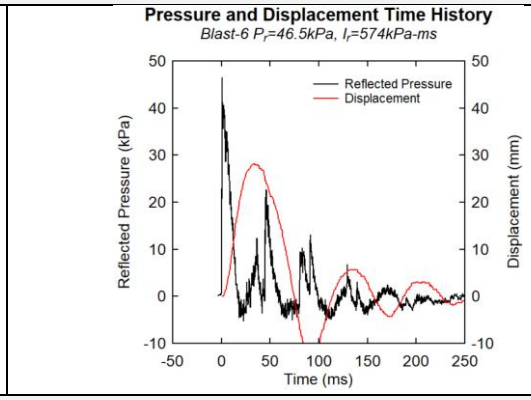

Shot 7-Blast 7

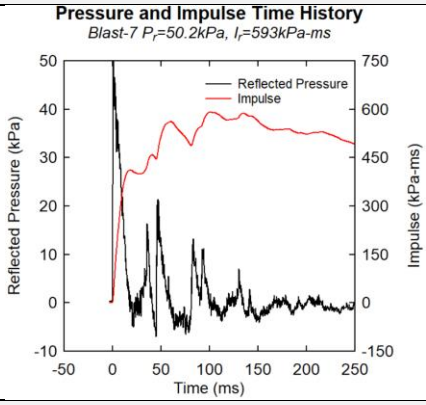

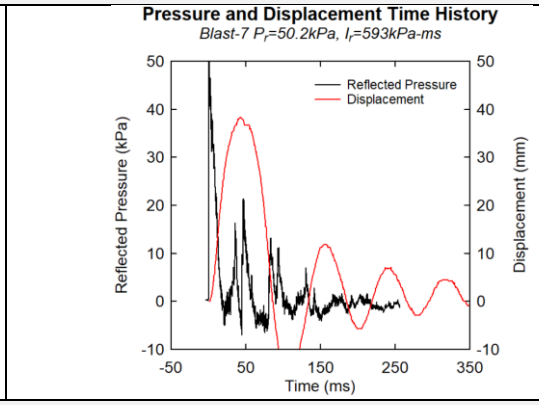

Shot 8-Blast 8

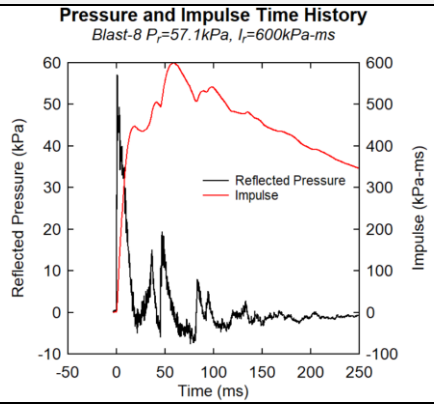

Figure 4-14. URM-S-N Pressure, Impulse and Displacement Time Histories

A) Wall Setup

B) Shot 2

C) Shot 3

D) Shot 4

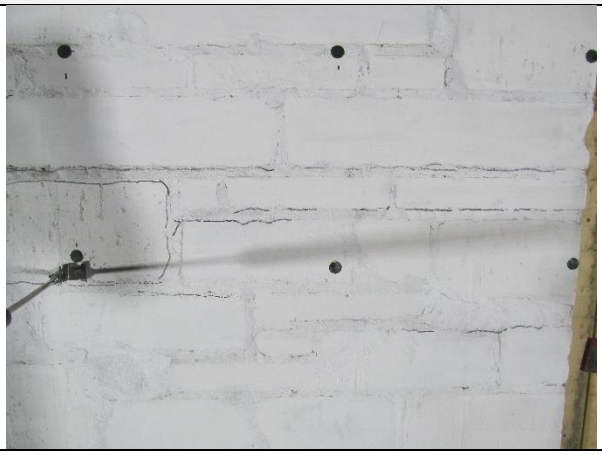

E) Shot 6

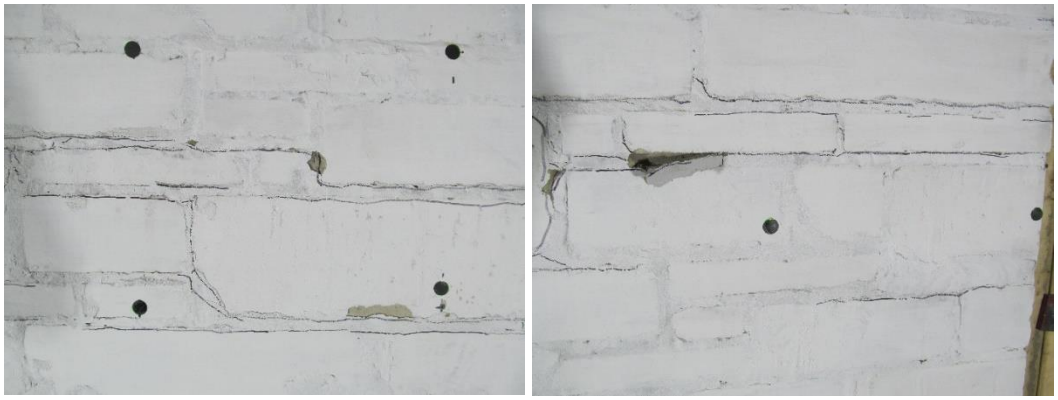

F) Shot 7

G) Shot 8 Failure

H) Displacement Profile

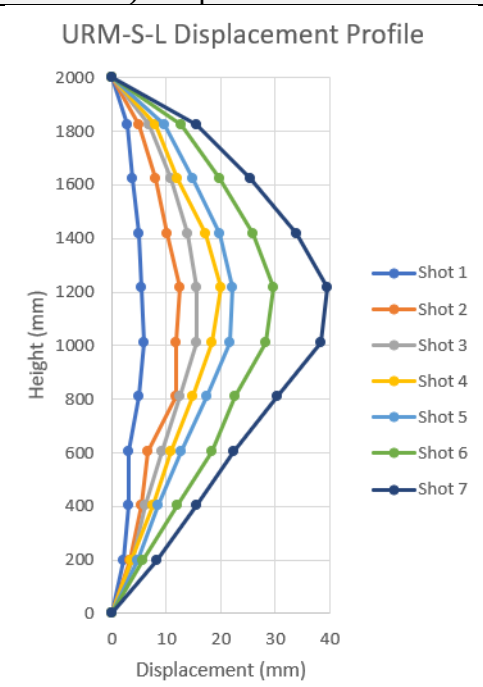

Figure 4-15. URM-S-L

A) Video stills showing Failure Mode at Shot 8

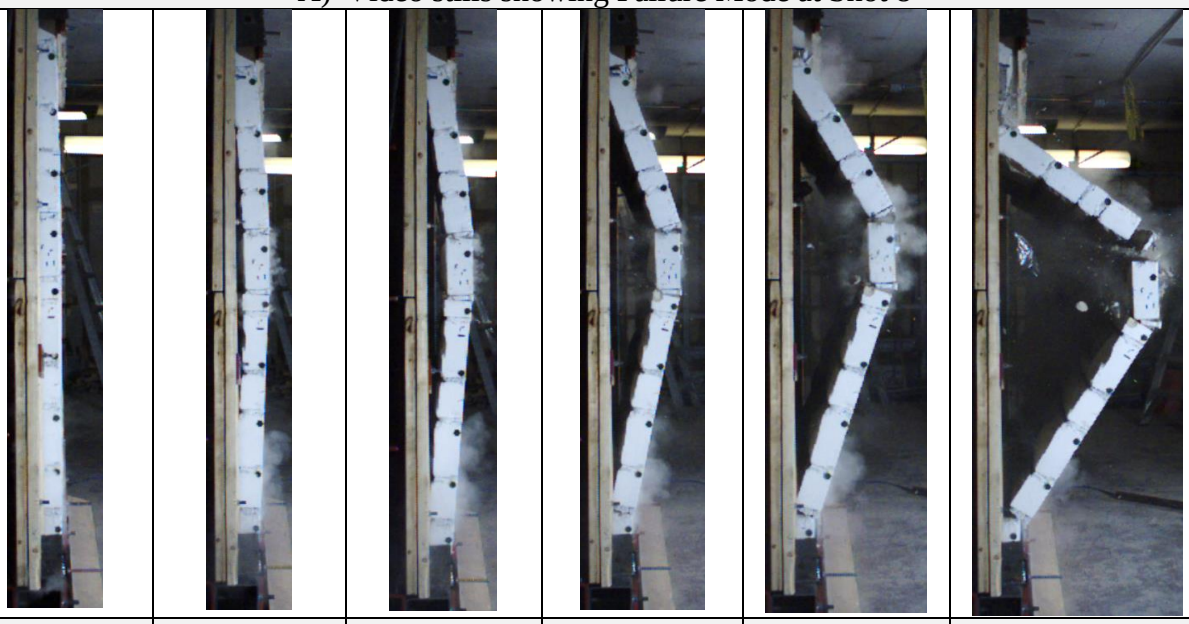

0ms	33ms	63.5ms	106.5ms	147.5ms	240.5ms

B) Video stills showing Failure Mode (Shot 8) – Angle view

0ms	47.5ms	72.5ms

97.5ms	147.5ms	222.5ms

Figure 4-16. Video stills showing Failure Mode

4.7.RMW-S-N

RMW-S-N was the fifth wall tested for this thesis. It was a retrofit stone infill wall. The mesh used was gage 2 in thickness and was welded to the top and bottom HSS supports. The shotcrete was applied in a thickness of 51mm from the same batch as RMW-S-L. **Table 4-9** details the blasts, deflections and main events for each shot. **Figure 4-18** shows the pressure, impulse and displacement time histories of each blast, while **Figure 4-19** A) displays the wall setup. **Figure 4-19** G) shows the displacement profiles for each blast. **Figure 4-20** shows the failure mode captured by camera.

The residual damage sustained by the wall is shown in **Figure 4-17**. No damage was sustained by the wall for the first two shots. On the third shot (**Figure 4-19** B), very minor cracking appeared on the face of the wall. On the fourth shot (**Figure 4-19** C), more minor cracks appeared on the face of the wall, and a vertical compression crack appeared at the side of a stone block in the second course from the top of the wall. After the fifth shot (Blast 10) (**Figure 4-19** D), the previous crack connected to form the main crack along the length of the wall (0.7mm). The main crack formed about mid-height of the wall. This main crack grew wider after the sixth shot (**Figure 4-19** E), to a width of 3mm. No new significant cracks were created by the sixth blast.

The wall failed at the seventh shot (**Figure 4-19** F). Failure occurred along the main crack formed in the previous test. The cracked section acted as a hinge in the wall, with the top and bottom portions of the wall acting as rigid bodies. However, the mesh did not completely rupture as it did for RMW-C-N.

Figure 4-21 shows the strain time histories for SG1, 2 and 3. SG4 and SG5 did not give meaningful results. SG2 achieved the highest strain, which was above mid height of the wall. SG2 was the first to achieve yielding at Shot 4, however, SG3 also yielded after Shot 5. The strain rate was calculated by finding the average slope of SG2.

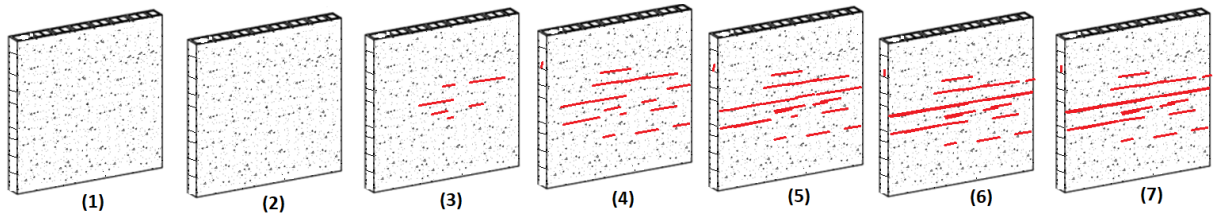

Figure 4-17. RMW-S-N

Table 4-9. RMW-S-N

Shot #	Blast #	P_r (kPa)	I_r (kPa-ms)	d_{max} (mm)	d_{res} (mm)	Comments
1	2	29.3	305.6	8.8	1.4	No damage
2	5	48.3	501.9	15.4	3.7	No damage
3	7	59.3	577.9	18.3	3.3	Minor horizontal cracks
4	9	70.1	1020	21.8	2.5	Minor horizontal cracks, vertical compression crack
5	10	97	915.8	27.1	3.4	Main crack at 0.7mm wide
6	11	102.9	940	33.5	9.4	Main crack widened 3mm
7	14	113.8	1177	146	n/a	Wall failed along main crack

Shot 1-Blast 2

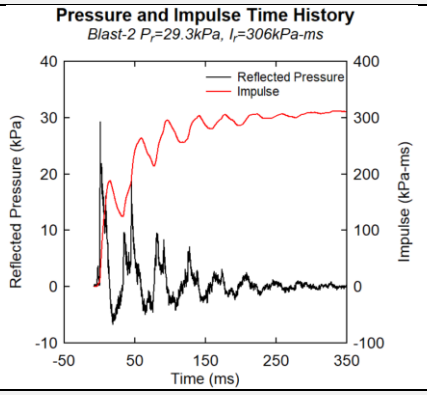

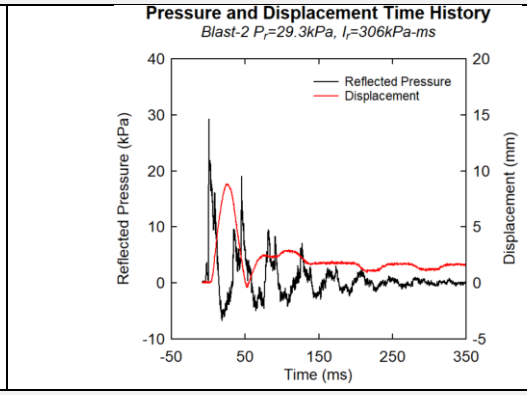

Shot 2-Blast 5

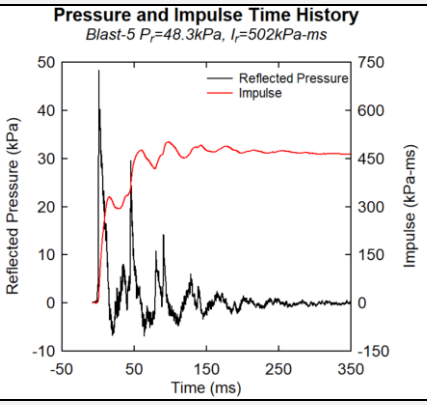

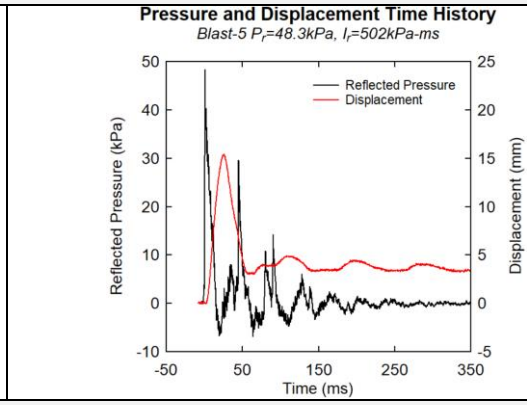

Shot 3-Blast 7

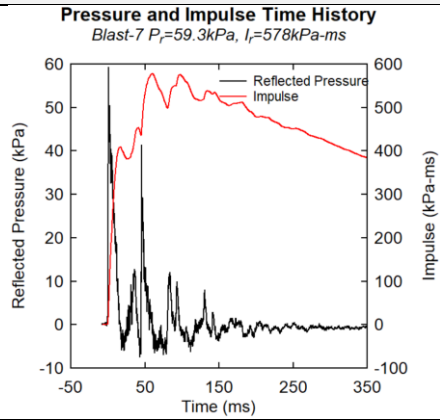

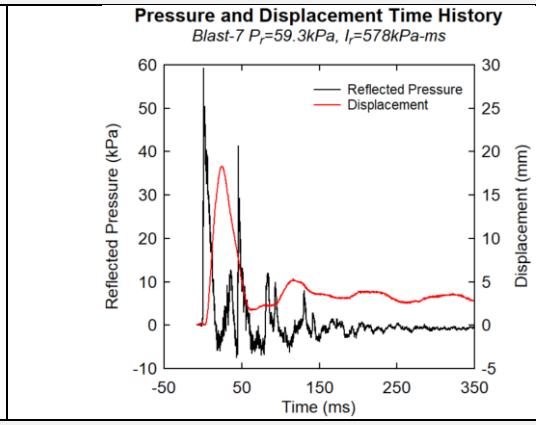

Shot 4-Blast 9

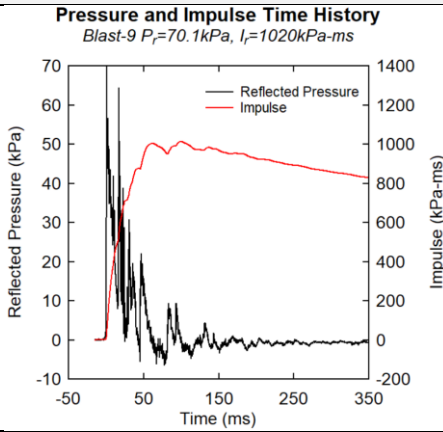

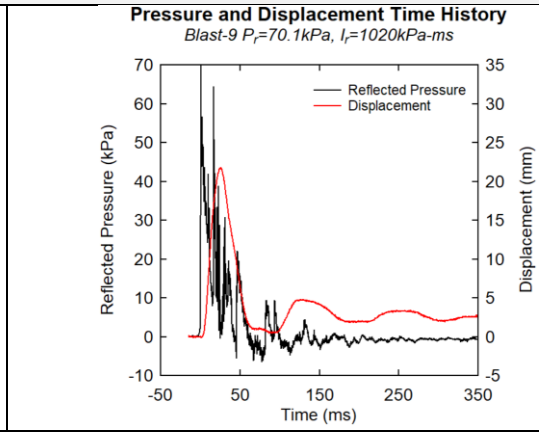

Shot 5-Blast 10

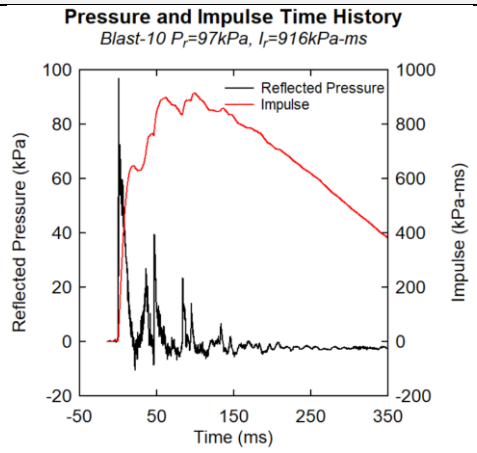

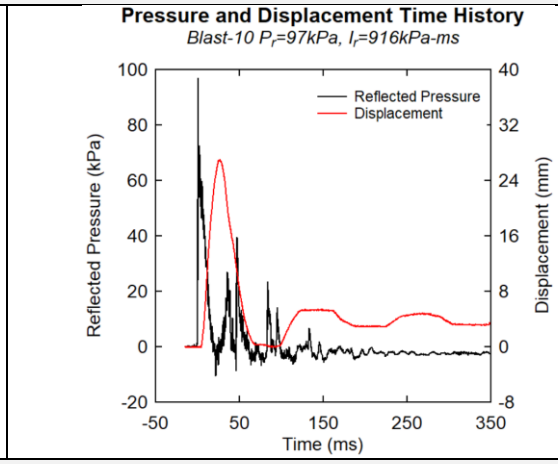

Shot 6-Blast 11

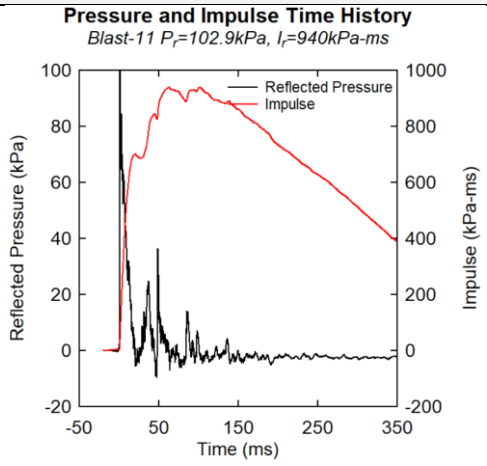

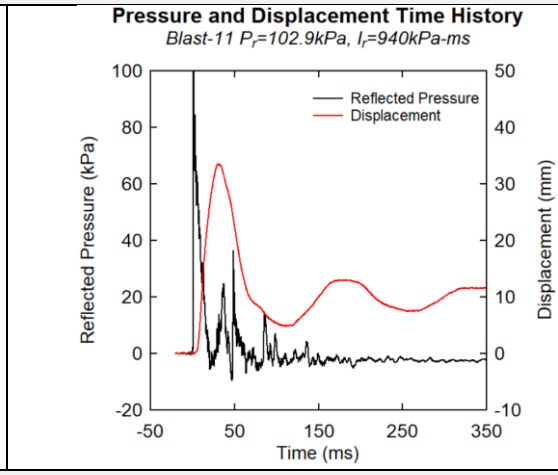

Shot 7-Blast 14

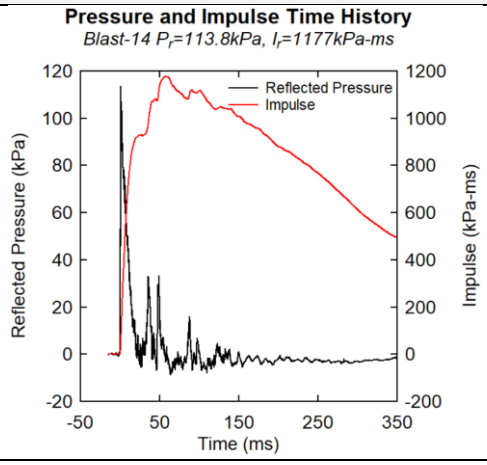

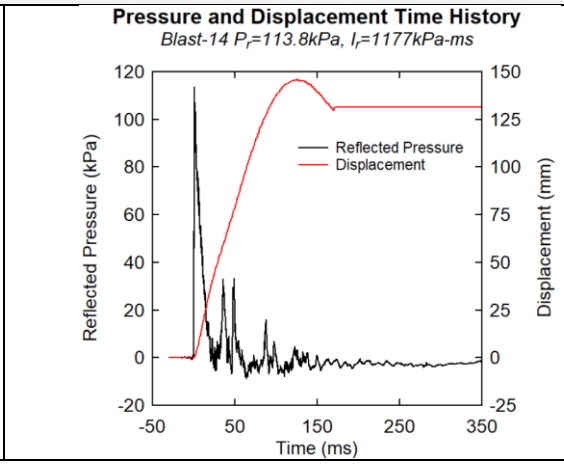

Figure 4-18. RMW-S-N Pressure, Impulse and Displacement Time Histories

A) Wall Setup

B) Shot 3

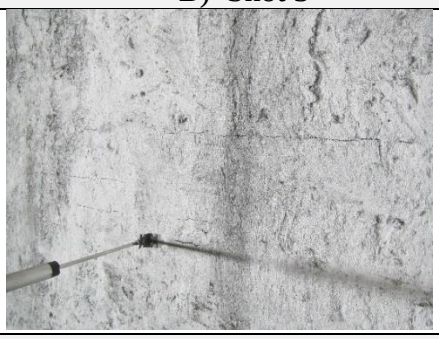

C) Shot 4

D) Shot 5. Main Crack appears

E) Shot 6

F) Shot 7 Failure

G) Displacement Profile

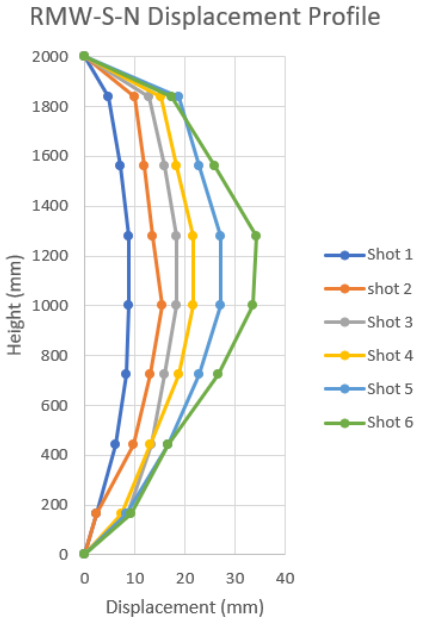

Figure 4-19. RMW-S-N

A) Video stills showing Failure Mode (Shot 7)

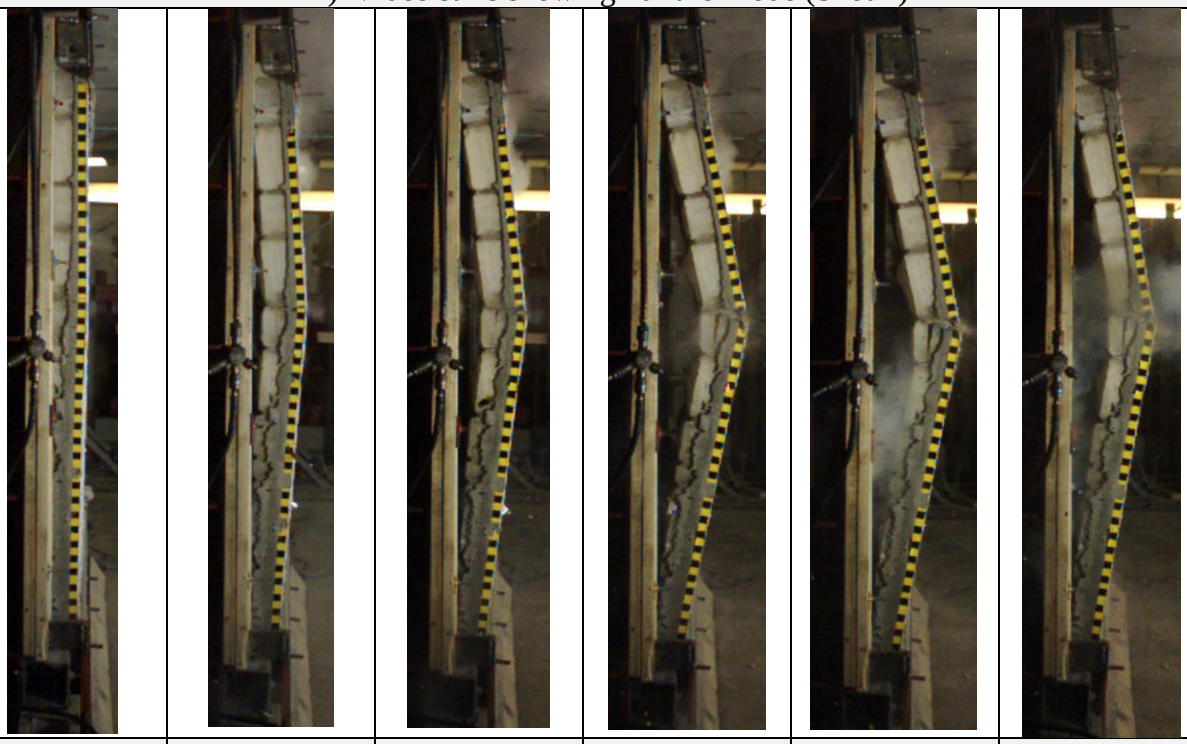

0ms	28ms	54.5ms	103.5ms	156.5ms	241ms

Figure 4-20. Video Stills Showing Failure Mode

Shot 1-Blast 2 (ė=0.02s^{-1})	Shot 2-Blast 5 (ė=0.08s^{-1})
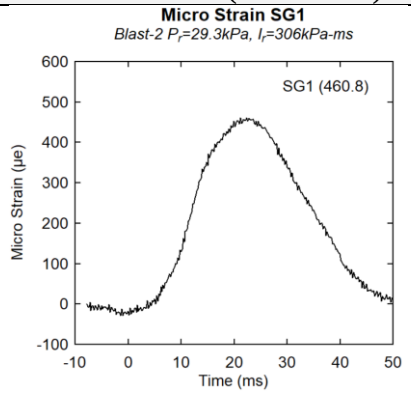	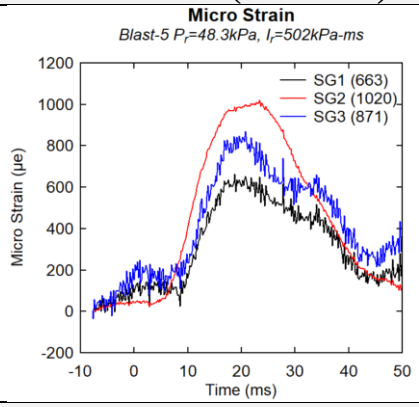
Shot 3-Blast 7 (ė=0.13s^{-1})	Shot 4-Blast 9 (ė=0.18s^{-1})
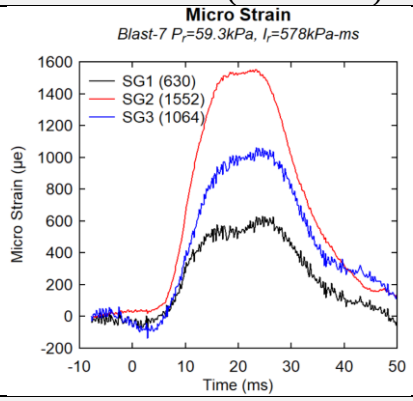	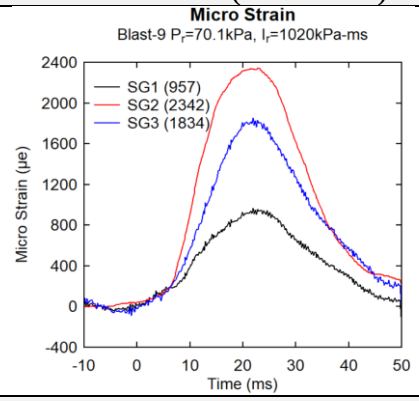
Shot 5-Blast 10 (ė=0.23s^{-1})	Shot 6-Blast 11 (ė=0.43s^{-1})
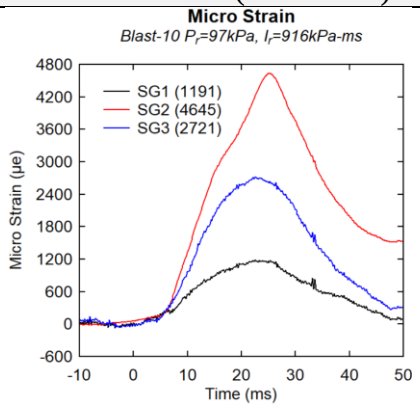	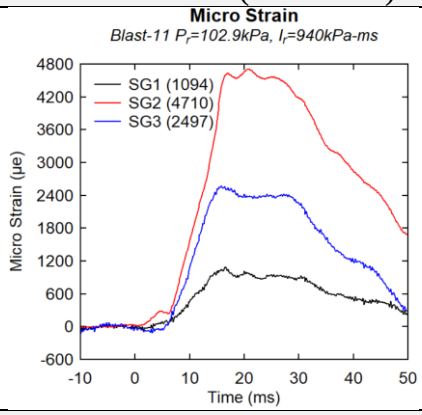
Shot 7-Blast 14 (ė=0.47s^{-1})	
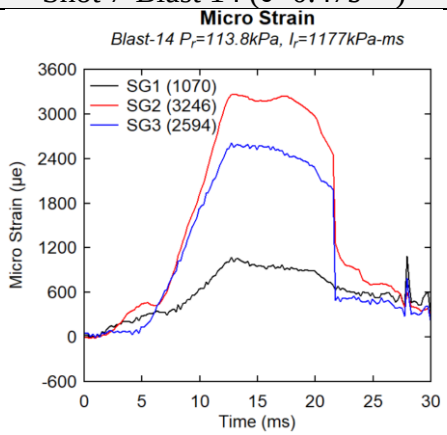	

Figure 4-21. RMW-S-N Strain data

4.8. RMW-S-L

RMW-S-L was the sixth wall tested for this thesis. It was a retrofit stone load-bearing wall. The mesh used was gage 2 in thickness and was welded to the top and bottom HSS supports. The shotcrete was applied in a thickness of 51mm from the same batch as RMW-S-N.

Table 4-10 details the blasts, deflections and main events for each shot. **Figure 4-23** shows the pressure, impulse and displacement time histories of each blast, while **Figure 4-24** A) displays the wall setup. **Figure 4-25** shows the failure mode captured by camera. **Figure 4-26** shows the strain data time histories for each blast and strain gage.

The residual damage is shown in **Figure 4-22**. No damage was sustained by the wall for the first three shots. On the fourth shot, two small cracks appeared on the side of the wall. On the fifth shot (**Figure 4-24** B), one horizontal hairline crack appeared above mid-height of the wall. After the sixth shot (**Figure 4-24** C), more hairline cracks appeared on the face of the wall. The cracks appeared near mid-height of the wall, likely where the horizontal mesh was near the surface of the shotcrete. The top HSS support was beginning to warp at this test. Vertical compression cracks were visible in the block at the top left of the wall. The seventh shot created more cracks along the face of the wall, extending the damage made in the previous tests (**Figure 4-24** D).

The wall failed at the eighth shot (Blast 15) (**Figure 4-24** E). The driver length was increased to 2743.2mm for this shot. The blast damaged the wall further, connecting the cracks from the previous test and widened the main crack to a width of 7mm. The microfibers could be seen spanning the gap. The failure crack was nearly horizontal at mid-height of the wall. The mesh did not rupture when the wall failed.

Figure 4-26 shows the strain time histories for SG1 through SG5. SG2 achieved the highest strain, which was above mid height of the wall. SG2 was the first to achieve yielding at Shot 6, however, SG3 also yielded at Shot 7. The strain rate was calculated by finding the average slope of SG2.

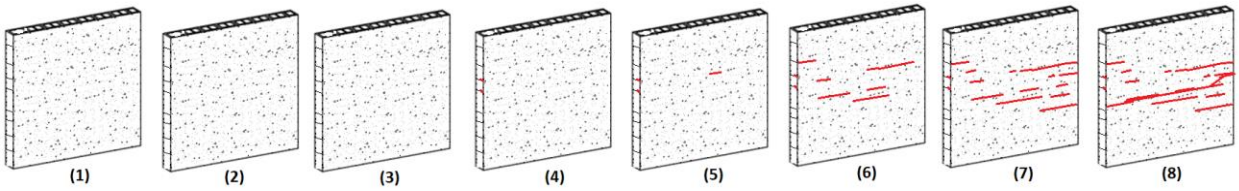

Figure 4-22. RMW-S-L Damage Progression

Table 4-10. RMW-S-L

Shot #	Blast #	P_r (kPa)	I_r (kPa-ms)	d_{max} (mm)	d_{res} (mm)	Comments
1	2	34.1	321.1	4.9	1.1	No damage
2	5	56.4	497.8	8.1	2.6	No damage
3	7	61.9	615.3	9.5	2.4	No damage
4	9	75.6	738.4	11.4	3.4	Minor cracks on the side
5	10	86	936.9	13.9	2.8	Hairline crack above mid-height
6	12	100.7	1192.6	19.8	5.5	More cracks along face of wall. Compression cracks in stone blocks
7	13	107.1	1209.5	20.6	5.1	Cracks lengthen on face of wall
8	15	109.9	1734.7	139.4	n/a	Failure at main crack (7mm width)

Shot 1-Blast 2

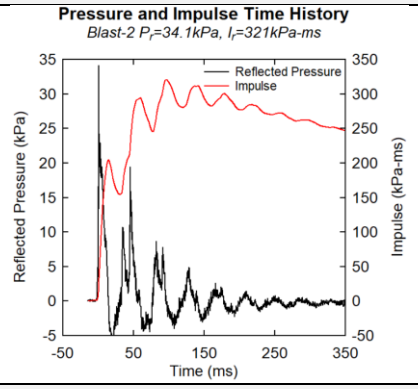

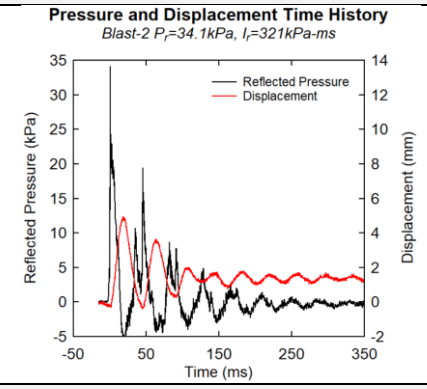

Shot 2-Blast 5

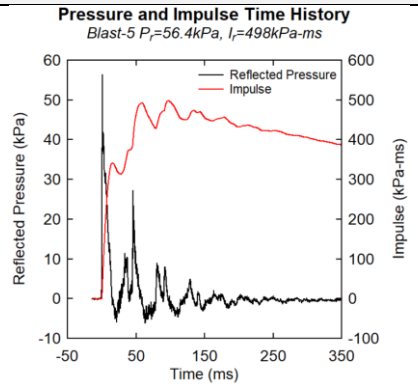

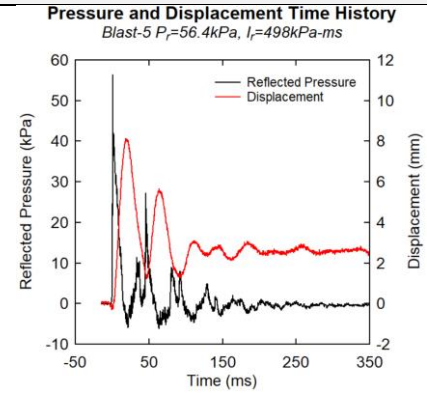

Shot 3-Blast 7

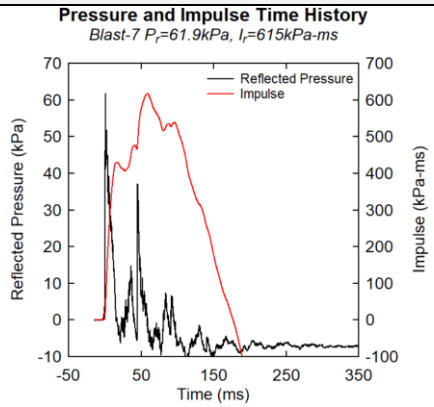

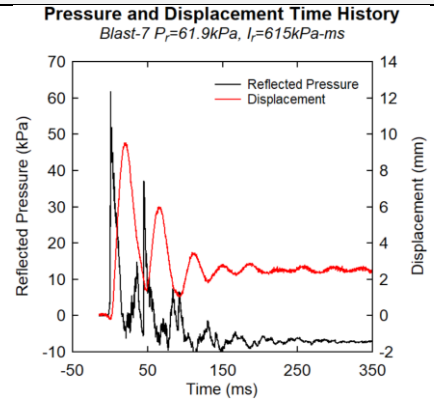

Shot 4-Blast 9

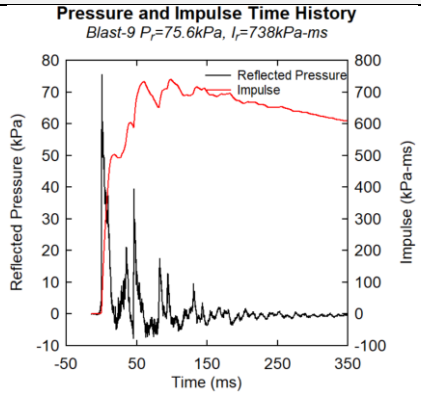

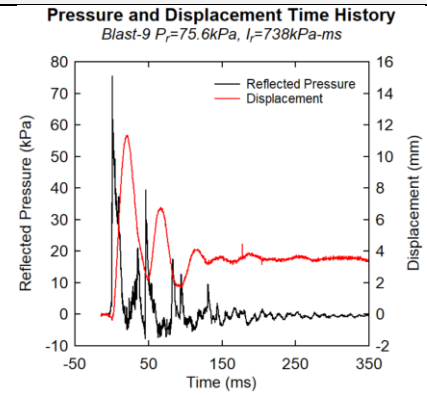

Shot 5-Blast 10

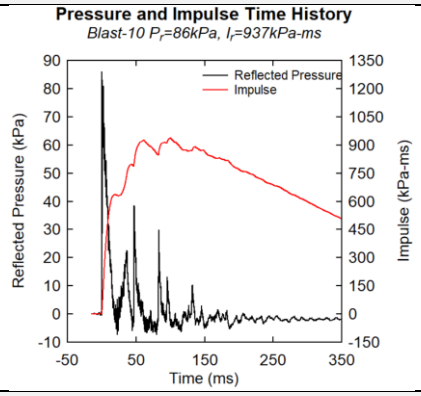

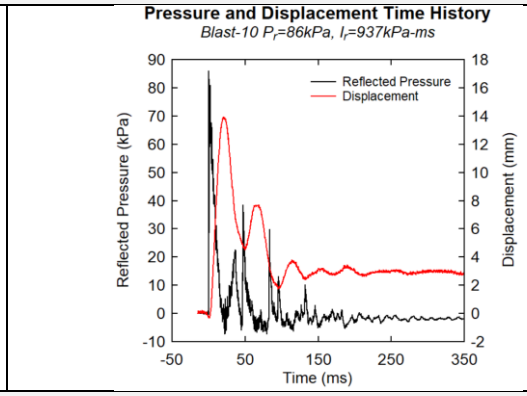

Shot 6-Blast 12

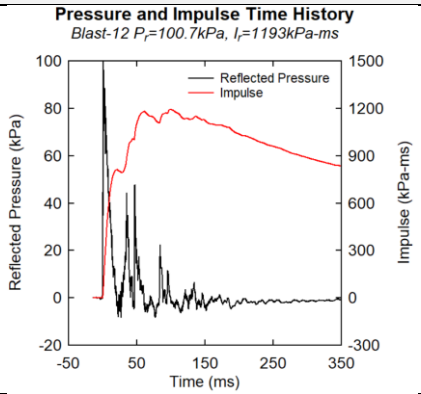

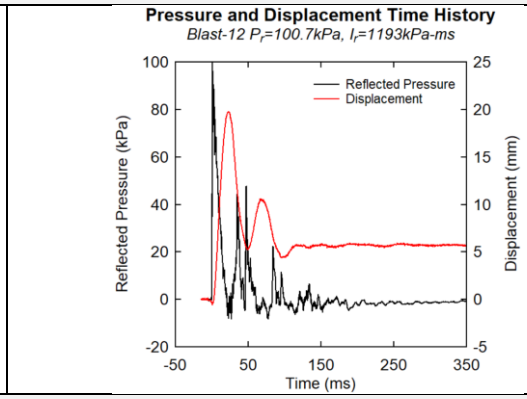

Shot 7-Blast 13

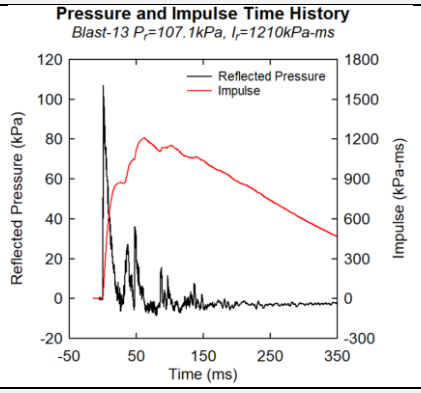

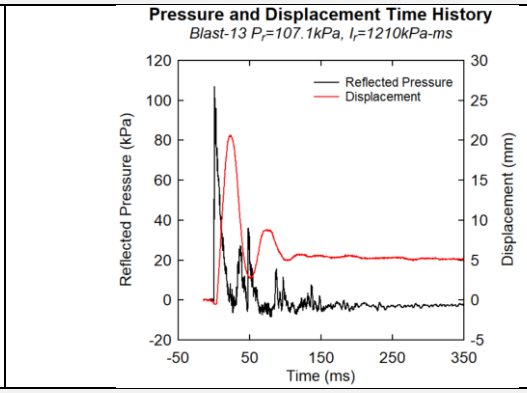

Shot 8-Blast 15

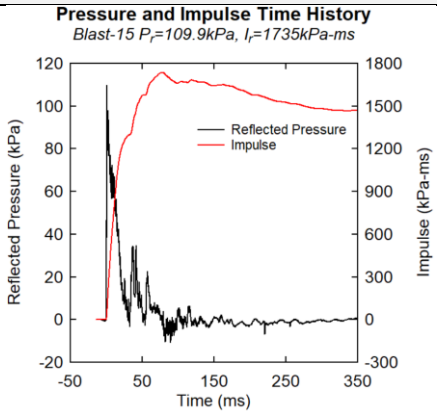

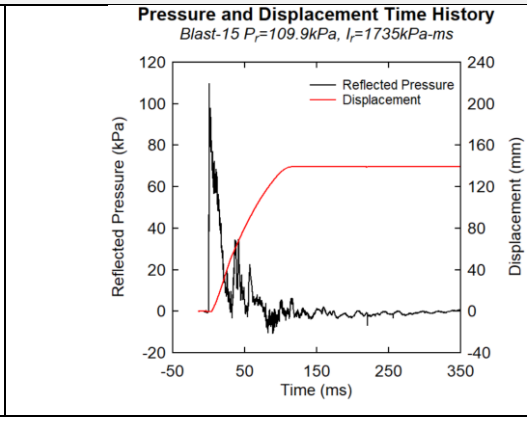

Figure 4-23. RMW-S-L Pressure, Impulse and Displacement Time Histories

A) Wall Setup


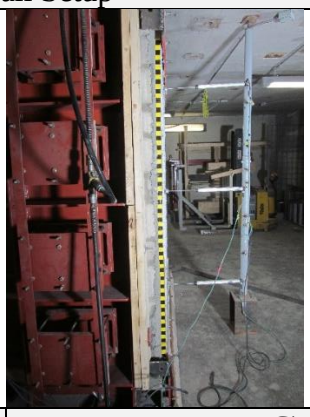

B) Shot 5

C) Shot 6

D) Shot 7


E) Shot 7 Failure


F) Displacement Profile

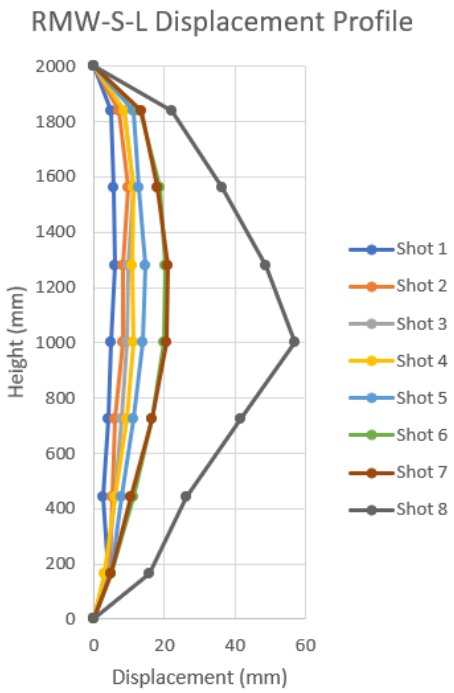

Figure 4-24. RMW-S-L

A) Video still showing Failure Mode (Shot 7)

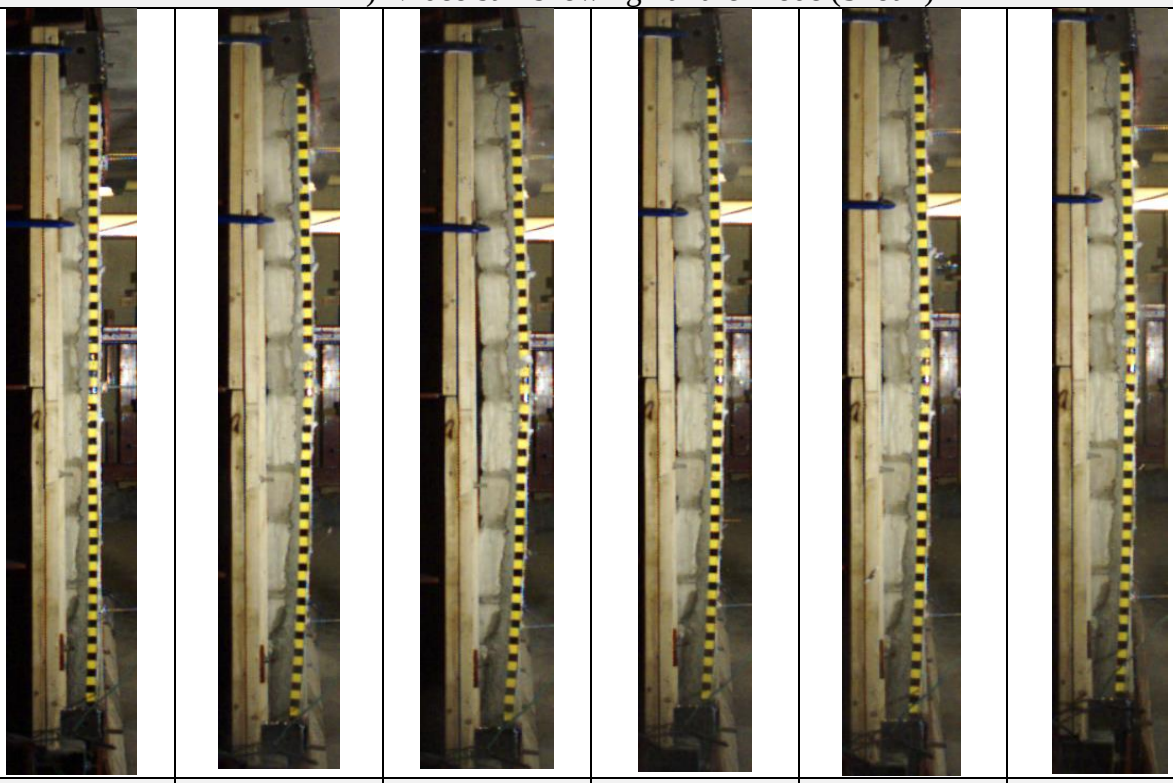

0ms	19.5ms	33ms	53ms	99ms	197.5ms

Figure 4-25. Video Stills Showing Failure Mode

Shot 1-Blast 2 (ė=0.01s^{-1})	Shot 2-Blast 5 (ė=0.05s^{-1})
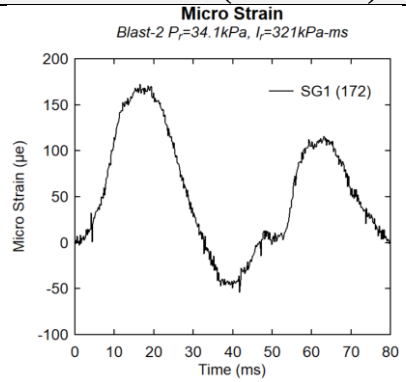	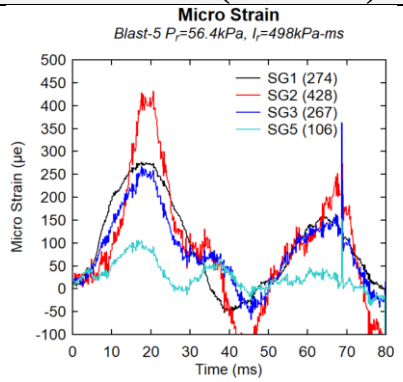
Shot 3-Blast 7 (ė=0.04s^{-1})	Shot 4-Blast 9 (ė=0.07s^{-1})
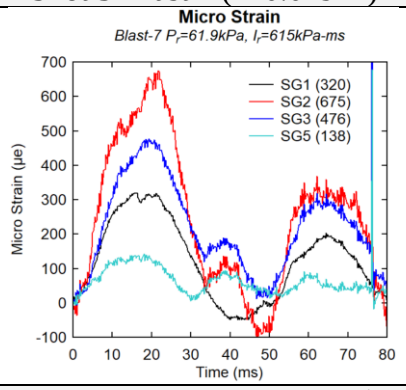	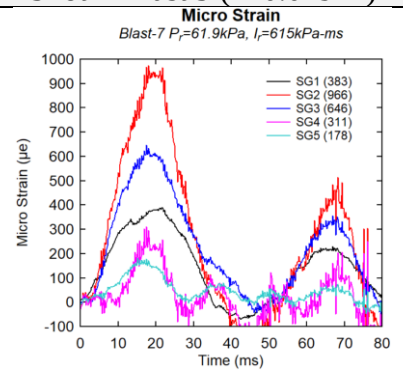
Shot 5-Blast 10 (ė=0.12s^{-1})	Shot 6-Blast 12 (ė=0.13s^{-1})
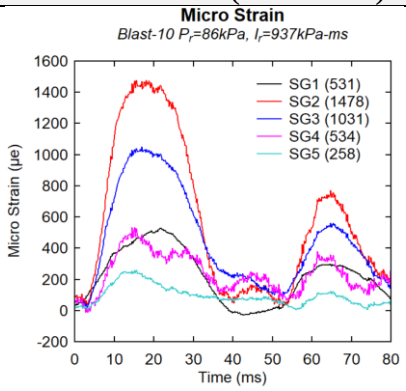	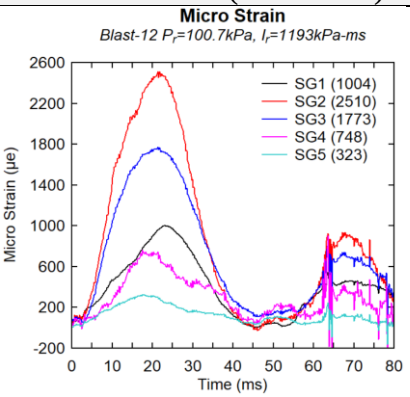
Shot 7-Blast 13 (ė=0.19s^{-1})	Shot 8-Blast 15 (ė=0.69s^{-1})
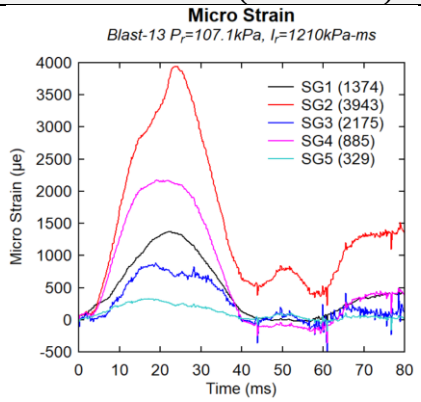	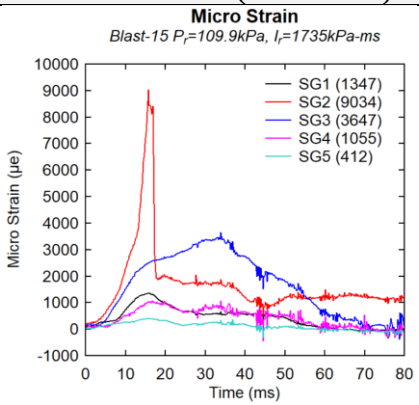

Figure 4-26. RMW-S-L Strain data

CHAPTER 5. DISCUSSION

5.1. CHAPTER OVERVIEW

This chapter discusses the results presented in Chapter 4. The criteria for discussion include midpoint displacement, residual displacement, number of tests, magnitude of pressure, failure mode and degree of fragmentation. The parameters discussed include the effects of the type of block (CMU vs STONE), the effect of axial load, and the effect of the retrofit. The response of the shotcrete retrofit system is also compared to the response of a polyurea retrofit system tested by Ciornei (2012).

5.2. GENERAL OBSERVATIONS

This section provides a general overview of the test results which compliments the data previously presented in Chapter 4. The load displacement response of the shotcrete which correlates the load to the crack width is presented in **Figure 5-1**. Section A refers to the elastic response prior to first cracking, Section B refers to hardening of the shotcrete due to fiber activation, Section C refers to softening due to fiber pullout, and Section D refers to when the fibers no longer resist significant tensile load. The response of the various specimens in terms of maximum and residual displacements and failure is presented graphically in **Figure 5-2**.

From the results, it can be observed that the retrofit significantly enhanced the blast performance of the URM walls, in both the CMU and STONE series. Moreover, the results show that the performance is affected by masonry type and axial load level. Further discussions on the effects of the test parameters is provided in the sections that follow.

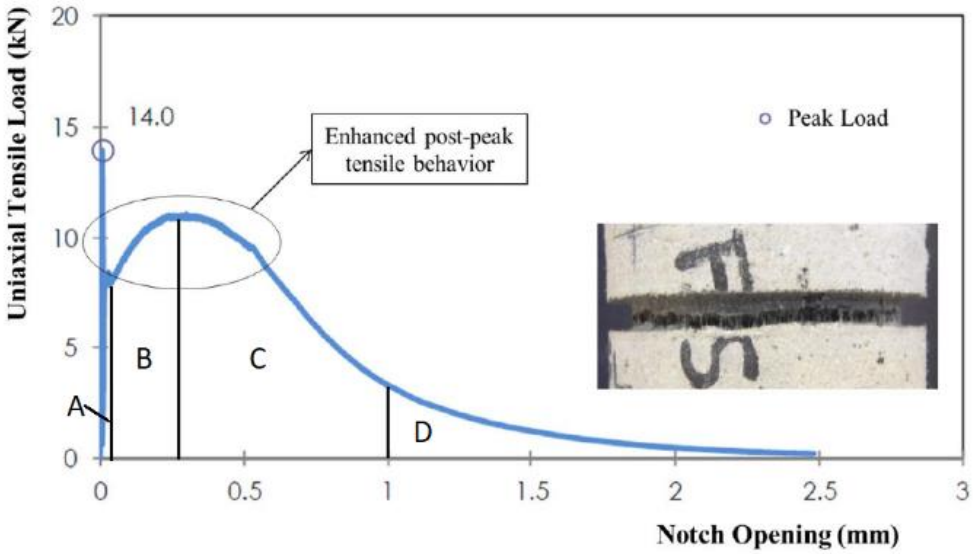

Figure 5-1. Tensile Load Displacement Relationship, emphasis mine (Ginouse et al., 2015)

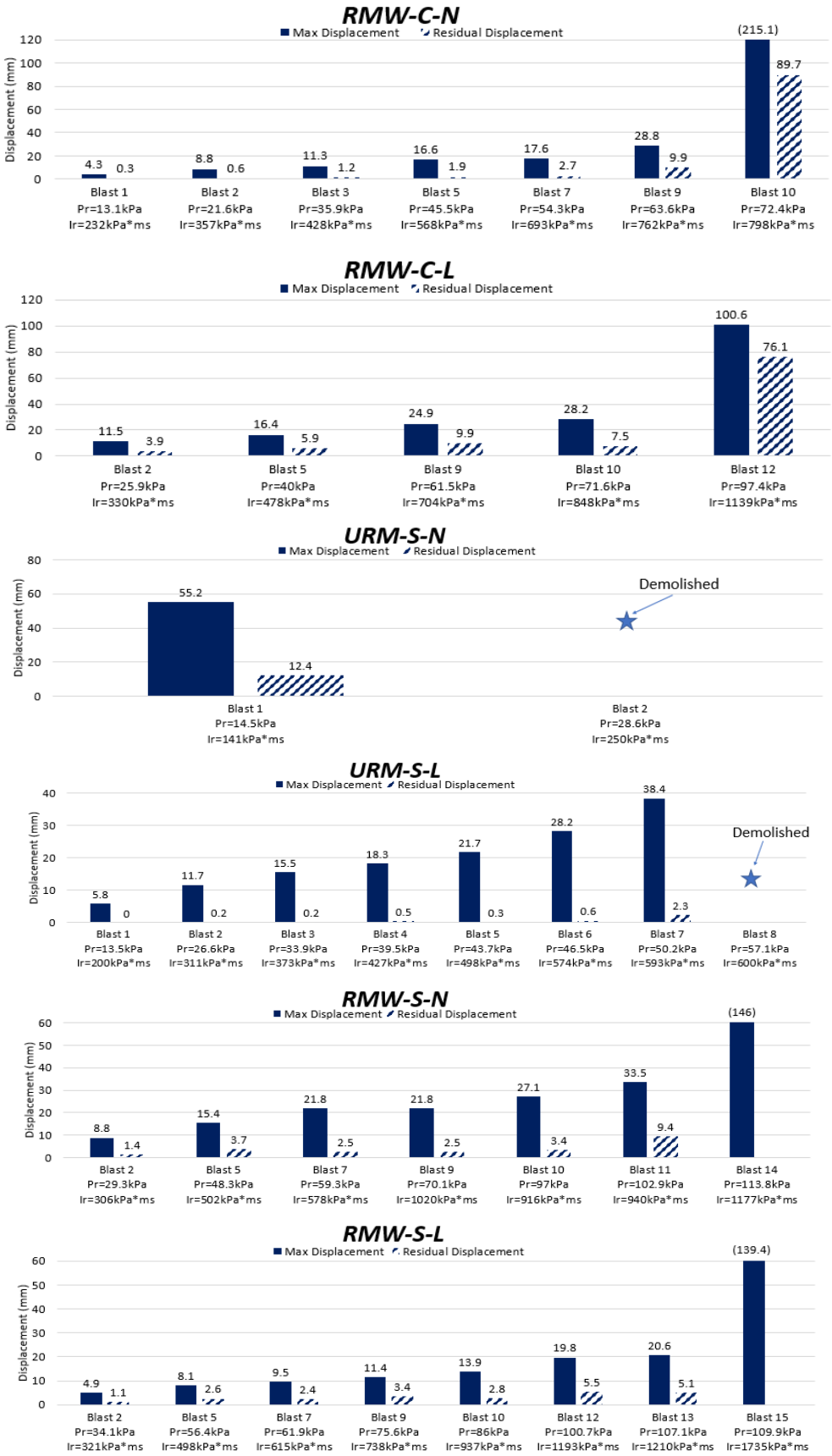

Figure 5-2. Maximum and Residual Displacements for Each Wall

5.3. CMU SERIES RETROFIT COMPARISON

5.3.1. Infill Walls (URM vs Retrofit)

The effect of the shotcrete retrofit is first examined by comparing the response of URM-1 (tested by Ciornei, 2012) and RMW-C-N. URM-1 was built as an unreinforced concrete masonry (CMU) infill wall with a 6mm gap at the top. RMW-C-N was built in the same manner as URM-1, save that the shotcrete retrofit system was applied to the face of the wall and the gap at the top of the wall was filled with high strength grout.

Figure 5-3 compares the displacements sustained by the walls over the course of testing and shows selected displacement time history graphs and maximum/residual displacement comparisons. **Figure 5-4** shows photos of the walls during testing.

It was found that the retrofit greatly increased the blast capacity of the wall. The steel mesh and the fibers in the shotcrete improved the moment resistance of the wall to prevent premature failure in the out-of-plane direction. URM-1 was demolished after four tests at Blast 3 (34.9kPa, 400kPa-s), but the retrofit wall delayed failure for seven shots until Blast 10 (81.8kPa, 875kPa-ms). The increase in reflected pressure and reflected impulse is 134% and 119%, respectively.

In addition to increasing blast capacity, the retrofit also improved control of displacements at equivalent blasts by increasing the stiffness and mass of the wall. The maximum displacements were larger for the control when compared to the retrofit at Blast 1 (13.3 kPa, 191 kPa-ms) and Blast 2 (27.7 kPa, 312 kPa-ms). At these blasts, the retrofit reduced maximum displacements by 82% (Blast 1), and 84% (Blast 2).

The damage observed on these walls can be correlated to the displacements experienced during the tests. Damage in the retrofit wall consisted of hairline cracks in the shotcrete until shot 5 (Blast 7, 56.4kPa, 620kPa-ms) which produced crack widths of 0.3mm (section B in **Figure 5-1**). At the sixth test (Blast 9, 67.7kPa, 806kPa-ms), the retrofit wall had a crack width of 4mm which accounts for the sudden increase in maximum displacement when comparing to the previous shot (past section D in **Figure 5-1**). Since the micro fibers had completely pulled out at this point, the wall shows a large increase in displacement during the seventh shot (Blast 10, 81.8kPa, 875kPa-ms), which caused the steel mesh to rupture and the wall to shear along the critical crack.

As previously stated, the control wall was completely demolished, creating many projectiles and fragments at failure. In comparison, the retrofit wall failed with very minimal projectiles. Despite the brittle failure caused by the rupture of the steel mesh, the shotcrete kept the blocks together very well, with no delamination between the shotcrete overlay and masonry. Since the shotcrete held both pieces strongly, and the mesh was welded to the top and bottom supports, the wall did not fall over, but remained upright. The use of a more ductile mesh with larger cross-sectional area is one possible solution to improve the ductility of the retrofit.

Retrofit Performance - Infill CMU Walls

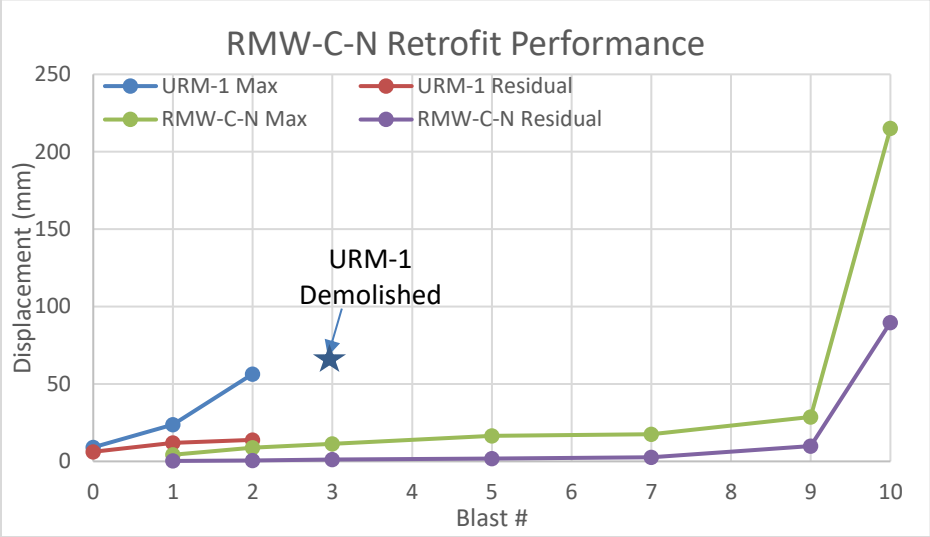

Displacement Time History Comparison

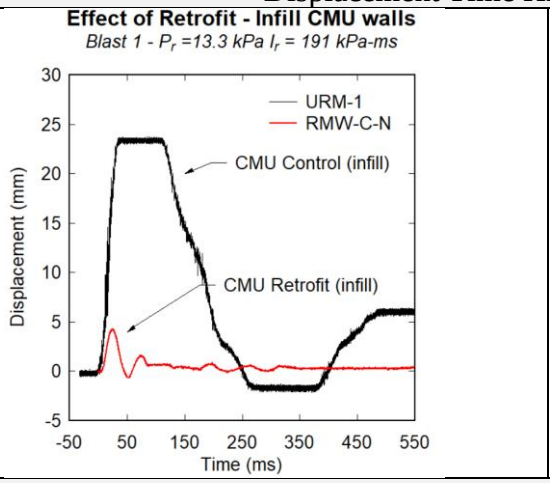

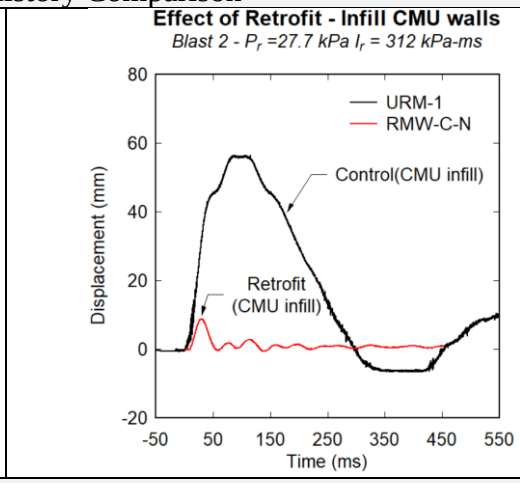

Maximum and Residual Displacements

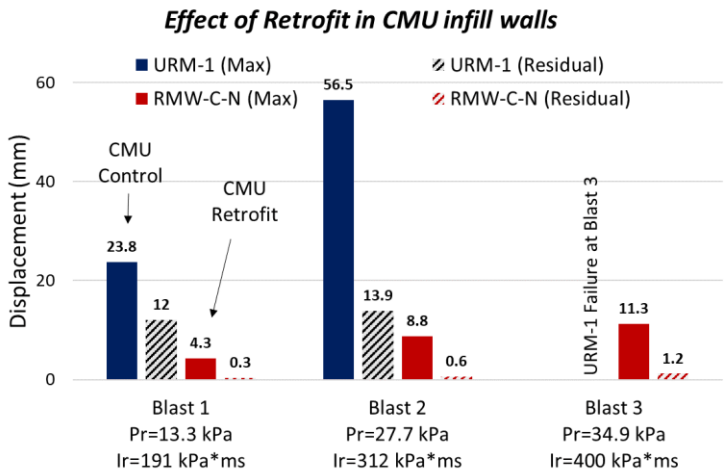

Figure 5-3. Retrofit Performance of Infill CMU Walls (URM-1 data from Ciornei, 2012)

Blast 2 Damage Comparison (Left: Ciornei, 2012)

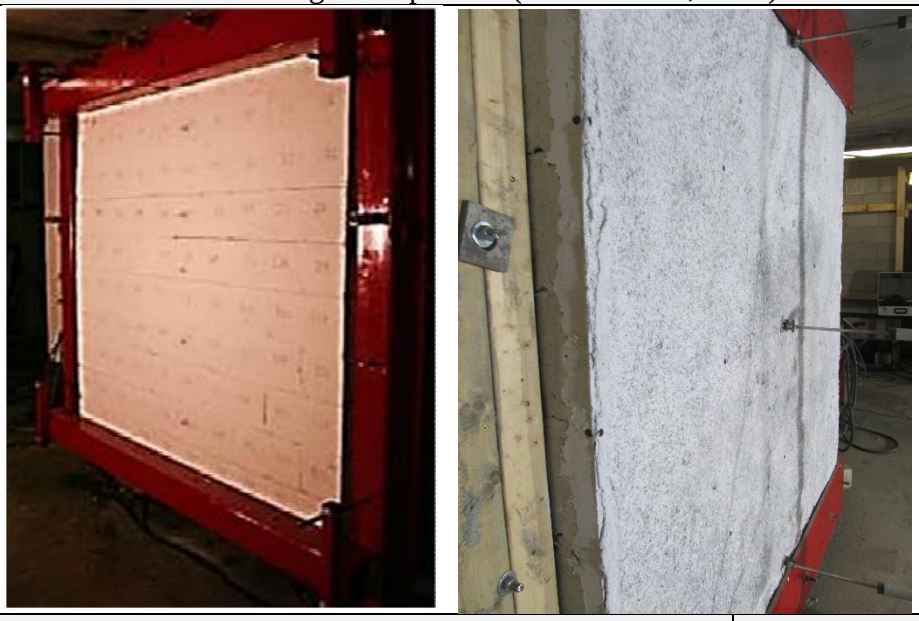

Blast 3 Damage Comparison (Left: Ciornei, 2012) | Retrofit Failure Mode

Figure 5-4. Non-Load Bearing CMU Walls Retrofit Comparison

5.3.2. Load Bearing Walls (URM vs Retrofit)

The effect of the retrofit in the CMU series is further examined by comparing the performance of load bearing walls URM-3 (tested by Ciornei, 2012) and RMW-C-L. URM-3 was designed as an unreinforced, load bearing concrete masonry (CMU) wall (tested by Ciornei, 2012). RMW-C-L was designed to be identical to URM-3, save that the shotcrete retrofit system was applied to the tension face of the wall. The axial load was 10% of the wall capacity for both walls; 123 kN URM-3 and 146 kN for RMW-C-L.

Figure 5-5 compares the displacements sustained by the walls over the course of testing and shows selected displacement time history graphs and maximum/residual displacement comparisons. **Figure 5-6** shows photos of the walls during testing.

It was found that the retrofit greatly increased the out-of-plane capacity of the wall due to the steel mesh and FRS improving the moment resistance of the wall. URM-3 was demolished after seven tests at Blast 6 (46.5kPa, 574kPa-ms). In comparison, the retrofit wall failed at Blast 12 (99.1kPa, 1166kPa-ms) after five tests were performed, representing an 103% increase in reflected impulse at failure.

The maximum displacements of the retrofit wall were substantially lower than those of the control wall due to its enhanced stiffness and greater mass. The displacements can be compared at Blasts 2 and 5 (27.7kPa, 312kPa-ms; 44.4kPa, 509kPa-ms) which were common to both walls. At Blasts 2 and 5, the retrofit wall reduced maximum deflections by 31%, and by 61% when compared to the deflections sustained by the control. However, the residual displacements of both the retrofit and control walls were largely similar. At Blast 2, the retrofit wall had an 18% increase in residual displacement, which can be explained by the relatively low deformations of both walls at this blast. On the other hand, the residual displacement at Blast 5 was decreased by 32%.

The damage sustained by the wall during testing can be compared to the corresponding displacements for that test. The cracks in the shotcrete remained hairline in width until shot 4 (Blast 10, 81.8kPa, 875kPa-ms), where the main crack opened to 1.2mm, which corresponds to Section D of **Figure 5-1**. Due to the fiber pullout at Shot 4, the retrofit wall experienced a large increase in displacement at Shot 5 (Blast 12, 99.1kPa, 1166kPa-ms), resulting in failure.

The retrofit wall failed in a similar manner as the infill retrofit counterpart (RMW-C-N). The main crack formed above the wall midpoint, with the wall breaking into two pieces. The crack was not completely horizontal due to the presence of stronger repair concrete on the backside of the wall. As with the infill retrofit wall, the shotcrete held the blocks together very well. There was some delamination in areas with the repair concrete. In comparison, the control wall was completely demolished, creating many projectiles and debris at failure.

Retrofit Performance – Load Bearing CMU Walls

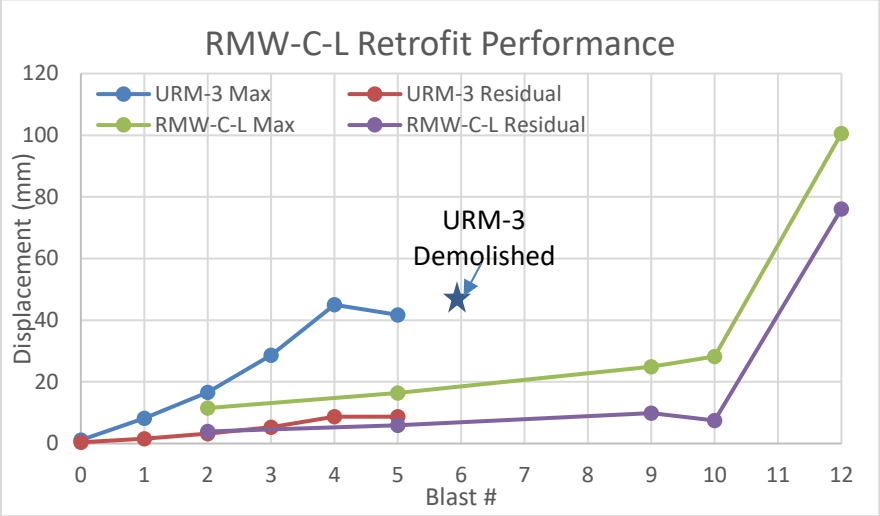

Displacement Time History Comparison

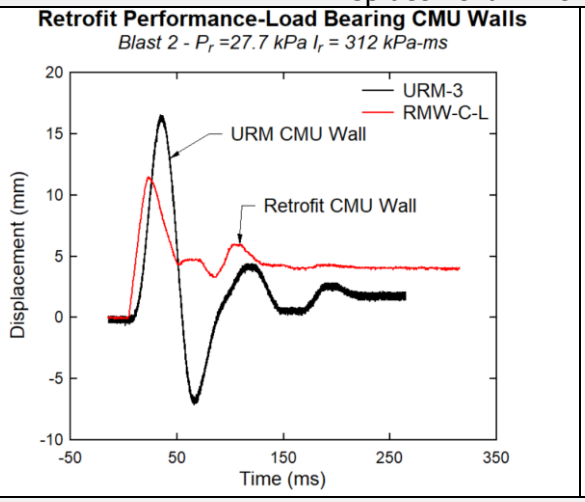

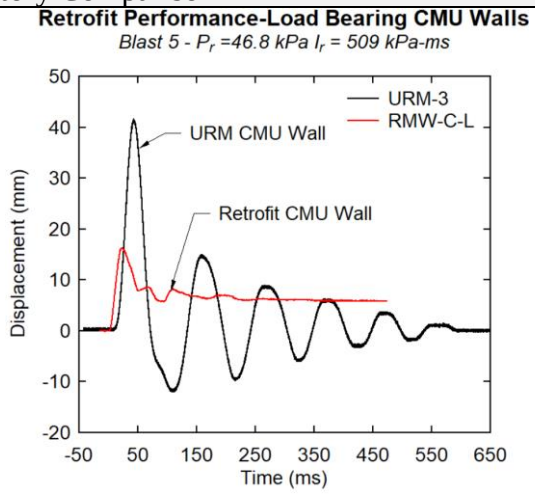

Maximum and Residual Displacements

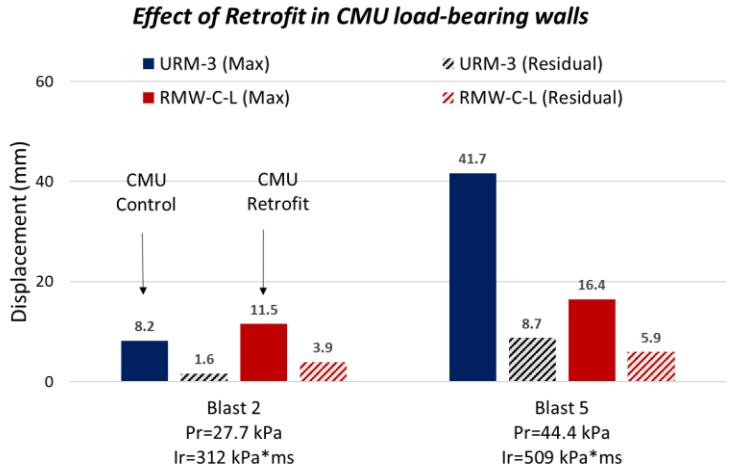

Figure 5-5. Retrofit Performance of CMU Walls (URM-3 data from Ciornei, 2012)

Damage Comparison (Left: Blast 3 (Ciornei, 2012). Right: Blast 2)

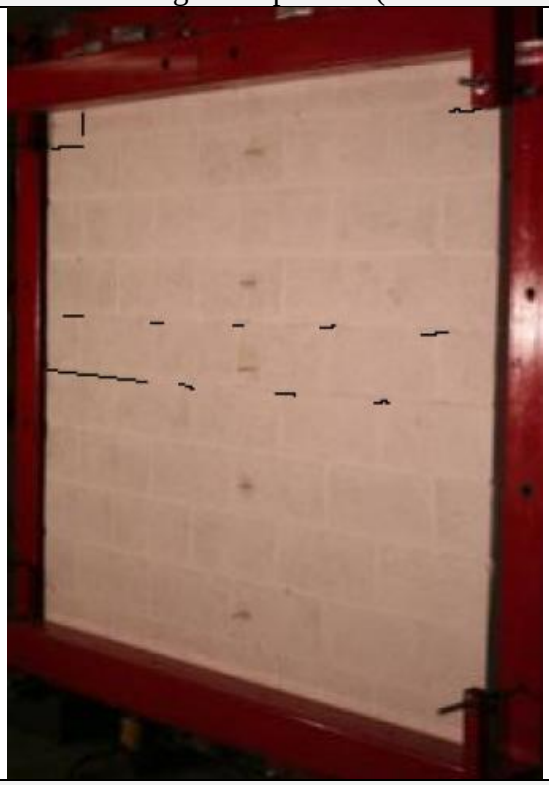

Blast 5 Comparison (Left: Ciornei, 2012)	Retrofit Failure Mode

Figure 5-6. Load Bearing CMU Walls Retrofit Comparison

5.4. STONE SERIES RETROFIT COMPARISON

5.4.1. Infill Walls (URM vs Retrofit)

The effect of the retrofit is examined next by comparing the performance of walls URM-S-N and RMW-S-N. URM-S-N was designed as an unreinforced infill stone masonry wall, with the top gap filled with high strength grout. RMW-S-N was designed to be the same as URM-S-N, save that the shotcrete retrofit system was applied on the tension face of the wall.

Figure 5-7 compares the displacements sustained by the walls over the course of testing and shows selected displacement time history graphs and maximum/residual displacement comparisons. **Figure 5-8** shows photos and video stills of the walls during testing.

URM-S-N was demolished after the second test, at Blast 2 (27.7kPa, 312kPa-ms). The early failure of the stone wall is surprising and may be due to the construction of the specimen. The critical crack followed the near horizontal mortar joint above mid-height of the wall. Since the critical crack was not located at mid-height, the arching resistance could not develop fully, thus decreasing the out-of-plane resistance of the wall. Nevertheless, the results demonstrate the very low out-of-plane blast resistance of infill stone walls. In comparison, the retrofit wall performed much better than the control due to the enhanced moment resistance provided by the FRS and steel mesh. The first shot applied on the retrofit wall corresponded to Blast 2 and resulted in very little damage and deformations; in contrast this blast caused complete failure in the control wall. The retrofit wall survived six tests and failed at the seventh shot, at Blast 14 (113.8kPa, 1177kPa-ms). The maximum and residual displacements of the retrofit wall up to the sixth test (Blast 11, 102.9kPa, 940kPa-ms) are much smaller than that of the control wall during the one blast it resisted due to its higher stiffness and mass.

The shotcrete overlay also decreased the damage sustained on the retrofit wall. The control wall sustained a crack width of 2.5mm after the first shot, whereas the retrofit wall had either no damage or hairline cracks up until the fourth shot (Blast 9, 67.7kPa, 806kPa-ms). At shot 5 (Blast 10, 81.8kPa, 875kPa-ms), the maximum crack width in the shotcrete was 0.7mm (Section C in **Figure 5-1**), increasing to 3mm at shot 6 (Blast 11). As the fibers had pulled out at this point, the wall failed at shot 7 (Blast 14). As the crack widths increase, so does the maximum displacement. Similarly, once the fibers start to pullout the wall experiences a large increase in maximum displacement which ultimately causes failure.

The retrofit also affected failure mode. The control wall was demolished after the second test, creating many projectiles and fragments. In comparison, the retrofit wall failed along a main crack, with very minimal projectiles. The main crack appeared slightly above midpoint of the wall. The shotcrete kept the stone blocks firmly together, preventing complete collapse of the wall. The mesh was almost completely ruptured; all that was left was the horizontal portion of the mesh spanning the crack in multiple places. As seen by the sudden increase in deflection between Blast 10 and 14, the retrofit failure is relatively brittle, though the wall did not deflect as much as its CMU counterpart (RMW-C-N).

Retrofit Performance - Infill Stone Walls

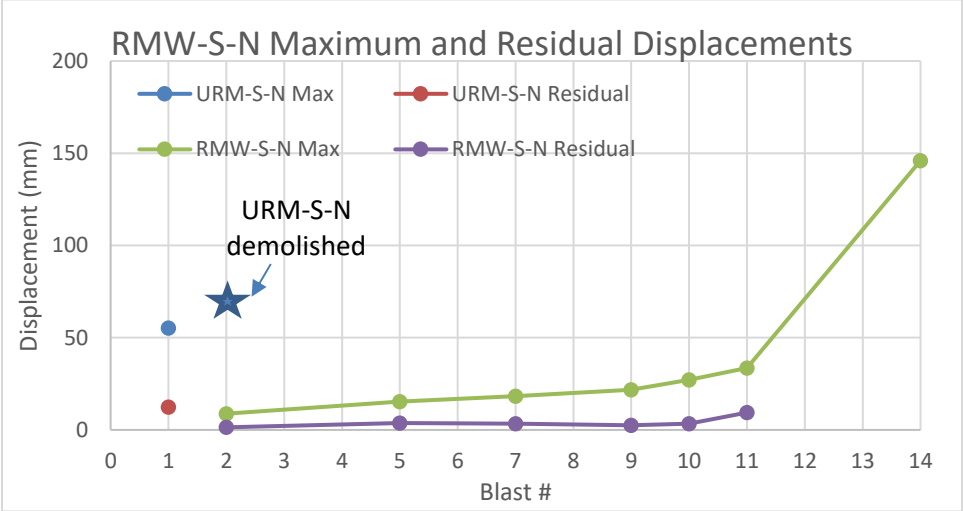

Displacement Time History Comparison

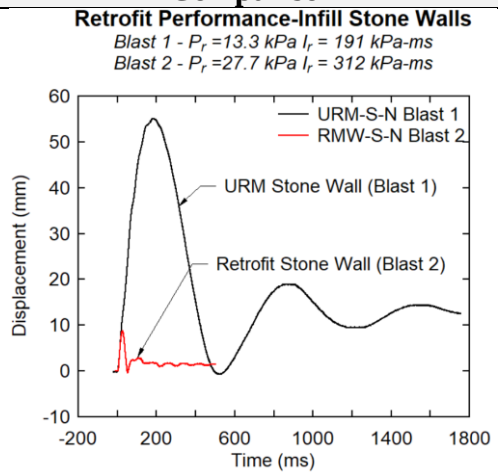

Maximum and Residual Displacements

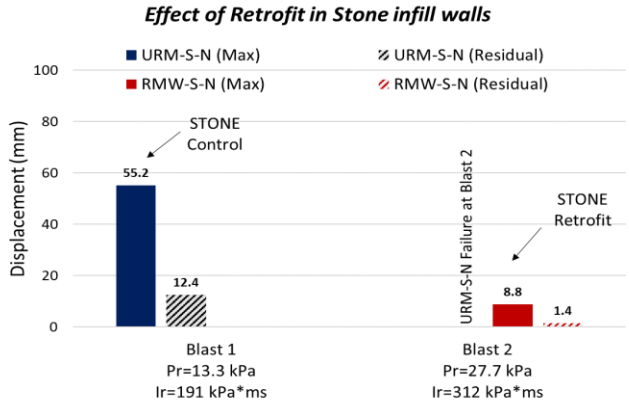

Figure 5-7. Retrofit Performance of Infill Stone Walls

Blast 2 Damage Comparison		Retrofit Failure Mode
		
Failure Mode Video Stills		
		
0ms	72.5ms	222.5ms
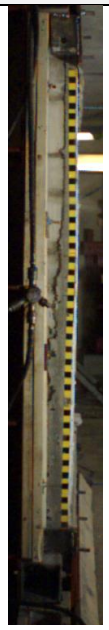	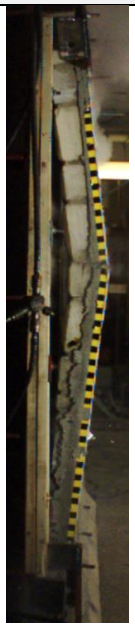	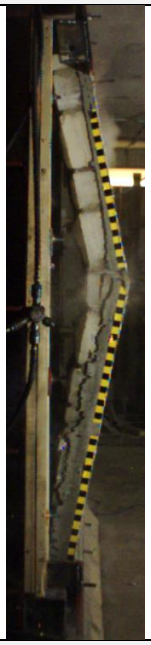
0ms	54.5ms	103.5ms

Figure 5-8. Non-Load Bearing Stone Wall Retrofit Comparison

5.4.2. Load Bearing Walls (URM vs Retrofit)

The effect of the retrofit can also be analyzed by comparing the performance of walls URM-S-L and RMW-S-L. URM-S-L was designed as a load bearing URM stone wall. RMW-S-L was designed to be like URM-S-L, save that the shotcrete retrofit system was applied to the tension face of the wall. The axial load applied to the walls correspond to 4% of the axial capacity, which is 171 kN.

Figure 5-9 compares the displacements sustained by the walls over the course of testing and shows selected displacement time history graphs and maximum/residual displacement comparisons. **Figure 5-10** shows photos and video stills of the walls during testing, as well as displacement profile comparisons.

Continuing the trend observed in the previous series, the use of fiber-reinforced shotcrete and steel mesh resulted in significant enhancements in overall blast capacity. Because of the axial load, wall URM-S-L survived a total of seven tests with failure occurring at the eight shot, at Blast 8 (57.1kPa, 600kPa-ms). The companion retrofit wall failed after eight tests as well, but experienced smaller deflections, and resisted higher blast loads, failing at Blast 14 (113.8kPa, 1177kPa-ms).

The retrofit was also found to reduce the displacements of the wall due to its higher stiffness and mass. At Blast 2 (27.7kPa, 312kPa-ms), 5 (44.4kPa, 509kPa-ms) and 7 (56.4kPa, 620kPa-ms), the retrofit wall reduced maximum displacements by 58%, 63% and 75% respectively. The residual deflections were largely similar between the retrofit and control; the deflections consistently had differences of only ~ 2mm at these blast levels.

The crack widths were much smaller in the retrofit wall as well. Cracks began appearing in the control wall at Blast 3 (34.9kPa, 400kPa-ms). The control wall experienced spalling of mortar over the course of testing, with the maximum crack width was 7mm at the shot before failure. On the other hand, cracking only became apparent in the retrofit at Blast 9 (67.7kPa, 806kPa-ms). Additionally, the cracks in the shotcrete remained hairline in width until failure, indicating that the shotcrete was in the hardening stage (Section B in **Figure 5-1**) until failure.

The control wall was completely demolished at failure, creating many projectiles and fragments. On the other hand, the retrofit wall failed with a main crack forming in the shotcrete at wall mid-height. Unlike all the other retrofit walls, the main crack did not completely separate the top and bottom wall sections; the steel mesh was not ruptured, and the microfibers were still spanning the crack (although some of the fibers were partially pulled out). The enhanced ductility can be explained by the combined effects of increased steel mesh area and axial load in this retrofit specimen.

Retrofit Performance – Load Bearing Stone Walls

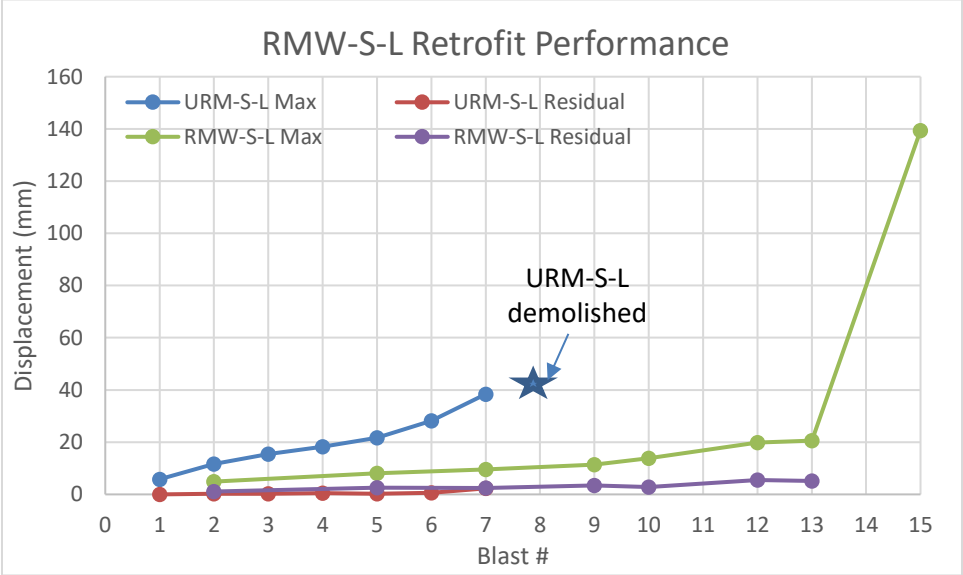

Displacement Time History Comparison

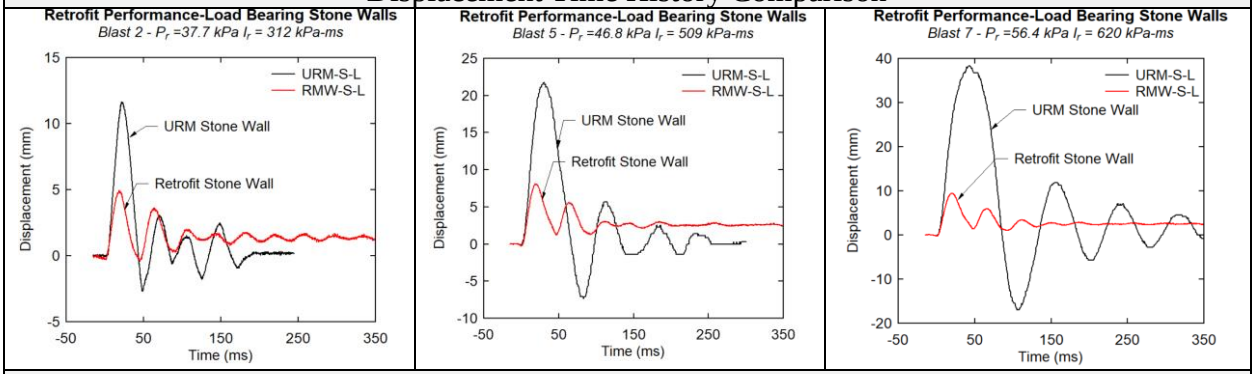

Maximum and Residual Displacements

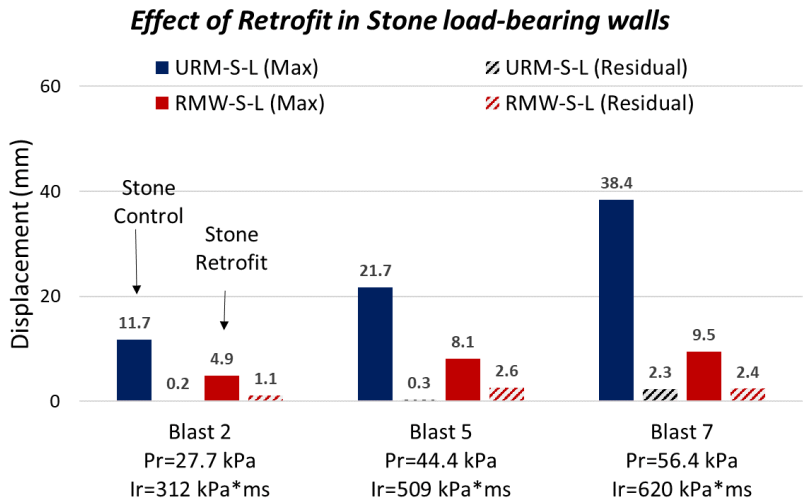

Figure 5-9. Retrofit Performance of Load Bearing Stone Walls

URM-S-L (Blast 8, left) vs RMW-S-L (Blast 7, right)		Retrofit Failure Blast 15
		
Failure Mode Video Stills		**Displacement Profile Comparisons**
	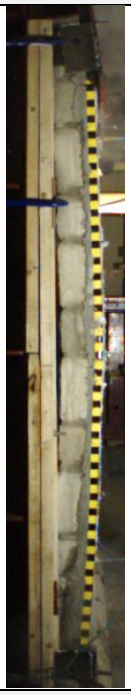	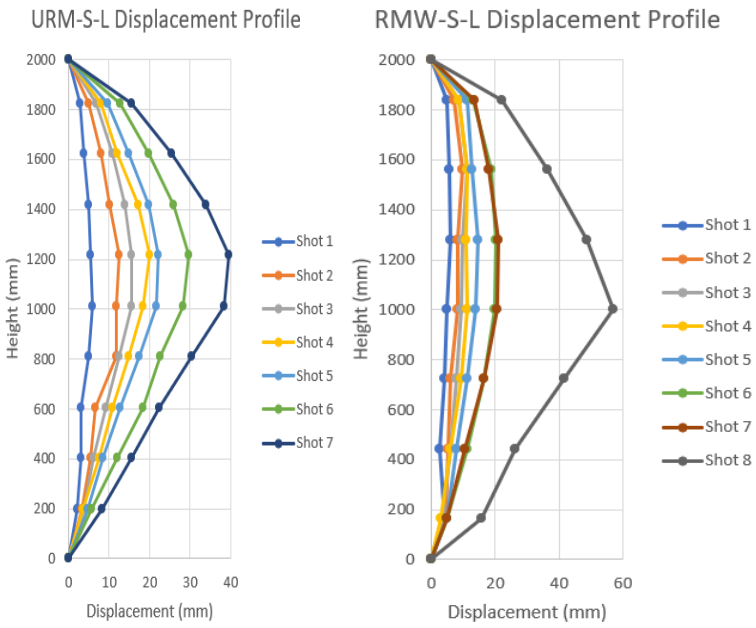
240.5ms	33ms	

Figure 5-10. Load Bearing Stone Wall Retrofit Comparison

5.5. EFFECT OF AXIAL LOAD – CONTROL WALLS

5.5.1. CMU Control Walls (Infill vs Load Bearing)

This section provides a summary of the comparison drawn by Ciornei (2012) between walls URM-1 and URM-3 to determine the effect of axial load. Wall URM-1 was designed as an infill wall and was tested without axial load, with the top edge gap between the wall and the supporting steel frame reduced to 6 mm using structural steel filler. Load-bearing wall, URM-3 was constructed with no top edge gap. The axial load was 123 kN, representing 10% of the wall capacity.

Figure 5-11 compares the displacements sustained by the walls over the course of testing and shows selected displacement time history graphs and maximum/residual displacement comparisons as reported by Ciornei (2012). **Figure 5-12** shows photos of the walls during testing (Ciornei, 2012).

The results show that the application of axial load affected the blast capacity of the walls. It was found that the "increase in capacity [of the load bearing wall] is due to the presence of axial loading that added to the sectional moment capacity as well as arching action" (Ciornei, 2012). Additionally, the axial load resulted in better control of mid-span displacements. As shown in **Figure 5-11**, the maximum and residual deflections are smaller for the load-bearing wall when compared to the companion infill wall. The failure mode was similar for both walls, with "formation of a hinge at mid-height of the wall, followed by the opening of the middle mortar bed joint, sequentially followed by the other mortar bed joints" (Ciornei, 2012).

Effect of Axial Load - CMU series URM Walls

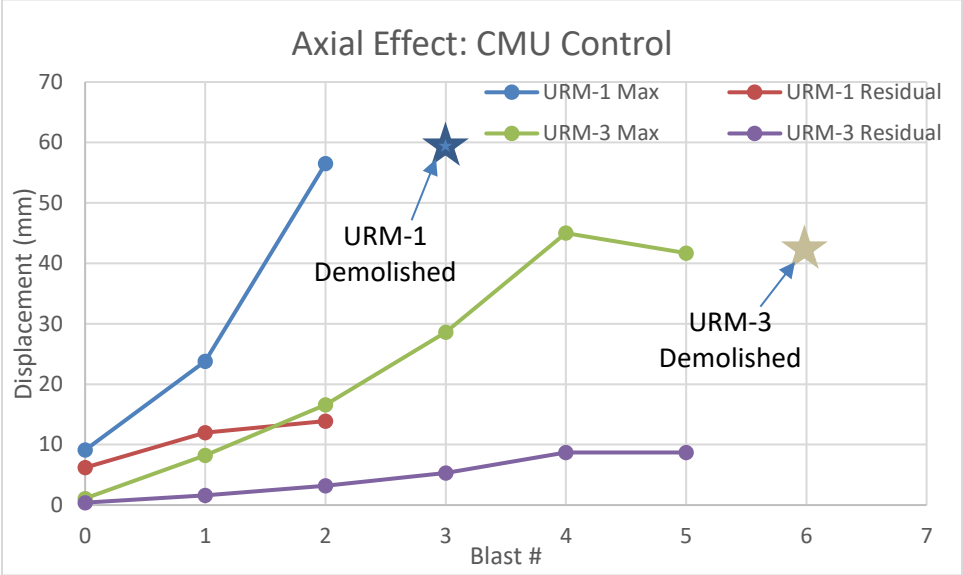

Displacement Time History Comparison

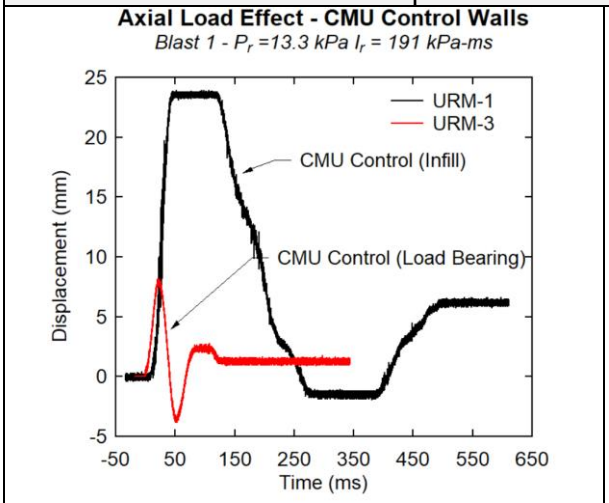

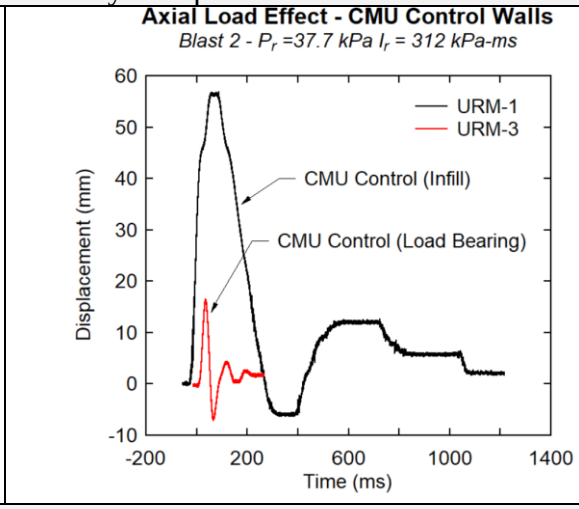

Maximum and Residual Displacements

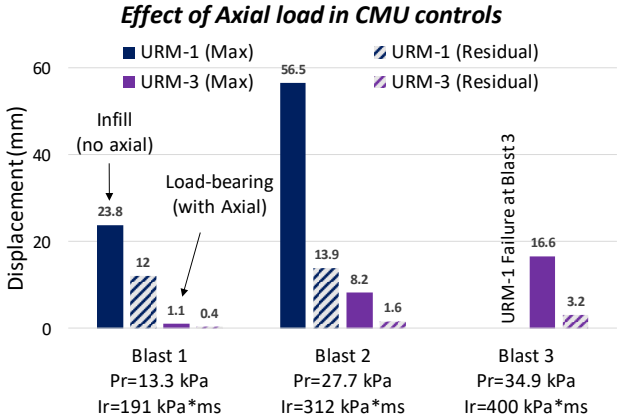

Figure 5-11. Axial Effect on CMU Control Walls (data from Ciornei, 2012)

URM-1 (Ciornei, 2012)		
Blast 1	Blast 2	Blast 3
		
URM-3 (Ciornei, 2012)		
Blast 3	Blast 4	Blast 6
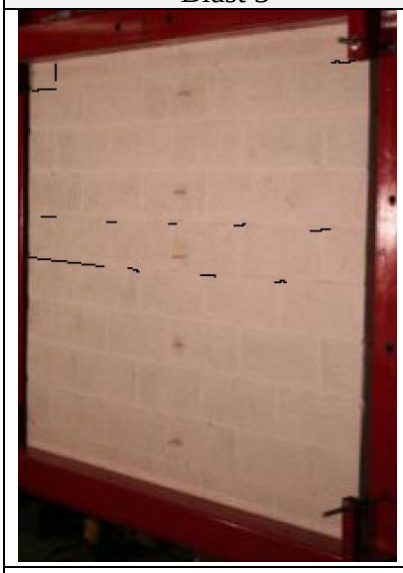	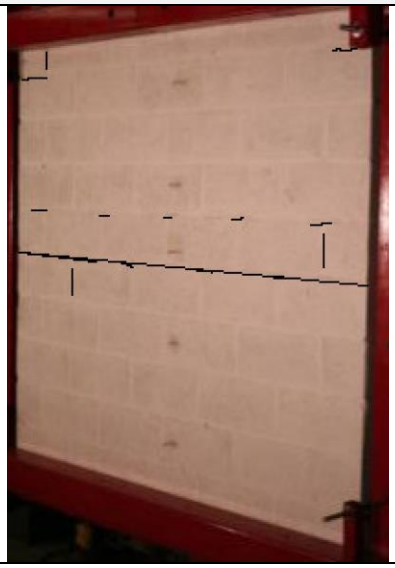	

Figure 5-12. URM-1 and URM-3 Axial Effect Comparisons

5.5.2. Stone Control Walls (Infill vs Load Bearing)

The effect of axial load can also be examined in the stone series URM walls by comparing the performance of walls URM-S-N and URM-S-L. Both walls were constructed in the same manner, with the top edge filled with high-strength mortar. The axial load level in wall URM-S-L corresponded to approximately 4% P_o (171kN), while wall URM-S-N was tested as an infill wall.

Figure 5-13 compares the displacements over the course of testing and shows selected displacement time history graphs. The figure also compares the maximum and residual displacements at select blasts. **Figure 5-14** shows photos and video stills of the walls during testing.

A study of the results show that the axial load increased the blast capacity of the stone masonry walls due to the presence of significant arching action. The non-load bearing infill stone wall (URM-S-N) was demolished at the second test at Blast 2 (27.7kPa, 312kPa-ms). In comparison, the load bearing control (URM-S-L) was demolished after eight tests at Blast 8 (57.1kPa, 600kPa-ms), representing a 92% increase in failure impulse. Examining the limited displacement data available for this set, it can be seen that the maximum and residual displacements of wall URM-S-L were significantly reduced when compared to URM-S-N at Blast 1 (13.7kPa, 191kPa-ms) due to the enhanced rigidity caused by axial loading (reductions of 89% and 100% in d_{max} and d_{res}, respectively).

While the failure mode of both walls was similar, cracking at earlier blast levels was better controlled in wall URM-S-L which had axial load. The first cracks appeared immediately in the stone infill wall (URM-S-N) and had a width of 2.5mm after the second shot. In comparison, cracks remained hairline in width during the first two shots in the load-bearing wall due to its smaller residual displacements. The next three shots produced cracks widths of 0.1, 0.4 and 0.7mm in wall URM-S-L. The wall experienced gradual spalling of the mortar during the next two blasts, then was demolished. The increase in crack widths in consistent with the increase of maximum displacements. The failure mode for both walls was identical with the complete collapse of the walls and the formation of significant blast fragments.

Effect of Axial Load - Stone series URM Walls

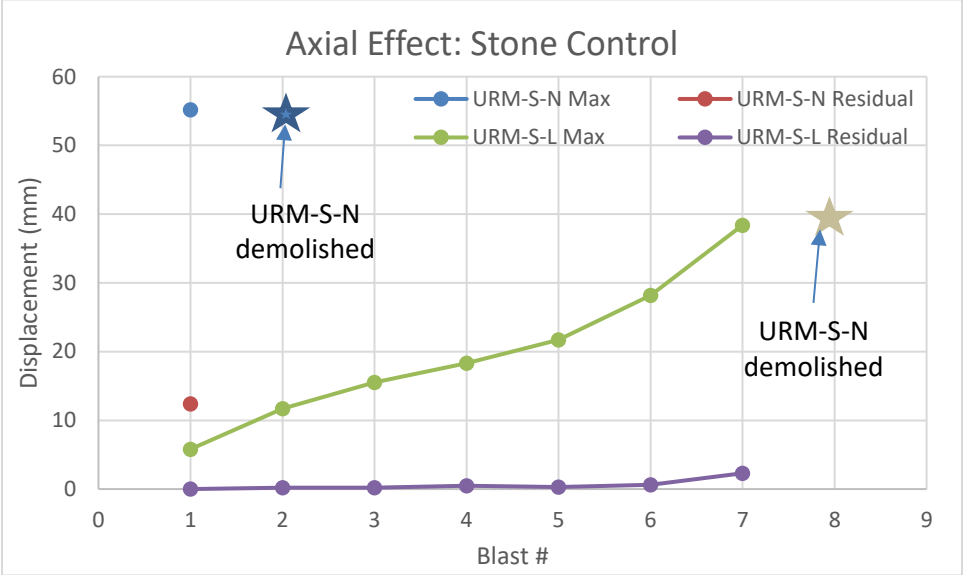

Displacement Time History Comparison	Maximum and Residual Displacements

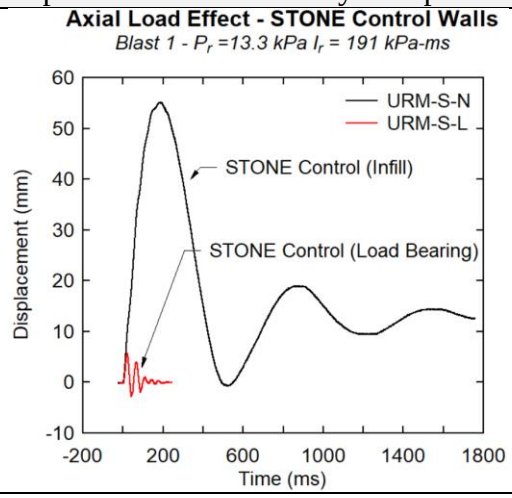

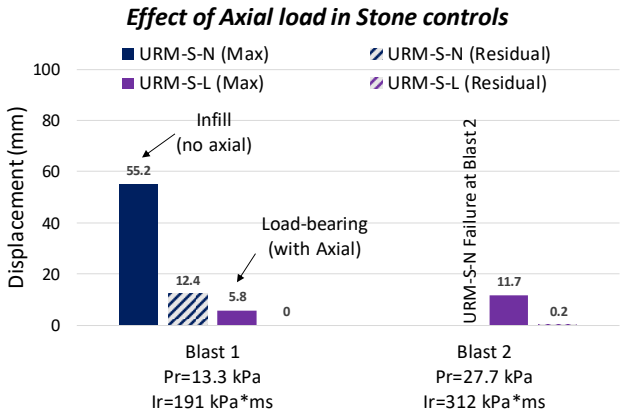

Figure 5-13. Axial Effect on Stone Control Walls

Blast 1 Damage Comparison (Left: Infill. Right: Load Bearing)					
					
Failure Mode: URM-S-N			Failure Mode: URM-S-L		
					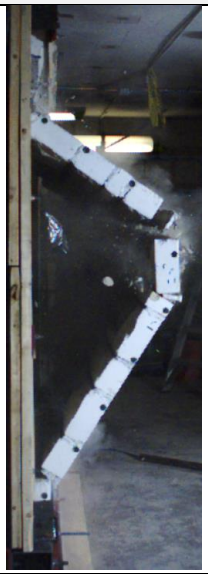
0ms	72.5ms	222.5ms	0ms	63.5ms	240.5ms
					
222.5ms			222.5ms		

Figure 5-14. URM-S-N and URM-S-L Axial Effect Comparisons

5.6. EFFECT OF AXIAL LOAD – RETROFIT WALLS

5.6.1. CMU Retrofit Walls (Infill vs Load Bearing)

As demonstrated in the previous section, the application of axial load affected the performance of the control CMU walls. The effect of this parameter in the retrofit CMU walls is examined by comparing the performance of walls RMW-C-L and RMW-C-N, which were tested with and without axial load, respectively. It is noted that the top edge gap was completely filled with high-strength grout in both walls, with the axial load kept at 10% of P_o (146 kN) in wall RMW-C-L.

The performance of the two retrofit CMU walls can be examined in **Figure 5-15** which compares the displacements sustained by the walls over the course of testing and at select blasts. **Figure 5-16** shows photos and video stills of the walls during testing.

Interestingly, the applied axial load on the retrofit walls did not change the maximum and residual displacements significantly. This may be due to the damage sustained by RMW-C-L during installation. The damaged wall may have experienced premature crushing of the CMU blocks, which would leave the retrofit as the governing condition to control displacements. The displacements are largely similar up until Blast 9 (67.7kPa, 806kPa-ms). However, the axial load increased blast capacity and delayed failure due to significant arching action, with failure in infill wall RMW-C-N at Blast 10 (81.8kPa, 875kPa-ms) and failure in load bearing wall RMW-C-L at Blast 12 (99.1kPa, 1166kPa-ms).

The axial load also reduced crack widths and damage in the shotcrete layer. Examining the high-speed videos, it is apparent that the cracks in wall RMW-C-L widen as the wall deflects, but then close as the wall returns back to its residual position. This can explain the reduced crack widths in wall RMW-C-L when compared to wall RMW-C-N. For example, at Blast 10, the load bearing wall had a maximum crack width of 1.2mm, while the crack reached 4mm in the infill wall (both walls experienced fiber pullout at this stage, Section D in **Figure 5-1**).

The mode of failure in the walls was similar. Both walls failed with the formation of a main horizontal crack, with complete fiber pullout and rupture of the steel mesh. Nonetheless, failure in wall RMW-C-L was delayed to Blast 12 instead of Blast 10. Moreover, while the steel mesh failed in both walls, the mesh did not completely sever across the crack in wall RMW-C-L. However, the load-bearing wall experienced greater spalling of concrete blocks at the top of the wall, which may have been caused by the axial load or by the damage sustained by the wall during transfer (i.e. test setup). Wall RMW-C-L also experienced its failure crack higher than mid-height, which can significantly decrease its out-of-plane resistance.

Effect of Axial Load – Retrofit CMU Walls

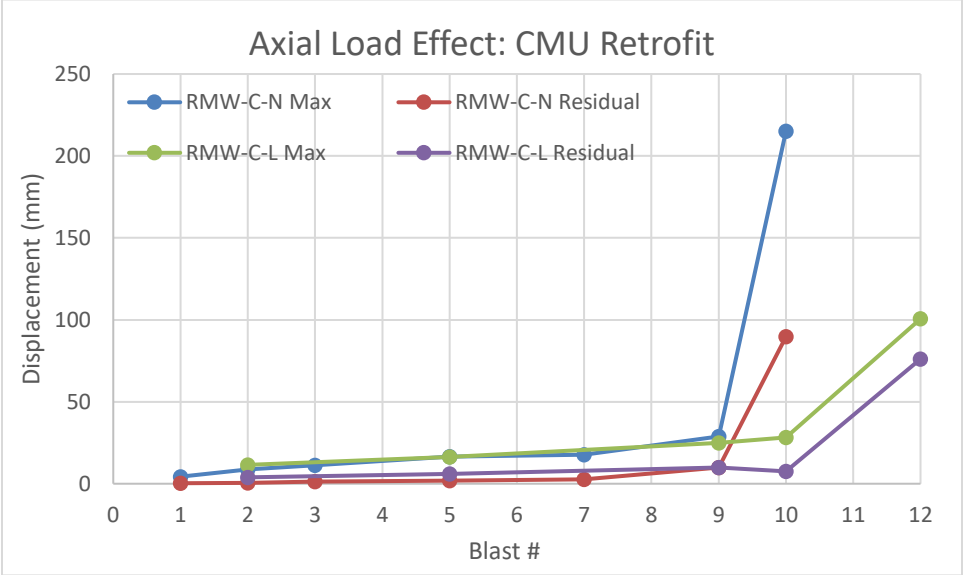

Displacement Time History Comparison

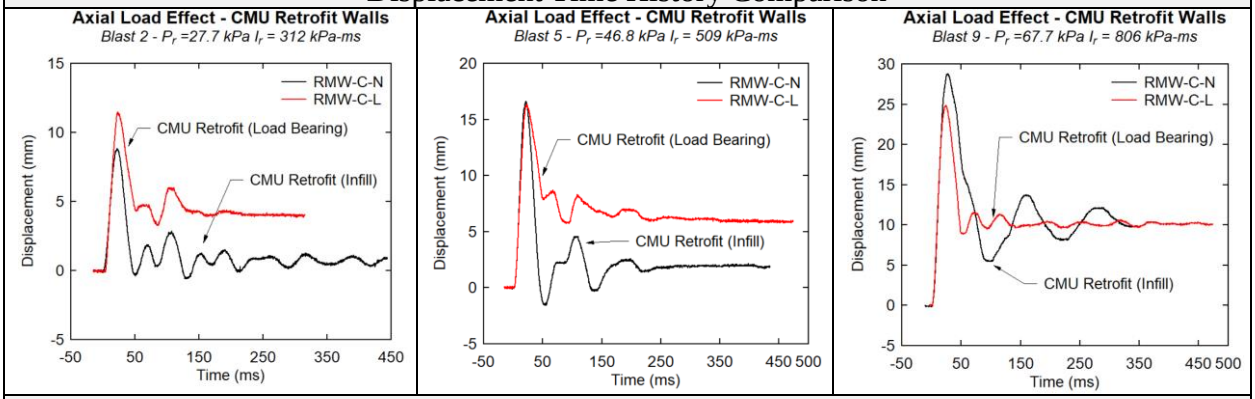

Maximum and Residual Displacements

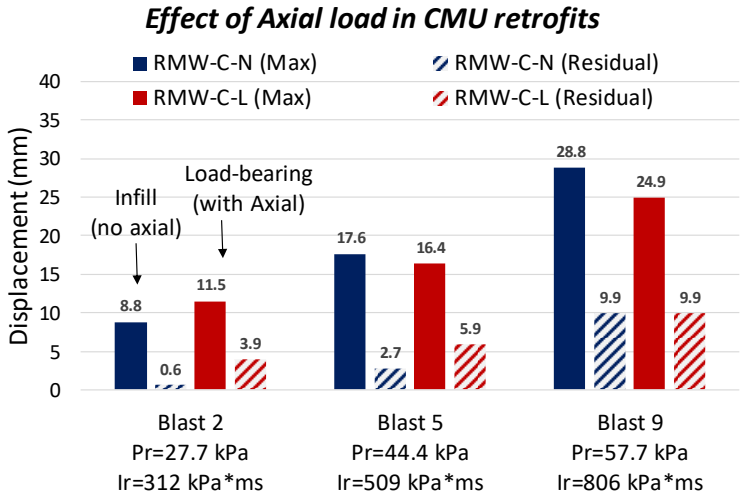

Figure 5-15. Effect of Axial Load in Retrofit CMU Walls

RMW-C-N		
Blast 5	Blast 9	Blast 10
		
RMW-C-L		
Blast 9	Blast 10	Blast 12
		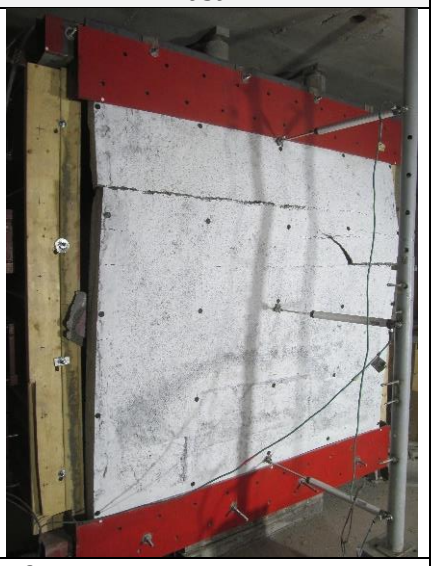

Figure 5-16. Axial Effect on CMU Retrofit Walls

5.6.2. Stone Retrofit Walls (Infill vs Load Bearing)

As demonstrated in the previous section, the application of axial load significantly affected the performance of the control URM stone walls. The effect of axial load in the stone series can also be studied by comparing the performance of retrofit walls RMW-S-N and RMW-S-L. Both walls were built with stone masonry and retrofitted with shotcrete in the same manner but were tested as infill and load-bearing walls (4% P_o, 171kN), respectively.

Figure 5-17 compares the displacements over the course of testing, shows selected displacement time history graphs, and compares the maximum and residual displacements at select blasts. **Figure 5-18** shows photos and video stills of the walls during testing.

The axial load significantly increased the capacity of the wall through arching action. The infill stone retrofit wall failed after seven tests, at Blast 14 (113.8kPa, 1177kPa-ms), while the load bearing stone retrofit wall failed after eight tests at Blast 15 (109.9kPa, 1735kPa-ms). The axial load helped delay the failure of the wall by one test, although the increase in blast impulse is quite significant. Furthermore, the application of axial load affected control of mid-span displacements by increasing the rigidity of the wall. Wall RMW-S-L shows maximum displacements which are consistently lower when compared to wall RMW-S-N, which was tested without axial load. A study of the data from Blasts 2 to 10 shows that d_{max} was decreased by 44% (Blast 2, 27.7kPa, 312kPa-ms), 47% (Blast 5, 46.8kPa, 509kPa-ms), 48% (Blast 7, 56.4kPa, 620kPa-ms), 48% (Blast 9, 67.7kPa, 806kPa-ms) and 49% (Blast 10, 81.8kPa, 875kPa-ms). The non-load bearing wall was then subjected to Blast 11 (91kPa driver pressure), and the load bearing wall was subjected to Blast 12 (100kPa driver pressure). The cause for the lower driver pressure in Blast 11 was the premature rupture of the aluminum foils in the shock-tube when testing the infill wall. The average reflected properties for Blast 11 are P_r =102.9kPa and I_r = 940kPa-ms, and the average properties for Blast 12 are P_r = 99.1kPa and I_r =1166kPa-ms. Even though Blast 12 has a relatively higher impulse than Blast 11, the load bearing wall still performed better than the infill companion, with a 41% decrease in maximum displacement. The applied load did not affect the residual displacements noticeably.

The load bearing wall also exhibited less damage than the infill wall. The first cracking in walls RMW-S-N and RMW-S-L occurred during the third and fourth shots, respectively. For the infill wall, the next two shots produced crack widths of 0.7 (softening) and 3mm (fiber pullout) in the shotcrete, then failure. In contrast, the load bearing wall had only hairline cracks (hardening, section B in **Figure 5-1**) in its overlay throughout testing, with the exception of the final blast which caused the crack width to grow to 7mm in width due to fiber pullout. A study of the steel mesh strain data also shows that strains in the load bearing wall remained consistently lower when compared to those in the companion infill wall (see Chapter 4, **Table 4-3**).

Both walls failed along a main crack at mid-height, however the failure in the infill wall was much more serious; the crack went completely through the shotcrete layer and almost severed all bars in the steel mesh. The failure in the load bearing wall consisted of a 7mm crack, with the microfibers still spanning the crack. The mesh did not rupture, leading to a relatively more ductile failure.

Effect of Axial Load – Retrofit Stone Walls

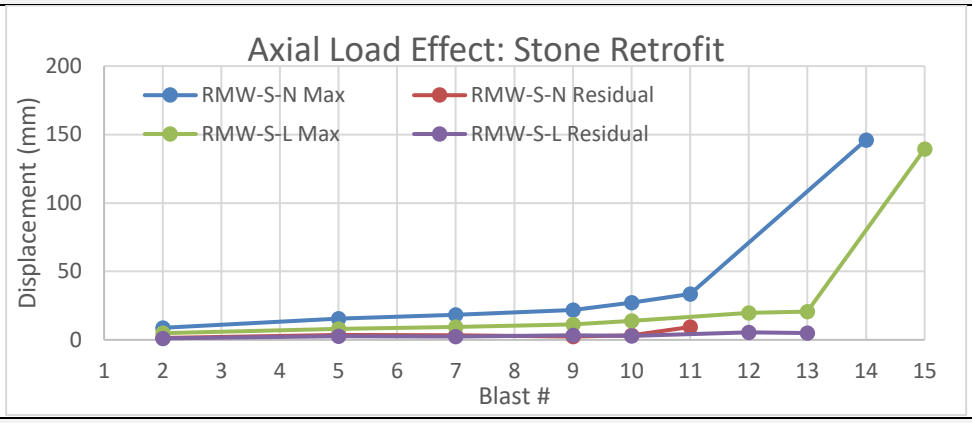

Displacement Time History Comparison

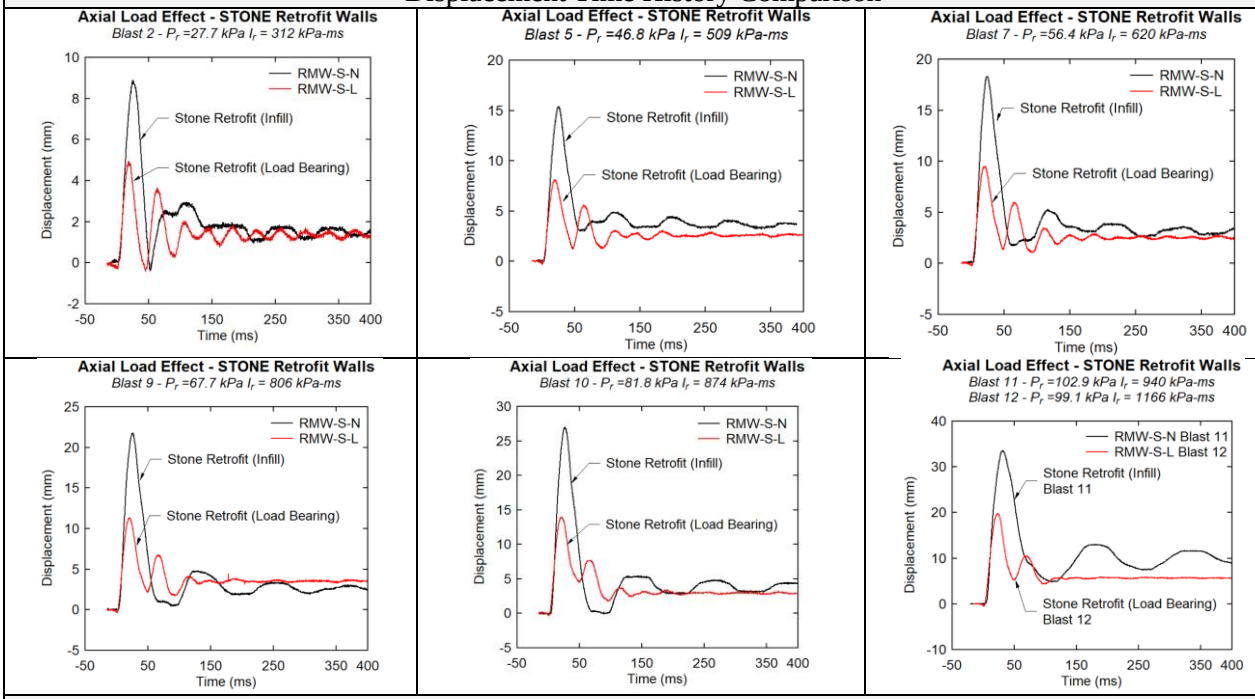

Maximum and Residual Displacements

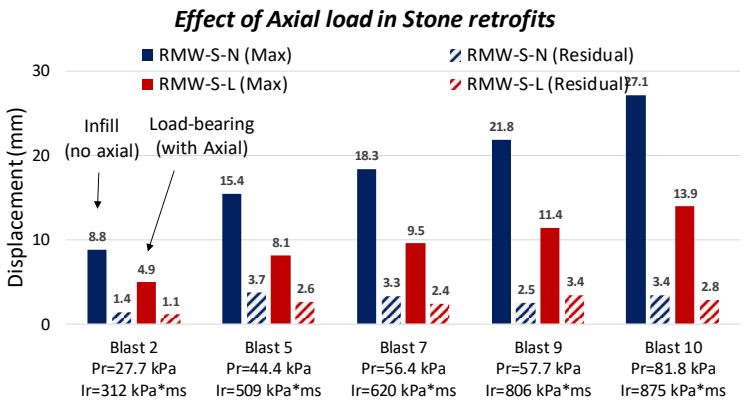

Figure 5-17. Effect of Axial Load in Retrofit STONE Walls

Infill (Blast 13, left) vs Load Bearing (Blast 14, right)	RMW-S-L Failure Blast 15
	

Failure Mode Video Stills		Displacement Profile Comparisons
	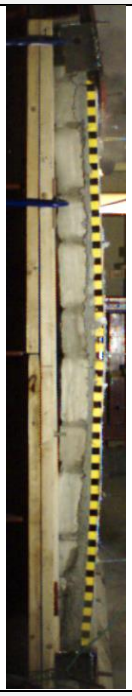	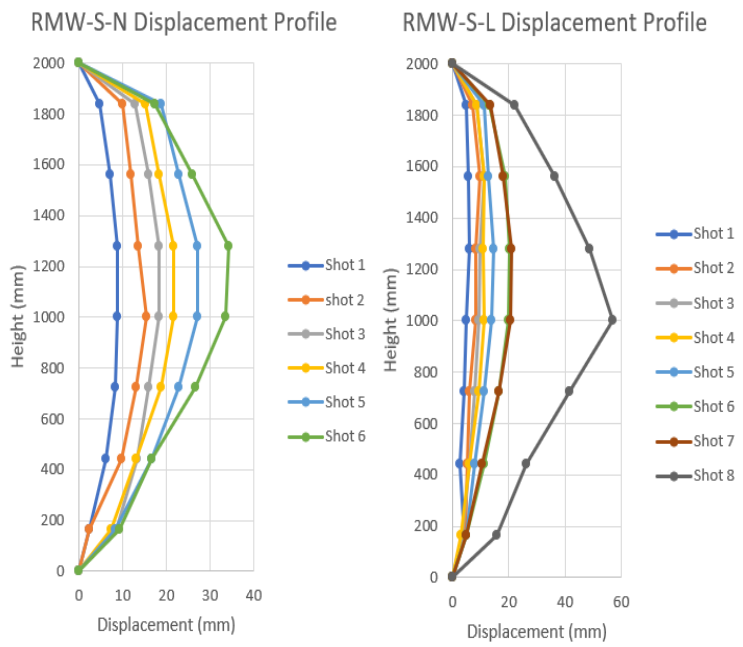
Infill @ 241ms	Load @ 33ms	

Figure 5-18. Axial Effect on Stone Retrofit Walls

5.7. EFFECT OF MASONRY TYPE-URM WALLS

5.7.1. Infill URM Walls (CMU vs STONE)

The effect of masonry type on the non-load bearing (infill) unreinforced masonry walls can be analysed by comparing the performance of walls URM-1 (tested by Ciornei, 2012) and URM-S-N. URM-1 was built as a CMU infill wall with a 6mm gap at the top. URM-S-N was built as a stone infill wall, but the gap was filled with high strength grout.

Figure 5-19 compares the displacements sustained by the walls over the course of testing and shows select displacement time histories and comparisons of displacements at equivalent blasts. **Figure 5-20** compares photos and video stills of the walls during testing.

The CMU infill wall performed better than the stone infill wall, resisting more tests and higher blast loads. The CMU infill wall failed after four shots at Blast 3 (34.9kPa, 400kPa-ms), while the stone infill wall failed after two shots, at Blast 2 (27.7kPa, 312kPa-ms). The low blast capacity of the stone wall may have been caused by the construction and pattern of the blocks which led to the creation of the critical crack above mid-height of the wall. In addition to showing increased blast capacity and delaying failure, the CMU infill wall showed a 57% reduction in maximum displacements at Blast 1 (13.7kPa, 191kPa-ms), despite having less mass than the stone wall. Both walls were completely demolished at failure.

Effect of Masonry Type - Infill URM Walls

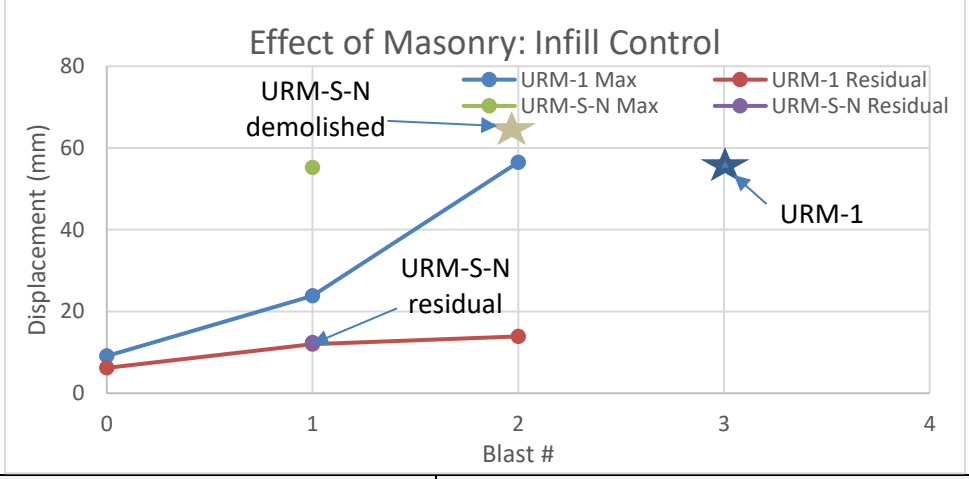

Displacement Time History Comparison

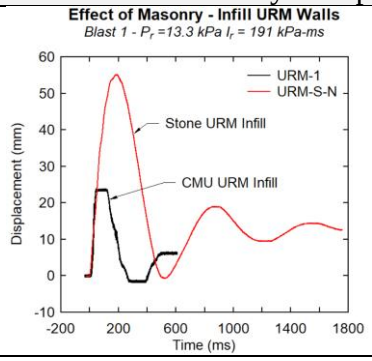

Maximum and Residual Displacements

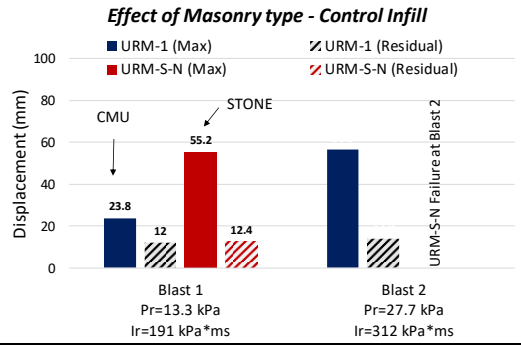

Figure 5-19. Effect of Masonry for Infill URM Walls (URM-1 data from Ciornei, 2012)

URM-1 (Ciornei, 2012)		
Blast 1	Blast 2	Blast 3
		
URM-S-N		
Blast 1	Blast 2	
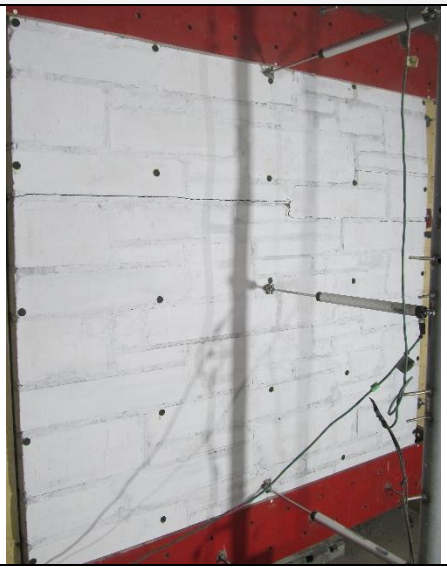		

Figure 5-20. URM-1 (Ciornei, 2012) and URM-S-N Effect of Masonry Type Comparisons

5.7.2. Load Bearing URM Walls (CMU vs STONE)

The effect of masonry type in the load-bearing control unreinforced masonry walls can be examined by comparing the results for walls URM-3 and URM-S-L which were designed with CMU and stone blocks respectively. It is noted that while both walls were tested under axial loading, the axial load level was different: 10% P_o (122 kN) for URM-3 vs. 4% P_o (171 kN) for URM-S-L.

Figure 5-21 compares the displacements sustained by the walls over the course of testing and shows select displacement time histories and comparisons of maximum and residual displacements at equivalent blasts. **Figure 5-22** shows photos and video stills of the walls during testing.

Unlike the infill series, the control stone wall in the load bearing series performed much better than the CMU wall in every aspect. The stone blocks may have performed better than the CMU blocks due to their higher mass and superior axial capacity and thus improved arching resistance. The axial load applied to the stone wall was also higher than the load applied to the CMU wall; thus the stone wall would experience a higher degree of rigidity due to compression. The CMU wall in this set survived six shots and was demolished at Blast 6 (46.5kPa, 574kPa-ms). The stone wall survived seven shots and failed at Blast 8 (57.1kPa, 600kPa-ms), representing a moderate increase in blast capacity. Likewise, the maximum and residual displacements were smaller for the stone wall throughout testing. The use of stone blocks reduced maximum deflections by 29%, 30%, 46%, 59%, 48% at Blasts 1 (13.7kPa, 191 kPa-ms), 2 (27.7kPa, 312 kPa-ms), 3 (34.9kPa, 400 kPa-ms), 4 (39.5kPa, 427 kPa-ms), and 5 (46.8kPa, 509 kPa-ms), respectively. The residual deflections were also decreased in the stone wall by 100%, 94%, 96%, 94% and 97% at these same blasts. Nonetheless, the masonry type did not affect the failure mode; both walls were completely demolished at failure.

Effect of Masonry Type - Load Bearing Non-Retrofit Walls

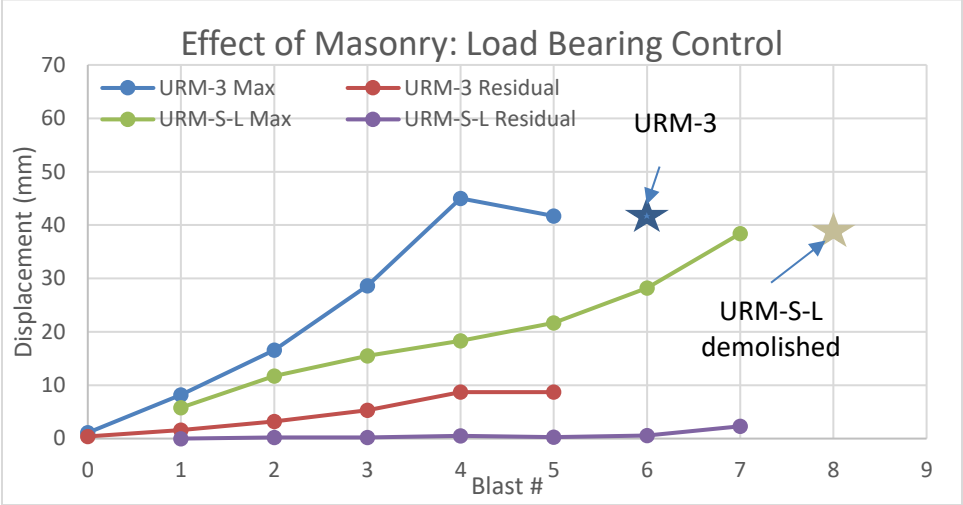

Displacement Time History Comparison

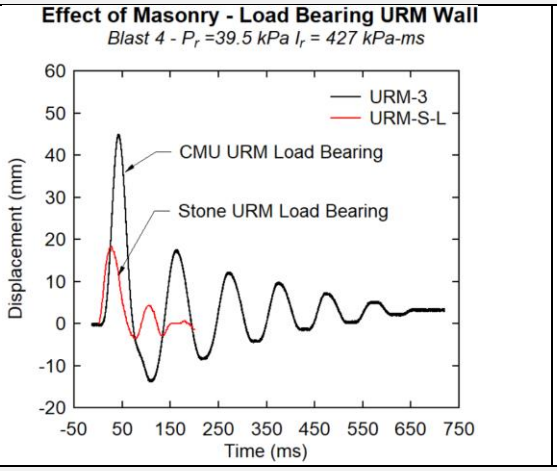

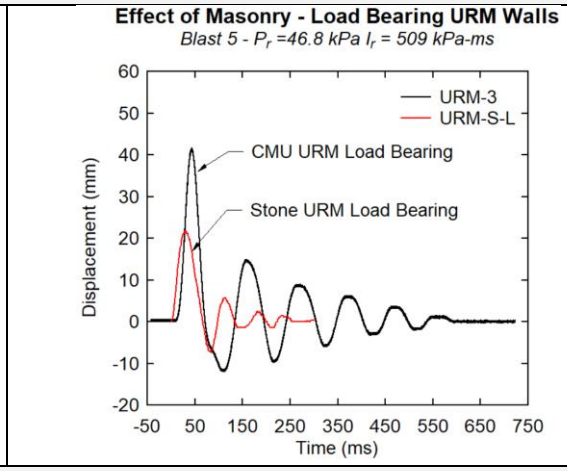

Maximum and Residual Displacements

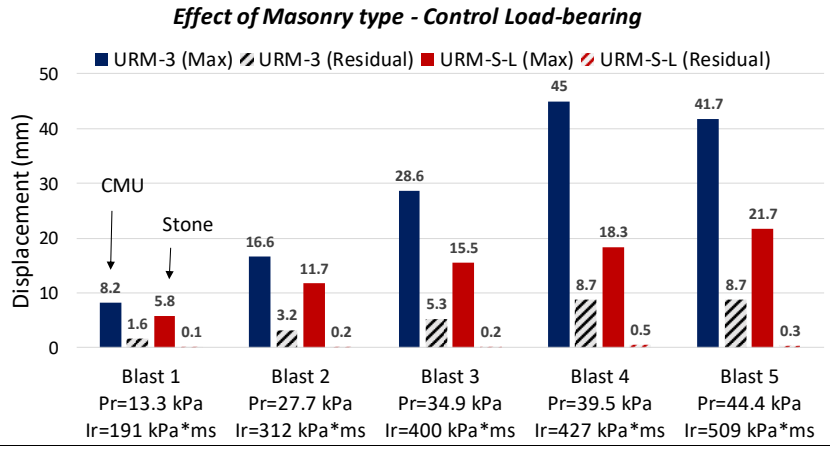

Figure 5-21. Effect of Masonry for Infill URM Walls (URM-3 data from Ciornei, 2012)

URM-3 (Ciornei, 2012)		
Blast 3	Blast 4	Blast 6
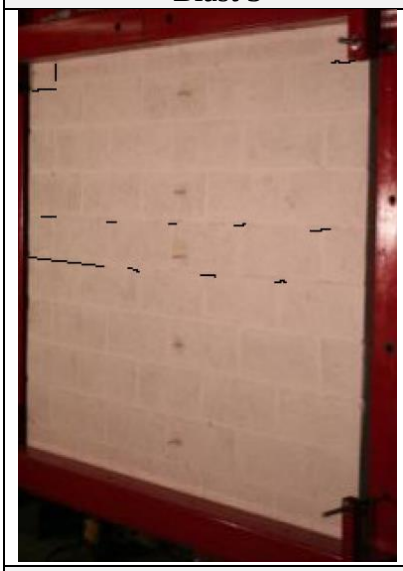	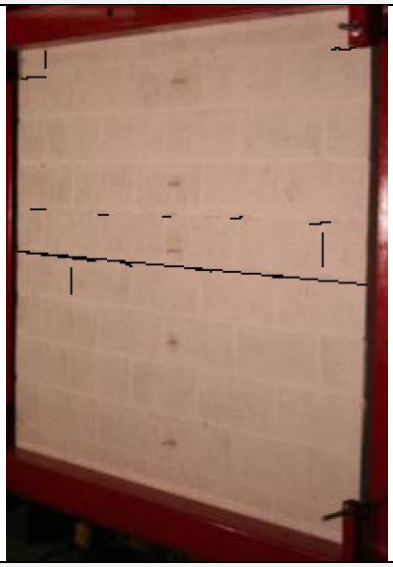	
URM-S-L		
Blast 4	Blast 6	Blast 8
		

Figure 5-22. URM-3 and URM-S-L Axial Effect Comparisons

5.8. EFFECT OF MASONRY TYPE - RETROFIT WALLS

5.8.1. Infill Retrofit Walls (CMU vs STONE)

The effect of masonry type in the retrofit series is first examined by comparing the performance of infill walls RMW-C-N and RMW-S-N. RMW-C-N was built with CMU blocks, with the top gap filled with high strength grout. RMW-S-N was built with stone blocks, also with the top gap filled with high strength grout. Both walls were retrofit with the shotcrete system, but RMW-C-N had gage 6 wire mesh while RMW-S-N had gage 2 wire mesh.

Figure 5-23 compares the displacements in the walls over the course of testing and shows selected displacement time histories and displacement comparisons. **Figure 5-24** compares photos of the walls during testing.

When comparing the mid-span displacements, there appears to be no significant difference in the performance of the walls until Blast 9 (67.7kPa, 806kPa-ms). The reason that responses of both walls were similar may be because the shotcrete overlay is the controlling factor for these walls tested despite the higher mass of the stone wall. At Blast 9, the stone wall shows reductions of 24% and 75% in maximum and residual displacements, respectively. Failure of the CMU retrofit wall would occur at the next shot (Blast 10, 81.8kPa, 875kPa-ms), while the companion with stone blocks survives two more shots, with failure occurring at Blast 14 (113.8kPa, 1177kPa-ms). The stone wall had a higher out-of-plane resistance than the CMU wall likely due to the enhanced arching resistance of the stones due to their higher axial capacity.

Cracking in the shotcrete appeared earlier and at lower blast magnitudes for the CMU wall than for the stone wall. The shotcrete layer in the CMU wall experienced hairline cracks starting at Blast 2 (27.7kPa, 312kPa-ms), which grew to 0.3mm at Blast 7 (56.4kPa, 620kPa-ms) which indicates activation of the fibers in the shotcrete (section B in **Figure 5-1**). The crack grew to 4mm at Blast 9 (67.7kPa, 806kPa-ms) which corresponds to nearly complete fiber pullout. The next shot failed the CMU wall. In comparison, the shotcrete in the stone wall first experienced hairline cracks at Blast 7, which grew to 0.7mm at Blast 10 (81.8kPa, 875kPa-ms) which corresponds to the softening and partial fiber pullout (section C in **Figure 5-1**). The next shot opened the cracks to 3mm at Blast 11 (102.9kPa, 940kPa-ms) which indicates nearly complete fiber pullout. The stone wall failed at the next shot.

Both walls show similar failure modes, however the steel mesh did not completely rupture in the stone wall while it did for the CMU wall. This can be explained by the increased steel mesh area used in the stone retrofit wall.

Effect of Masonry - Infill Retrofit Walls

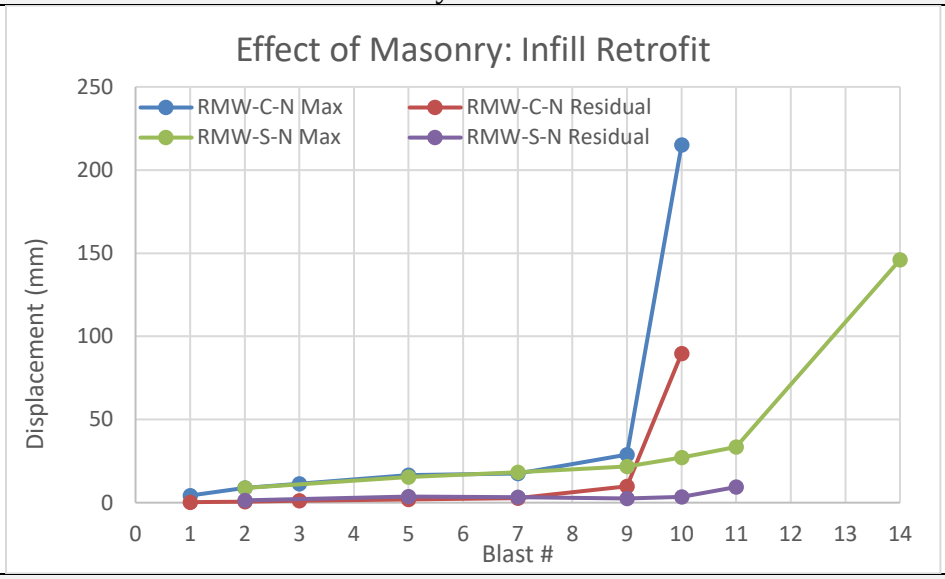

Displacement Time History Comparison

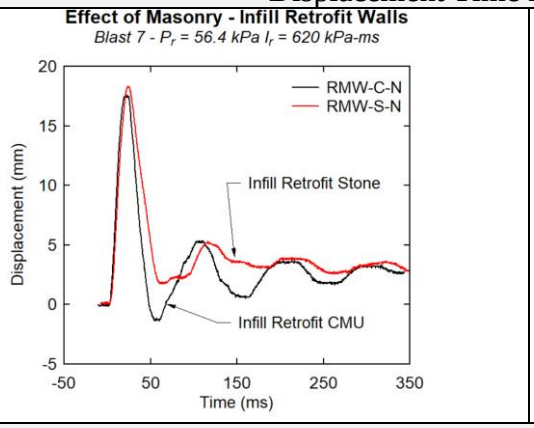

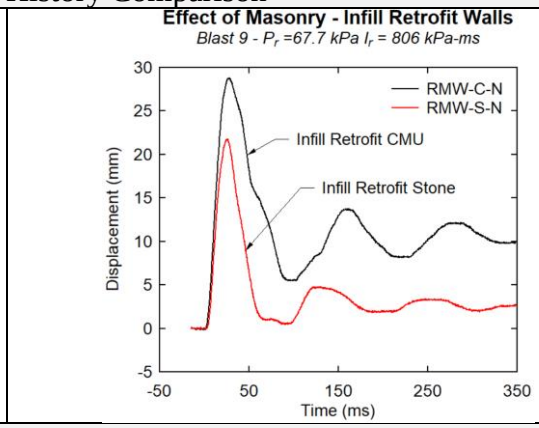

Maximum and Residual Displacements

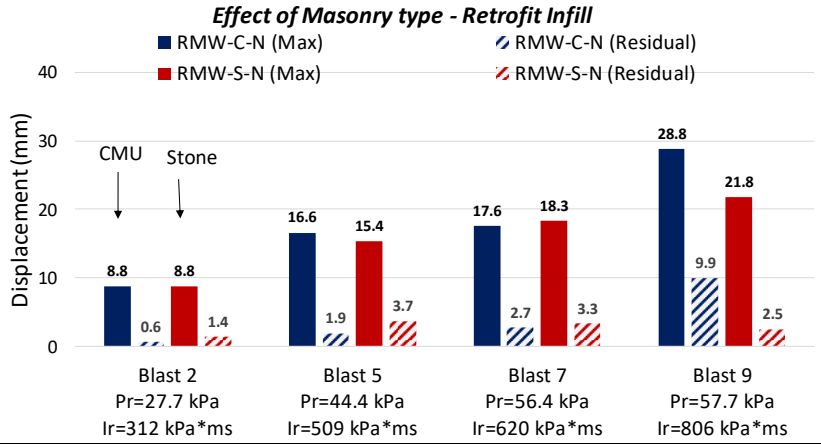

Figure 5-23. Effect of Masonry for Infill Retrofit Walls

RMW-C-N		
Blast 7	Blast 9	Blast 10
		
RMW-S-N		
Blast 9	Blast 10	Blast 14
		

Figure 5-24. RMW-C-N and RMW-S-N Effect of Masonry Comparison

5.8.2. Load Bearing Retrofit (CMU vs STONE)

The effect of masonry type in the retrofit load-bearing walls can also be examined by comparing the results for walls RMW-C-L and RMW-S-L, which were designed with concrete and stone blocks, respectively. Both walls were retrofit with the shotcrete system with the top gap filled with high strength grout, but RMW-C-L had gage 6 welded wire mesh while RMW-S-L had gage 2 welded wire mesh. It is noted that while both walls were tested under axial loading, the axial load level was different: 10% P_o (146 kN) for RMW-C-L vs. 4% P_o (171 kN) for RMW-S-L.

Figure 5-25 compares the displacements sustained by the walls over the course of testing and shows select displacement time histories and comparisons of maximum and residual displacements at equivalent blasts. **Figure 5-26** shows photos of the walls during testing.

The results show that the mid-span displacements were consistently lower in the retrofit stone wall when compared to the CMU wall. The stone wall likely performed better than the CMU wall due to the presence of higher axial load; thus the stone wall experienced higher rigidity due to compression. Furthermore, the stone blocks had a higher axial capacity than the CMU blocks and thus experienced improved arching action. The use of stone blocks in wall RMW-S-L reduced maximum deflections by 57%, 51%, 54% and 51% for Blasts 2 (27.7kPa, 312kPa-ms), 5 (46.8kPa, 509kPa-ms), 9 (67.7kPa, 806kPa-ms), and 10 (81.8kPa, 876kPa-ms), respectively. Residual deflections in the stone wall were also reduced by 72%, 56%, 76%, 55% at these same blasts.

The stone wall sustained less damage than the CMU wall. Hairline cracks in the shotcrete appeared in wall RMW-C-L (CMU retrofit) at Blast 2. These cracks remained hairline in width until Blast 10, where they became 1.2mm wide, indicating fiber pullout (section D in **Figure 5-1**). For wall RMW-S-L (Stone retrofit), hairline cracks only appeared after Blast 9 (section B in **Figure 5-1**). The cracks remained hairline until just prior to failure, at Blast 15 (109.9kPa, 1735kPa-ms).

The type of masonry also affected the blast capacity of the retrofit walls, with failure in RMW-C-L and RMW-S-L occurring at Blasts 12 and 15 (reflected impulse of 1166kPa-ms vs. 1735kPa-ms), respectively. The CMU wall failed along a main crack in the shotcrete, roughly three quarters up the wall. The crack was not completely straight but followed the outline of the repair concrete. The crack separated the wall into two sections, and while the steel wire mesh was not completely ruptured, it was severed in several locations. In comparison, the stone wall failed along a primary crack at mid-height, with the some of the microfibers in the shotcrete still spanning the crack (7mm). The steel mesh was still intact, resulting in a more ductile response. The improved response can be explained by the increased steel mesh area used in the stone series wall.

Effect of Masonry - Retrofit Load Bearing Walls

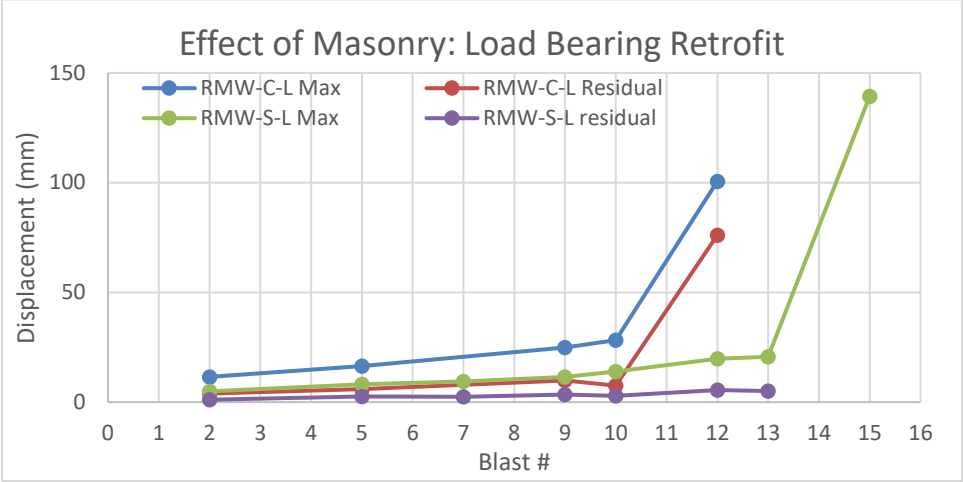

Displacement Time History Comparison

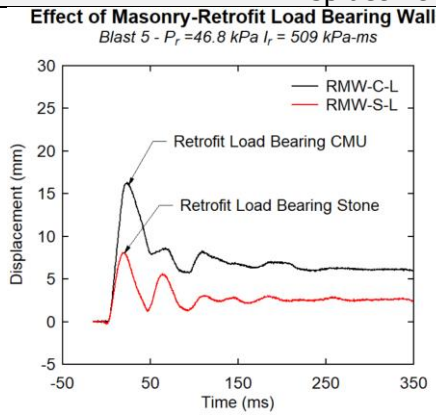

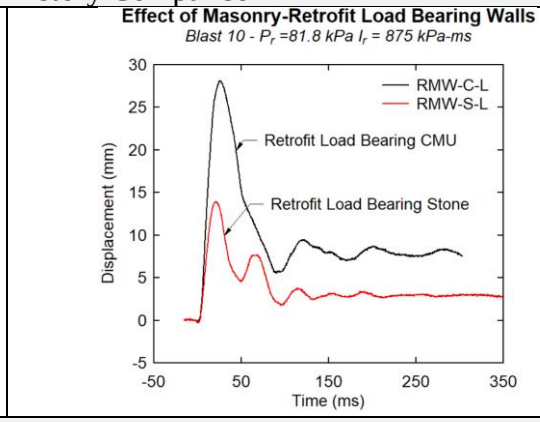

Maximum and Residual Displacements

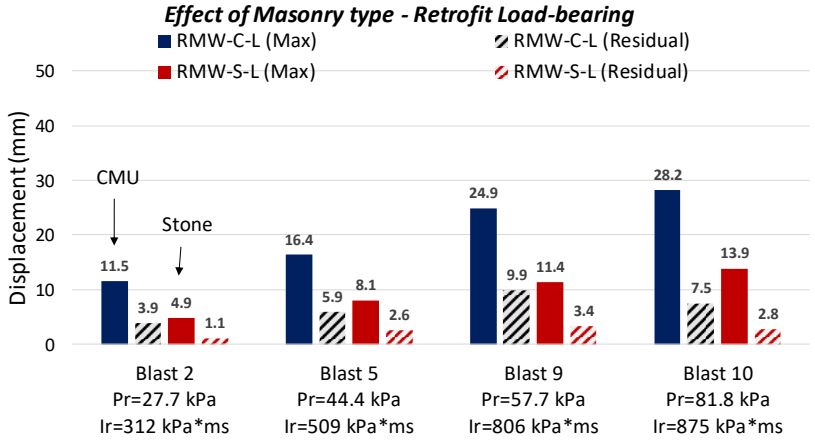

Figure 5-25. Effect of Masonry for Retrofit Load Bearing Walls

RMW-C-L		
Blast 5	Blast 10	Blast 12
		
RMW-S-L		
Blast 10	Blast 12	Blast 15
		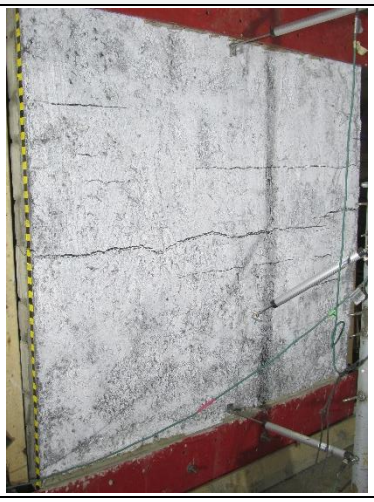

Figure 5-26. RMW-C-L and RMW-S-L Effect of Masonry Comparison

5.9. COMPARISON TO POLYUREA RETROFIT SYSTEMS

This section compares the performance of the shotcrete retrofit with the polyurea-based retrofit studied by Ciornei (2012). Included in the comparison are walls RMW-C-N and RMW-C-L from the current study and walls URM-2 and URM-4 tested by Ciornei (2012). URM-2 was an infill wall sprayed with a layer of polyurea, while URM-4 was load-bearing with a retrofit system comprised of smooth steel wires sprayed with a layer of polyurea. All walls in this comparison were built with concrete masonry (CMU).

5.9.1. Infill CMU Walls (Shotcrete vs Polyurea)

The performance of the shotcrete and polyurea-based retrofit is first studied in infill walls RMW-C-N and URM-2. **Figure 5-27** compares the maximum and residual displacements over the course of testing, as well as select photos of tests.

The shotcrete system substantially increased the stiffness of the wall when compared to the polyurea retrofit. As a result, wall RMW-C-N consistently experienced lower maximum and residual displacements when compared to URM-2, with the degree of reduction in deformations becoming more significant as the blast magnitude increased. The shotcrete system reduced maximum displacements by 33%, 15%, 51%, 67%, 80%, 82% for Blasts 1 (13.3kPa, 191kPa-ms), 2 (27.7kPa, 312kPa-ms), 3 (34.9kPa, 400kPa-ms), 5 (44.4kPa, 509kPa-ms), 7 (56.4kPa, 620kPa-ms) and 9 (67.7kPa, 806kPa-ms). It should be noted that for Blast 9, the test conducted by Ciornei (2012) on URM-2 had a larger reflected pressure of 84.4kPa, although the reflected impulse was considerably lower at 597kPa-ms. The shotcrete system also shows better control of residual displacements, with average reductions of 87% for Blasts 1 through 9. Interestingly, the maximum displacement of the shotcrete retrofit was found to be nearly identical with the residual displacement of the polyurea system up until Blast 9.

The two retrofit systems sustained different damage throughout testing. The polyurea retrofit system sustained damage at Blast 7 (56.4kPa, 620kPa-ms) in the form of debonding of the polyurea membrane. At Blast 9 (67.7kPa, 806kPa-ms), the polyurea system sustained extensive debonding and started tearing. For the shotcrete system, hairline damage was sustained much earlier on, during Blast 2, due to the nature of the retrofit (concrete overlay). The cracks remained hairline in width until Blast 7 where the cracks became 0.3mm in width. At Blast 9, the cracks widened to 4mm. At no point did the shotcrete debond from the CMU wall.

While both systems failed at Blast 10, the retrofit system altered the failure mode. The polyurea ripped at mid-height, partially along the length of the wall. The concrete blocks around the tear were damaged and a few small projectiles were created in the blast. In comparison, the shotcrete failed along the main crack, completely separating the top and bottom portions of the wall. The steel mesh ruptured as well, indicating a relatively more brittle failure. However, virtually no projectiles were created during the blast.

Polyurea and Shotcrete Retrofit Comparison for Infill Walls

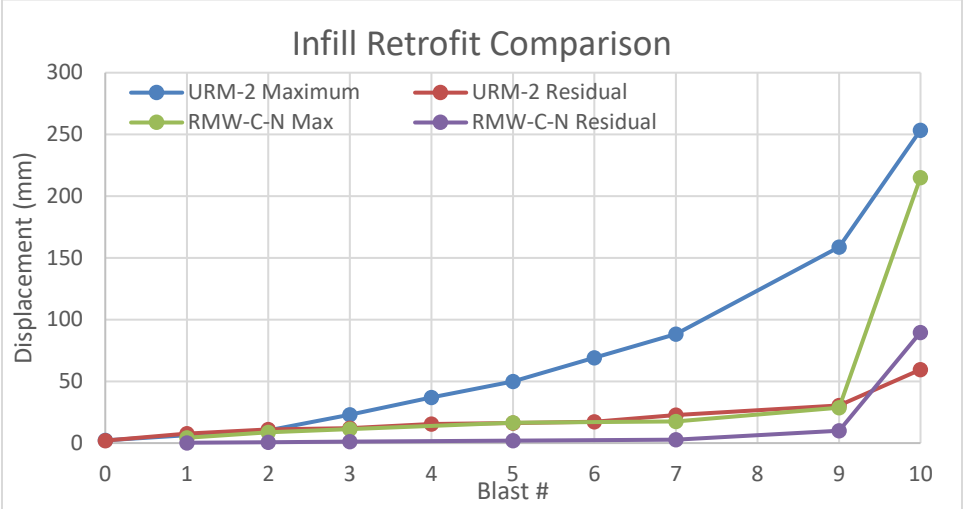

Damage Sustained by Polyurea System

Damage Sustained by Shotcrete System

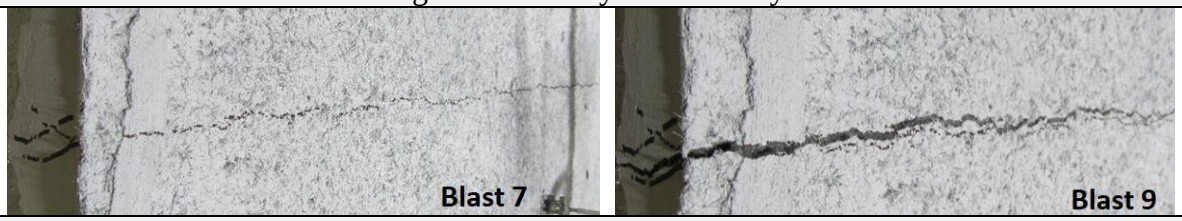

Failure Mode Comparison

Figure 5-27. Polyurea Retrofit Comparison (Polyurea photos from Ciornei, 2012)

5.9.2. Load-Bearing CMU Walls (Shotcrete vs Polyurea)

The effect of retrofit method is further examined by comparing the performance of wall URM-4, tested by Ciornei (2012), and wall RMW-C-L from the current study. Both walls were made of concrete masonry units and were tested under axial load corresponding to 10% P_o, 122kN and 146kN, respectively. **Figure 5-28** compares the maximum and residual displacements over the course of testing, as well as select photos of tests.

The maximum and residual displacements between the two retrofit methods are largely similar. The polyurea retrofit system shows noticeably larger displacements during Blast 9 (67.7kPa, 806kPa-ms) and 10 (81.8kPa, 875kPa-ms) by 46% and 95% respectively. It should be noted that for Blast 9, the reflected impulse for Ciornei (2012) was 676kPa-ms. The differences in residual displacements between both systems are not significant until Blast 12 (99.1lkPa, 1166kPa-ms), when RMW-C-L fails. The polyurea system delayed failure until Blast 16. Blast 16 was not performed in the current study; Ciornei (2012) increased the driver length to 16ft, and the resulting reflected pressure and impulse was 97.3kPa and 1995kPa-ms, respectively.

The polyurea system did not experience any damage until Blast 12 (99.1kPa, 1166kPa-ms). At this point, wall URM-4 experienced excessive displacement, as well as compression cracks in the middle course blocks. The shotcrete system in RMW-C-L experienced hairline cracks from Blast 1 (13.7kPa, 191kPa-ms) to Blast 9 (67.7kPa, 806kPa-ms). It should be noted this wall was damaged while being transported during initial setup, which may have lowered the integrity of the wall. At Blast 10 (81.8kPa, 875kPa-ms), the cracks widened to 1.2mm, with the wall ultimately failing at the next shot, at Blast 12.

The two retrofit systems also showed different failure modes. The polyurea wall failed in a ductile manner, with excessive midpoint displacement at Blast 16. The middle course blocks were split, and the wall could not hold axial load. Given the extent of damage, the retrofit proved excellent in containing debris and projectiles. In comparison, the shotcrete system behaved in a nearly elastic manner, but its failure was relatively more brittle. The deflections were very small leading up until failure, and then the main crack completely separated the top and bottom halves of the wall. The steel mesh, which was placed to provide ductile behaviour, was mostly ruptured. However, given the irregularly shaped crack, parts of the steel mesh remained intact. Despite this mode of failure, the shotcrete was excellent to contain and limit projectiles. Very little debonding was seen in areas with the repair concrete.

Polyurea and Shotcrete Retrofit Comparison for Load Bearing Walls

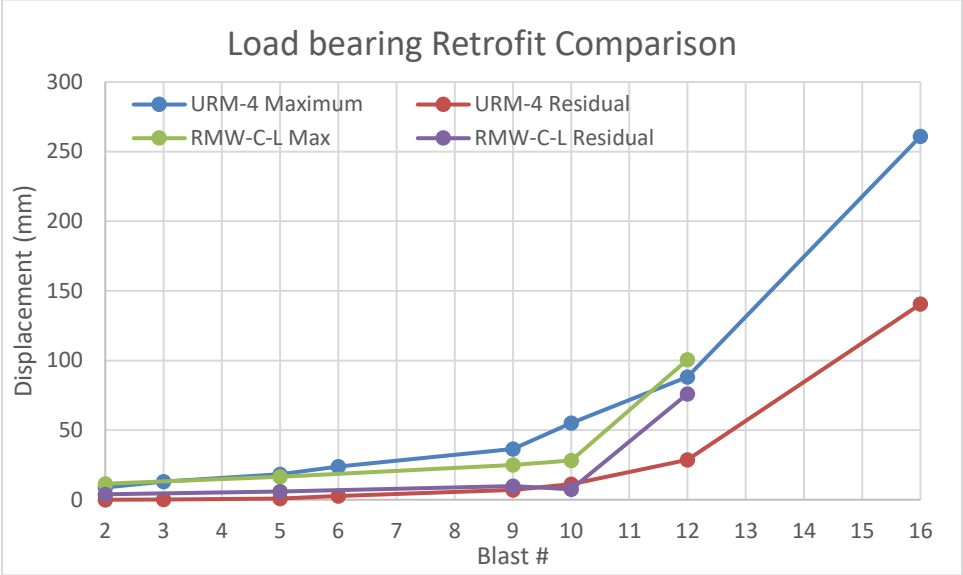

Damage Sustained by Polyurea and Shotcrete Systems

Failure Mode Comparison: Polyurea (left) and Shotcrete (right)

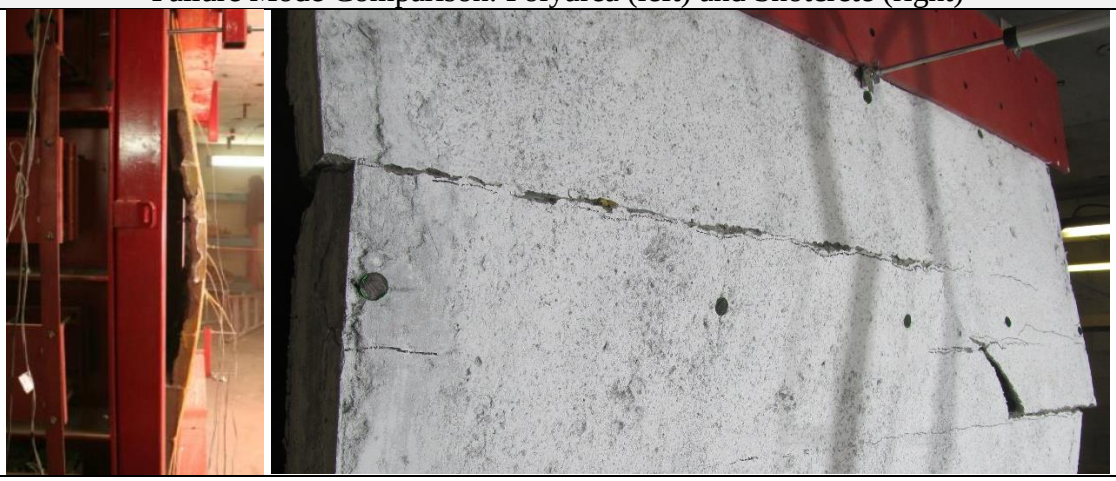

Figure 5-28. Polyurea and Shotcrete Retrofit Comparison (Polyurea from Ciornei, 2012)

5.10. SUMMARY OF DISCUSSION

5.10.1. Effect of Retrofit

The shotcrete retrofit system proved to be very effective in delaying catastrophic failure of the CMU and stone masonry walls. The blast resistance of the retrofit walls was significantly greater than that of the control walls, since the FRS and steel mesh improved the moment capacity of the wall. The maximum displacements of the retrofit walls were also greatly reduced due to the significant improvement in stiffness and mass. In the infill series, the residual displacements were also reduced by the retrofit; however, the load bearing walls did not have significantly different residual displacements. The damage sustained by the retrofit was also greatly reduced; the crack widths were smaller, and no spalling of mortar occurred. The mode of failure remained largely brittle due to the premature rupture of the steel mesh in the shotcrete; however, the walls were not demolished, and remained standing although they were unable to bear axial load. The larger area of steel for RMW-S-L provided a relatively more ductile response, indicating the benefits of increasing the steel mesh size. The retrofit was very effective in preventing fragmentation and projectiles.

5.10.2. Effect of Axial Load

The presence of axial load was shown to be effective in delaying failure in the CMU and stone walls, both in the control and retrofit series. The load bearing walls experienced higher magnitudes of blasts before failure due to the presence of significant arching action. The URM walls benefited more from the axial load, as the maximum and residual displacements were both reduced due to the higher rigidity caused by the axial load. The CMU retrofit walls did not have significant differences in maximum or residual displacements, save that the load bearing walls delayed failure to a later blast. A likely explanation may be that the damage sustained by RMW-C-L during transport reduced its capacity for arching action. However, the stone retrofit walls did see an improvement with axial load; RMW-S-L had smaller maximum displacements than RMW-S-N due to the activation of significant arching action and enhanced rigidity. The axial load lowered the damage sustained by the retrofit walls for each blast; the crack widths were smaller for these walls. In fact, the videos recorded that the crack widths would open during the blast tests, but then were closed due to the axial load. The failure modes did not change for the control walls, however, the load bearing retrofit walls did not experience as much mesh rupture as the retrofit infill walls.

5.10.3. Effect of Masonry Type

For the URM infill walls, the stone wall performed much more poorly than the CMU wall despite having a higher mass. The stone specimen failed after the second shot, while the CMU wall failed after the fourth shot. The maximum displacement was larger for the stone wall; however, the residual displacement was not significantly different between the two walls. For the URM infill walls tested, it is likely that the main component that resisted the out-of-plane loading is the number and location of mortar joints; it can be understood that higher quality masonry walls will withstand blast effects better than lower quality walls. Therefore, one factor that determined the walls out-of-plane resistance is the care that the stone mason takes in construction. Furthermore, the position of the critical crack can significantly lower the out-of-plane resistance if the crack is located higher than mid-height of the wall. With axial load, the stone URM wall performed better than the CMU URM wall. The failure was delayed for the stone wall, and the maximum and

residual displacements were reduced in comparison. The type of masonry did not change the failure mode. For the URM load bearing walls tested, the stone blocks may have performed better than the CMU blocks due to their higher mass, and superior axial capacity leading to improved arching resistance.

For the infill retrofit walls, the stone shotcrete specimen performed better than its CMU companion only because the failure was delayed; the stone wall resisted higher magnitude blasts before failure. However, the maximum and residual displacements were largely identical. The pattern of damage was similar, as well as the failure mode, though the mesh did not completely rupture for the stone wall. The behavior of both walls was similar, likely because the shotcrete overlay is the controlling factor in the response of these walls. For the load bearing retrofit walls, the stone wall performed better than the CMU wall. The stone wall resisted higher blast loads before failing, and consistently reduced the maximum and residual displacements over the CMU wall. The stone retrofit wall also sustained less damage at failure. The stone wall likely performed better than the CMU wall due to the presence of axial load; the stone blocks had a higher axial capacity than the CMU blocks which enhances arching action. Another factor was the increased steel mesh area which prevented brittle failure in the stone specimen.

5.10.4. Polyurea and Shotcrete Retrofit Comparison

Overall, the performance of the shotcrete retrofit system greatly reduced the maximum and residual deflection in comparison the polyurea retrofit system. Both systems resisted similar blasts, but the load bearing polyurea system (with steel rebar) failed at a higher blast than the load bearing shotcrete system. The behaviour of the polyurea systems was more ductile than the shotcrete. While both systems prevented debris very well, the shotcrete contained projectiles better, since the non-load bearing polyurea tore near mid-height and allowed a moderate number of projectiles to be formed.

CHAPTER 6. ANALYTICAL INVESTIGATION

6.1. CHAPTER OVERVIEW

This chapter presents an analytical investigation which focuses on predicting the restoring force functions and dynamic responses of the walls tested in this research study. In Section 6.2 the restoring force-displacement relationships of the walls are approximated using the equation of motion and the total inertial forces acting on the walls. The restoring force functions for the retrofit and URM walls are then compared. The effect of damage and repeated blasts is also discussed. The ultimate capacity and stiffness of the walls is then estimated through analysis to develop idealized lateral restoring force-displacement relationships for the types of walls considered in this study (Section 6.3). Using these idealized functions, SDOF analysis is used to predict the maximum displacement response of the walls (Section 6.4).

6.2. RESTORING FORCE DISPLACEMENT RELATIONSHIP

6.2.1. Restoring Force Displacement Relationship Formulation

The restoring force-displacement relationships for the walls at each test can be calculated using the single-degree-of-freedom (SDOF) equation of motion shown below (Equation 6.2.1) as performed by Abou-Zeid et al. (2011), where m = mass; $u(t)$, $\dot{u}(t)$ and $\ddot{u}(t)$ = displacement, velocity and acceleration as a function of time; c = damping coefficient; k = stiffness; and $F(t)$ = applied load as a function of time.

$$m\ddot{u}(t) + c\dot{u}(t) + ku(t) = F(t) \qquad [\mathbf{6.2.1}]$$

Ignoring damping, the generalized SDOF model for each wall is represented in Equation 6.2.2:

$$K_{LM}m\ddot{u}(t) + R(t) = F(t) \qquad [\mathbf{6.2.2}]$$

where $R(t)$ is the wall restoring force, m is wall mass, $\ddot{u}(t)$ is the acceleration of the midpoint of the wall, and K_{LM} is a load mass factor which converts the real system into an equivalent SDOF system, with the governing degree of freedom being the wall mid-height. This factor depends on the wall shape function (UFC 3-340-02). $F(t)$ is the forcing function which describes the loading over time.

The total inertial force acting on the wall for each test can be found by multiplying the calculated acceleration at wall mid-height by the generalized mass ($K_{LM} \times m \times \ddot{u}(t)$). The acceleration was obtained numerically by twice differentiating the displacement function measured during the tests. In order to smooth out the measured displacement, a sixth-degree polynomial was used to fit the displacement data. Since the mass (m) and acceleration ($\ddot{u}(t)$) are known quantities, and the forcing function is measured for each test, the restoring force, $R(t)$ can then be found by rearranging Equation [6.2], i.e. $R(t) = F(t) - K_{LM}m\ddot{u}(t)$. These forces were then plotted against the wall mid-height displacements to determine the restoring force-displacement relationships for each specimen, at each blast test. The procedure and results for RMW-S-L-7 are shown in **Figure 6-1**.

Restoring Force Determined using Equation of Motion

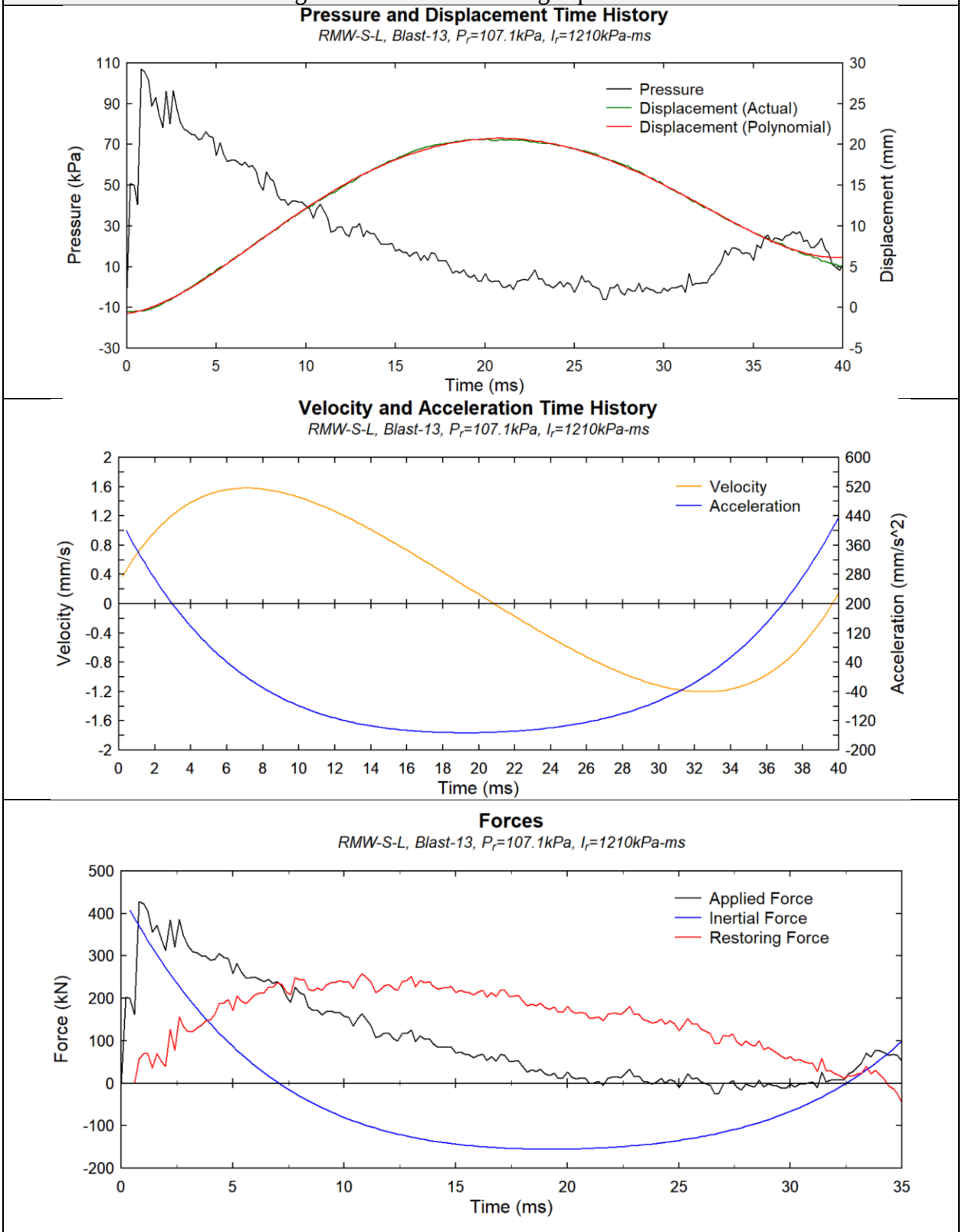

Figure 6-1. Procedure to Determine Restoring Force in Walls

6.2.2. Effect of Axial Load and Masonry Type

The force displacement relationships of the walls for the tests just before failure are shown in **Figure 6-2**. There are no restoring force-displacement relationships for the infill URM walls (URM-1 and URM-S-N) due to the sensitive nature of deriving the acceleration from the displacement as well as the small inertial forces present in the infill control walls. Also, there are no restoring force-displacement relationships for the tests that failed the walls since the assumptions governing the SDOF system break down upon failure of the wall.

The axial load affected the resistance of the CMU retrofit walls (RMW-C-N vs RMW-C-L), as shown in **Figure 6-2** A). The applied axial load increased the ultimate resistance for the CMU retrofit walls but did not change the stiffness significantly. For the Retrofit CMU Infill wall, the restoring force-displacement relationship seems to increase linearly until it reaches a plateau at 10mm. In comparison, the capacity of the load bearing retrofit wall continues to increase past the plateau to its maximum at about 12mm, then slowly returns to back to a capacity which is similar to the ultimate resistance of the infill wall (at 30mm).

The axial load also affected the resistance of the retrofit stone walls, RMW-S-L and RMW-S-N (**Figure 6-2** B). For the load bearing wall, the stiffness of the wall decreases until it reaches its ultimate resistance at about 8mm. The resistance plateaus until 20mm, after which it descends as the wall goes to its residual position. The infill wall, in contrast, does not have a significant stiffness at first. A likely explanation for this may be that there was a small space existing between the filler grout and the top HSS support.

The restoring force-displacement relationships of the load bearing URM walls (URM-3 and URM-S-L) are shown in **Figure 6-2** C). The first part of the of the curves seem nearly identical for both walls, with a steep increase in the CMU wall resistance to its peak at about 6mm, before decreasing. The stone wall then plateaus until 30mm before increasing again. The sudden increase at the end is likely caused by a rebound shockwave, and the wall deflects a total of 40mm. The masonry type also affected the restoring force-displacement relationships of the retrofit walls as shown in **Figure 6-2** D) (RMW-C-L and RMW-S-L). The two walls behaved similarly, both reached their peak resistance at about 10mm, but the CMU wall ultimately deflected to about 28mm while the stone wall only to 21mm. However, the stone wall achieved a higher maximum resistance than the CMU wall.

Restoring force-displacement relationships

A) Effect of Axial Load on Retrofit CMU Walls

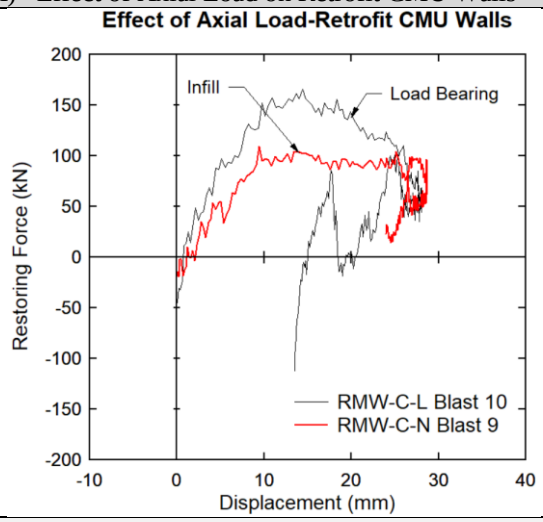

B) Effect of Axial Load on Retrofit Stone Walls

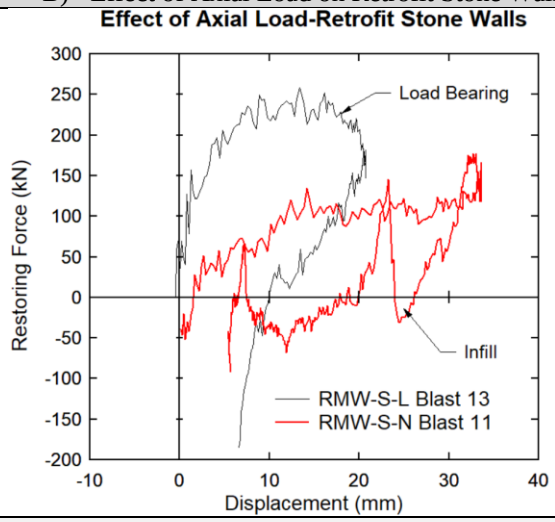

C) Effect of Masonry on URM Load-Bearing Walls

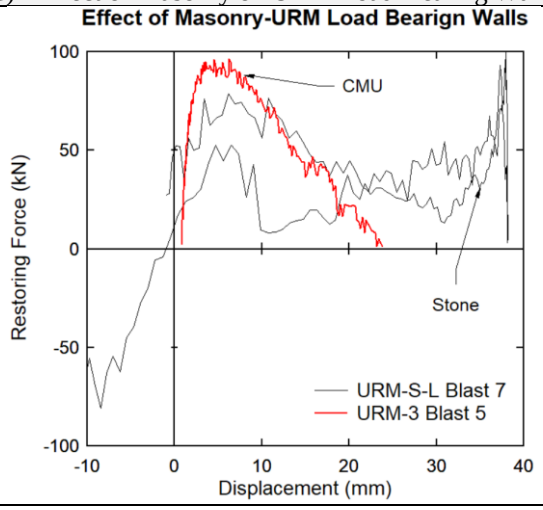

D) Effect of Masonry on Retrofit Load-Bearing Walls

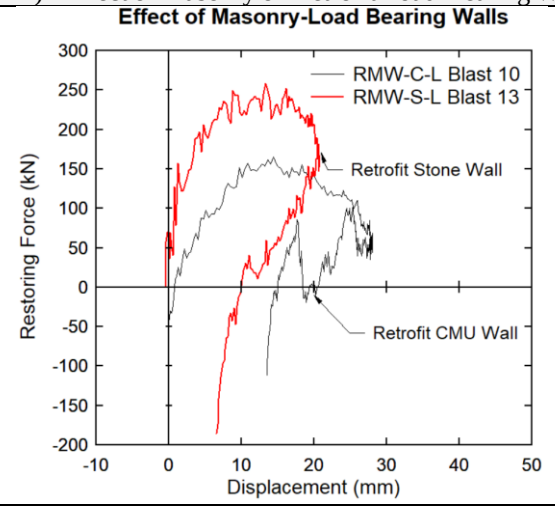

Figure 6-2. Restoring force-displacement relationships

6.2.3. Effect of Retrofit

The effect of the retrofit on the restoring force-displacement relationships can be examined in **Figure 6-3**. Included in the comparison are load-bearing walls URM-3 vs. RMW-C-L and URM-S-L vs. RMW-S-L, which were made of CMU and stone masonry, respectively. As in the previous section the curves were obtained for the tests just prior to failure. For both series, the retrofit wall achieved a higher resistance (ultimate capacity) than the companion URM wall. For the CMU load bearing walls, the retrofit increased wall resistance by 71%, while the improvement reached 152% for the stone wall. Furthermore, the retrofit walls absorbed more energy than the companion unreinforced masonry specimens, where the energy is taken as the area underneath the restoring force-displacement curves. The total energy for the retrofit CMU wall is 3120kNmm, compared to 2207kNmm with no retrofit, marking a 41% increase. Likewise, the retrofit stone wall absorbed a total energy of 4256kNmm compared to 1979kNmm with no retrofit, an increase of 115%.

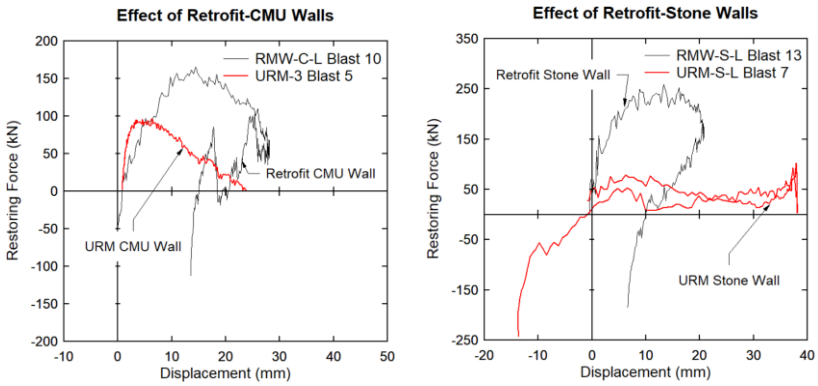

Figure 6-3. Effect of Retrofit for Load Bearing CMU and Stone Walls

6.2.4. Effect of Damage and Repeated Blasts

The restoring force-displacement relationships calculated using the method described in Section 6.2.1 represent the internal restoring forces of the wall for that particular test, not the ultimate resistance of the wall. This can be seen in **Figure 6-4**, which shows the restoring force-displacement relationships of wall RMW-S-L over three tests. Moreover, no meaningful curve could be found from the test which caused failure since the assumptions governing the SDOF system break down upon failure of the wall. As a result, the actual ultimate resistance of the wall is higher than measured resistance presented in the previous sections. Furthermore, over the course of testing the wall sustained accumulated damage which affects the wall's stiffness and ultimate strength.

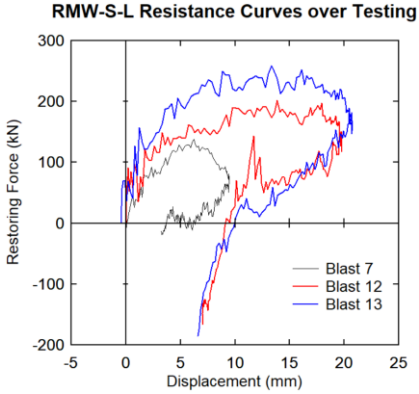

Figure 6-4. RMW-S-L Restoring force-displacement relationships over several tests

6.3. ANALYSIS

This section presents the formulation of the idealized restoring force-displacement relationships which are used to predict the maximum displacement of the walls using SDOF analysis.

6.3.1. Strength and Dynamic Increase Factors

In order to consider the properties of the materials used in the testing under high strain rates, the DIF values shown in **Table 6-1** are used.

Table 6-1. DIF Values

	DIF
Concrete	1.2
Steel (yield)	1.2
Steel (ultimate)	1.1
Masonry	1.2

6.3.2. Material Properties

The material properties used in the analysis are those measured during the experiments and are shown in **Table 6-2** (refer to Chapter 3 for further details). No direct tensile test was conducted for the shotcrete; therefore, the tensile strength of the shotcrete was estimated using the equation $0.33 * \sqrt{f'c}$.

Table 6-2. Material Properties

					Steel				Shotcrete		
Mortar Cube	**CMU Prism**		**Stone Prism**		**Gage 6**		**Gage 2**		**Batch 1**	**Batch 2**	**Both**
f'j (MPa)	f'm (MPa)	E (MPa)	f'm (MPa)	E (MPa)	Fy (MPa)	E (MPa)	Fy (MPa)	E (MPa)	f'c (MPa)	f'c (MPa)	E (MPa)
16.6	9.5	3193	22.2	3632	922	295 000	590	263 000	31.4	20.9	4533

6.3.3. URM Wall Analysis

The ultimate capacities (maximum resistance) of the load bearing URM walls were obtained using the procedure outlined in Section 6.3.3.1. The results of the analysis are shown in **Table 6-3**. The calculated maximum resistance (Fu) agree very well with the measured values (Fu_{test}) for URM-S-L and for URM-3, with calculated-to-measured load ratios of 100% and 92%. Since the measured values (Fu_{test}) are likely lower than the actual ultimate resistance of the wall (as explained in Section 6.2.4), the calculated-to-measured ratios are expected to be lower than those presented here.

Table 6-3. Control Wall Analysis Results

	P (kN)	γ	H (mm)	Δ (mm)	Wu (N/mm)	Fu (N)	Fu_{test} (N)	Fu/Fu (test)
URM-3*	122	0.90	2000	3.2	39.5	79038	85549	0.92
URM-S-L	171	0.90	2000	3.4	39.4	78835	78523	1.00

*Tested by Ciornei (2012)

The idealized restoring force-displacement functions are also compared to the actual curves in **Figure 6-5**. The analytical restoring force-displacement relationships were built in accordance with the method described in Section 6.3.3.1.

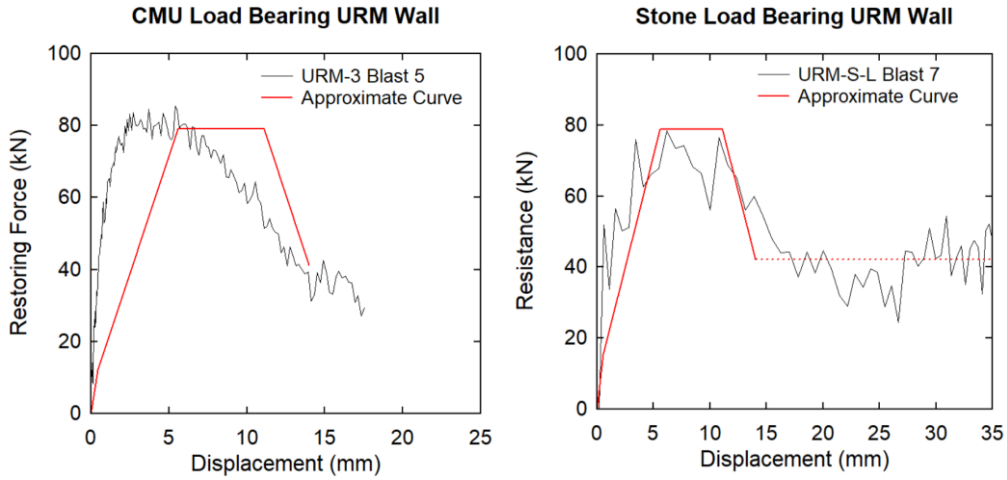

Figure 6-5. Approximate Resistance Functions for Load Bearing URM Walls

6.3.3.1. Load Bearing URM Walls

The idealized resistance curve shown in **Figure 6-6** was used to develop the restoring force-displacement relationships of the URM load-bearing walls. The idealized function consists of four linear segments: 1) elastic behavior up to cracking, 2) post-cracking response up to ultimate resistance, 3) constant plastic region and 4) strength decay region.

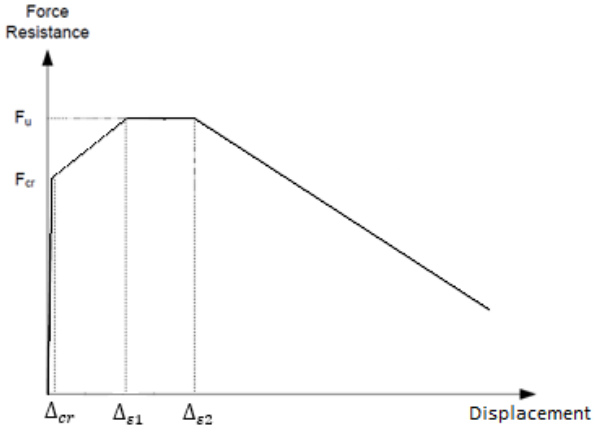

Figure 6-6. Idealized Restoring Force-Displacement Function

In order to determine the cracking moment (M_{cr}), Equation 6.3.1 was used, where I is the moment of inertia of the wall, c is the location of the neutral axis with respect to the extreme tension fiber which was taken to be half the wall thickness, P is the axial load, A is the cross-sectional area of the wall, and f_{mr} is the modulus of rupture which was taken to be 0.8MPa for Type S mortar (CSA S304.1-04, 2012). Equation 6.3.2 relates the cracking moment (M_{cr}) to the distributed load (W_{cr}) that would cause cracking, where H is the height of the wall. Setting Equations 6.1 and 6.2 equal to each other, the distributed load (W_{cr}) that causes cracking can be found. Equation 6.3.3 was then used to find the total cracking force on the wall.

$$M_{cr} = \frac{I}{c}\left(\frac{P}{A} + f_{mr}\right) \quad [\mathbf{6.3.1}]$$

$$M_{cr} = \frac{W_{cr}H^2}{8} \quad [\mathbf{6.3.2}]$$

$$F_{cr} = W_{cr}H \quad [\mathbf{6.3.3}]$$

Once the load that causes cracking is known, the deflection at which cracking occurs can be determined with Equation 6.3.4, where E is the elastic modulus of the wall.

$$\Delta_{cr} = \frac{5w_{cr}H^4}{384EI} \quad [\mathbf{6.3.4}]$$

Beyond cracking, it was assumed that the wall experiences three hinges, two at the top and bottom and one at mid-height. Furthermore, the two segments of the wall were assumed to remain elastic and remain under uniform compression while they rotate, as denoted by λ. This uniform compression caused by the rotation of the wall segments results in axial shortening (2δ). The assumptions are shown in **Figure 6-7**.

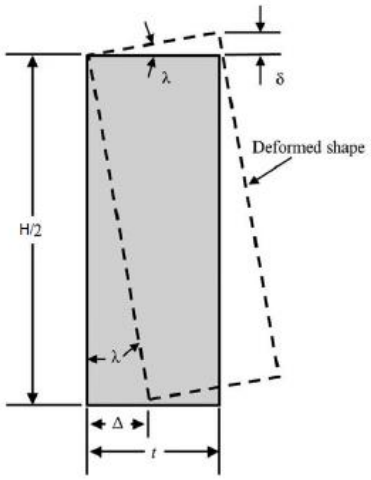

Figure 6-7. Assumed Axial Shortening after Cracking (Gagnet et al, 2017)

The strain can then be defined by Equation 6.3.5, and the trigonometric relationship of the wall rotation is defined by Equation 6.3.6. These two equations can be rearranged as shown by Equation 6.3.7, were the deflection is a function of the wall height, H, the wall thickness, t, and the strain in the mortar, ε.

$$\varepsilon = \frac{2\delta}{\frac{H}{2}} \quad [\mathbf{6.3.5}]$$

$$tan\lambda = \frac{\Delta}{\frac{H}{2}} = \frac{\delta}{t} \quad [\mathbf{6.3.6}]$$

$$\Delta = \frac{\varepsilon H^2}{8t} \quad [\mathbf{6.3.7}]$$

Load-bearing masonry walls show a very short but stable plastic region due to the crushing of the mortar joints (Saatcioglu et al., 2018). The strain range at which the crushing of mortar was assumed to occur is from 0.001 (ε_1) to 0.002 (ε_2). By using Equation 6.3.7, the deflections at these strains ($\Delta_{\varepsilon 1}\ and\ \Delta_{\varepsilon 2}$) can be calculated.

The final decaying segment represents the failure of the wall as the critical mortar joint crushes and the eccentricity of the arching forces reduce. The negative slope of this segment was taken as equal to the positive post-cracking stiffness (Saatcioglu et al., 2018). For the purpose of the SDOF analysis, a final branch shown by the dotted horizontal segments added at the end to better represent the measured restoring force-displacement relationships (**Figure 6-5**).

The maximum lateral load resistance (Fu) of the load-bearing URM walls was calculated by considering that the arching action caused by the axial load resists the out-of-plane force acting on the wall. In order to determine the out-of-plane resistance, the resisting moment caused by arching action is equated to the moment caused by the uniformly distributed blast load. The force diagram of a URM wall resisting an out-of-plane load through arching action is shown in **Figure 6-8**.

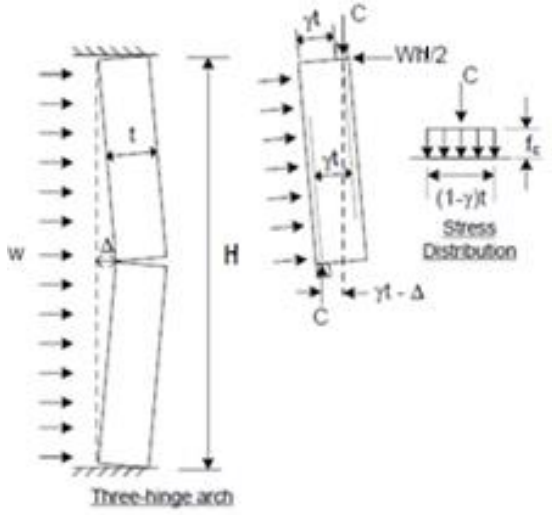

Figure 6-8. Force Diagram of URM Wall (Saatcioglu et al., 2018)

The compressive force per unit horizontal length of the wall (C) was calculated with Equation 6.3.8, where $f_c = 0.85 * f_j'$ and where f_j' is the compressive strength of the mortar joints as determined from standard cube tests. The stress f_c represents the uniform stress in the rectangular compressive stress block for the mortar in the joint at crushing.

$$C = f_c(1-\gamma)\mathrm{t} \qquad [\mathbf{6.3.8}]$$

$$\frac{\mathrm{W_u H^2}}{8} = C(\gamma \mathrm{t} - \Delta) \qquad [\mathbf{6.3.9}]$$

The factor $(1-\gamma)\mathrm{t}$ "represents the length of the compression zone in wall critical sections, at the wall ends or at mid-height" (Saatcioglu et al., 2018). The value of γ was taken to be 0.9, as suggested by the British Code BS5628 (1985). The factor γ is the ratio between the length of the moment arm (wall section depth from the extreme tension fiber to the beginning of the rectangular stress block) and the thickness of the wall, t. Equation 6.3.9 shows the relationship between the moment caused by arching action to the moment caused by the applied distributed load, $\mathrm{W_u}$, where

H is the height of the wall, and Δ is the displacement of the wall. In order to find the maximum force that the wall can withstand (F_u), Equation 6.3.3 was used by replacing W_{cr} with W_u.

6.3.4.CMU Retrofit Wall Analysis

The calculated and measured values for the ultimate capacity of the CMU retrofit walls (Fr and Fr_{test}) are displayed in **Table 6-4**. The maximum capacities were determined using the procedure outlined in Section 6.3.4.1 and 6.3.4.2.

Incorporating the shotcrete overlay, it was found that the analysis over estimated the actual capacity of the wall during the test before failure, at 152% and 141% for the infill and load bearing wall, respectively. The over estimation is expected however, since the actual restoring force-displacement relationships do not represent the ultimate resistance of the walls, but rather the resistance of the walls during the last test before failure. It is expected that the true ultimate resistance of the wall would be closer to these values.

The resistance of the wall that excluded the shotcrete overlay was also calculated. In neglecting the shotcrete overlay, the analysis was closer to the actual resistance, with calculated-to- measured maximum load ratios of 83% for the infill wall and 99% for the load bearing wall.

The comparison between the analysis with and without shotcrete (in **Table 6-4** and in **Figure 6-9**) is not meant to be used to judge the effectiveness of the shotcrete overlay. However, the comparison gives an indication of the effect of the accumulated damage sustained over the course of testing, which affects the strength and stiffness of the wall.

Table 6-4. CMU Retrofit Wall Analysis

Load	Infill		Load Bearing	
	w/o Shot.	w Shot.	w/o Shot.	w Shot.
Measured ultimate resistance, Fr_{test} (kN)	109.1	109.1	165.5	165.5
Predicted ultimate resistance, Fr (kN)	90.6	165.5	163.4	232.7
Calculated-to-measured Load ratio %	83.0	151.7	98.7	140.6

Figure 6-9 compares the idealized and actual restoring force-displacement relationships for the CMU retrofit walls. The functions were built according to the method shown in Sections 6.3.4.1 and 6.3.4.2 below. As stated above, if the actual restoring force-displacement relationship (shown in black in **Figure 6-9**) represented the true ultimate resistance of the wall, then it is expected that the curve would be closer to the analysis including shotcrete (shown in the first two graphs in **Figure 6-9**).

	Retrofit CMU Infill Wall	Retrofit CMU Load Bearing Wall
Analysis with Shotcrete	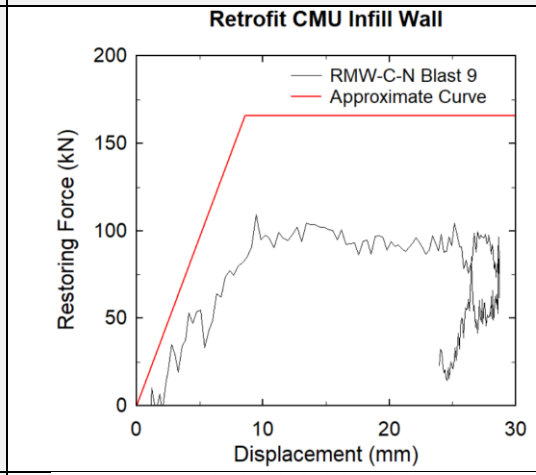	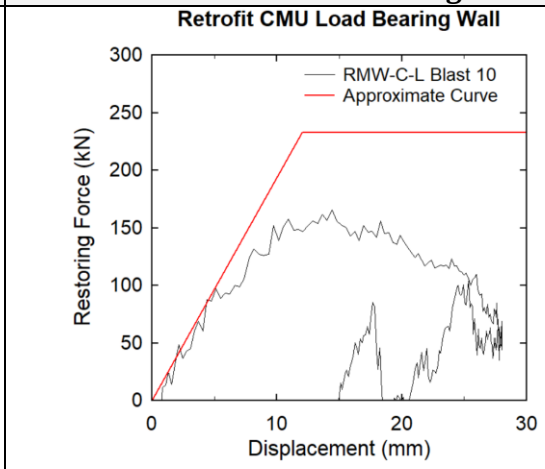
Analysis w/o Shotcrete	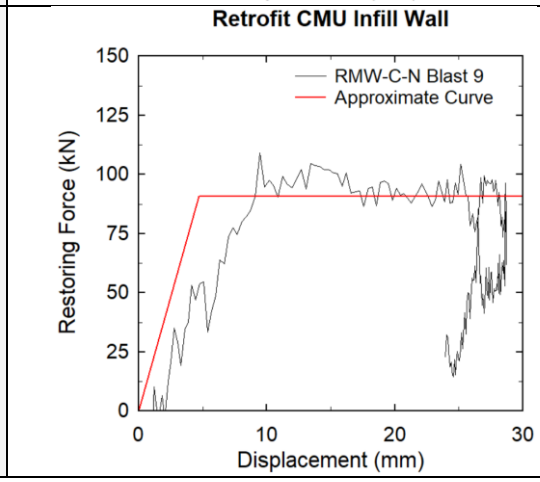	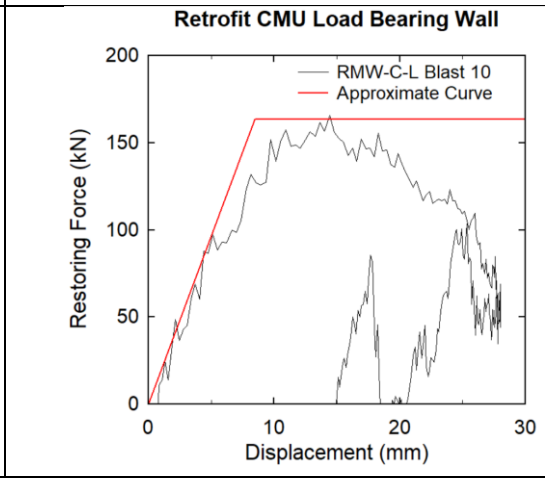

Figure 6-9. Approximate Resistance Functions for Retrofit CMU Walls

6.3.4.1.CMU Infill Retrofit Wall

This section explains the procedure used to derive the maximum resistance and idealized restoring force-displacement relationship of the CMU infill retrofit wall.

The initial stiffness of the wall was calculated assuming simply supported conditions using Equation 6.3.10, with E representing the elastic modulus, and H the height of the wall. The gross moment of inertia, I_g, was used instead of the cracked moment of inertia since it was assumed the shotcrete held the stone and mortar intact throughout most of the testing.

$$K = \frac{384EI}{5H^3} \qquad [\mathbf{6.3.10}]$$

A sectional analysis was then performed in order to calculate the ultimate load the wall could sustain. The assumed strain profile and corresponding stress blocks are illustrated in **Figure 6-10**. The thickness of the shotcrete, t_{sh}, is 51mm with the mesh embedded at the center of the layer. The depth, h, of the wall is 141mm.

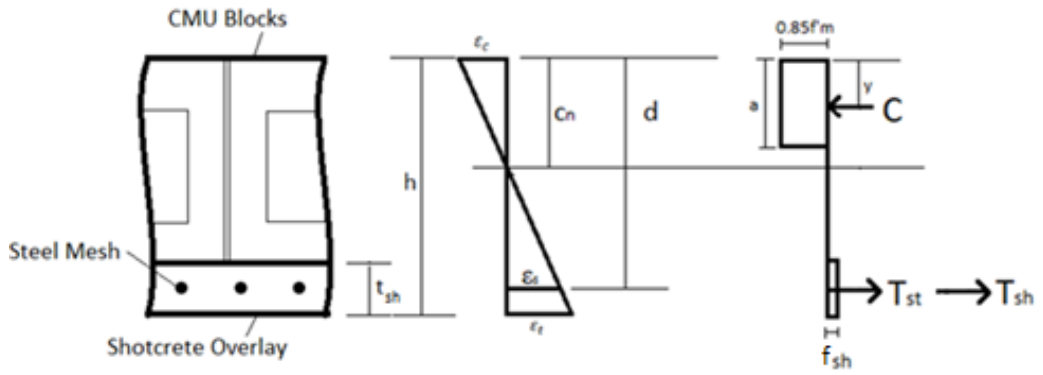

Figure 6-10. Strain Profile, Simplified Stress Distribution and Internal Forces

The tension in the shotcrete (T_{sh}) and the steel mesh (T_{st}) must be equal to the compression in the masonry (C), as described in Equation 6.3.11. Stress blocks were assumed to approximate the compressive stress in the masonry, as shown in Equation 6.3.12. The compressive strength of the masonry, (f'_m), is measured from prism tests, 'a' is the depth of the stress block and l is the length of the wall being analyzed. The tension in the steel mesh is found with Equation 6.3.13, where f_s is assumed to be the stress of the steel bars at yielding and A_s is the area of steel reinforcement. The tension in the shotcrete is computed using a uniform stress block according to Equation 6.3.14, where f_{sh} is the tensile stress in the shotcrete and A_{sh} is the area of the shotcrete in tension.

$$C = T_{st} + T_{sh} \qquad [\mathbf{6.3.11}]$$

$$C = 0.85 f'_m a l \qquad [\mathbf{6.3.12}]$$

$$T_{st} = f_{st} A_{st} \qquad [\mathbf{6.3.13}]$$

$$T_{sh} = f_{sh} A_{sh} \qquad [\mathbf{6.3.14}]$$

The internal yielding moment M_p can be solved with Equation 6.3.15, where y is the distance from the extreme compression fiber to the centroid of the compression stress block and d is the distance from the extreme compression fiber to the steel mesh. Assuming pinned-pinned boundary conditions, the distributed load that causes the plastic moment in the wall can be calculated with Equation 6.3.16, where H is the height of the wall. The maximum resistance of the wall was then calculated with Equation 6.3.3 by replacing W_{cr} with W_u.

After peak, the restoring force-displacement relationship is assumed to plateau, until reaching the maximum displacement observed in the experimental restoring force-displacement relationship.

$$M_p = C(d - y) \qquad [\mathbf{6.3.15}]$$

$$W_u = \frac{8 M_p}{H^2} \qquad [\mathbf{6.3.16}]$$

6.3.4.2.CMU Load Bearing Retrofit Wall

The following explanation shows how the axial load was considered in the derivation of the idealized restoring force-displacement relationship of the CMU load bearing retrofit wall.

Equation 6.3.10 was used to calculate the stiffness, using the gross moment of inertia since it was assumed the shotcrete held the stone and mortar intact. The ultimate capacity for the CMU load bearing walls was calculated using sectional analysis, with the strain profile and stress blocks depicted in **Figure 6-11**. The thickness of the shotcrete, t_{sh}, is 51mm with the mesh embedded at the center of the layer. The depth, h, of the wall is 141mm.

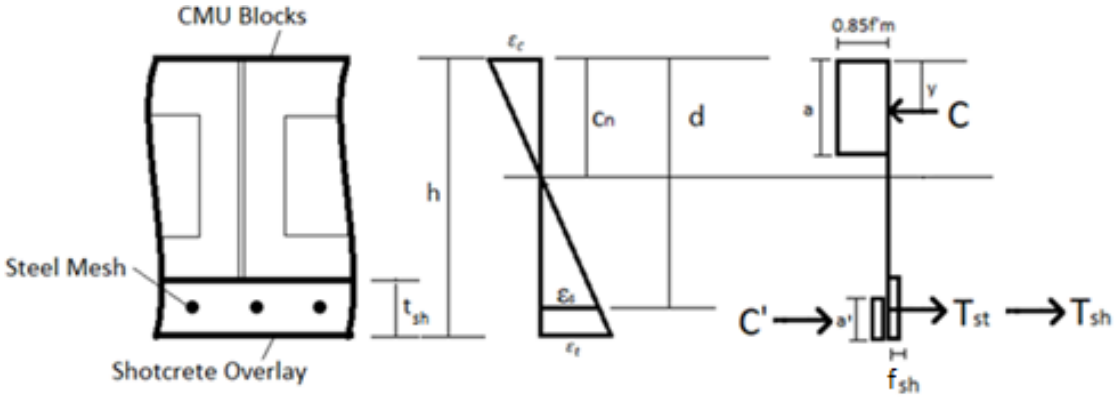

Figure 6-11. Strain Profile, Simplified Stress Distribution and Internal Forces with Axial Load

The tension in the shotcrete (T_{sh}) and the steel mesh (T_{st}) as well as the compressive forces from arching action (C') must be equal to the compression in the masonry (C), as described in Equation 6.3.17. C' represents the compressive force due to arching action and was assumed to be the axial load, however during the test, the arching force would increase as the wall deflects.

$$C = T_{st} + T_{sh} + C' \qquad [\mathbf{6.3.17}]$$

The internal yielding moment M_p can be solved with Equation 6.3.18, where y is the distance from the extreme compression fiber to the centroid of the compression stress block, d is the distance from the extreme compression fiber to the steel mesh, h is the depth of the wall and a' is the length of the compression block caused by arching action. Assuming pinned-pinned boundary conditions, the distributed load that causes the plastic moment in the wall can be calculated with Equation 6.3.16, and the resulting maximum force the wall can sustain was calculated with Equation 6.3.3 (replacing W_{cr} with W_u).

After peak, the restoring force-displacement relationship is assumed to plateau, until reaching the maximum displacement observed in the experimental restoring force-displacement relationship.

$$M_p = -Cy + C'\left(h - \frac{a'}{2}\right) + T_{st}d + T_{sh}d \qquad [\mathbf{6.3.18}]$$

6.3.5. Stone Retrofit Wall Analysis

The calculated and measured values for the ultimate capacity of the CMU retrofit walls (Fr and Fr_{test}) are displayed in **Table 6-5**. The maximum capacities were determined using the procedure outlined in Section 6.3.5.1 and 6.3.5.2.

Incorporating the shotcrete overlay, it was found that the analysis over estimated the actual capacity of the wall, at 152% and 116% for the infill and load bearing wall, respectively. The over estimation is expected however, since the actual restoring force-displacement relationships do not represent the ultimate resistance of the wall, but rather the resistance of the wall during the last test before failure. It is expected that the true ultimate resistance of the wall would be closer to these values.

The resistance of the wall that excluded the shotcrete overlay was also calculated. In neglecting the shotcrete overlay, the analysis was closer to the actual resistance, with calculated-to-measured maximum load ratios of 111% for the infill wall and 91% for the load bearing wall.

The comparison between the analysis with and without shotcrete (in **Table 6-5** and in **Figure 6-12**) is not meant to be used to judge the effectiveness of the shotcrete overlay. However, the comparison gives an indication of the effect of the accumulated damage sustained over the course of testing, which affects the strength and stiffness of the wall.

Table 6-5. Stone Retrofit Wall Analysis

Load	Infill		Load Bearing	
	w Shot.	w/o Shot.	w Shot.	w/o Shot.
Measured ultimate resistance, Fr_{test} (kN)	134.6	134.6	258.7	258.7
Predicted ultimate resistance, Fr (kN)	204.4	148.9	299.6	236
Calculated-to-measured Load ratio %	151.9	110.6	115.8	91.2

Figure 6-12 compares the idealized and actual restoring force-displacement relationships for the CMU retrofit walls. The functions were built according to the method shown in Sections 6.3.5.1 and 6.3.5.2 below. As stated above, if the actual restoring force-displacement relationship (shown in black in **Figure 6-12**) represented the true ultimate resistance of the wall, then it is expected that the curve would be closer to the analysis including shotcrete (shown in the first two graphs in **Figure 6-12**).

	Retrofit Stone Infill Wall	Retrofit Stone Load Bearing Wall
Analysis with Shotcrete	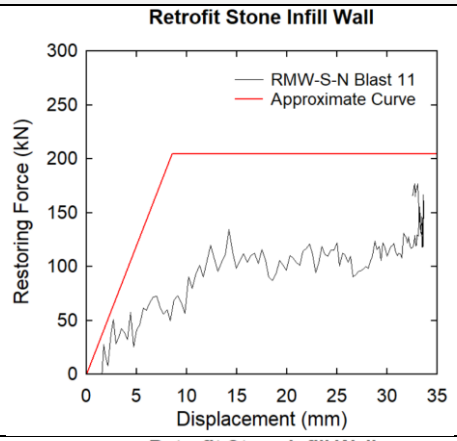	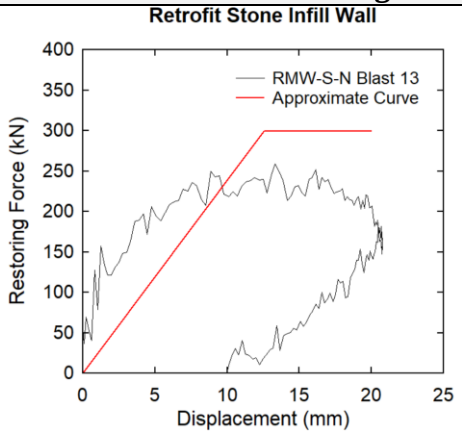
Analysis w/o Shotcrete	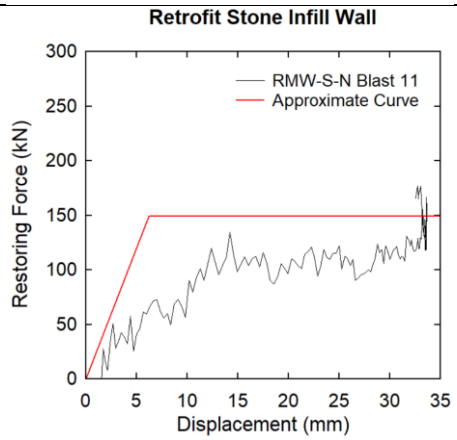	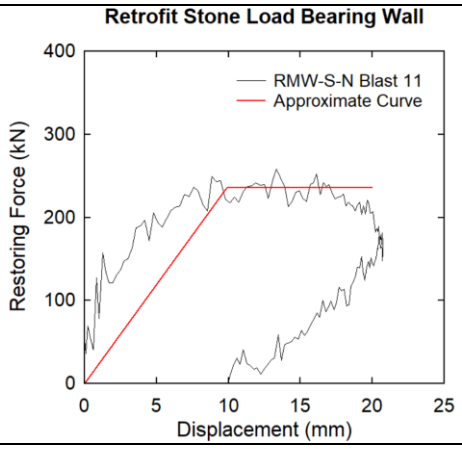

Figure 6-12. Approximate Resistance Functions for Retrofit Stone Walls

6.3.5.1. Stone Infill Retrofit Walls

The ultimate capacity for the stone infill retrofit walls was found using sectional analysis. The method used to develop the restoring force-displacement function is identical to the one described in Section 6.3.4.1.

6.3.5.2. Stone Load Bearing Retrofit Walls

The ultimate capacity for the stone load bearing wall was calculated using sectional analysis to find the resisting moment from the wall and arching action (see Section 6.3.4.2).

6.4. SDOF ANALYSIS

An SDOF analysis was performed for all the walls tested in this thesis, save for URM-S-N, since no restoring force-displacement relationship could be generated using the described method in Section 6.2.1.

Using the built idealized restoring force-displacement relationships and an estimation of the mass of the wall, an SDOF analysis was performed using software RC Blast (Jacques, 2014) to estimate the displacement time history of the walls for each test. The governing equation used in the SDOF analysis is shown in Equation 6.3.19. The equation is the same as Equation 6.2.2, save that the forcing function is in terms of pressure which is idealized as a triangular function, and surface area of the wall ($4m^2$). The load mass factor was assumed to be 0.78 during elastic response and 0.66 during plastic response, which corresponds to the factors for simply supported members (UFC 3-340-02).

$$K_{LM}m\ddot{u}(t) + R\big(u(t)\big) = AP_r(t) \qquad [\mathbf{6.3.19}]$$

The SDOF analysis results for the load bearing URM wall and the retrofit walls are presented in **Table 6-6** and **Table 6-7**, respectively. The statistical data is found in **Table 6-8**. **Figure 6-13** shows sample comparisons between experimental and analytical displacements for the retrofit walls while **Figure 6-14** shows sample displacement time histories for the load bearing URM wall. **Figure 6-15** compares all the analytical and experimental results.

The analysis for the URM load bearing stone wall had a mean error of 31%, with a maximum error of 50% and a minimum error of 16%. The analysis consistently underestimated the actual displacement tests by on average 5mm. Due to the lower values of deflection in the earlier tests, the percent error in the earlier tests are higher than those during the later tests. It is recommended that future research is directed into analyzing the resistance relationship of URM walls.

For the analysis that accounted for the shotcrete overlay, it was found that the mean error was 30%, with a maximum error of 50% and a minimum of 8%. In general, the larger error was found in the tests performed at the start of the series, where the difference between measured and calculated displacements were under 5 mm, but still resulted in high percent error. At the start of testing, it is possible that the wall was settling against its restraints, which can also increase the error. Over the course of testing, it seems that the error decreased but remained relatively high. As damage was sustained by the wall, it is expected that the measured values would be larger than the analytical values.

For the analysis that neglected the shotcrete overlay, it was found that the mean error was 28%, with the maximum at 50% and the minimum at 7%. This method was found to align better with the measured values for the later tests on the wall. For example, for RMW-C-N, the error at blast 7 and 9 was 26% and 34% for the analysis with shotcrete, but without the shotcrete the error was 6.8% and 6.6%. It seems that the analysis without shotcrete tends towards the actual values as the damage in the shotcrete increases.

Table 6-6. SDOF Analysis for URM Load Bearing Wall

Walls	Blast #	Idealized Shockwave properties[1]			Maximum Mid-span Displacements[2]		
		P_r	I_r	t_d	δ_{max}	δ_{anls}	% Error
		(kPa)	(kPa·msec)	(msec)	(mm)	(mm)	
URM-S-L	1	13.5	96	14.2	5.8	2.9	50.0%
	2	26.6	194	14.6	11.7	6.6	43.6%
	3	33.9	270	15.9	15.5	10	35.5%
	4	39.5	316	16	18.3	13.1	28.4%
	5	43.7	350	16	21.7	17.4	19.8%
	6	46.5	379	16.3	28.2	21.7	23.0%
	7	50.2	444	17.7	38.4	32.3	15.9%
	8	57.1	514	18	n/a	failed	n/a

Table 6-7. SDOF Analysis for Retrofit Walls

Walls	Blast #	Idealized Shockwave properties[1]			Maximum Mid-span Displacements[2]				
		P_r	I_r	t_d	δ_{max}	δ_{anls}		% Error	
		(kPa)	(kPa·msec)	(msec)	(mm)	w Shot. (mm)	w/o Shot. (mm)	w Shot.	w/o Shot.
RMW-C-N	1	13.1	100	15.3	4.3	2.7	2.7	37.2%	37.2%
	2	21.6	164	15.2	8.8	4.4	4.4	50.0%	50.0%
	3	35.9	276	15.4	11.3	7.5	8.2	33.6%	27.4%
	5	45.5	369	16.2	16.6	9.9	12.8	40.4%	22.9%
	7	54.3	459	16.9	17.6	13	18.8	26.1%	6.8%
	9	63.6	604	19	28.8	18.9	30.7	34.4%	6.6%
	10	72.4	688	19	215.1	23.9	Failed	n/a	n/a
RMW-C-L	2	25.9	216	16.7	11.5	5.7	5.7	50.4%	50.4%
	5	40	336	16.8	16.4	8.8	8.8	46.3%	46.3%
	9	61.5	581	18.9	24.9	14.9	17.4	40.2%	30.1%
	10	71.6	730	20.4	28.2	19.7	25	30.1%	11.3%
	12	97.4	920	18.9	100.6	30.9	Failed	n/a	n/a
RMW-S-N	2	29.3	208	14.2	8.8	4.5	4.5	48.9%	48.9%
	5	48.3	372	15.4	15.4	7.9	8	48.7%	48.1%
	7	59.3	474	16	18.3	10	10.9	45.4%	40.4%
	9	70.1	529	15.1	21.8	11.7	13.2	46.3%	39.4%
	10	97	868	17.9	27.1	23.2	29.8	14.4%	10.0%
	11	102.9	1029	20	33.5	29.9	Failed	10.7%	n/a
	14	113.8	1155	20.3	146	Failed	Failed	n/a	n/a
RMW-S-L	2	34.1	247	14.5	4.9	5.3	5.4	8.2%	10.2%
	5	56.4	437	15.5	8.1	9.3	9.3	14.8%	14.8%
	7	61.9	501	16.2	9.5	10.5	10.5	10.5%	10.5%

	9	75.6	677	17.9	11.4	13.6	14.4	19.3%	26.3%
	10	86	774	18	13.9	15.8	17.4	13.7%	25.2%
	12	100.7	1022	20.3	19.8	21.7	Failed	9.6%	n/a
	13	107.1	1125	21	20.6	24.8	Failed	20.4%	n/a
	15	109.9	1638	29.8	139.4	Failed	Failed	n/a	n/a

Table 6-8. Statistical Data for SDOF Analysis

		Retrofit Walls		Control Wall	All walls
	$\delta_{anls}/\delta_{max}$	w shotcrete	w/o shotcrete		
Statistical Data	Mean	30.4%	28.2%	30.9%	28.9%
	Std Dev.	0.150	0.156	0.117	0.148
	Max.	50.4%	50.4%	50.0%	50.4%
	Min.	8.2%	6.6%	15.9%	6.6%

SDOF Analysis Compared with Experimental Data for Retrofit Walls

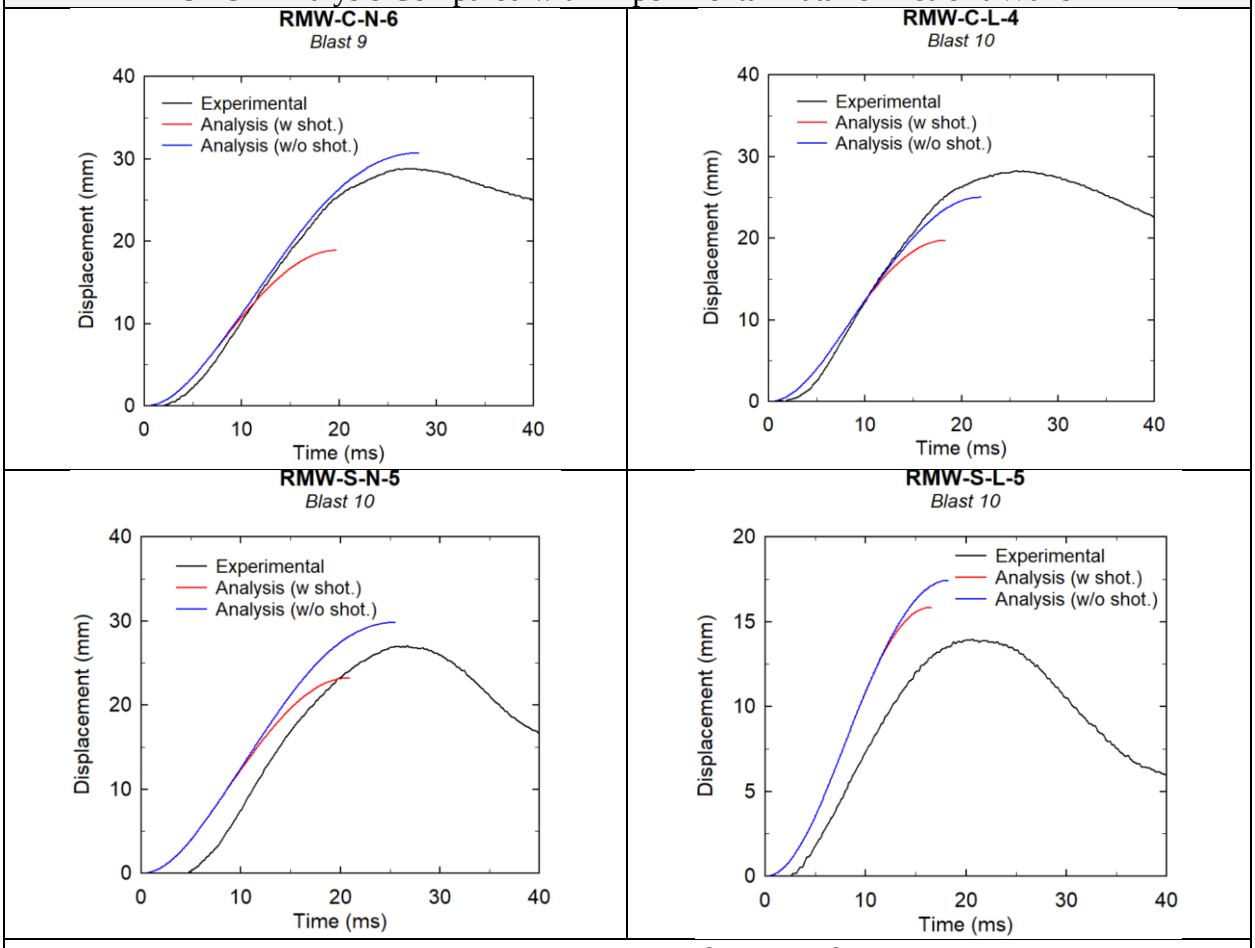

Figure 6-13. SDOF Analysis for Retrofit Walls

SDOF Analysis Compared with Experimental Data for Stone URM Wall

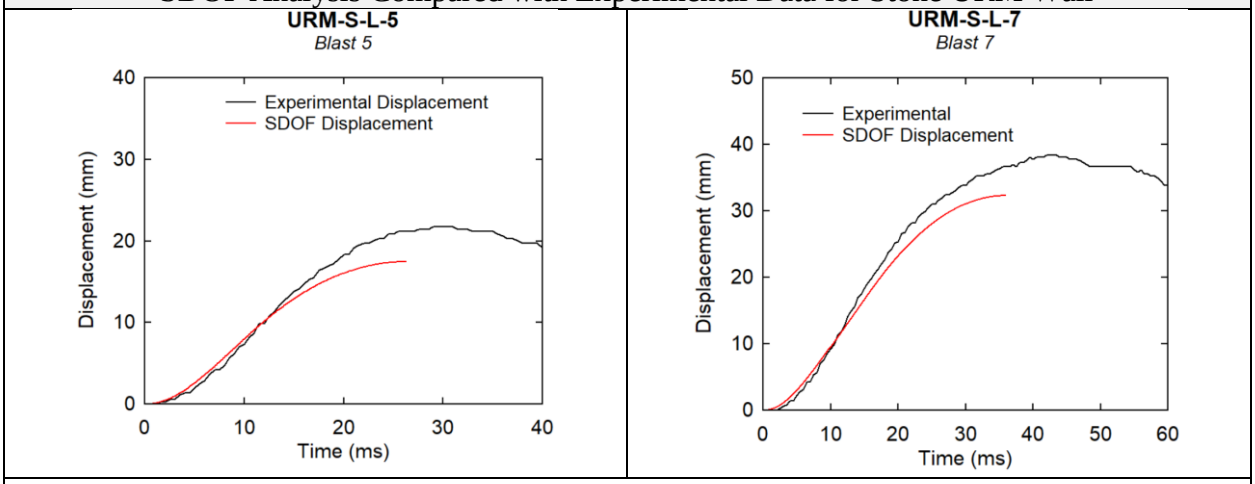

Figure 6-14. SDOF Analysis for Stone Load Bearing URM Wall

Analytical vs. Experimental Displacements

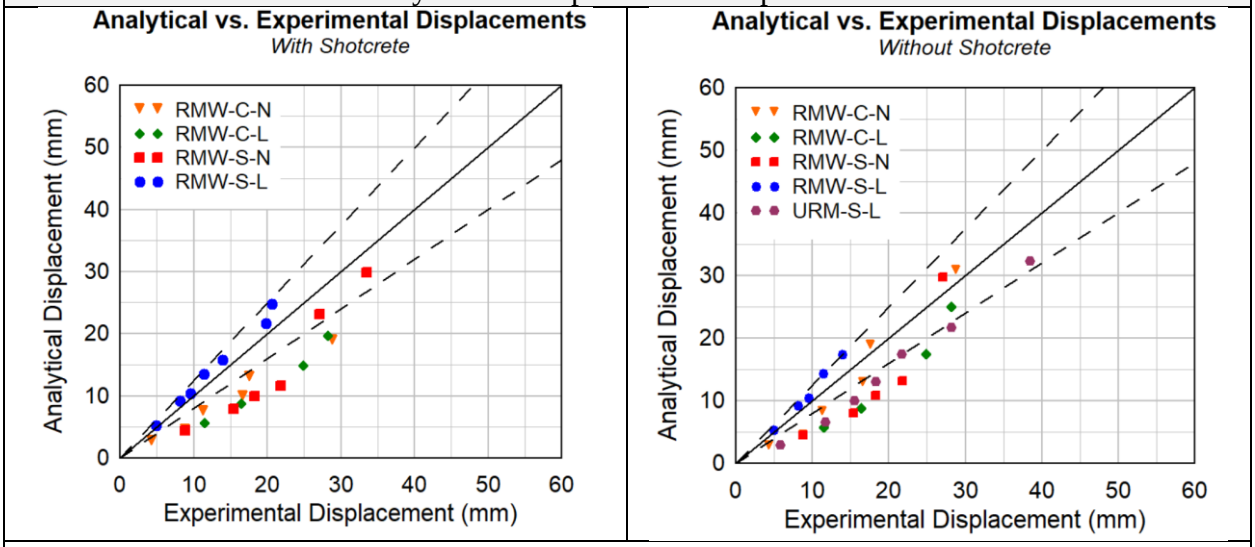

Figure 6-15. Analytical vs. Experimental Displacements

CHAPTER 7. CONCLUSION

7.1. CONCLUSION

This thesis presented a research program designed to test the effectiveness of using a high-performance fiber-reinforced shotcrete system (ECC) to improve the blast performance of existing URM walls. The motivation for this research was the lack of experimental data relating to ECC as a material used in blast resistant design of URM walls.

Six walls were built for this research to test several parameters including the effect of the shotcrete retrofit system, the effect of axial load and the effect of masonry type (CMU vs stone). The walls were tested in the University of Ottawa's Shock-tube chamber with repeated blast loads until failure.

The main conclusions for the walls tested in this thesis are outlined below:

- The use of an ECC shotcrete retrofit system can greatly strengthen the out-of-plane resistance of URM masonry walls. The ultimate resistance of the walls was significantly increased by the retrofit, and the maximum and residual displacements were greatly reduced. Furthermore, the system reduced the damage sustained by the walls.
- The shotcrete retrofit system generally improved the mode of failure of the URM walls. The retrofit was able to contain virtually all debris and prevented complete collapse of the walls. The shotcrete bonded very well to the masonry which kept the wall from falling apart, even at failure.
- The use of a ductile steel mesh in the ECC shotcrete is highly recommended, since the shotcrete system failed in a brittle manner. When the fibers experience complete pullout, the mesh is intended to provide a secondary resisting mechanism which can ensure ductile failure; however, if the area of steel is not large enough, the mesh will rupture.
- The presence of axial load was found to strengthen the out-of-plane resistance of the control and retrofit walls. The load bearing retrofit walls survived larger blasts than their infill counterparts. However, the load did not have as major of an effect on maximum and residual displacements for the retrofit walls as it did for the control URM walls. The URM walls greatly benefited with the presence of axial load by increasing the capacity and lowering the maximum and residual displacements due to the effect of arching action; this was particularly evident in the stone series wall tests. The axial load was also shown to decrease the damage sustained by the walls, since the cracks in the shotcrete would close when the wall reverted to its residual state.
- The masonry type was not found to greatly affect the performance of the retrofit system for infill walls, save that the stone retrofit wall had a higher out-of-plane resistance than the CMU retrofit wall. These retrofit infill walls largely experienced the same maximum and residual displacements. However, for the load bearing retrofit walls, the stone wall had a higher ultimate resistance than the CMU wall, as well as a greater stiffness. Furthermore, the stone wall sustained less damage than the CMU wall.
- The masonry type was also found to affect the behaviour of the control walls. In the infill series, the CMU wall performed much better than the stone wall, which showed very limited out-of-plane blast resistance. However, application of axial load significantly improved the performed of the URM stone wall. As a result, the load bearing URM stone series specimen outperformed its CMU counterpart.

- Resistance functions were developed for the walls by subtracting the inertial forces of the wall from the forcing function as described by the equation of motion. The idealized restoring force-displacement relationships were developed analytically for the control load bearing walls using a trilinear approach. Resistance functions were also developed for the retrofit wall using a sectional analysis approach which accounts for axial load, masonry, steel mesh and shotcrete contributions.
- Using the developed resistance functions, a dynamic inelastic SDOF analysis was performed to predict the maximum response of the walls. In general, the analysis under-predicted the response of the retrofit walls, since it didn't account for accumulated damage and pullout of the fibers in the shotcrete. For most of the walls, better results were obtained when conservatively ignoring the fiber contribution.

7.2. RECOMMENDATIONS FOR FUTURE RESEARCH

The following points are recommended for future studies to further improve our understanding of ECC shotcrete retrofit systems:

- Further investigate the effect caused by the thickness of the shotcrete overlay
- Determine the effect of different fiber types in the shotcrete. Evaluate the performance of different types of FRC, as well as UHP-FRC as a blast retrofit for URM walls.
- Complete research regarding the effect of the mesh size and types to promote more ductile modes of failure, as well as anchoring methods at the supports
- Evaluate the tensile behaviour of ECC shotcrete under high strain rates
- Evaluate the behaviour of retrofit URM walls under close-in blast (near field) conditions
- Determine the restoring force-displacement relationship of a URM wall retrofit with ECC shotcrete through static loading
- Determine the resistance of a URM wall in the strength decay region
- Perform FEM analysis on retrofit URM walls subjected to blast loads.

REFERENCES

Abou-Zeid, B. M., El-Dakhakhni, W. W., Razaqpur, A. G., & Foo, S. (2011). Response of arching unreinforced concrete masonry walls to blast loading. Journal of Structural Engineering, 137(10), 1205-1214.

Alsayed, S. H., Elsanadedy, H. M., Al-Zaheri, Z. M., Al-Salloum, Y. A., & Abbas, H. (2016). Blast response of GFRP-strengthened infill masonry walls. Construction and Building Materials, 115, 438-451. Retrieved Jul, from Article database.

Baylot, J. T., Bullock, B., Slawson, T. R., & Woodson, S. C. (2005). Blast response of lightly attached concrete masonry unit walls. Journal of Structural Engineering-Asce, 131(8), 1186-1193. Retrieved Aug, from Article database.

Braimah, A., (2017). Blast Threat Risk Analysis [Powerpoint]. Retrieved from Carleton University Blast Loads on Structures cuLearn website.

Broekaert, M. (2002). Polyurea spray coatings. The Technology and Latest Developments. Paint & Coatings Industry, 18(10), 80-82.

Bruneau, M. (1994). State-of-the-art report on seismic performance of unreinforced masonry buildings. Journal of Structural Engineering, 120(1), 230-251.

Cengiz, O., & Turanli, L. (2004). Comparative evaluation of steel mesh, steel fibre and high-performance polypropylene fibre reinforced shotcrete in panel test. Cement and Concrete Research, 34(8), 1357-1364. Retrieved Aug, from Article database.

Chen, L., Fang, Q., Fan, J. Y., Zhang, Y. D., Hao, H., & Liu, J. C. (2014). Responses of Masonry Infill Walls Retrofitted with CFRP, Steel Wire Mesh and Laminated Bars to Blast Loadings. Advances in Structural Engineering, 17(6), 817-836. Retrieved Jun, from Article database.

Ciornei, L., (2012). Performance of polyurea retrofitted unreinforced concrete masonry walls under blast loading. Ottawa-Carleton Institute for Civil Engineering

Davidson, J. S., Fisher, J. W., Hammons, M. I., Porter, J. R., & Dinan, R. J. (2005). Failure mechanisms of polymer-reinforced concrete masonry walls subjected to blast. Journal of Structural Engineering-Asce, 131(8), 1194-1205. Retrieved Aug, from Article database.

Davidson, J. S., Porter, J. R., Dinan, R. J., Hammons, M. I., & Connell, J. D. (2004). Explosive testing of polymer retrofit masonry walls. Journal of Performance of Constructed Facilities, 18(2), 100-106. Retrieved May, from Article database.

Dinan, R., Fisher, J., Hammons, M. I., & Porter, J. R. (2003). Failure mechanisms in unreinforced concrete masonry walls retrofitted with polymer coatings. Air Force Research Lab Tyndall AFB FL.

Doherty, K., Griffith, M. C., Lam, N., & Wilson, J. (2002). Displacement ‐ based seismic analysis for out ‐ of ‐ plane bending of unreinforced masonry walls. Earthquake engineering & structural dynamics, 31(4), 833-850.

Drysdale, R., Hamid, A., (2005). Masonry Structures: Behaviour and Design. Canadian Edition. Canada Masonry Design Centre, Mississauga, Ontario.

ElGawady, M. A., Lestuzzi, P., & Badoux, M. (2006, March). Retrofitting of masonry walls using shotcrete. In 2006 NZSEE Conference, Paper (Vol. 45).

ElSayed, M., El-Dakhakhni, W., & Tait, M. (2015). Resilience Evaluation of Seismically Detailed Reinforced Concrete-Block Shear Walls for Blast-Risk Assessment. Journal of Performance of Constructed Facilities, 30(4), 04015087.

Gagnet, E. M., Hoemann, J. M., & Davidson, J. S. (2017). Assessment of resistance definitions used for blast analysis of unreinforced masonry walls. International Journal of Protective Structures, 8(1), 125-151.

Ginouse, N. Reny, S. and Jolin, M. "Engineered Fiber Reinforced Shotcrete for Efficient and Fast Ground Support Installation" in "Shotcrete for Underground Support XII", Professor Ming Lu, Nanyang Technological University Dr. Oskar Sigl, Geoconsult Asia Singapore PTE Ltd. Dr. GuoJun Li, Singapore Metro Consulting Eds, ECI Symposium Series, (2015). http://dc.engconfintl.org/shotcrete_xii/16

Glanville, J. I., Ben-Omran, H., & Hatzinikolas, M. (1996). Engineered masonry design: limit states design. Winston House.

Gupta, P., Banthia, N., & Yan, C. (2000). Fiber reinforced wet-mix shotcrete under impact. Journal of Materials in Civil Engineering, 12(1), 81-90. Retrieved Feb, from Article database.

Hofler, J., Schlumpf, J. (2004). Shotcrete in Tunnel Construction. Retrieved from Sika Website. http://can.sika.com/en/solutions-and-products/document-download/Admixture_Manual.html

Impi Wire. (n.d.). Image retrieved from https://www.impiwire.co.za/mesh/diamond-mesh/

Irshidat, M., Al-Ostaz, A., Cheng, A. H. D., & Mullen, C. (2011). Nanoparticle Reinforced Polymer for Blast Protection of Unreinforced Masonry Wall: Laboratory Blast Load Simulation and Design Models. Journal of Structural Engineering-Asce, 137(10), 1193-1204. Retrieved Oct, from Article database.

Ismail, N., & Ingham, J. M. (2016). In-plane and out-of-plane testing of unreinforced masonry walls strengthened using polymer textile reinforced mortar. Engineering Structures, 118, 167-177. Retrieved Jul, from Article database.

Jaques, E. (2014). RC Blast. Version 0.5.1. Retrieved from http://www.rcblast.ca/

Johnson, C. F., Slawson, T. R., Cummins, T. K., & Davis, J. L. (2004). Concrete masonry unit walls retrofitted with elastomeric systems for blast loads. Engineer Research And Development Center Vicksburg MS.

Jolin, M. J.-D. Lemay, N. Ginouse, B. Bissonnette, and É. Blouin-Dallaire., (2015). "The Effect Of Spraying On Fiber Content And Shotcrete Properties" in "Shotcrete for Underground Support XII", Professor Ming Lu, Nanyang Technological University Dr. Oskar Sigl, Geoconsult Asia Singapore PTE Ltd. Dr. GuoJun Li, Singapore Metro Consulting Eds, ECI Symposium Series. http://dc.engconfintl.org/shotcrete_xii/14

King Shotcrete Solutions. (n.d.). FS-T3 UG4 Datasheet.

Kolsch, H. (1998). Carbon fiber cement matrix (CFCM) overlay system for masonry strengthening. Journal of Composites for Construction, 2(2), 105-109.

Lampropoulos, A., Tsioulou, O., & Dritsos, S. (2018). Numerical Investigation of Strengthened Unreinforced Masonry (URM) Structures with Ultra High Performance Fibre Reinforced (UHPFRC) Layers. High Tech Concrete: Where Technology and Engineering Meet. 156-164. DOI 10.1007/978-3-319-59471-2_20

Lin, Y., Lawley, D., Wotherspoon, L., & Ingham, J. M. (2016). Out-of-plane Testing of Unreinforced Masonry Walls Strengthened Using ECC Shotcrete. Structures, 7, 33-42. Retrieved Aug, from Article database.

Lloyd, A. (2010). Performance of reinforced concrete columns under shock tube induced shock wave loading (Doctoral dissertation, University of Ottawa (Canada)).

Maalej, M., Lin, V. W. J., Nguyen, M. P., & Quek, S. T. (2010). Engineered cementitious composites for effective strengthening of unreinforced masonry walls. Engineering Structures, 32(8), 2432-2439. Retrieved Aug, from Article database.

Maalej, M., Zhang, J., Quek, S. T., & Lee, S. C. (2004). High-velocity impact resistance of hybrid-fiber engineered cementitious composites. In Proc. 5th Int. Conf. on Fracture Mechanics of Concrete and Concrete Structures (FraMCoS-5) (pp. 1051-1058).

Maji, A. K., Brown, J. P., & Urgessa, G. S. (2008). Full-scale testing and analysis for blast-resistant design. Journal of Aerospace Engineering, 21(4), 217-225. Retrieved Oct, from Article database.

Makris, N., & Konstantinidis, D. (2003). The rocking spectrum and the limitations of practical design methodologies. Earthquake engineering & structural dynamics, 32(2), 265-289.

Meisl, C. S., Elwood, K. J., & Ventura, C. E. (2007). Shake table tests on the out-of-plane response of unreinforced masonry walls This article is one of a selection of papers published in this Special Issue on Masonry. Canadian Journal of Civil Engineering, 34(11), 1381-1392.

Melançon, C. (2016). Effect Of High-Performance Concrete And Steel Materials On The Blast Performance Of Reinforced Concrete One-Way Slabs. University of Ottawa. Canada

Myers, J. J., Belarbi, A., & El-Domiaty, K. A. (2004). Blast resistance of FRP retrofitted un-reinforced masonry (URM) walls with and without arching action. The Masonry Society Journal, 22(1), 9-26.

Oesterle, M. G., Hegemier, G. A., & Morrill, K. B. (2009). Response of concrete masonry walls to simulated blast loads. In Structures Congress 2009: Don't Mess with Structural Engineers: Expanding Our Role (pp. 1-10).

Papanicolaou, C. G., Triantafillou, T. C., Papathanasiou, M., & Karlos, K. (2008). Textile reinforced mortar (TRM) versus FRP as strengthening material of URM walls: out-of-plane cyclic loading. Materials and Structures, 41(1), 143-157. Retrieved Jan, from Article database.

Saatcioglu, M., Eldabelsy, G., Majeed, M. (2018) Determination of the influence of masonry bond pattern on the out-of-plane resistance of historic masonry walls. Submitted to: Natural Resources Canada, Canadian Explosives Research Laboratory

Sabri, A. (2018). Seismic Retrofit of Unreinforced Masonry Walls with Reinforcing and Prestressing Steel. Research Proposal. University of Ottawa.

Sahmaran, M., Lachemi, M., Hossain, K. M. A., Ranade, R., & Li, V. C. (2009). Influence of Aggregate Type and Size on Ductility and Mechanical Properties of Engineered Cementitious Composites. Aci Materials Journal, 106(3), 308-316. Retrieved May-Jun, from Article database.

Sharif, I., Meisl, C. S., & Elwood, K. J. (2007). Assessment of ASCE 41 height-to-thickness ratio limits for URM walls. Earthquake Spectra, 23(4), 893-908.

Simsir, C. C., Aschheim, M. A., & Abrams, D. P. (2004, August). Out-of-plane dynamic response of unreinforced masonry bearing walls attached to flexible diaphragms. In 13th World Conference on Earthquake Engineering (pp. 1-6).

Soleimani-Dashtaki, S., Soleimani, S., Wang, Q., Banthia, N., & Ventura, C. E. (2017). Effect of high strain-rates on the tensile constitutive response of Ecofriendly Ductile Cementitious Composite (EDCC). Procedia engineering, 210, 93-104.

Soleimani-Dashtaki, S., Ventura, C. E., & Banthia, N. (2017). Seismic strengthening of unreinforced masonry walls using sprayable eco-friendly ductile cementitious composite (EDCC). Procedia engineering, 210, 154-164.

Stacey, T. R., & Ortlepp, W. D. (2001). Tunnel surface support - capacities of various types of wire mesh and shotcrete under dynamic loading. Journal of the South African Institute of Mining and Metallurgy, 101(7), 337-342. Retrieved Oct, from Article database.

Standard, A.S.T.M. (2010). Standard Test Methods for Compressive Strength of Cylindrical Concrete Specimens. ASTM C39.

Standard, A.S.T.M. Standard Practice for Preparing and Testing Specimens from Shotcrete Test Panels. ASTM ‐ C1140

Standard, A.S.T.M. Standard Test Method for Compressive Strength of Hydraulic Cement Mortars (Using 2 ‐ in. or [50 ‐ mm] Cube Specimens). ASTM ‐ C109. C109/C109M ‐ 13

Standard, A.S.T.M. Standard Test Method for Flexural Performance of Fiber-Reinforced Concrete (Using Beam with Third-Point Loading). ASTM ‐ C1609

Standard, A.S.T.M. Standard Test Method for Obtaining and Testing Drilled Cores of Shotcrete. ASTM ‐ C1604

Standard, American Concrete Institute. (2008). ACI 506.1. Guide to Fiber Reinforced Shotcrete.

Standard, American Concrete Institute. (2018). ACI CT-18. ACI Concrete Terminology.

Standard, American Society of Civil Engineers. (2014). ASCE-41-13. Seismic Evaluation and Retrofit of Existing Buildings.

Standard, British Standards Institution, (1985). BS 5628. "Code of Practice for Use of Masonry: Part 1 – Structural Use of Unreinforced Masonry," BSI, London.

Standard, Canadian Standards Association. (2004). CSA S304. 1-04: Design of masonry structures. Mississauga, ON, Canada.

Standard, Canadian Standards Association. (2012). CSA S850-12. Design and Assessment of Buildings Subjected to Blast Loads. CSA Group. ISBN 978-1-55491-824-9

Standard, USACE (U.S. Army Corps of Engineers). (2008). "Structures to resist the effect of accidental explosions." UFC 3-340-02, Naval Facilities Engineering Command, and Air Forces Civil Engineer Support Agency, Washington, DC.

Tan, K. H., & Patoary, M. K. H. (2009). Blast Resistance of FRP-Strengthened Masonry Walls. I: Approximate Analysis and Field Explosion Tests. Journal of Composites for Construction, 13(5), 422-430. Retrieved Sep-Oct, from Article database.

Teng, J. G., Chen, J. F., Smith, S. T., & Lam, L. (2003). Behaviour and strength of FRP-strengthened RC structures: A state-of-the-art review. Proceedings of the ICE - Structures and Buildings, 156(1), 51-62. doi:10.1680/stbu.2003.156.1.51

The Canadian Press. (July, 2016). *Lac Megantic residents call for rail safety on anniversary of tragedy*. Retrieved from https://www.macleans.ca/news/lac-megantic-residents-call-for-rail-safety-on-anniversary-of-tragedy/

Urgessa, G. S., & Maji, A. K. (2010). Dynamic Response of Retrofitted Masonry Walls for Blast Loading. Journal of Engineering Mechanics-Asce, 136(7), 858-864. Retrieved Jul, from Article database.

Wang, J., Ren, H., Wu, X., & Cai, C. (2016). Blast response of polymer-retrofitted masonry unit walls. Composites Part B: Engineering.

Zhang, J., Maalej, M., & Quek, S. T. (2007). Performance of hybrid-fiber ECC blast/shelter panels subjected to drop weight impact. Journal of Materials in Civil Engineering, 19(10), 855-863.